Université de Lille

Ecole doctorale : Sciences de la Matière, du Rayonnement et de l'Environnement

UMR 8207 CNRS, Unité Matériaux Et Transformations

INSERM U1008, Unité Advanced Drug Delivery Systems

Thèse de doctorat

Préparée et soutenue publiquement **le 18/12/2023, par**

Charline Hénaff

Pour l'obtention du grade de

Docteur en Sciences des Matériaux

Spécialité : Milieux denses, matériaux et composants

Formulation à l'état amorphe : cas de la chlorhexidine et de la riboflavine

Formulation in the amorphous state: the cases of chlorhexidine and of riboflavin

Jury

Pr. Thomas Rades	Université de Copenhague	Rapporteur
Pr. Clare Strachan	Université d'Helsinki	Rapporteur
Pr. Guy Van den Mooter	Université de Leuven	Examinateur
Dr. Maria-Inês Ré	IMT Mines d'Albi	Examinateur
Pr. Florence Siepmann	Université de Lille	Examinateur/Président
Dr. Jean-François Willart	Université de Lille	Directeur de Thèse
Pr. Juergen Siepmann	Université de Lille	Co-directeur de Thèse

Remerciements

Dans un premier temps je souhaiterais remercier mon directeur de thèse, **Dr. Jean-François Willart**, pour cette opportunité d'effectuer une thèse sous sa supervision dévouée. J'aimerais particulièrement vous remercier pour votre gentillesse, votre bienveillance ainsi que pour tout le temps que vous m'avez accordée durant cette thèse, que ce soit pour me diriger, me conseiller, me transmettre vos précieuses connaissances, ou encore pour tout votre soutien durant la rédaction de ce manuscrit.

Dans un second temps, j'aimerais remercier mon co-directeur de thèse, **Pr. Juergen Siepmann**, pour cette collaboration intéressante et pour l'opportunité d'avoir travaillé dans son unité. Je vous remercie également pour la confiance que vous m'avez accordée durant ces 3 années ainsi que pour les conseils que vous avez pu m'apporter, qui ont contribué à l'élaboration de cette thèse ainsi qu'au développement de mes connaissances.

Merci également au programme **PEARL** pour avoir rendu cette thèse encore plus enrichissante et au financement apporté par le programme recherche et innovation « **European Union's Horizon 2020** » sous la convention de subvention **Marie Sktodowska-Curie No 847568**.

Je tiens également à remercier le **Pr. Florence Siepmann** pour sa contribution à ce projet, son partage de connaissances et pour ces qualités humaines qui m'ont été bénéfiques tout au long de cette thèse. Je vous remercie également d'avoir accepté mon invitation à faire partie de mon jury de thèse.

Mes remerciements vont ensuite au **Pr. Thomas Rades** et au **Pr. Clare Strachan**, qui me font l'immense honneur de juger et d'évaluer ces 3 années de travail. Je vous remercie également pour nos discussions intéressantes, accompagnées de vos précieux conseils, lors de nos rencontres au PSSRC.

Je remercie également le **Pr. Guy Van den Mooter**, pour son accueil chaleureux au sein de son laboratoire à la KU Leuven ainsi que pour ses précieux conseils et d'avoir pris le temps de partager ses connaissances avec moi. Je vous remercie également pour avoir accepté mon invitation à faire partie de mon jury de thèse. J'en profite également pour remercier **Sien** pour son accompagnement, son partage et sa bonne humeur, ainsi que **Eline** et **Hannah**, qui ont permis de rendre ce séjour encore plus chaleureux.

Un grand merci également au **Dr. Maria Inês Ré**, de m'avoir accueillie quelques jours au sein de son laboratoire sur la plateforme Gala à Castres. Je vous remercie pour votre partage et pour vos précieux conseils donnés lors de ce séjour mais aussi lors de mon comité de suivi de thèse. Je vous remercie également pour avoir accepté mon invitation à faire partie de mon jury de thèse.

es et avec qui je partage mes plus beaux souvenirs. Je ne remercierai jamais assez la vie de m'avoir permise de croiser ton chemin.

List of abbreviations

API	Active Pharmaceutical Ingredient
ASD	Amorphous Solid Dispersion
BCS	Biopharmaceutics Classification System
BDDCS	Biopharmaceutics Drug Disposition Classification System
Chx	Chlorhexidine
CM	Co-milled
Cp	Heat Capacity
DCS	developability classification system
DMSO	Dimethyl sulfoxide
DSC	Differential Scanning Calorimetry
FaSSIF	Fasted State Simulated Intestinal Fluid
FDA	Food and Drug Administration
GI	Gastro-Intestinal
GRAS	Generally Recognized As Safe
HME	Hot melt extrusion
HPLC	High Performance Liquid Chromatography
HPMC	HydroxyPropyl Methyl Cellulose
M	Milled
MCC	Microcrystalline cellulose
MDSC	Modulated Differential Scanning Calorimetry
NCE	New Chemical Entities
NMR	Nuclear Magnetic Resonance
PEG	Polyethylene Glycol
PM	Physical mixture
PVA	Polyvinyl alcohol
PVP	Polyvinylpyrrolidone
PVP-VA	Poly(vinylpyrrolidone-co-vinyl acetate)
RCS	Refrigerated Cooling System
Rf	Riboflavin
RH	Relative Humidity
rpm	rotation per min
RT	Room Temperature
SEM	Scanning Electron Microscopy
Tg	Glass transition temperature
TGA	Thermogravimetric analysis
Tm	Melting temperature
T_t	transition temperature
T_{tr}	transformation temperature
XRPD	X-Ray Powder Diffraction

Table of Contents

INTRODUCTION

General context

A significant percentage of the new drugs introduced in the pharmaceutical pipeline exhibit a low solubility in the crystalline state and therefore never reach the patient[1]. As solubility presents itself as a significant limiting factor in the development of innovative medical treatments, it is of the most importance to focus on approaches to enhance the solubility and, hence, to improve the dissolution and the bioavailability of these drugs. To that extend, a very promising strategy consists in the formulation of the Active Pharmaceutical Ingredients (APIs) in the amorphous state[2–5]. Indeed, as the amorphous state consists of a structurally disordered solid, it possesses a higher-free energy compared to its crystalline counterpart and should thus present a higher saturation solubility[6–9]. A crystal can also exist in different forms, called polymorphic forms, which exhibit a different crystalline order[10–12]. These forms are metastable and often have stabilities and solubilities between those of the stable crystal and the amorphous form.

Apart from the physico-chemical characteristics of the API which strongly influence the selection of the amorphization process, it also has to be selected depending on the desired characteristics of the amorphous material. Indeed, the amorphization process can have an influence on many parameters such as the physical stability, the energetic level, the particle morphology or even the pharmaceutical performance of the API.

Many processes were developed in order to render a crystalline API amorphous and can be categorized in three main categories including heat/melt-based (e.g. liquid quench or hot melt extrusion[13,14]), solvent-based (e.g. spray-drying[15,16] or freeze-drying[17,18]) and mechanical based techniques (e.g. cryo-milling or ball-milling). From an industrial point of view, spray-drying and hot-melt extrusion (HME) represent the most favorite techniques for the solvent-based and the heat/melt based approaches respectively[19]. Indeed, spray-drying is considered as a continuous and commercially scalable drying process[20] meanwhile HME is considered as both a green technology (solvent-free) and a high-throughput continuous process which can also easily be scaled up for industrial purposes[21]. However, for APIs presenting thermal degradations or poor solubility in organic solvent, another approach must be considered. To that extend, mechanical-based techniques such as high-energy milling can be used. Indeed, milling is known to frequently modify the structural state of drugs by placing them in non-

equilibrium situations directly in the solid state[22] which might either lead to an amorphization[23–26], or to a polymorphic transformation[27–30]. It was reported that milling at a temperature below the glass transition temperature (Tg) of the material would often induce an amorphization whereas milling above Tg would often induce polymorphic transformations[24,31]. Fully understanding those transformations and controlling them is thus an objective of significant importance in the development of new pharmaceutical formulations using a milling stage.

Due to the inherent instability of the high-energy configuration of the amorphous state and to the eventual recrystallization into a more stable crystalline state (lower energy), APIs are rarely developed as amorphous solids[3]. Therefore, the formulation of Amorphous Solid Dispersions (ASDs) was developed in order to improve the physical stability of the drug in its amorphous state. ASDs are defined as a molecular dispersion of an amorphous API in an amorphous carrier, usually a polymer[2,32]. Indeed, it was reported that a polymer with a high Tg can have an anti-plasticizing effect on the API and, hence, hinder the nucleation and subsequent growth of crystals[33]. This feature is considered as a significant advantage for the storage of ASDs for which the API is in super-saturated conditions in the API/polymer mixture. Indeed, as long as the Tg of the mixture is above the storage temperature, the amorphous API is expected to remain kinetically stable for a long period due to the low molecular mobility. Moreover, the polymer also allows a thermodynamic stability of the amorphous as long as the API fraction in the ASD is lower than its solubility in the polymer[34]. However, the storage is not the only concern as ASDs are expected to maintain the supersaturation levels in the GI tract during the dissolution process[35]. Therefore, multiple factors are to be considered during the selection of the polymer including its hygroscopicity, aging and tackiness[36].

As a final dosage form, the oral route in the form of tablets or capsules are the most currently used for marketed ASDs[37]. However, it was reported that the compression, by inducing a mechanical stress to the ASD, could either lead to an amorphous-amorphous phase separation or to a physical stability enhancement depending on the concentration of the API, the compression force and the polymer carrier[38].

In this context, a complete understanding of the behavior of both the API (crystalline and amorphous) and of the API/polymer mixture is of most importance in order to fully control the eventual transformations and the drug properties.

Main objectives

The main objective of this thesis is to produce amorphous solid dispersions (ASDs) of poorly-soluble drugs and to compare the solubility as well as the physical stability of the APIs thus formulated with those of the pure APIs in different forms, i.e. crystalline, metastable polymorphs and amorphous form.

For this work, two model drugs are chosen including chlorhexidine free base (Chx) and riboflavin free base (Rf). Indeed, as those drugs are very-poorly soluble and crystalline, the aim is to enhance their solubility by producing formulations in the amorphous state. However, before preparing an optimized formulation, it is of the most importance to have a good understanding of the physical characteristics of the drug and of the influence of the amorphization process on the latter. Furthermore, as these specific drugs are both prone to thermal degradation and practically insoluble in most organic solvents, neither heat-based nor solvent-based amorphization processes can be used. Therefore, the amorphization must be performed directly in the solid state and to that extend, high-energy milling is selected.

After a deep investigation of the physical characteristics of the crystalline drug, the milling-induced amorphous drug is produced and followed by a physical characterization. Finally, the dissolution performances of the drug in both its crystalline and milling-induced amorphous state are evaluated for different experimental set-ups. The physical characterizations are carried out using X-ray diffraction (XRD), differential scanning calorimetry (DSC), thermogravimetric analysis (TGA) and scanning electron microscopy (SEM). The dissolution performances are tested using powder dissolution (sink and non-sink conditions), intrinsic dissolution and tablet dissolution.

The next step consists in stabilizing the drug in its amorphous state in a formulation. To that extend, the drug is molecularly dispersed in a polymer matrix by co-milling of a physical mixture of the crystalline drug and the polymer. Therefore, two polymers are chosen including polyvinylpyrrolidone (PVP) as it is widely used in the production of ASDs and Lycoat RS720, a starch-based polymer graciously offered by the company Roquette.

Furthermore, in order to assess the advantage of having an amorphous drug molecularly dispersed in the polymer in terms of drug release, three different mixtures are tested for each polymer including:

- A physical mixture of crystalline drug and polymer
- A physical mixture of milling-induced amorphous drug and polymer
- A co-amorphous mixture of drug and polymer obtained by co-milling.

For these mixtures, the physical characterizations are carried out using XRD and DSC and the drug release is evaluated for different experimental set-ups including: powder dissolution (sink and non-sink conditions), intrinsic dissolution and tablet dissolution.

Organization of the thesis

This thesis is divided in 6 chapters.

The first chapter aims to present the general concepts of condensed matter physics and the different approaches related to the formulation of amorphous solid dispersions. In particular, the concepts regarding structure and dynamics of both crystalline and amorphous state are described to give the required knowledge to have a good understanding of this work. The different amorphization processes are also presented with a focus on high-energy milling as it was the main process used in this work. The criteria to consider to choose the appropriate process were also discussed. The role and the choice of the polymer in the formulation of ASDs are also pointed out along with the physical notions and considerations regarding the drug/polymer mixtures. Finally, the different final galenic forms are also presented along with a focus on the formulation of oral tablets.

The second chapter is devoted to the presentation of the different materials and experimental techniques used during this work. Particularly, the physical characterization techniques along with the experimental set-ups for the determination of dissolution performances are deeply presented.

The third chapter presents a detailed investigation of the structural and thermodynamic impacts of both the heating and the milling on chlorhexidine free base. Particularly, the polymorphism of Chx is explored and its amorphization kinetics upon milling are determined. The dissolution performances of both

crystalline and milling-induced amorphous Chx are also studied using several experimental-ups (powder dissolution, intrinsic dissolution and tablet dissolution).

The fourth chapter is focused on the stabilization of milling-induced amorphous Chx by performing a co-amorphization with a polymer. Two polymers are studied in this chapter including PVPK12 and Lycoat RS720. Particularly the co-amorphization feasibility using milling and the evolution of the Tg of the mixture against the drug fraction are investigated. Finally, 3 different mixtures for each polymer are studied including: a physical mixture of crystalline Chx and the polymer, a physical mixture of amorphous Chx and the polymer and a co-amorphous mixture of Chx and the polymer obtained by milling. Indeed, these mixtures were chosen in order to explore the influence of the physical state of the drug on the dissolution performances for several experimental set-ups (powder dissolution, intrinsic dissolution and tablet dissolution).

The fifth chapter presents a detailed investigation of the structural and thermodynamic impacts of milling on riboflavin free base. Particularly, the recrystallization behavior of milling-induced amorphous Rf and the polymorphism of the drug are deeply studied. The dissolution performances of each form of Rf are also evaluated using several experimental-ups (powder dissolution, intrinsic dissolution and tablet dissolution).

The sixth chapter is focused on the stabilization of milling-induced amorphous Rf by performing a co-amorphization with a polymer. Two polymers are studied in this chapter including PVPK12 and Lycoat RS720. Particularly the co-amorphization feasibility using milling, the evolution of the Tg of the mixture against the drug fraction and the solubility of the drug in the polymer are investigated. Finally, 3 different mixtures for each polymer are studied including: a physical mixture of crystalline Chx and the polymer, a physical mixture of amorphous Chx and the polymer and a co-amorphous mixture of Chx and the polymer obtained by milling. Indeed, these mixtures were chosen in order to explore the influence of the physical state of the drug on the dissolution performances for several experimental set-ups (powder dissolution, intrinsic dissolution and tablet dissolution).

CHAPTER I - STATE OF THE ART AND GENERALITIES

I.1 Bioavailability challenges of the Active Pharmaceutical Ingredients (APIs)

Until recently, the primary criterion for the screening of New Chemical Entities (NCEs) as promising drug candidates was a high in vitro potency at their target[39]. However, it was reported that around 70% of those drug candidates were poorly water-soluble, which could hinder their oral bioavailability[40]. Concerning immediate release oral drugs, approximately 30 to 40% were considered as practically insoluble (solubility range <0.1 mg/mL)[41]. Therefore, the physico-chemical properties associated with high in vitro potency are usually incompatible with a good oral bioavailability[39].

I.1.1 The Biopharmaceutics Classification System (BCS)

In order to tackle the issue of the increasing amount of poorly water-soluble drug candidates in the pharmaceutical development pipelines, a universal classification that aimed to correlate the in vitro solubility and the permeability of NCEs to their in vivo oral bioavailability had to be considered. To that extend, the Biopharmaceutics Classification System (BCS) was developed in 1995 and divided APIs in four different categories[42]. An API is defined as highly soluble when the highest marketed dosage can be dissolved in 250mL over the entire Gastro-Intestinal (GI) tract, i.e. in a pH range of 1.2 to 6.8 at 37°C ± 1°C[43,44]. The permeability is considered as high when the absorbed fraction of the API after an oral administration is equal or above 85%[43,44].

As represented in Figure 1, BCS class I drugs show a high solubility and high permeability, which makes them the most promising candidates for oral administration. On the opposite, class IV drugs show both low solubility and permeability, which makes them poor candidates for oral administration. Class II drugs are limited by their solubility and dissolution rate as they show a low solubility and a high permeability. On the contrary, class III drugs are limited by their GI membrane permeation as they show a high solubility and a low permeability.
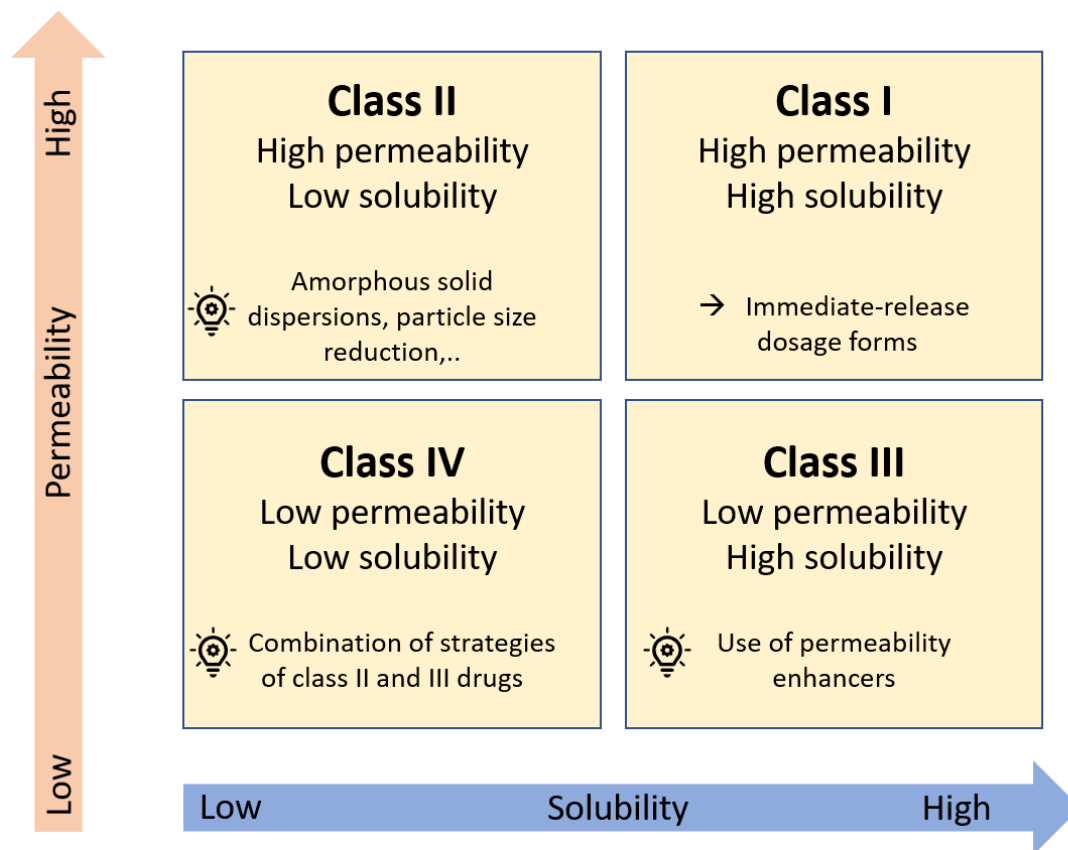
Figure 1 - BCS classification and formulation strategies to increase the solubility and/or the permeability of APIs. Adapted from Amidon et al[42] and from Pandi et al[45].

However, this classification showed some limitations as the definition of high solubility was for instance considered too strict for weak acids which were classified as class II drugs even if their solubility and their permeability in the small intestine was considered adequate[46]. This is why some extensions of the BCS classification were proposed such as:

- the ABΓ [47] system which categorizes the APIs depending on the fraction of the API that is absorbed.

- the developability classification system (DCS)[48] which introduced two subclasses for class II drugs including the dissolution rate limited and the solubility limited. The volume in which the API had to be dissolved was also increased from 250mL to 500mL and a new biorelevant dissolution medium was developed such as the Fasted State Simulated Intestinal Fluid (FaSSIF).

- the Biopharmaceutics Drug Disposition Classification System (BDDCS)[49,50] propounded to replace the permeability criterion of the BCS with the metabolic clearance of the drug.

I.1.2 Solubility and dissolution rate

As stated in the above, the bioavailability of an API can be limited either by its dissolution rate or by its solubility. It is thus important to have a good understanding of these two notions and to see how they differ. The dissolution is defined by the mixing of two separate phases which leads to a homogenous phase called a solution[51,52]. The possibility of this mixing and its degree strictly depend on the physico-chemical nature of each phase and external conditions such as temperature, pH and pressure[53,54]. The notion of dissolution is commonly used when a solid, representing the minor component and called solute, is dissolved in a liquid, representing the major component and called the solvent[52,55]. For the particular case of a crystalline API, the solvent molecules interact with any exposed surface of the solute, which induces disruptions in the crystal lattice making the API molecules to pull away from one another[2,56]. As shown in Figure 2, the separation of the API molecules allows the appearance of vacancies in the solvent, which makes room for the diffusion of the API molecules into those vacancies. This diffusion during which the API molecules are interacting with the solvent molecules is called the hydration/solvation and takes place until the molecules are uniformly dispersed throughout the solvent[57]. When a crystalline API is placed in excess in a solution, it dissolves until it reaches an equilibrium meaning that it reaches a maximum concentration in the solution which corresponds to the thermodynamic solubility[54]. This equilibrium is represented by the competition between the solvation and the precipitation and at this point, the solvent is incapable of dissolving more API[58]. However, this implies that the solid form of the API does not change over time and that it is the most stable form that is present in the solution. The notion of apparent solubility was also introduced and corresponds to the solubility of a compound when the equilibrium in a solution is reached with one of its metastable forms[59].
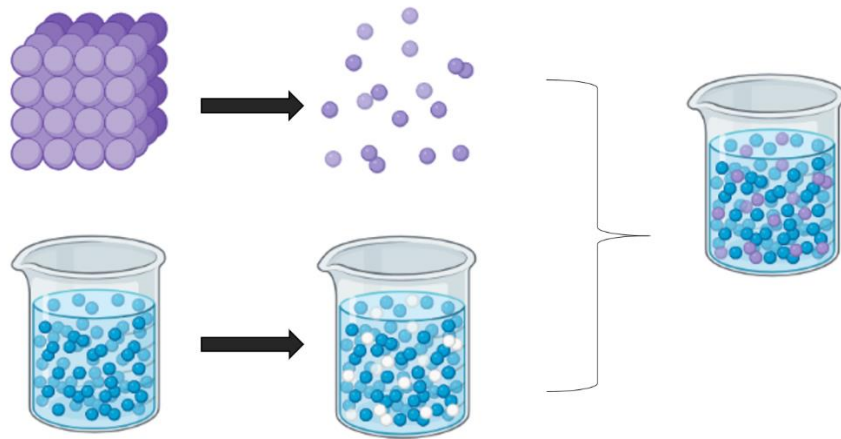
Figure 2 - The dissolution process in a solvent (blue particles and the vacancies are represented in white) of a crystalline solid (purple particles). Modified from Bellantone, 2014[56].

The dissolution rate of an API is related to kinetics as it is defined as the rate at which it passes into solution. The first model describing the dissolution was a result of the work of Noyes and Whitney[60]. In that model, the dissolution was proportional to the difference between the solubility of the solute in the solvent (saturated concentration) and the bulk concentration of the solute in the solvent. Then, a new important parameter was considered for this diffusion-based model, which was the surface area of the dissolving particle. This led to the Nernst-Brunner equation which is still used nowadays[61,62]:

$$\frac{dC}{dt} = \frac{DS}{Vh}(C_s - C_t) \quad (1)$$

Where:

- dC/dt represents the concentration of the API over time
- D is the diffusion coefficient of the solute in the solvent
- S is the specific surface area of the solute
- V is the volume of the dissolution medium (bulk fluid)
- h is the thickness of the diffusion layer of the solute
- C_s is the saturation concentration of the API (solubility)
- C_t is the concentration of the API at a given time t

Given this equation, an increase in specific surface area allows an increase in the dissolution rate, which is why particle size reduction of the crystalline API is a widely used option to improve the dissolution rate[63]. Another strategy to improve the dissolution rate is to increase the API solubility. To that extend, several approaches are available, including the addition of solubilizers such as cyclodextrins[64], the formation of salts[65] or prodrugs[66], the use of micelles[67] or the use of solid-lipid nanoparticles[68]. Recently, another approach related to the amorphous form of the API was strongly investigated and showed great promises[69]. In this thesis, the focus will be directed to the formulation of ASDs in order to improve the solubility and the dissolution rate of poorly-water soluble drugs.

I.2   Physical states of APIs

The different matter states are classified in three categories: solid, liquid and gas. Their differences mainly lie in their structures and dynamic of thermodynamic behaviors. The ideal gas is composed of single molecules with very low densities which do not interact with each other. Therefore, their positions and orientations are uncorrelated. Liquids and solids are both qualified as condensed matter but their response regarding shear stress is completely different. Indeed, as a fluid, a liquid continuously deforms itself when subjected to a shear stress whereas a solid will resist to it.

As a solid, the physical state of an API is determined depending on its molecular arrangement and can be categorized into two main types: the crystalline and the amorphous states. A crystal is characterized by a repeating pattern (an atom or a group of atoms, an ion, a molecule…) which periodically extends over long distances in a three-dimensional lattice. On the opposite, the molecules composing amorphous materials do not show any long range order but might present a certain local order for very short distances[70].
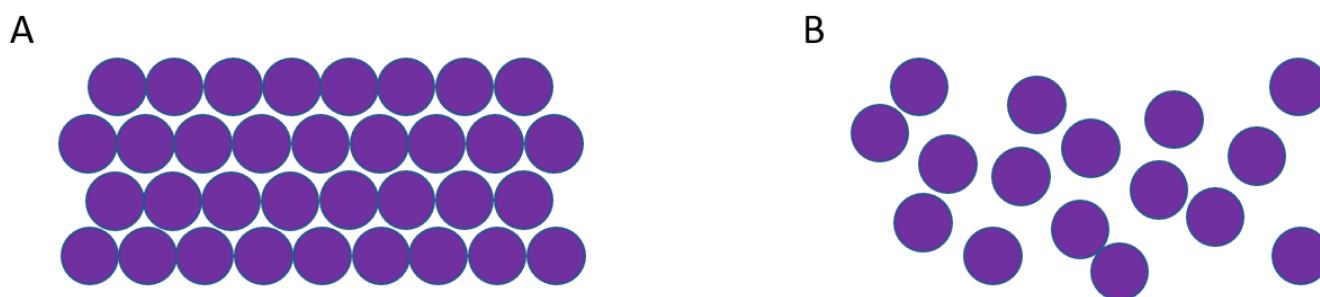
Figure 3 - Schematic representation in 2D of a material in a crystalline state (A) and in the amorphous state (B).

A same material can be found in both amorphous or crystalline state from different energetic levels. The relative stability of the different states at determined pressure and temperature is given by its Gibbs free energy G:

$$G = H - TS \qquad (2)$$

Where H is the enthalpy (heat content of the system), T is the temperature and S is the entropy (level of molecular disorder).

At a given temperature, the state with the lowest G is considered as the most stable whereas the other states are defined as metastable. This particular situation is illustrated in Figure 4, which schematizes the state Gibbs diagram of a material for both its crystalline and amorphous forms. Below the melting temperature (T_m), the Gibbs free energy of the crystal (G_{cryst}) is lower compared to the one of the amorphous form (G_{am}) whereas above the T_m, G_{am} is lower than G_{cryst}. Therefore, below T_m, the crystal is the most stable form whereas above T_m, the amorphous form becomes the most stable form.
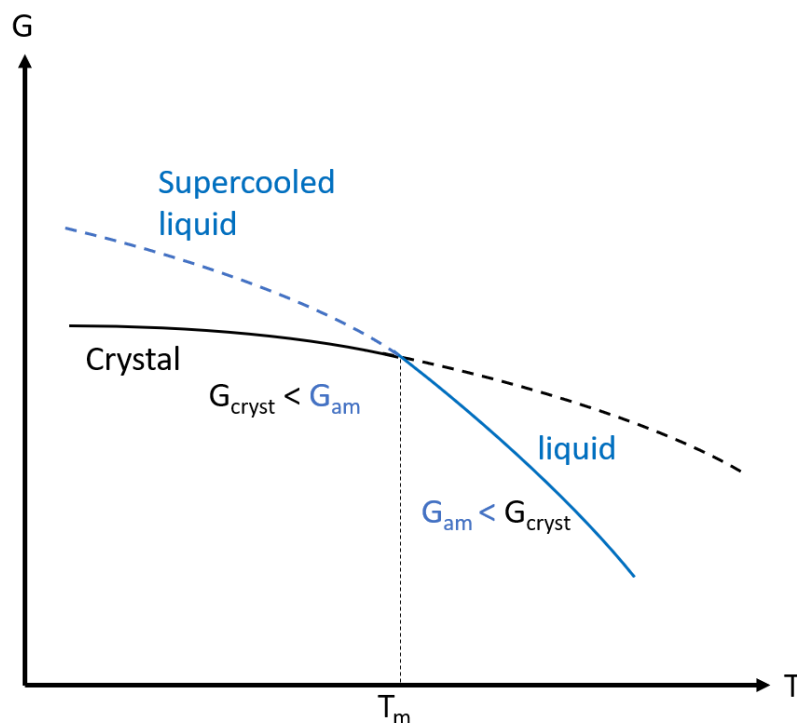
Figure 4- Gibbs diagram scheme showing the Gibbs free energy variations of a material in its crystalline and amorphous state (liquid) against temperature. G_{cryst} and G_{am} respectively represent the Gibbs free energy of the crystal and of the amorphous form.

I.2.1 The amorphous state

The most common route to obtain the amorphous form of a material is the quench of the liquid. This technique consists in the fast cooling of a formerly melt crystal in order to prevent its recrystallization below Tm as depicted in Figure 5. In that case, the amorphous material will be in a state of a supercooled liquid below the melting point, which will allow to maintain the structural disorder characteristic of a liquid. Meanwhile, several thermodynamic values including the enthalpy, the entropy, the heat capacity (C_p) and the molar volume (V) or dynamic values such as the viscosity (η) or the molecular mobility will be greatly influenced by the temperature. During the cooling stage, the molar volume decreases whereas the viscosity increases, generating a speed reduction in the different molecular movements (rotation, vibration, …). Upon cooling, structural reorganizations occur in the undercooled liquid to maintain the thermodynamic equilibrium of the system. For high temperatures, the structural relaxations happen in a relative short range of time. On the opposite, for low temperatures, the high viscosity leads to longer relaxation times compared to the cooling rate, preventing the system from operating its structural modifications to maintain the thermodynamic equilibrium. This entrance of an amorphous material into a non-equilibrium situation is called the glass transition. In that case, a high viscosity, a strong decrease of the heat capacity and of the molar volume are observed. Hence, at a molecular level, the amorphous material is similar to a liquid whereas at a macroscopic level it appears as a solid[2]. The evolution of the heat capacity and of the dilatation coefficient (α) against temperature and at a constant pressure is represented by the equations below:

$$C_p = \left(\frac{dH}{dT}\right) \qquad (3)$$

$$\text{and } \alpha = \frac{1}{V}\left(\frac{dV}{dT}\right) \quad (4)$$

The slope change observed in the evolution of the enthalpy against temperature (Figure 5) leads to both a C_p and an α jump characteristic of the transition of the supercooled liquid into the glass state during the cooling stage (Figure 6). This transition is referenced as a glass transition and occurs at a specific temperature (T_g).
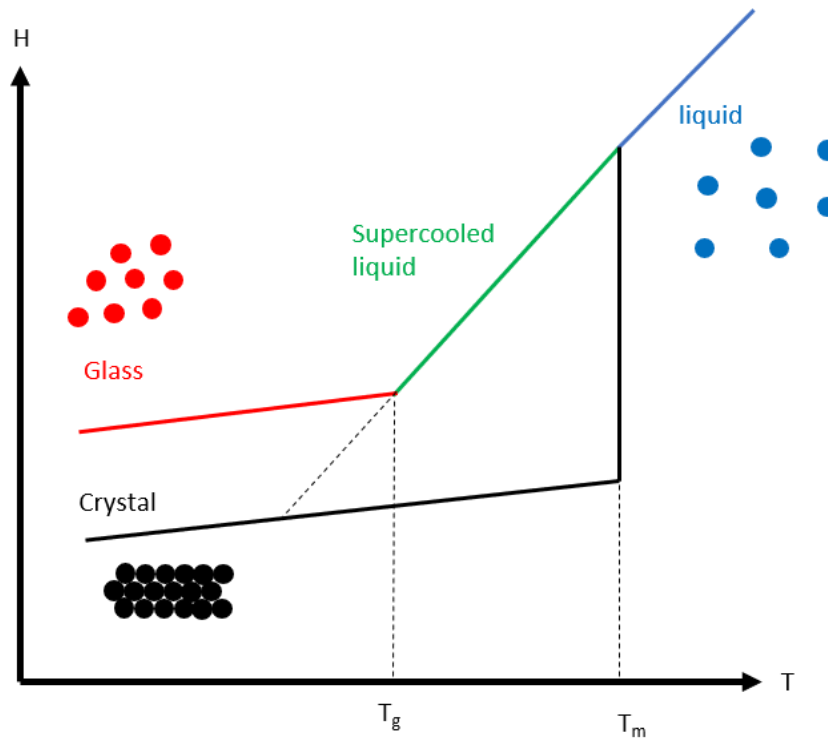
Figure 5- Enthalpy diagram of the various states of an API against temperature. Adapted from Hancock and Zografi, 1997[71].
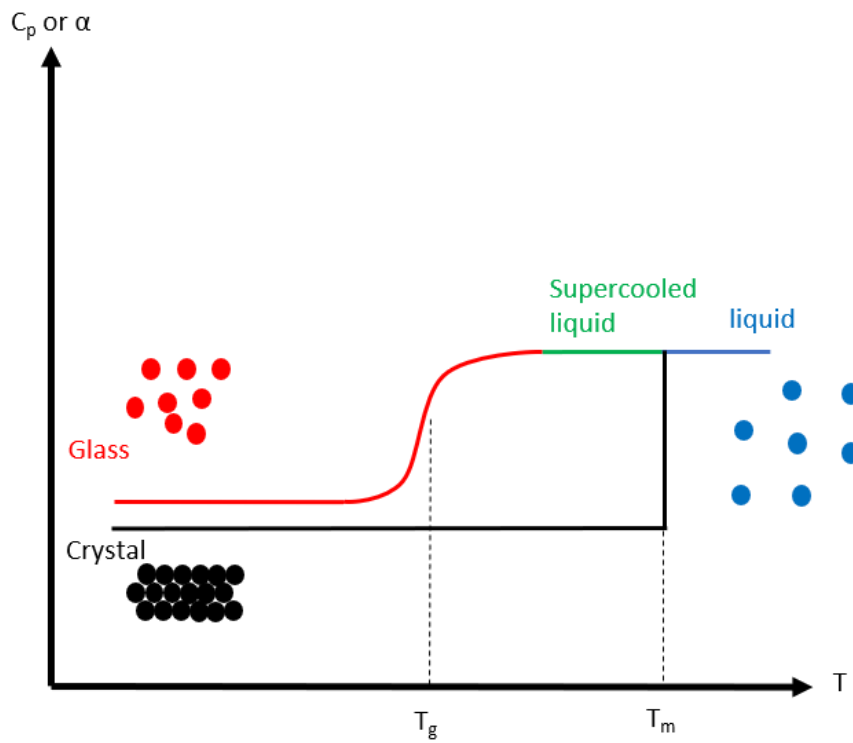
Figure 6– Heat capacity (C_p) or dilatation coefficient (α) diagram of the various states of an API against temperature.

I.2.2 From amorphous to crystalline form

As presented in the previous part, below the melting point, the material is in the supercooled liquid state and thus metastable. Hence, it will likely transform back to a more stable state with a lower energetic level, i.e to a crystalline form. The crystallization is a first order transformation amorphous → crystal with a complex mechanism which involves two different steps including the nucleation and the growth[72–75]. Whereas several theories were given to explain this mechanism[76], this phenomenon remains generally described using the classical nucleation and growth theory[77–79].

The nucleation consists in the appearance of nucleuses of a significant size to prevent their disintegration or their disappearance. The nucleation mechanism is considered heterogeneous when triggered by the presence of impurities or defects in the amorphous material[76] and homogeneous otherwise. The appearance of the nuclei depends on the competition between the interfacial energy crystal/liquid which obstructs the nuclei formation and the driving force corresponding to the Gibbs energy difference per volume unit between the crystal and the liquid. The Gibbs energy corresponding to the difference between the liquid and the crystal is given by:

$$\Delta G = G1 + G2 = 4\pi r^2 \gamma - \frac{4}{3}\pi r^3 \Delta Gv \qquad (5)$$

Where:

- γ is the interfacial free energy between the liquid and the crystal
- r is the radius of the nuclei
- ΔGv is the Gibbs energy difference per volume unit between the crystal and the liquid
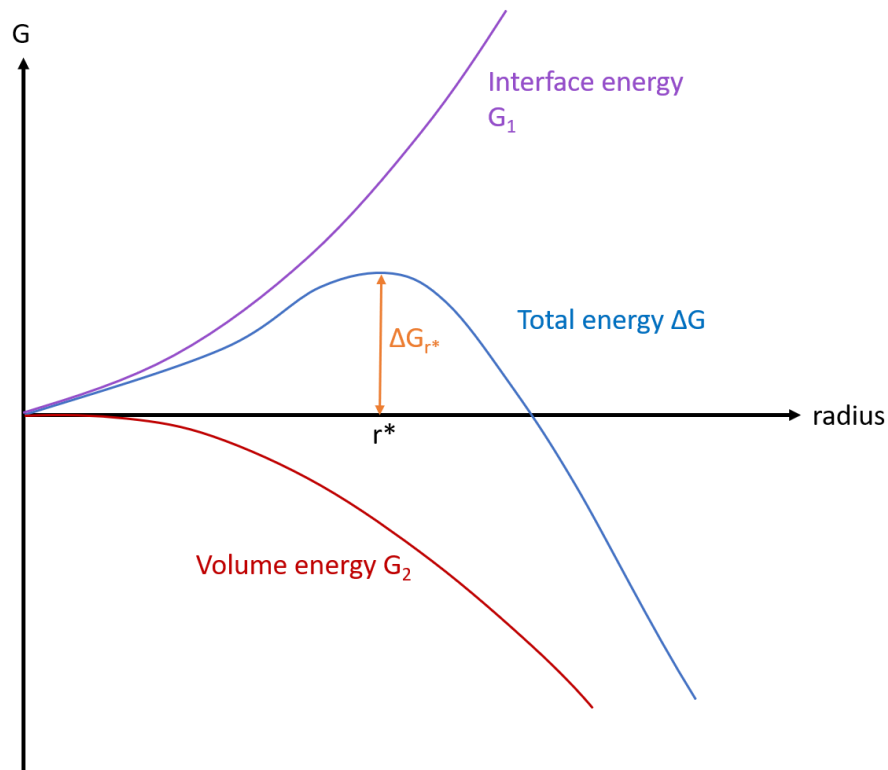
Figure 7- Evolution of the different energies, total (blue curve), interface (purple curve) and volume (red curve) against the radius of the nuclei.

Figure 7 shows the evolution of the volume energy (proportionate to r^3), the interface energy (proportionate to r^2) and the total energy against the nuclei radius. It can be noticed that the total energy ΔG reaches a maximum ΔG_{r*} for a specific radius r*. ΔG_{r*} and r* refer to the energetic barrier of the critical radius, respectively. As a result, for energy minimization considerations, nuclei for which r<r* will have a tendency to decrease and vanish, while those for which r>r* will have a tendency to grow[80].

The nucleation rate corresponds to the probability to produce stable nucleuses N per volume unit and per time unit. This rate is given by both the Arrhenius law and the homogenous nucleation rate law:

$$N \propto -\exp\left(-\frac{Q_d}{kT}\right)\exp\left(-\frac{\Delta G*}{kT}\right) \quad (6)$$

Where:

- v_d corresponds to the frequency of attachment of the atoms or of the nuclei molecules and depends on diffusion coefficient of those molecules in the liquid
- k corresponds to the Boltzman constant
- Q_d corresponds to the diffusion coefficient

The nucleation is thus more prone to occur at a low temperature. However, in this range of temperatures, kinetic phenomena can restrain the nucleation and have to be considered. The nucleation thus depends on both the fluctuations of ΔG_{r*} (thermodynamic phenomenon) and on the attachment frequency of the molecules to the nuclei (molecular mobility, kinetic phenomenon).

Figure 8 shows the evolution of the nucleation rate against temperature which is represented by a bell-shaped curve. Indeed, the nucleation reaches a maximum (top of the orange curve) at a temperature for which the energetic barrier ($\Delta G*$) is low enough to allow the formation of an energetically stable nuclei and the molecular mobility is high enough to allow the binding of the surrounding molecules to the nuclei. However, for lower temperatures, the molecular mobility decreases which leads to a decrease of the nucleation rate. For higher temperatures, even though the molecular mobility increases, the energetic barrier increases even more, leading to a decrease in the nucleation rate.
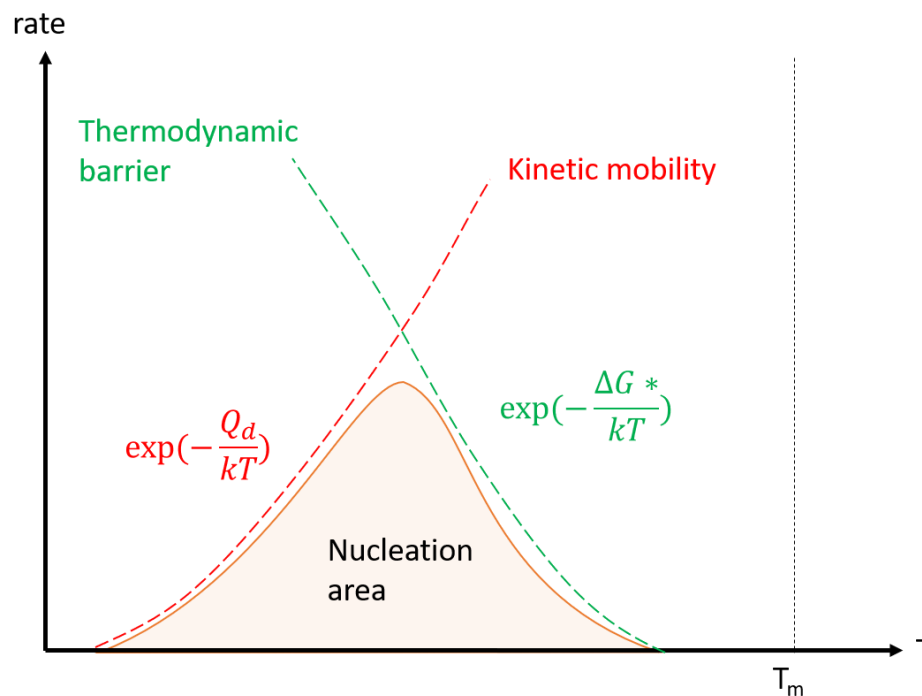
Figure 8 - Schematic representation of the nucleation rate against temperature (orange curve). The red and green dashes represent the evolution of the molecular mobility and of the thermodynamic barrier respectively.

The growth occurs when the stable nuclei (r>r*) grows with time by forming aggregates with the new molecules. The nucleation-growth theory stipulates that the growth rate is also ruled by both thermodynamic and kinetic phenomena[72,73,75,76,81]. Indeed, this rate depends on the competition between the crystallization energy (ΔG_v) and the energy barrier (ΔG_d) involved in the diffusion mechanism. During the growth, new molecules stick to the nuclei surface while other molecules are coming off it. The difference between the rates of molecules that are gained and of the ones that are lost determines the global growth rate and can be described by the Turnbull equation[82]:

$$G(T) = r\, p\, exp\left(-\frac{\Delta G_d}{kT}\right)\, exp\left(-\frac{V\Delta G_v}{kT}\right) \quad (7)$$

Where:

- p is the probability that a molecular jump contributes to the growth
- A is the energy barrier involved in the diffusion mechanism
- V is the molecular volume

Figure 9 shows the typical temperature evolutions observed for both the nucleation and the growth rates. It appears that these two rates reach their maximum for different temperatures. Generally, the maximum of the nucleation rates is located at a lower temperature compared to the maximum of the growth rate. As a result, upon cooling, there is generally no nuclei present in the liquid when passing through the zone where the growth rate is maximum. This situation explains why many liquids can be easily undercooled. On the contrary, when heating an undercooled liquid, the temperature corresponding to the maximum nucleation rate is crossed before reaching that corresponding to the maximum growth rate which causes the recrystallization of the undercooled liquid. The shift between the maxima of the nucleation and growth rates thus explains that the crystallization of liquids can often be avoided upon cooling but rarely avoided upon heating.
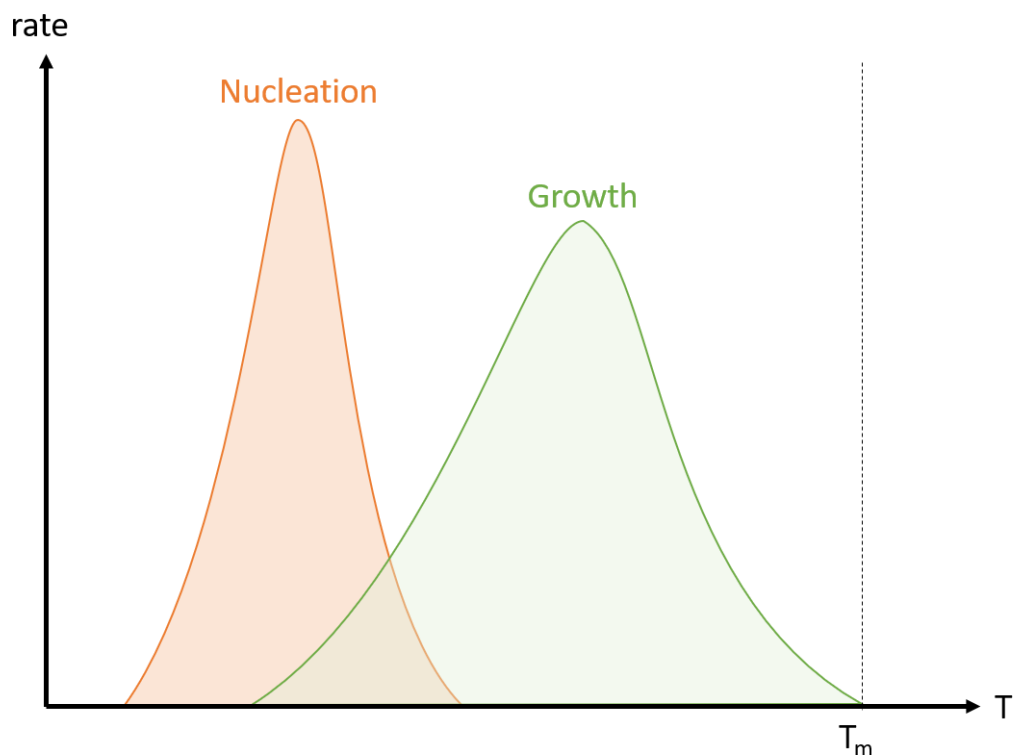
Figure 9- Schematic representation of the nucleation (N) and the growth (G) rates against temperature.

I.2.3   Polymorphism

Polymorphism is defined as the possibility for a molecule to exist in at least two distinct crystalline structures. The difference in the crystalline structure induces different physical and chemical properties for the polymorphs. It is thus crucial to identify as exhaustively as possible the different polymorphs of a drug as well as the stability relations between these forms.

The stability of the different polymorphs is governed by the thermodynamic as it depends on the temperature. Figure 10 shows the evolution of free Gibbs enthalpy (G = H - TS) of two polymorphs of the same API (A and B) against temperature. The entropy, which represents the disorder degree of the different forms is given by the slope of the curves. The liquid state, as it corresponds to a complete disorder, shows a steeper slope compared to the polymorphic forms. Even if they show different entropies, the curves of the polymorphic forms might cross at a given temperature. Depending on this given temperature, two situations are distinguished:

- Enantiotropism: as represented on Figure 10 (1), the curves cross at a transition temperature (T_t) located below the melting temperatures of both forms. In this case, polymorph A is the most stable form below T_t as G(A) < G(B) and polymorph B is thus more stable compared to polymorph A above T_t as G(B) < G(A). During the heating of polymorph A, an endothermic reversible transition A → B is therefore expected at T_t as the entropy of form B is higher compared to the one of form A. However, due to a low molecular mobility, crystal-crystal transitions kinetics are usually very slow, leading to their delay or even their bypass if the heating rate is too high in regard to the transformation kinetics.

- Monotropism: as represented on Figure 10 (2), the curves cross at a transformation temperature (T_{tr}) located above the melting temperatures of both forms so that polymorphic transition between polymorphs A and B is virtual and cannot be observed experimentally. In this case, polymorph A is the most stable form in the whole temperature range as G(A) < G(B). Thus, polymorph B is metastable in the whole range of temperature.

From a practical point of view, the enantiotropism or the monotropism between the polymorphic forms can be determined using calorimetry applying the Burger rules[83,84]:

- Two polymorphic forms show enantiotropism if the polymorph which shows the lowest melting enthalpy also possesses the highest melting temperature.

- Two polymorphic forms show monotropism if the polymorph which shows the highest melting enthalpy also possesses the highest melting temperature.
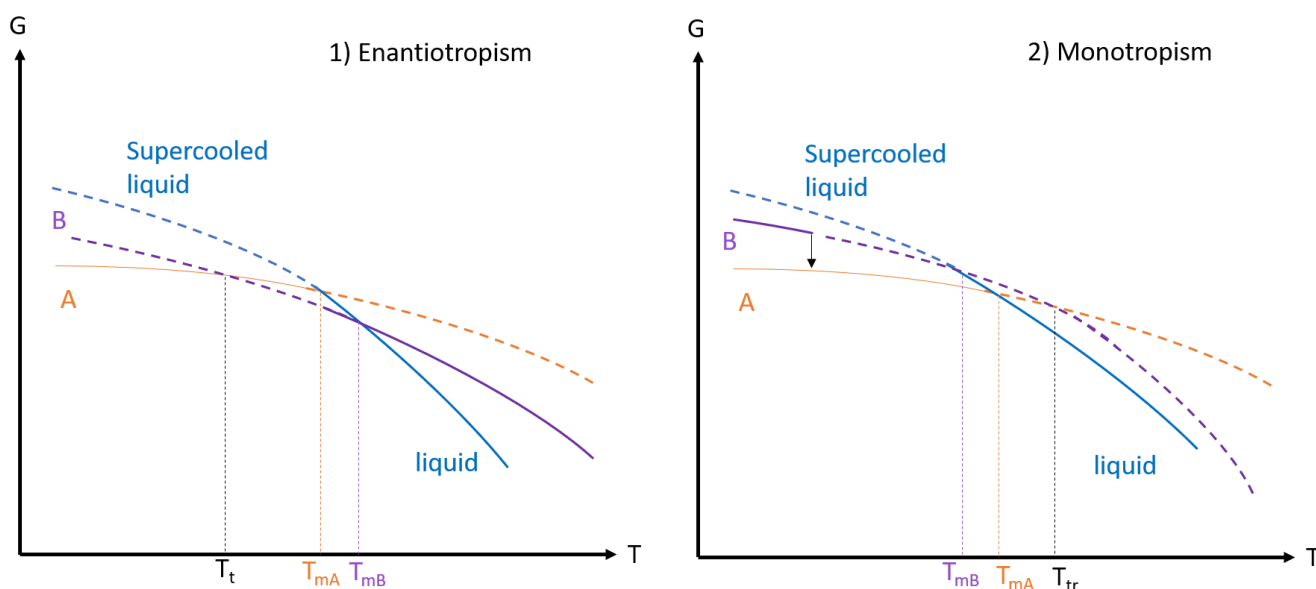
Figure 10- Schematic representation of the Gibbs free energy against temperature in the case of enantiotropism (1) and of monotropism (2). A and B are two polymorphic forms of the same API.

Additionally, each polymorph can possess different nucleation and growth zones. It is thus crucial to determine the nucleation and growth kinetics of the different polymorphic forms in order to direct the recrystallization towards the most suitable polymorphic form for formulations. However, as previously observed by Ostwald et al. [85], the most stable crystalline form is not necessarily the first form to appear during the recrystallization stage of an amorphous material. Indeed, the amorphous form often recrystallizes through a succession of transformations involving different polymorphs of decreasing free energy (G) (and thus increasing stability) to finally reach the most stable polymorphic form.

I.3   Amorphous material manufacturing

Apart from the classical liquid quench, presented in the previous section, several manufacturing techniques enable the production of amorphous materials. However, the physico-chemical characteristics of the API have to be well-known and understood as they can have a strong influence on the selection of the appropriate amorphization process. Furthermore, the chosen amorphization process can have an influence on the stability, the particle morphology or even the pharmaceutical performance of the API, which is why it also has to be selected depending on the desired characteristics of the amorphous material.

I.3.1 Different amorphization processes

The different amorphization techniques can be sorted into three different categories: heat/melt based, solvent based and mechanical based techniques. Considering the lab-scale methods, it has been reported that 56% of the techniques employed are solvent-based, whereas the heat-based and the mechanical based methods only represent 35% and 7% of the techniques used, respectively[86]. The 2% remaining represent a combination of different techniques such as hot melt extrusion (HME) with electrospinning or solvent-antisolvent precipitation with sonication[86]. New techniques are still emerging such as "Kinetisol® Dispersing" which involves the fusion/heat and the frictional/shear energies[87], the vacuum drum drying[88] or the microwave induced in situ amorphization[89]. A non-exhaustive list of the different techniques used is presented in Table 1.

Table 1 - Overview of the existing amorphization processes (non-exhaustive list)[3,5,20]

Heat-based techniques	Solvent-based techniques	Mechanical-based techniques
Liquid-quench	Spray-drying	Ball-milling
Hot-melt extrusion	Freeze-drying	Cryo-milling
Kinetisol® dispersing	Solvent-antisolvent precipitation	Micronization
Spray-congealing	Spray-coating	
3D-printing	Electrospinning	
Microwave heating	Fluidized-bed technology	
Ultrasonic assisted compaction	Solvent casting	
	Co-precipitation	
	Spray-freeze drying	
	Super-critical fluids	
	Solvent evaporation	
	Vacuum drum drying	

If a large amount of techniques are available for the production of amorphous materials, spray-drying and HME remain the favorite techniques from an industrial point of view[19]. Indeed, spray-drying is considered as a continuous and commercially scalable drying process[20] and HME is considered as a green technology as it is solvent-free and as a high-throughput continuous process which can also easily be scaled up for industrial purposes[21]. On the contrary, the milling technique is usually used in the

pharmaceutical industry for its particle size reduction capacity even if it has been widely used on the laboratory scale to produce amorphous materials[90–92]. The major drawback of this method is that usually, the amorphous form obtained by milling is less stable compared to other manufacturing methods such as the liquid quench[93]. Indeed, the stability of the milling induced amorphous material is usually threatened due to the residual crystallinity (seeds) which can lead to a recrystallization due to the growth phenomenon[20]. Furthermore, the local order of the milling-induced amorphous form, the higher specific surface and the higher molecular mobility can also lead to instabilities.

As briefly mentioned, the physico-chemical characteristics of the API greatly influence the selection of a suitable amorphization process. The primary criterion to be considered is related to the thermal stability and the melting point of the API. Indeed, it was reported that if the melting point of an API is below 150°C and if the melting is not accompanied with degradation, a heating-based process (as mentioned in Table 1) can be used[19]. However, if the thermal stability is compromised or if the shear forces can induce degradation, a solvent based approach (as mentioned in Table 1) can be chosen[94]. In this case, the solubility of the API in the solvent, the boiling point of the solvent as well as its toxicity have to be considered in order to choose the most appropriate method[20]. However, on the laboratory scale, in the case of an API presenting both thermal instability and a poor solubility in any suitable solvent, a mechanical based technique such as ball milling or cryo-milling has to be considered.

Apart from those characteristics, additional criteria can also be considered for larger scale production including process efficiency and yield, particle properties, environmental impact, toxicity and safety.

In the following paragraph, the ball-milling technique will be deeply discussed as it was the major technique investigated in this work.

I.3.2 High-energy ball milling

As briefly mentioned in the previous section, mechanical milling is often used in the pharmaceutical industry as is allows a higher specific surface of the powder, which improves the bioavailability of the drug[95,96]. In addition, the size reduction of the particles usually improves the cohesion, which is an interesting feature for the compaction and thus for the production of tablets[97].

Besides the micro-structural modifications, the use of high energy milling can also lead to structural modifications such as an amorphization[23–26] or a polymorphic transformation[27–30]. In both cases, the new

physical forms produced can have different therapeutic properties and are usually unstable, which might not be in adequation with either their pharmaceutical purpose or with the regulations. Fully understanding those transformations and controlling them is thus an objective of significant importance in the development of new pharmaceutical formulations.

The milling-induced amorphization can be explained as a competition between a disordering process resulting from ballistic jumps of the molecules due to the mechanical shocks and a reordering process which results from thermally activated motions of the molecules. As a result, a complete amorphization generally requires that the material is milled below its glass transition temperature[91,98]. In this particular case, the low molecular mobility prevents the structural reordering of the amorphized fractions of the material in the time scale of the milling process which allows a total amorphization of the drug[99–101].

The milling induced amorphization also possesses the valuable advantage that it occurs directly in the solid state. This thus can prevent the melting of the API which can lead to degradation[92] or the dissolution in a solvent which can lead to toxic solvent residues or to chemical changes of the API such as mutarotations[102].

Several theories were developed to explain the milling-induced amorphization mechanisms. Amongst them, three are briefly explained below:

- The Lindemann's model which explores the atomic vibrations (μ^2_{vib}) in the system[103]. In the crystal lattice, atoms are constantly vibrating around their equilibrium positions. The amplitude of those vibrations increases when the temperature is increasing. According to this model, if the amplitude of the vibrations exceeds half of the interatomic spacing, the system starts to melt. The critical mean square displacement (μ^2_{crit}) for which the system melts is thus represented by:

$$\mu^2_{vib}(T_m) \geq \mu^2_{crit} \qquad (8)$$

By considering the atomic motion due to the static disorder (μ^2_{stat}) generated by milling (e.g. dislocations, vacancies, …) it becomes:

$$\mu^2_{vib} + \mu^2_{stat} \geq \mu^2_{crit} \qquad (9)$$

This model thus implies that the melting of a crystal could happen either when heating a crystal (increasing μ^2_{vib}) or by introducing enough defects in the crystal (increasing μ^2_{stat}) even below the melting temperature. The crystal will melt upon milling when the atomic displacement (μ^2_{stat})

becomes higher than (μ^2_{crit}). However, this model presents limitations as it cannot explain the polymorphic transformations that a crystal can undergo upon milling.

- The Fecht's model[104] focuses on the defects induced on the crystal upon milling resulting in an increase in the Gibbs free energy. For a crystal without defects the melting condition is given by:

$$\Delta G = G_{liq} - G_{cryst} = 0 \quad (10)$$

When the defects are considered, this equation becomes:

$$\Delta G^* = \Delta G - \Delta G^d = 0 \quad (11)$$

$$\text{And } \Delta G^d = C(\Delta H^d - T\Delta S^d) + kT(ClnC + (1-C)ln(1-C)) \quad (12)$$

Where ΔG^d is the Gibbs free energy variation resulting from the defects, C is the defects concentration and ΔH^d and ΔS^d are the variations of enthalpy and entropy, respectively.

The temperature at which the defective crystal melts corresponds to the temperature T for which $\Delta G^* = 0$. Given those equations and as illustrated in Figure 11, the higher the defects concentration, the lower the melting temperature of the defective crystal will be. It can thus be deduced that for a limiting concentration of defects (C_{d2}), the Gibbs free energy of the defective crystal will become tangent to the one of the liquid. In that case, if the temperature of the system is lower compared to its glass transition temperature, a direct crystal to glass transformation will occur.
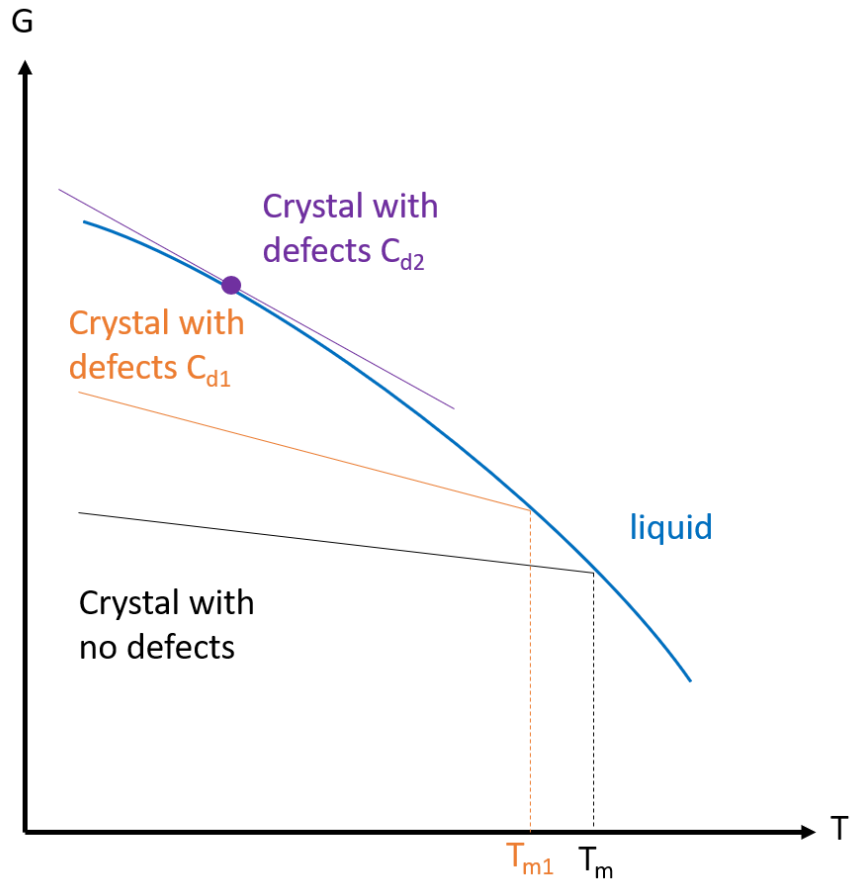
Figure 11 – Schematic representation of a Gibbs diagram of a crystal with no defects (black curve) and of two different crystals with defects. The first one has a concentration C_{d1} of defects (orange curve) and the second one has a concentration C_{d2} of defects which is higher than C_{d1} (purple curve).

However, this model encounters the same limitation as the Lindemann's model as it cannot predict the polymorphic transformations.

- The model of Martin and Bellon, also known as the driven alloys theory, was first aiming to predict the behavior of metallic alloys under irradiation[105] and was then extended to the process of mechanical milling[106]. In this model, it is implied that under external solicitations, an alloy is governed by the simultaneous action of two mechanisms: the jump of atoms thermally induced and the "ballistic jumps" resulting from the external solicitations. The "thermal jumps" depend on the temperature whereas the "ballistic jumps" depend on the intensity of the external solicitation which is correlated in space and time. This model also introduces the term of effective temperature under perturbation (T_{eff}). When a material is milled at a temperature T, the

corresponding state of the material would be observed at this T_{eff} in absence of milling. This effective temperature is given by:

$$T_{eff} = T\left(1 + \frac{D_{bal}}{D_{th}}\right) \quad (13)$$

Where D_{th} and D_{bal} corresponds to the rate of thermal jumps and to the frequency of ballistic jumps, respectively.

The frequency of ballistic jumps depends exclusively on the milling intensity. This model highlights the competition between those two effects and predicts the nature of the physical states reached under solicitations such as amorphization upon high milling energy or upon low enough temperature.

I.4 Stabilization of the amorphous state

As the amorphous state represents the highest energetic level of a material, it would be expected that these materials possess a strong advantage in terms of solubility and dissolution rate. However, as the amorphous state is far from the equilibrium, this advantage comes at the expense of the thermodynamic stability leading to an uncontrolled (and generally unavoidable) recrystallization of the API[107].

To overcome the stability issues, the amorphous API can first be formulated as an ASD or glass solution. Indeed, for commercial purposes, amorphous APIs are generally formulated in combination with excipients (usually amorphous) to stabilize the amorphous state and to prevent the recrystallization during the storage[2] or the dissolution stage[82].

I.4.1 Amorphous solid dispersion, the formation of an API/polymer molecular alloy

The term solid dispersion is defined as the dispersion of an API in an inert carrier in the solid state prepared by solvent, melting or solvent-melting method[109]. However, nowadays this term is mostly related to glass solutions of poorly-water soluble APIs with an amorphous carrier, which is usually a polymer[2]. Several phenomena can explain the stabilization induced by the use of a polymeric carrier, including the reduced molecular mobility by an increase in viscosity, the anti-plasticizing effect[110], or the API-polymer interactions[111,112] due to hydrogen-bonding or dipolar interactions. However, it was

reported that the presence of hydrogen bonding cannot be considered as an insurance for the stability of the amorphous API as it depends on the degradation mechanism of the API[113] or on the solubility of the polymer in the amorphous API[114]. Besides, it was reported that the anti-plasticizing effect can alone prevent the recrystallization of the API when using a polymer with a high enough T_g[33].

Considering a co-amorphous mixture, the miscibility of the API and the polymer depends on the size and on the structural flexibility of the molecules but also on the free Gibbs energy. The evaluation of the physical stability of the mixture thus implies the evaluation of the free Gibbs energy of the mixture (ΔG_{mixing}), which is given by:

$$\Delta G_{mixing} = \Delta H_{mixing} - T\Delta S_{mixing} \quad (14)$$

Where ΔH_{mixing} and ΔS_{mixing} correspond to the enthalpy and to the entropy of the mixture, respectively.

From this statement several cases can be described:

- The mixture is considered ideal (at a constant temperature T) if $\Delta H_{mixing} = 0$ and $\Delta S_{mixing} = 0$. In this case, the mixture always corresponds to a homogeneous solution at any temperature and any composition of the mixture.
- The mixture is considered as regular (non-ideal) if $\Delta H_{mixing} \neq 0$ and $\Delta S_{mixing} \neq 0$. In this particular case, ΔS_{mixing} will always have a positive value. Depending on the temperature and on the value of ΔH_{mixing}, three cases are distinguished:
    - $\Delta H_{mixing} < 0$ which implies that $\Delta G_{mixing} < 0$. In this case, the mixture will always correspond to a homogeneous solution at any temperature and any composition of the mixture.
    - $\Delta H_{mixing} > 0$ which implies a competition between the enthalpy and the entropy. In this case, at low temperatures, $T\Delta S_{mixing} < \Delta H_{mixing}$ so that $\Delta G_{mixing} > 0$ meaning that the mixture is going to form a heterogeneous mixture (demixing) composed of areas enriched with the API and others enriched with the polymer. For high temperatures, it is the opposite case, $T\Delta S_{mixing} > \Delta H_{mixing}$ so that $\Delta G_{mixing} < 0$ and the mixture will always correspond to a homogeneous solution at any composition of the mixture.

In the case of a homogeneous co-amorphous mixture (API and polymer completely miscible), the typical signature of such a mixture consists in a single T_g which is usually located at a temperature between the ones of the pure materials[59,115,116]. Several models were developed to predict the evolution of the T_g

against the composition of the mixture. Amongst them, the most widely used is the one of Gordon Taylor et al[117] where the T_g of the mixture is given by:

$$T_{g(mixture)} = \frac{\varphi_1 T_{g1} + K\,\varphi_2 T_{g2}}{\varphi_1 + K\varphi_2} \qquad (15)$$

And in the case of an ideal mixture $\qquad K = \dfrac{\Delta C_{p2}}{\Delta C_{p1}} \quad (16)$

Where:

- T_{g1} and T_{g2} correspond to the glass transition temperatures of components 1 (lowest T_g) and 2 (highest T_g) respectively.
- Φ_1 and $\Phi_2 = 1 - \Phi_1$ correspond to the volume fractions of components 1 and 2, respectively.
- K represents the coefficient which defines the curve of the evolution of the T_g against the composition of the mixture.

It can be deduced, from the presence of any deviation from the theoretical curve obtained for an ideal mixture, that either interactions might exist between the API and the polymer or that a plasticizer such as water might be present or even that a phase separation could be taking place[59,115,116]. A positive deviation usually indicates that the interactions between the API and the polymer, such as hydrogen bonding, are stronger compared to the ones of the individual materials[118] whereas a negative deviation can suggest a loss of strength of the interactions upon mixing[59].

I.4.2   Phase diagram of an API/polymer system

The physical stability of the ASD strongly depends on both the system molecular mobility[119] and on the solubility/miscibility limitations[120].

If the API is in the crystalline state (stable crystal or metastable polymorphic form), the solubility of the API in the polymer is defined as the maximum amount (mass fraction) of the API which can be dissolved in the polymer at a given temperature. The solubility of the polymorphic forms of an API are usually different, i.e. for a same temperature, the maximum amount of API dissolved will differ. The solubility curve is usually difficult to obtain experimentally. Indeed, the polymer is usually characterized by a high viscosity which induces a low molecular mobility and thus a very slow dissolution of the API in the

polymer[121]. In theory, there are four experimental techniques to reach the equilibrium state of an API/polymer mixture at a given temperature:

- Monitoring the API dissolution (increasing concentration) in the polymer from an under-saturated solution using an isothermal (constant temperature) until the equilibrium solubility is reached.

- Monitoring the API demixing from a super-saturated solution using an isothermal (constant temperature) until the equilibrium solubility is reached.

- Measuring the temperature corresponding to the total dissolution of the API in the polymer from a physical mixture (melting point depression).

- Measuring the temperature corresponding to crystallization of the API from a super-saturated solution (crystallization point depression).

Following those techniques, multiple methods were established to obtain an equilibrium in an API/polymer mixture at a given temperature[120–127] and 3 of them will be developed in this section.

- **Dissolution of an API in a polymer using an isothermal.** This method developed by Sun et al[121] consists in the preparation of a physical mixture API/polymer at a given composition which will be milled in order to obtain a homogenous partially co-amorphous molecular dispersion of the API in the polymer. Indeed, the milling must be stopped before the total amorphization of the API but the mixture obtained will be super-saturated. Afterwards, an annealing is performed on the mixture for a sufficient period of time to allow the equilibrium state to be reached. Then, this mixture is heated using the DSC and two situations can be observed. If the annealing temperature is lower than the solubility temperature for this composition, a fraction of the API will remain in its crystalline form and, upon heating, an endothermic event corresponding to the dissolution of this residual crystalline fraction will be observed. On the contrary, if the annealing temperature is higher than the solubility temperature, all the API will be dissolved in the polymer and no dissolution peak will be observed upon heating. The correlation between the composition of the mixture and the solubility temperature thus determined allows to obtain a solubility curve point. If this method is considered as very precise, it is also very time consuming. Furthermore, as the super-saturation is reached, a crystallization could occur during the annealing which would lead to a corresponding dissolution peak in the DSC upon heating.

- **Demixing of the API in the polymer.** This method developed by Mahieu et al[120], consists in the preparation of a milling-induced supersaturated glass solution. Indeed, the milling will force the dissolution of the API in the polymer as the milling temperature is lower than the Tg of the glass solution obtained. Then, this mixture is heated using the DSC until a given temperature is reached which will correspond to the one at which the solubility is to be determined. It must be noted that this temperature is higher than the Tg of the mixture, which will lead to the crystallization of the API. When this solubility temperature is reached, an annealing is performed in order to allow the progressive crystallization of the API until the equilibrium is reached. Once it is, the mixture is heated again using the DSC and the Tg of the thus obtained mixture is measured. Using the Gordon-Taylor curve, the fraction of API dissolved in the polymer at this solubility temperature is determined. The advantage of this method relies in the fact that the demixing kinetics (crystallization) is faster compared to the dissolution kinetics. However, this method is reliable for API which act as plasticizer on the polymer as it is necessary to enhance the molecular mobility in order to increase the crystallization rate. Furthermore, this method remains time consuming as it has to be repeated on a new sample for each point of the solubility curve.

- **Dissolution of the API from a molecular/crystalline dispersion.** This method developed by Latreche et al[127], consists in the production of molecular/crystalline dispersions where the API is dispersed in the polymer both at a molecular level and in the form of small crystallites in order to enhance the dissolution rate of those crystallites. Indeed, as the molecular dispersion has a plasticizing effect, the molecular mobility is enhanced in the amorphous matrix. Furthermore, the dispersion of the small crystallites in the amorphous matrix allows the reduction of distances over which the API molecules have to diffuse to homogenously dissolve into the polymer. To that extend, a milling-induced super-saturated API/polymer glass solution is prepared and then an annealing is performed in a plasticizing solvent atmosphere in order to allow the recrystallization of the excess of API dissolved in the polymer. The partially recrystallized sample is then dried to remove all traces of the solvent and the sample obtained is thus in the form of a molecular/crystalline dispersion which is repeatedly heated using DSC. For each new scan, the final temperature is increased by 10°C compared to the previous one and an annealing is performed at each final temperature in order to reach the equilibrium. For each scan, the Tg is measured and using the Gordon-Taylor curve, the fraction of API dissolved is determined. This

method allows a to obtain several solubility curve points with only one sample which constitute a considerable time gain compared to the other methods.

As illustrated in Figure 12, the phase diagram of the API/polymer system depicts the evolution of the T_g (Gordon-Taylor curve) and of the solubility of the API in the polymer depending on the composition of the mixture. Four different areas can be distinguished:

- 1: The mixture is above the solubility curve (under-saturation in API) and the temperature is below T_g. In this case, the mixture is a glass solution, both thermodynamically and kinetically stable. No demixing or recrystallization can occur.
- 2: The mixture is still above the solubility curve (under saturation in API) but also above the Gordon-Taylor curve. The mixture is thus a liquid solution where no demixing or recrystallization can occur.
- 3: The mixture is below the solubility curve and thus super-saturated in API. As a result, there is an effective risk of partial recrystallization of the API. However, as it is also under the Gordon-Taylor curve, the molecular mobility is considered low enough to significantly slows down the demixing or recrystallization kinetics. The mixture is thus a kinetically stable glass.
- 4: The mixture is below the solubility curve (super-saturated in API) and above the Gordon-Taylor curve (high molecular mobility). In this case, the mixture is a both thermodynamically and kinetically unstable solution leading to a certain and rapid demixing/recrystallization of the API.
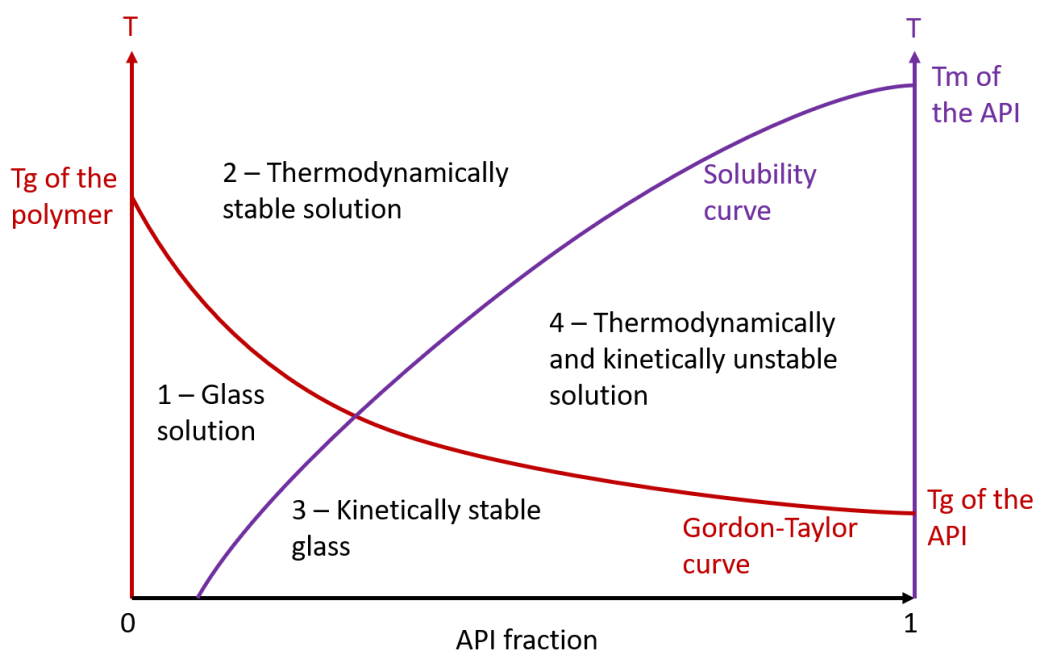
Figure 12- Phase diagram of the API/polymer mixture. The Gordon-Taylor curve (red) and the solubility of the API in the polymer matrix (purple) divide the diagram in 4 distinct areas: (1) glass solution, (2) thermodynamically stable solution, (3) kinetically stable glass and (4) thermodynamically and kinetically unstable solution. Adapted from Lehmkemper et al. [34]

I.4.3 Polymer selection

During the selection process of the polymer, the miscibility between the API and the polymer is an important parameter to consider. Hence, the determination of the phase diagram presented above, represents a great asset to facilitate this selection process. However, other criteria need to be considered in order to produce the most successful ASD. Indeed, a hydrophilic polymer can impose an advantageous effect on the dissolution behavior of the API as it will rapidly dissolve in the GI fluids, leading to the release of the molecularly dispersed API[59]. Nevertheless, the super-saturated state generates a thermodynamic driving force for the mechanisms of recrystallization and eventually precipitation[128]. Therefore, ASDs are expected to maintain the supersaturation levels in the GI tract during the dissolution process [35]. To that extend, multiple factors are to be considered during the selection of the polymer including its hygroscopicity, aging and tackiness[36].

The selected polymer should meet the following criteria[3,129]:

- It should act as an inert carrier and should be non-toxic and Generally Recognized As Safe (GRAS) but should also be economical.
- It should be water soluble or swellable in order to induce the release of the drug and should be soluble in a variety of solvents.
- It should be thermally stable and chemically compatible with the API.
- It should preferably have a higher T_g compared to the one of the API.

Many homopolymers were used for ASDs production including, hydroxypropyl methyl cellulose (HPMC) and derivatives, polyethylene glycol (PEG), polyvinyl pyrrolidone (PVP) and polyvinyl alcohol (PVA). But the use of copolymers such as Poloxamer®, PVP-vinyl acetate (PVP-VA), PVA-PEG, Eudragit® or Soluplus®, was also explored.

I.4.4 Formulation strategies: from ASDs to tablets

In spite of the physical stability issues recurring with ASDs, some of them were successfully marketed with an increasing number over the years as showed in Table 2. The oral route in the form of tablets is the most currently used administration dosage form. The marketed ASDs show the same preference as most of them are in the form of tablets or capsules. In this work, the focus will be on the tablet and thus on the compression process.

Tablets are produced by die compression of an ASD powder which can have been subjected to prior treatments such as the wet granulation[130] or the roller compaction dry granulation[131]. However, in this work, only the direct compression without any prior treatment will be developed.

Table 2 – Examples of the FDA approved ASDs (non-exhaustive list). Partially adapted from Tambe et al.[37]

Commercial name (and form)	API (and BCS class)	Amorphization process	Polymeric carrier(s)	Manufacturer	Year of approval
Cesamet® (Capsule)	Nabilone (II)	Solvent evaporation	Povidone	Meda Pharmaceuticals	1985
Sporanox (Capsule)	Itraconazole (II)	Fluid bed bead layering	Hypromellose, polyethylene glycol	Janssen	1992
Prograf (Capsule)	Tacrolimus (II)	Spray-drying	Hypromellose	Astellas Pharma	1994
NuvaRing (Vaginal ring)	Etonogestrel/ Ethinyl Estradiol (II)	Melt extrusion	Ethylene vinylacetate co-polymer	Merck	2001
Kaletra (tablet, capsule or oral solution)	Lopinavir/Ritonavir (IV/IV)	Melt extrusion	Co-povidone	AbbVie	2007
Zortress (tablet)	Everolimus (III)	Spray-drying	Hypromellose	Novartis	2010
Norvir (tablet)	Ritonavir (IV)	Melt extrusion	Co-povidone	AbbVie	2010
Zelboraf (tablet)	Vemurafenib (IV)	Solvent/anti-solvent precipitation	Hypromellose	Roche	2011
Zepatier (tablet)	Elbazvir/Grazoprevir (II/II)	Spray-drying	Vitamin E polyethylene glycol succinate, Co-povidone, Hypromellose	Merck	2016
Stivarga (tablet)	Regorafenib (II)	Solvent evaporation	Povidone	Bayer	2017
Erleada (tablet)	Apalutamide (II)	Spray-drying	Hypromellose acetate succinate	Janssen	2018
Symdeco (tablet)	Tezcaftor/Ivacaftor or Ivacaftor (II/II or IV)	Spray-drying	Hypromellose, Hypromellose acetate succinate	Vertex	2019
Braftovi (Capsule)	Encorafenib (II)	Melt extrusion	Co-povidone, poloxamer® 188	Pfizer	2020
Oriahnn™ (Capsule)	Elagolix/Estradiol/ norethindrone acetate (III/II/NA)	Melt extrusion	Co-povidone, Hypromellose	AbbVie	2020

It was reported that the compression, by inducing a mechanical stress to the ASD, could either lead to an amorphous-amorphous phase separation or to a physical stability enhancement depending on the concentration of the API, the compression force and the polymer carrier[38].

As represented in Figure 13, the compression involves three different steps including, the powder filling, the compression during which the powder first takes the shape of the die and is then subjected to pressure, and finally the ejection of the compact thus produced. During this process, the powder goes through several stages including, initial packing and particle rearrangement, temporary structures formation, elastic deformation, plastic deformation and particles breakage, bonds formation and consolidation and elastic recovery during the decompression step after the ejection[132–134]. Two major issues encountered during tablet production in the pharmaceutical industry are the lamination and the capping and are observed during the elastic recovery after the ejection of the tablet[133,135].
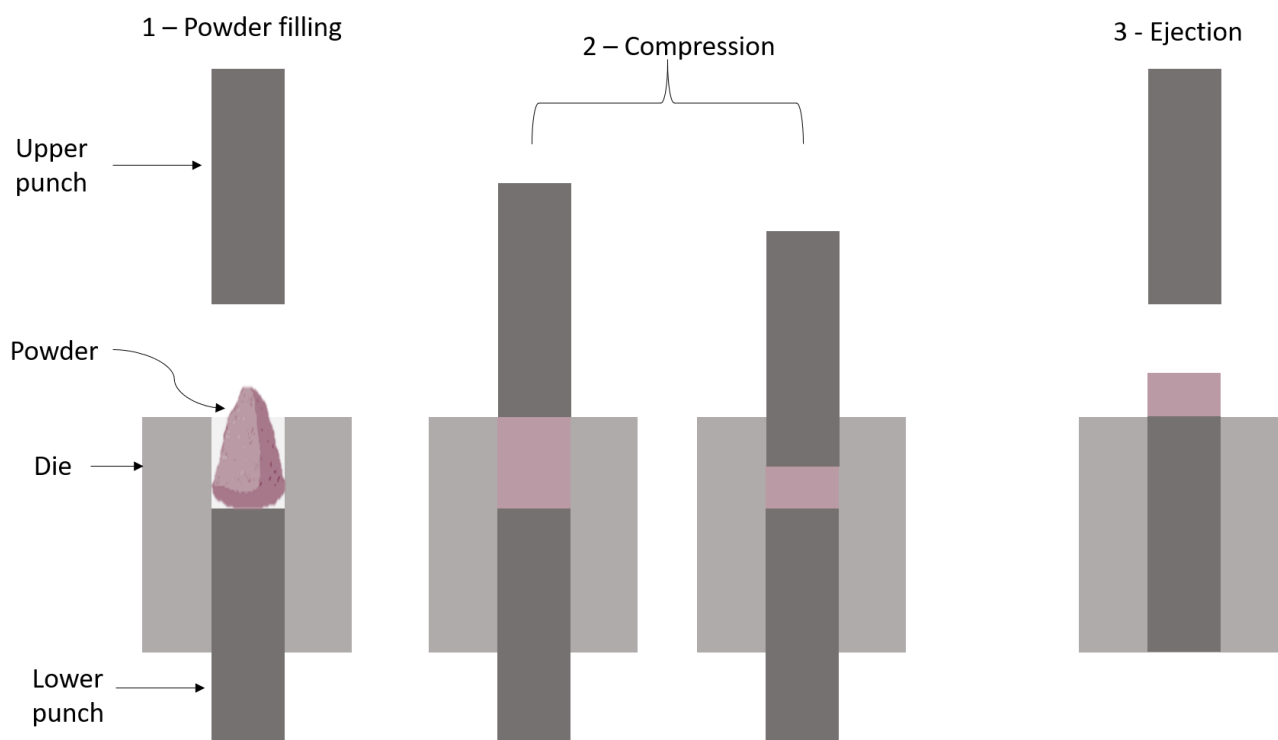
Figure 13 - Scheme representing the compression steps. Adapted from Al-Mangour, 2015[136]

There are critical parameters related to the ASD powder to take into account which can impose challenges for tableting including the grindability, the flowability the compressibility and the disintegration[130]. In order to improve the parameters mentioned or to give particular characteristics to the tablet, different excipients with specific roles are used[130,137,138]:

- Binders are used in conventional tablets to increase their hardness but in the case of ASDs tablets, the binder can be the polymer carrier that maintains the amorphous nature of the API. Typically, cellulose derivatives or the polymers listed as carriers for ASDs (PVP, Soluplus®, Eudragit®, …) are used.

- Fillers or diluents aim to improve the wettability of tablets and to provide bulk in order to obtain the required tablet weight. Usually, water-soluble fillers are used including lactose, dextrose, sorbitol, mannitol and microcrystalline cellulose (MCC).

- Glidants act as friction and adhesion reducers between the particles of the powder in order to improve its flowability and can also be used as anti-caking agents. Colloidal anhydrous silicon and other silica compounds can fulfill this role.

- Lubricants have a similar action to glidants but they are used to reduce the contact area between the powder particles and the die wall or the punches surface to prevent the powder from sticking to those surfaces. For this purpose, the stearic acid and its salts are chosen, the magnesium stearate being the most widely used. However, in the case of ASDs, lubricants may be a disadvantage as they can decrease the wettability of the tablet and thus increase the disintegration time.

- Disintegrants are used to facilitate and to accelerate the dissolution as they enhance the surface area exposed to the dissolution medium. Common disintegrants are starch, cellulose derivatives, crospovidone and sodium croscarmellose.

- Other excipients such as sweeteners and flavoring agents can be added to obtain a good mouthfeel and taste in order to improve the patient compliance.

CHAPTER II – MATERIALS AND METHODS

II.1 Materials

I.1.1 Drug molecules

Chlorhexidine ($C_{22}H_{30}Cl_2N_{10}$) free base (Chx) was purchased from Safic Alcan (Etampes, France) and was used as received.

Riboflavin ($C_{17}H_{20}N_4O_6$) free base (Rf) was purchased from ACROS organics (Geel, Belgium) and was used as received without any additional purification (purity >98%).

I.1.2 Excipients

Two polymers were chosen as polymeric matrices for the production of the amorphous solid dispersions:

- Kollidon 12 PF, also known as polyvinylpyrrolidone (PVP) was purchased from BASF (Ludwigshafen, Germany).
- Hydroxypropyl Pea Starch (Lycoat RS 720) was graciously given by Roquette (Lestrem, France).

For the tablet production, the excipients used for the formulation can be found, along with their function, in Table 3.

Table 3 - Overview of the excipients used for the tablet production.

Material	Supplier	Function
lactose monohydrate	Armorpharma (Saint Brice en Coglès, France)	Filler
microcrystalline cellulose (MCC)	Asahi Kasei corporation (Myasaki, Japan)	Binder
Croscarmellose sodium	JRS pharma gmbh & co (Rosenberg, Germany)	Disintegrant
Magnesium stearate	Fragron (Colombes, France)	Lubricant

I.1.3 Others

An overview of the rest of the materials used during this project is given in Table 4.

Table 4 - List of the other materials used.

Material	Supplier	Function
Acetonitrile, HPLC grade	Carlo Erba reagents (Val de reuil, France)	Organic solvent for mobile phase preparation
DMSO ACS grade	Euromedex (Souffelweyersheim, France)	NMR experiment
Formic acid	Sigma Aldrich (Seelze, Germany)	Reagent for mobile phase preparation
Phosphoric acid ± 98% pure	Acros Organics (Geel, Belgium)	Reagent for mobile phase preparation
Triethylamine	Acros Organics (Geel, Belgium)	Reagent for mobile phase preparation
Ultra-pure water	Veolia (Vendin le Vieil, France)	Dissolution medium

II.2 Amorphization processes

II.2.1 Liquid Quench

The usual route to obtain an amorphous form is the quench of the liquid. This process consists in the heating of the crystalline powder until the melting followed by a rapid cooling below the glass transition temperature of the liquid to avoid any crystallization. This thermal treatment was either performed using the DSC (TA instrument, France) or using a thermolyne tube furnace oven 21100 (Barnstead Thermolyne corporation, USA) when a larger amount of product was to be produced. In the latter, 1g of powder was wrapped in aluminum foil, melt in the oven, and then took out at room temperature for the quench. The quenched liquid thus obtained was then slightly crushed with pestle in a mortar for further experiments.

II.2.2 Milling

Mechanical milling was performed using a high-energy planetary grinder "Pulverisette 7" (Figure 14) (Fritsch GmbH, Germany). This equipment is composed of a support disk on which are screwed two milling vessels (45mL) containing seven milling balls ($\varnothing$ = 15 mm). Both the vessels and the balls are made of zirconium oxide which is a material known to be highly resistant to violent and repeated collisions (Figure 14).

Figure 14– Planetary mill (left) and milling vessel containing seven milling balls (right)

The working principle of the planetary mill is schematized in Figure 15.

The milling vessels are rotating on their own axis and in opposite directions with the support disk which generates antagonist centrifugal forces. The rotation speed of the disk and the vessel are identic but opposite in trajectory and can vary from 100 to 800 rpm. This configuration allows the sample material and the milling balls to be separated from the inner wall of the milling vessel. Then, the milling balls cross the vessel at high speed and create an impact with the sample material and the opposite vessel wall allowing further grinding. Furthermore, the impacts between the balls themselves on the sample material also contribute to the size reduction process.

a- Rotation of the milling vessel
b- Centrifugal force
c- Solar disk movement
d- milling balls movement
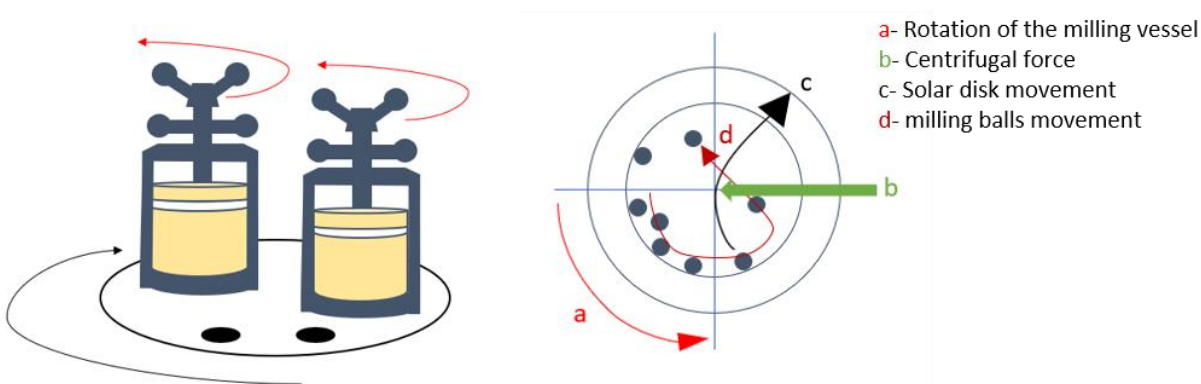
Figure 15 – Schematic representation of the working principle of the planetary mill

In order to have the most reproducible results, the following parameters were systematically used:

- 1.1g of sample material were placed into the milling vessel containing seven milling balls.
- The sample material was dried at 60°C in the milling vessel during 15min. The milling vessel was then closed, placed into the equipment and cooled down to room temperature before the milling.
- The rotation speed was set to 400rpm in reverse mode. This particular mode allows a change of rotation direction after each milling cycle.
- Milling periods of 20min were alternated with 10min pause periods to prevent the temperature of the milling vessel to increase due to the mechanical collisions during long processes.
- The samples were milled at room temperature for a range of effective milling times from 1min to 32 hours.

II.3   Characterization techniques

II.3.1 Thermogravimetric analysis (TGA)

The TGA consists in the measurement of the weight variations of a sample upon heating or upon a certain time period at a given temperature. Various events can generate a weight loss including a sublimation, a chemical degradation or a solvent evaporation whereas an oxidation can be observed by a weight gain of the sample. In this work, this technique was used to both evaluate water evaporation and the thermal degradation of the samples.

Those experiments were performed using the Q500 equipment (TA instruments, France) (Figure 16) and the results were analyzed using the Universal analysis software (TA instruments, France). This instrument allows a heating from room temperature to 1000°C with a heating rate varying from 0.1 to 100°C/min.

Figure 16 – TGA Q500 (TA instruments, France)

Each sample was analyzed using the following parameters:

- 5 to 8mg of sample are placed in an open aluminum pan with a weighing scale (sensibility 0.1µg, precision 0.01%).
- Both the sample and the weighing scale are put under a dry atmosphere using a constant 50 mL/min pure nitrogen flow rate.
- Heating rate was set to 5°C/min.
- The temperature reading was calibrated with the measurements of the Curie points of alumel and nickel provided by the supplier.
- The mass reading was calibrated using certified calibration weights (TA instruments).

II.3.2 Differential scanning calorimetry (DSC)

The DSC is used to evaluate the thermodynamic state of a sample during various thermal treatments. It allows for instance to observe several events including the glass transition, the melting, the recrystallization, the polymorphic transformation or the dissolution of a sample. To that extend, a reference and a sample are each placed on their dedicated platforms in an oven under a dry atmosphere. Each platform is linked to a thermocouple which continuously measures the temperature. Depending on the thermal treatment applied, the heat flow absorbed or transmitted by the sample is then measured by an estimation of the difference of temperature between the sample and the reference.

Those experiments were performed using either the Q20 calorimeter or the discovery calorimeter (Figure 17) (TA instruments, France) and the generated results were respectively analyzed with the Universal analysis software or the Trios software (TA instruments, France). Both calorimeters are equipped with a refrigerated cooling system (RCS 90) which allows the temperature to vary from -90°C to 550°C.

The samples were analyzed using the following parameters:

- 2-5 mg of sample were placed in open aluminum pans in order to allow any free water absorbed to evaporate upon heating

- For specific experiments, Tzero aluminum pans were used when a larger amount of product was needed. In that case, 15 to 25mg of sample were placed in those pans.

- For specific experiments, it was necessary to heat over the degradation temperature of the sample. In that case, high pressure aluminum pans were used and closed with a specific gasket.

- A continuous dry nitrogen flow was set to 50mL/min in the oven in order to improve the heat transfers and the homogeneity of the temperature.

- DSC experiments were performed from room temperature to the maximum temperature reachable before the degradation of the API or the polymer (determined with the TGA experiment) at a heating rate of 5°C/min.

- MDSC experiments were performed from room temperature to the maximum temperature reachable before during the degradation of the API or the polymer (determined with the TGA experiment) at a heating rate of 5°C/min, a modulation amplitude of 0.663°C and a period of 50s. Those parameters correspond to the "heat only" conditions which means that the sample was never cooled during the heating scan.

- Temperature and enthalpy readings were calibrated using pure indium at a heating rate of 5°C/min.

- The glass transition was defined as the inflection point of the C_p jump.

Figure 17 - DSCQ20 (TA instruments, France) on the left-hand side and DSC Discovery (TA instruments, France) on the right-hand side.

If indicated, Hyper DSC scans were performed using the Flash DSC2+ from Mettler Toledo (Viroflay, France) which allows scanning samples from -95°C to 1000°C using scanning rates up to 50 000°C/sec. These high scanning rates are used to by-pass some transformations which are kinetically slow, like recrystallizations or polymorphic transformations. In the case of polymorphic transformations, this allows to observe the melting of the initial polymorphic form. In the present study, samples were flushed with argon and analyzed using a heating rate of 300 °C/sec.

Figure 18 - DSC2+ (Mettler Toledo, France).

II.3.3 X-Ray powder diffraction (XRPD)

X-Ray powder diffraction is a direct and non-destructive characterization technique used to determine the structure and the microstructure of a material.

This technique consists in the irradiation towards a sample using an X-Ray beam at a specific wavelength λ. The interaction of the beam with the material then allows the diffraction of the beam through different angles whose intensities are measured when scanned by the detector. There are two types of experimental configurations:

- the Debye-Scherrer in transmission (beam focusing on the sample and defocusing on the detector) which is usually performed using capillaries on the curve detector *INEL*.
- the Bragg-Brentano in reflection (beam defocusing on the sample and focusing on the detector) which is typically performed on plates on the *X'pert* detector.

For a crystalline material the atoms/molecules are forming a lattice and the X-ray beam will be scattered by the crystal if the theta angle (θ) is satisfying the Bragg law:

$$2d_{hkl} \sin(\theta) = n\lambda \qquad (17)$$

where d_{hkl} is the inter-reticular distance of hkl crystallographic planes and λ is the wavelength of the incident X-ray beam. In that case diffraction peaks are observed at the corresponding 2θ angles as illustrated in Figure 19.
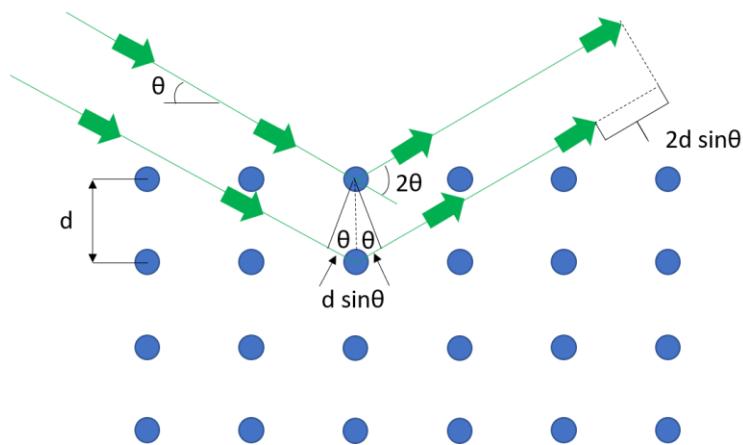
Figure 19 – Schematic representation of the Bragg law.

For an amorphous material, the atoms/molecules are randomly dispersed so the X-ray beam diffused will give rise to a diffusion halo.

In this work, measurements were performed with a PanAlytical X'PERT PRO MPD (Almelo, The Netherlands) diffractometer (λCuK_α = 1.5418 Å for combined $K_{\alpha1}$ and $K_{\alpha2}$), equipped with an X'celerator detector (Almelo, The Netherlands) allowing acquisition of diffraction patterns from 2θ= 3 to 60 °, with a scan step of 0.0167 °/s. This instrument is represented in Figure 20.

For samples containing riboflavin, the samples were placed into Lindemann glass capillaries ($\emptyset$ = 0.7 mm), installed on a rotating sample holder to avoid artifacts due to preferential orientations of crystallites. However, to observe the evolution of the sample upon heating, the sample was placed on a metallic plate, in an Anton Paar chamber at atmospheric pressure. The heating rate was set to 5 °C/min.

For samples containing chlorhexidine, the samples were always placed on a metallic plate, in an Anton Paar chamber at atmospheric pressure as it showed a better peak resolution compared to when placed in Lindemann glass capillaries. The heating rate was also set to 5 °C/min when the evolution upon heating was observed.

For tablets samples, the tablet was sanded in order to fit in the metallic plate.

Figure 20. PanAlytical X'PERT PRO MPD (Almelo, The Netherlands)

II.3.4 Scanning Electron Microscopy (SEM)

This technique was used to determine the morphology of the particles in the different samples. This was performed using a JEOL Field Emission SEM (JSM-7800F, Japan). Samples were mounted on an SEM stub using ribbon carbon double-sided adhesive. To avoid surface charging, samples were chromium coated (100 Å) by electro-sputting under vacuum prior to SEM observations. The observations were performed at 2 kV acceleration voltage, with small probe current and the lowest objective lens aperture to reduce beam damage on the sample surface. Secondary electron images were acquired at several magnifications (from 100 to 20000).

II.3.5 ^{1}H Nuclear Magnetic Resonance (NMR)

In order to assess the degradation of the samples, the ^{1}H NMR technique was used. This analysis was conducted on a Brucker AVANCE 300 MHz (Rheinstetten, Germany at 20°C. A few milligrams of material were dissolved in 5mm diameter NMR tubes containing 0.5 mL of DMSO. For each sample, 64 scans were recorded (1 scan/s) to improve the signal statistic.

II.4 Dissolution kinetics

The dissolution rate of an API and thus its bioavailability can be influenced by many factors including the following:

- Solid-state properties: The physical state (crystal, amorphous form, polymorphs) and the particle size and shape.
- Extrinsic factors (hydrodynamics): The test apparatus or the fluid flow.
- Test conditions: Medium, temperature, pH and stirring rate.

In order to test the dissolution performances of our samples, different dissolution set-ups were used on the different forms produced (powder, compacts, tablets). The different set-ups are schematized in Figure 21 and the experiment details can be found in the next sections.
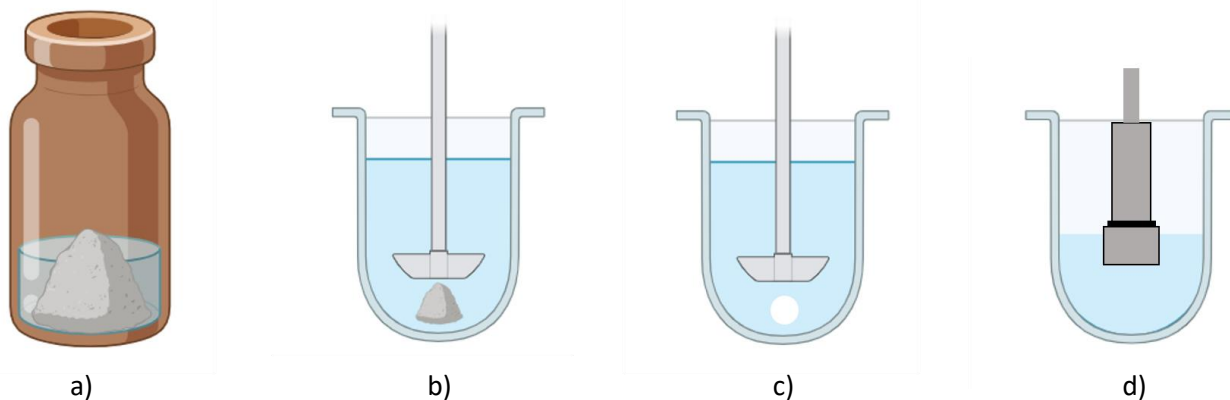
Figure 21. Schematization of the different dissolution set-ups. From left to right:

- *determination of the dynamic solubility*

- *dissolution kinetics of the powder in sink or non-sink conditions*

- *tablet dissolution*

- *intrinsic dissolution.*

II.4.1 Powder Dissolution

Determination of the dynamic solubility

The dissolution kinetics of the APIs for several days were determined in order to obtain their solubility limit. To that extend, the traditional shake flask method was used. Excess amounts of API (about 150mg) were exposed to 10mL ultra-pure water in amber flasks. The latter were placed into a horizontal shaker (37 °C, 80 rpm; GFL 3033; Gesellschaft fuer Labortechnik, Burgwedel, Germany). At predetermined timepoints, 300µL samples were withdrawn using 1mL syringes, and filtered (PTFE syringe filter 0.45µm for Chlorhexidine and PVDF syringe filter 0.22µm for Riboflavin, Agilent technologies, Santa Clara, USA) into 1.5 mL Eppendorfs. The samples were then diluted directly into amber glass vials for further analysis. For both APIs, samples were both diluted 10 times and 100 times. Each experiment was performed in triplicate. Mean values +/- standard deviations are reported in the results.

Dissolution kinetics

The dissolution kinetics of the APIs were determined in both sink and non-sink conditions. For the sink conditions, the amount of API was calculated as at least 3 times below the solubility limit of the crystalline form. For the non-sink conditions, 150mg of API were used.

The dissolution was performed using the USP II apparatus (Sotax, France). Each dissolution bath was filled with 800mL of ultra-pure water heated to 37°C ± 0.2 °C and the agitation was set to 100 rpm. At predetermined timepoints, 1mL samples were withdrawn using 1mL syringes and filtered (PTFE syringe filter 0.45μm for Chlorhexidine and PVDF syringe filter 0.22μm for Riboflavin, Agilent technologies, Santa Clara, USA) into amber glass vials. In the case of the non-sink conditions, the samples were directly diluted 10 times into amber glass vials. All samples were then frozen to -20°C for further analysis. Each experiment was performed in triplicate. Mean values +/- standard deviations are reported in the results.

II.4.2 Intrinsic dissolution

Compared to standard dissolution during which extrinsic factors are appropriate and the test conditions are maintained constant, the intrinsic dissolution also involves the condition of a constant surface area which allows the determination of the intrinsic dissolution rate[139]. In this particular case, the particles size and shape are taken out of the equation and the intrinsic dissolution rate will only be influenced by the physical state of the API.

For this work, the intrinsic dissolution devices (schematized in Figure 22) were purchased from ProSense (Oosterhout, The Netherlands) along with the ATLAS manual hydraulic press.

Prior to dissolution, the powder was compacted directly inside the die on the surface plate using the hydraulic press. For riboflavin samples, the force used was 2 tons whereas for chlorhexidine samples it was 1 ton. After compaction, the die was directly screwed to the holder and shaft assembly with the punch still in place and the surface plate was unscrewed.
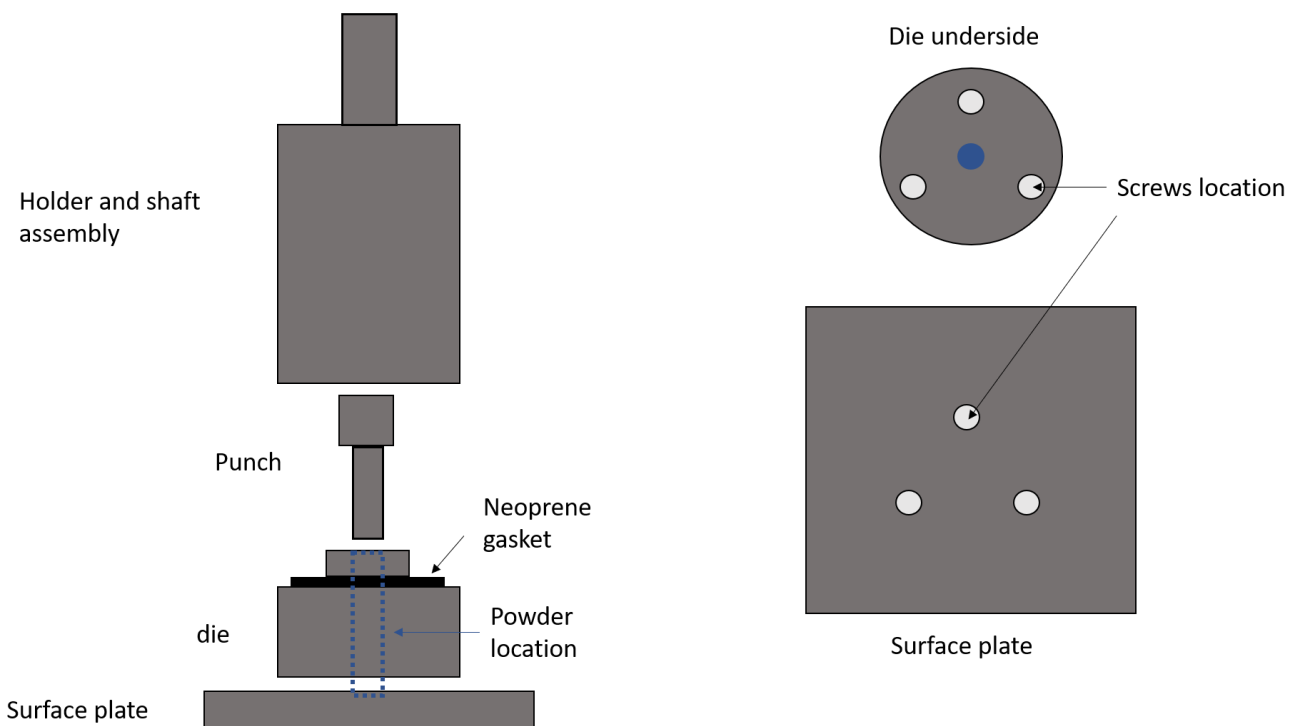
Figure 22. Schematic representation of the intrinsic dissolution device. Adapted from the U.S pharmacopeia[139].

The dissolution was performed using the USP II apparatus (Sotax, France) but in this case, the paddle was replaced by the intrinsic dissolution device (holder and shaft attached to the die). Each dissolution bath was filled with 400mL of ultra-pure water heated to 37°C ± 0.2 °C and the agitation was set to 50 rpm. At predetermined timepoints, 1mL samples were withdrawn using 1mL syringes and filtered (PTFE syringe filter 0.45µm for Chlorhexidine and PVDF syringe filter 0.22µm for Riboflavin, Agilent technologies, Santa Clara, USA) into amber glass vials. All samples were then frozen to -20°C for further analysis. Each experiment was performed in triplicate. Mean values +/- standard deviations are reported in the results.

II.4.3 Oral Tablets

The aim of this work was to evaluate the influence of the physical state of the API (crystalline or amorphous) and of the API/polymer blend during a dissolution which would fit the real-life conditions. To that extend, tablets meant for oral administration were produced.

- Tablet manufacturing

A model formulation of excipients containing a diluent, a binder, a disintegrant and a lubricant were used in order to prepare the tablets. It was decided to keep the API content constant to 30% for each formulation prepared. However, the physical state of the API or of the API/polymer blend would vary.

The formulation used for the compression was the following:

Table 5. Tablet formulation composition

Material	Pure API	API/Polymer blend (70:30)
API or API/polymer blend	30%	42.9 %
Lactose	42.5%	34.6%
Microcrystalline cellulose	20%	20%
Croscarmellose Sodium	2%	2%
Magnesium stearate	0.5%	0.5%

First, the lactose, the microcrystalline cellulose and the croscarmellose were mixed for 5 min together at 62 rpm using a turbula mixer (Willy A. Bachofen AG Maschinenfabrik, Switzerland). Then, the API or the API/polymer blend would be added and the mixture would spend again 5 min in the turbula mixer. Finally, the magnesium stearate would be added and the formulation would be mixed for 4 min in the turbula mixer.

The compression was performed using the STYL'One Nano (Medelpharm, France) simulator, showed in Figure 23.

Euro B flat punches ($\varnothing$ = 11.28 mm) were used with the suitable die. Due to the poor flowability of the powder, hand-filling was preferred. A V-shape profile (10mm/s) was selected for the compression with an automatic ejection using the filling shoe.

Figure 23 - Styl'One Nano simulator (Medelpharm, France).

It was decided to produce 500mg tablets so that the API content would be 150mg in order to be comparable to the powder dissolution in non-sink conditions (see section II.4.1). Furthermore, the tablet hardness was kept constant to 80N and for each formulation the corresponding lower punch force was determined (linear fit on the hardness with three different forces).

After the determination of the right lower punch force to obtain a hardness of 80N, it was decided to produce 18 tablets per formulation which would be used as follows:

- Hardness test in triplicates
- Disintegration test in triplicates
- DSC (one tablet)
- XRD (one tablet)
- Dissolution in triplicates
- 4 weeks stability in ICH conditions (5 tablets in total, 3 for dissolution, 1 for DSC and 1 for XRD)
- Supplementary tablets (2)

All the tablets would also be weighed and have their diameter and thickness measured as those are non-destructive tests.

The hardness was determined using a tablet hardness PTB (Pharmatest, Germany) and the disintegration test was performed using the tablet disintegration tester PTZ 100 (Pharmatest, Germany).

For the evaluation of the stability over 4 weeks, the tablets were kept into a desiccator containing a saturated solution of ammonium nitrate salt which was placed into an oven heated to 25°C. The aim of the use of this particular saturated salt solution was to keep a relative humidity of approximately 60%[140] in order to meet the long-term stability ICH conditions (25°C ± 2°C, 60% rh ± 5%)[141].

- Dissolution

The dissolution was performed using the USP II apparatus (Sotax, France). Each dissolution bath was filled with 800mL of ultra-pure water heated to 37°C ± 0.2°C and the agitation was set to 100 rpm. At predetermined timepoints, 1mL samples were withdrawn using 1mL syringes and filtered (PTFE syringe filter 0.45µm for Chlorhexidine and PVDF syringe filter 0.22µm for Riboflavin, Agilent technologies, Santa Clara, USA) into amber glass vials. As the API content in the tablets fitted the non-sink conditions, the samples were directly diluted 10 times into amber glass vials. All samples were then frozen to -20°C for further analysis. Each experiment was performed in triplicate. Mean values +/- standard deviations are reported in the results.

II.4.4 High Performance Liquid Chromatography (HPLC) analysis

The API content during the different dissolution experiments were determined using HPLC-UV analysis (Waters Alliance 2695 separation module, Waters 2489 UV/vis detector). Depending on the API, different methods and materials were used.

- Riboflavin

10µL of sample were injected into a polar column (Luna omega 3µm C18 100Å, 150mm x 4.6mm; Phenomenex, Le Pecq, France). The flow rate was set to 0.8 mL/min for a mobile phase blend A:B (85:15) and the running time was set to 10min for each sample. Eluent A was an aqueous solution containing 0.1% of formic acid and eluent B was pure acetonitrile. The column was kept at room temperature and the detection wavelength was set to 270nm. The calibration curve was determined for Rf concentrations ranging from 0.1 to 40 mg/L and was linear ($R^2 > 0.999$). Each experiment was performed in triplicate. Mean values +/- standard deviations are reported in the results.

- Chlorhexidine

10µL of sample were injected into a non-polar column (Gemini, 3µm C18 110Å, 150mm x 4.6mm; Phenomenex, Le Pecq, France). The flow rate was set to 1.5 mL/min for a mobile phase blend A:B (70:30) and the running time was set to 5min for each sample. Eluent A was an aqueous solution containing 115mM of orthophosphoric acid and 0.5% of triethylamine and eluent B was pure acetonitrile. The column was kept at room temperature and the detection wavelength was set to 239nm. The calibration curve was determined for Chx concentrations ranging from 1 to 40 mg/L and was linear ($R^2 > 0.999$).

CHAPTER III – SOLID-STATE AMORPHIZATION OF CHLORHEXIDINE (FREE BASE) UPON MILLING

Chlorhexidine is a broad-spectrum antimicrobial biguanide (as represented in Figure 24) used as a topical antiseptic and in dental practice for the treatment of inflammatory dental conditions, such as periodontitis[142–145]. This API was categorized as a BDDCS class III drug[146] and is thus supposed to exhibit a high solubility and a low permeability. However, according to the literature, Chx is generally referred to as poorly-soluble as this API exhibits an approximate solubility in water of 80mg/L[147,148]. Therefore, Chx is usually investigated in the form of water-soluble salts such as Chx digluconate or Chx diacetate. It was also reported that only five crystal structures of chlorhexidine salts have been reported in the Cambridge data base over the past 60 years[149], and therefore, to the best of our knowledge, the crystalline structure of Chx free base has not yet been determined. Furthermore, in terms of drug release, as the Chx salts present a better solubility compared to the free base, those are generally more investigated[150–152].
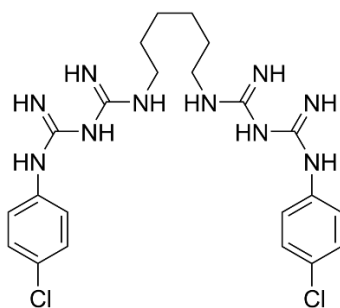
Figure 24 - Illustration of the molecule of chlorhexidine.

If little is known about the crystalline structure of Chx free base, its amorphous state was already produced by liquid quench and its glass transition temperature was found to be Tg = 62.85°C[153]. However, to the best of our knowledge, a deep physical characterization of the amorphous state of Chx was only performed for Chx dihydrochloride[92].

The objective of this chapter is to assess the possibility to obtain amorphous Chx free base by high energy milling of the crystal and to compare this solid state amorphization process with the traditional liquid quench. To that extend, a deep physical characterization is performed on both commercial Chx free base (crystalline) and on the milled material.

Then, in order to assess the advantage of the amorphous form compared to its crystalline counterpart, an evaluation of their dissolution performances in ultra-pure water are evaluated using different set ups including powder dissolution, intrinsic dissolution and tablet dissolution.

III.1 Physical characterization of chlorhexidine free base

The objective of this section is to assess the possibility to obtain amorphous chlorhexidine by high energy milling of the crystal and to compare this solid state amorphization process with the traditional liquid quench. This investigation is focused on a deep physical characterization in order to understand in detail the structural evolution of Chx during the milling process.

III.1.1 Effect of heating on the physical state of chlorhexidine free base

In Figure 25 is represented the TGA scan (5°C/min) of commercial Chx. A considerable weight loss is observed (about 85%), revealing a strong thermal degradation of the drug which starts at 150°C. Therefore, in order to avoid any degradation of samples in our investigation, the DSC heating scans of any sample containing Chx will not exceed 150°C.
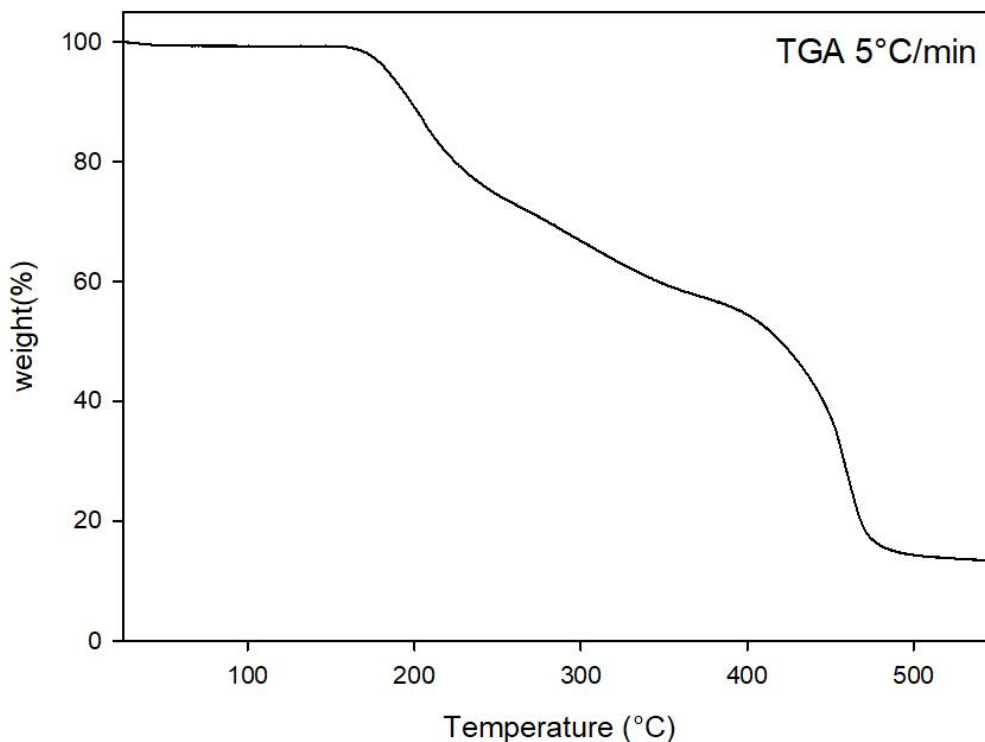
Figure 25 - TGA scan (5°C/min) of chlorhexidine free base (as received).

Figure 26 shows the DSC heating scan of commercial chlorhexidine (run 1, blue curve) in an open aluminum pan (no lid). This scan reveals two successive endothermic peaks: a small one around 122°C (ΔH = 7.6 J/g) and a bigger one around 135°C (ΔH = 76.7 J/g) which corresponds to the melting of the API[153]. The melt thus obtained was subsequently quenched using a cooling rate of 5°C/min until room temperature (RT) was reached. The corresponding DSC scan (run 2, black curve in Figure 26) shows no sign of crystallization upon cooling at such a rate which means that this liquid can easily be undercooled. The heating DSC scan (5°C/min) of the quenched liquid is also shown in Figure 26 (run 3, brown curve). It shows a Cp jump (ΔCp = 0.57 J/g/°C), characteristic of a glass transition at Tg = 58.8°C which indicates that the traditional quench of the liquid allows to obtain the amorphous form of Chx. Furthermore, it can be noted that no exothermic peak characteristic of a recrystallization can be detected above Tg, which reveals that the amorphous form obtained from the liquid quench is stable upon heating.
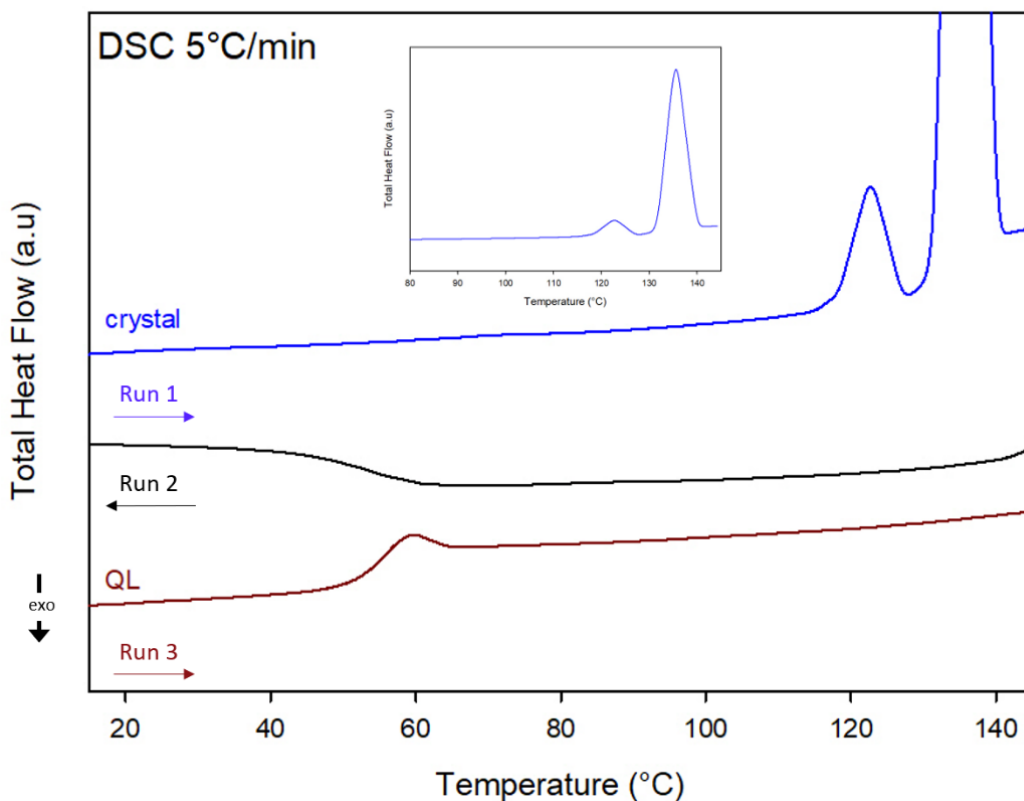
Figure 26 - DSC heating scans (5°C/min) of commercial chlorhexidine (run 1, blue curve) and of the subsequently obtained quenched liquid (run 3, brown curve). The quenched liquid was obtained by cooling the melt at 5°C/min (run 2, black curve). The insert shows the entire endothermic melting peak of the crystal (run 1).

In order to better understand the origin of the first endothermic event observed during the heating of commercial Chx, the structural evolution of the sample upon heating has been followed by powder X-ray diffraction. Figure 27 shows the diffractograms recorded at different temperatures ranging from RT to 134°C. It must be noted that the peak observed at 6.6° is due to the Anton Paar chamber used in order to record the diffractograms at the desired temperatures. The scan recorded at room temperature (blue curve) shows Bragg peaks characteristic of a crystalline form. It can be observed that at 120°C, the X-ray diffraction pattern is similar to the one recorded at RT except for some peak shifts due to the temperature change. This means that no structural changes occurred between RT and 120°C. However, between 124°C and 130°C, some new peaks are emerging (e.g. peaks marked with a ▲) whereas the peaks characteristic of the commercial Chx are disappearing (e.g. peaks marked with a ★). This reveals a phase transition between the initial form (called Form I) and the final form (called Form II).

At 130°C, the decreasing peaks characteristic of Form I have totally disappeared while those characteristic of Form II become stationary, indicating that the phase transition is completed. These results strongly suggest that the endothermic peak observed before the melting corresponds to the polymorphic transition Form I → Form II. This also means that the melting observed afterwards corresponds to the melting of the polymorphic form II.
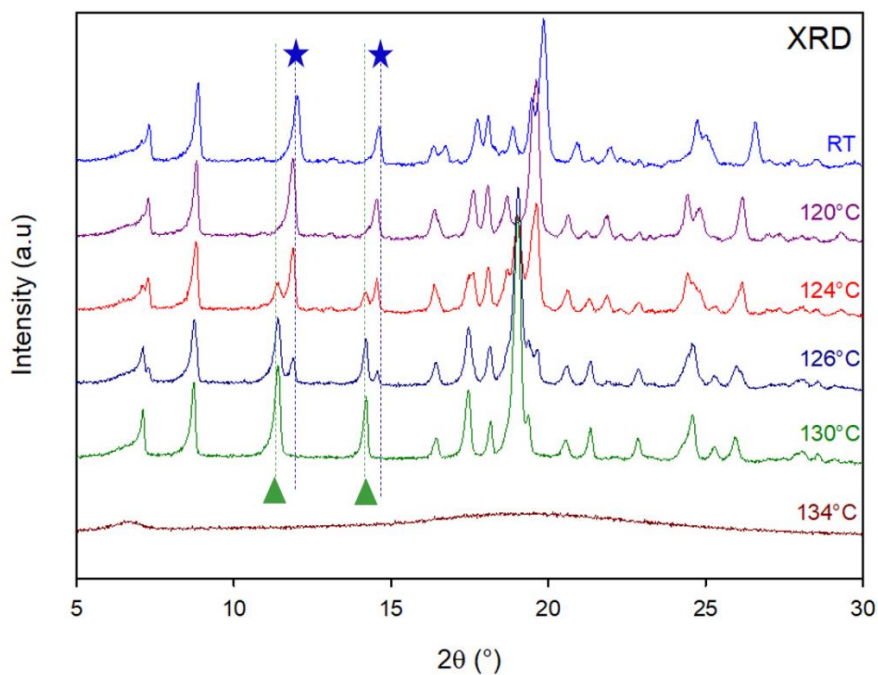
Figure 27 - X-Ray diffraction patterns of commercial chlorhexidine recorded upon heating. The temperatures at which the scans were recorded are reported on the right-hand side of each curve and the heating rate was set to 5°C/min.

This endotherm corresponding to the polymorphic transition was also investigated using DSC. Indeed, commercial Chx was heated to 127°C (at the end of the first endotherm) and rapidly cooled at an approximate rate of 40°C/min. The sample was then heated again (5°C/min) in order to observe the potential change in the thermal events. The corresponding DSC thermograms are illustrated in Figure 28. It can be noticed that during the cooling stage, an exothermic event is observed and during the second heating, the same two endotherms, as observed in the first heating of commercial Chx to 150°C (Figure 26), are present. These observations indicate that the first endothermic peak related to the polymorphic transition Form I → Form II is totally reversible as, upon cooling (even though as rapid as enabled by the instrument), Form I reappears and Form II disappears completely. Furthermore, it means

that Form II is not stable upon cooling and it is thus impossible to produce this polymorphic form using this method.
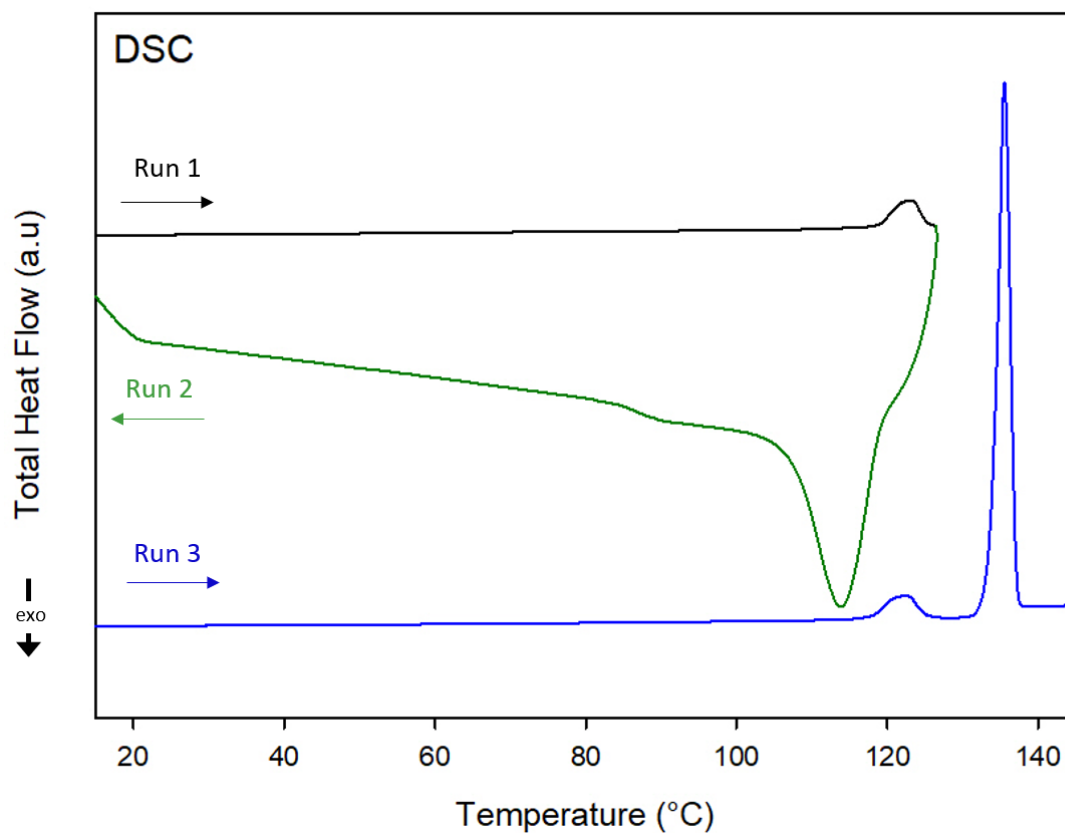
Figure 28 - DSC scans of commercial chlorhexidine after several thermal treatments: heating at 5°C/min to 127°C (run 1, black curve), subsequent cooling at 40°C/min (run 2, green curve) and subsequent heating to 150°C at 5°C/min (run 3, blue curve).

All these results allowed the determination of the phase diagram of Chx upon heating, as illustrated in Figure 29. It can be noticed that, as the polymorphic transition occurs before the melting peak and is illustrated by an endothermic event, Form I and Form II of Chx are thus enantiotropically related.
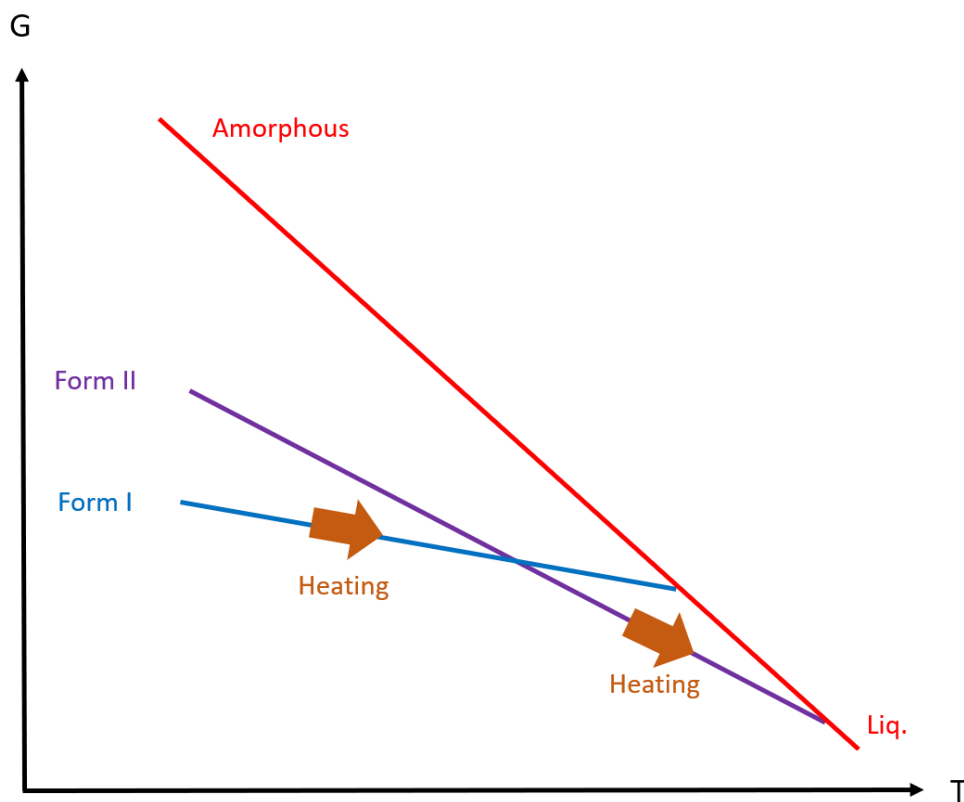
Figure 29 - Phase diagram of chlorhexidine upon heating. The arrows indicate the trajectory of Chx during the heating.

III.1.2 Effect of milling on the physical state of chlorhexidine free base

Figure 30 shows the ^{1}H NMR spectra of commercial Chx (as received), and of the quenched liquid prepared in either a DSC pan or in a tubular oven, after dissolution in DMSO. It must be noted that the purpose of preparing the quenched liquid in a tubular oven was to see if this amorphous form could be obtained in the required amounts for dissolution studies, compared to the small quantities which can be retrieved from the DSC pan. It can be noticed that the spectrum of the quenched liquid (QL) prepared in the tubular oven shows significant differences when compared to the one of commercial Chx as many peaks appeared after the melting (e.g. around 3.0 ppm, 6.5 ppm, between 6.8 and 7.0 ppm, 7.3 ppm and 7.8 ppm), which is characteristic of chemical degradation. However, the quenched liquid prepared in the DSC pan shows more similarities with Form I, except for a few additional peaks (e.g. around 6.5 and 6.9 ppm), which also suggests that a chemical degradation occurred but in lesser proportions. It must also be noted that the additional peak at 2.08 ppm present in the spectra of commercial Chx and of the

quenched liquid prepared in the tubular oven is attributed to an acetone residue[154] stemming from the cleaning of the NMR tubes.
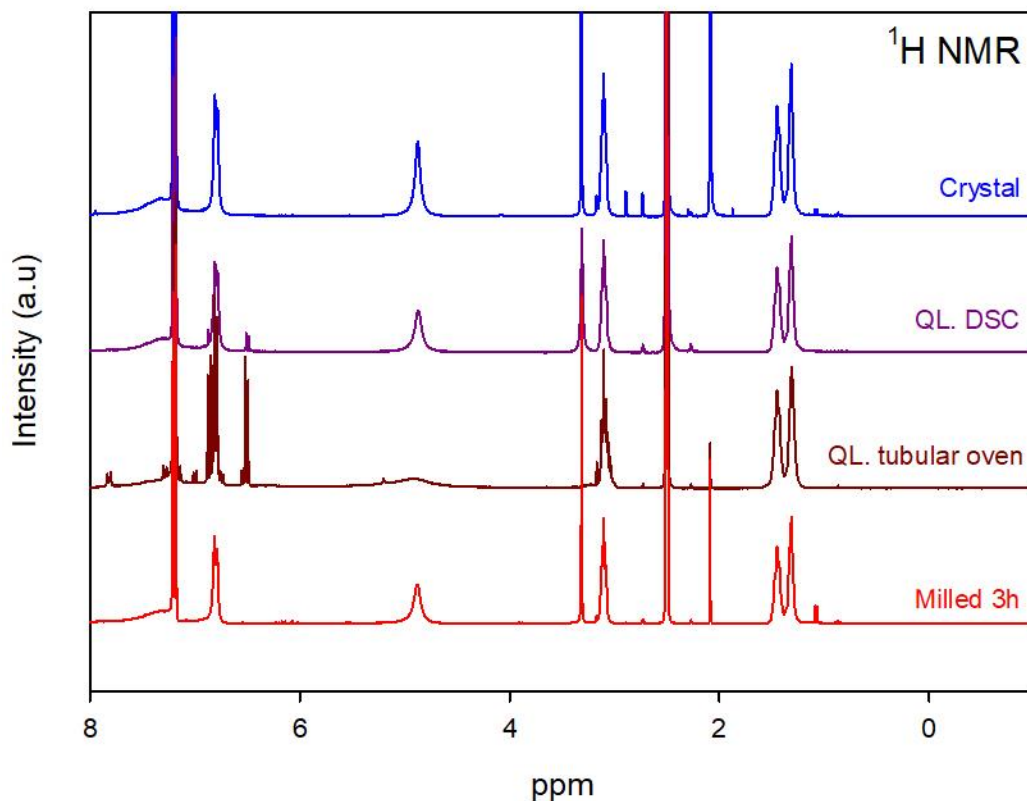
Figure 30 - ^{1}H NMR spectra of commercial Chx (crystal, as received), of Chx melted in either a DSC pan or a tubular oven and quenched (QL), and of Chx milled for 3 hours. The names of the samples are on the right side of each curve.

As the classical liquid quench of Chx led to chemical degradations, another amorphization process was tested in order to prevent those degradations. Due to the thermal instability of Chx and to its poor-solubility in organic solvents, a mechanical-based approach was used and high-energy ball milling was chosen. Indeed, it was assumed suitable as it was proven in the literature[100,155] to allow a direct crystal-to glass-transformation in the solid state.

Figure 31a shows the X-ray diffraction patterns of commercial Chx as received (blue curve), of the quenched liquid (brown curve) and after being submitted to 1 hour of high-energy milling (red curve). The peak observed at 6.6°, in both the quenched liquid and the milled Chx, is due to the signal of the Anton Paar chamber used for the analysis. It can be noticed that after the milling process, all the Bragg peaks characteristic of crystalline Chx disappeared, giving rise to a diffusion halo characteristic of an amorphous form. Furthermore, this diffractogram is identical to the one of the quenched liquid. This observation strongly suggests that the 1h of milling led to a complete amorphization of Chx.

Figure 31b shows the corresponding DSC heating scans (5°C/min) with, in addition, the Chx quenched from the melt of the crystal (brown curve) for comparison. The thermogram corresponding to the milled Chx (1h) shows a Cp jump (ΔCp = 0.59 J/g/°C) characteristic of a glass transition at Tg = 60.5°C. Those results indicate that a direct crystal-to-glass transformation occurred during the milling. Furthermore, as the Cp jump of the milling-induced amorphous Chx shows the same amplitude as the one observed for the quenched liquid, the 1h of milling led to a complete amorphization of Chx. Finally, it can be noticed that the Tg of the quenched liquid is slightly depressed compared to the one of the milled material, which suggests that a minor degradation occurred during the melting of the drug.

Further heating of the milling-induced amorphous Chx shows a wide exotherm characteristic of a recrystallization. This situation contrasts with that of the quenched liquid which do not show any sign of recrystallization for identical heating conditions. The milling-induced amorphous material thus appears to be less stable than the quenched liquid. This exothermic event partially overlaps a small endothermic peak which is directly followed by a second endotherm, higher and sharper. This pattern of two following endothermic events is similar to the one observed during the heating of crystalline Chx, which indicates that after the recrystallization, the polymorphic transition occurred, followed by the melting. Because of the superimposition of the exothermic event and of the endothermic peak associated with the polymorphic transition, the corresponding enthalpies cannot be accurately determined. The enthalpy of melting of the recrystallized fraction of the milling-induced amorphous Chx corresponds to 66.4 J/g which is lower than the value obtained for the melting for the non-milled Chx (76.7 J/g). Thus, a small fraction (~13.4%) of amorphous Chx has not recrystallized.
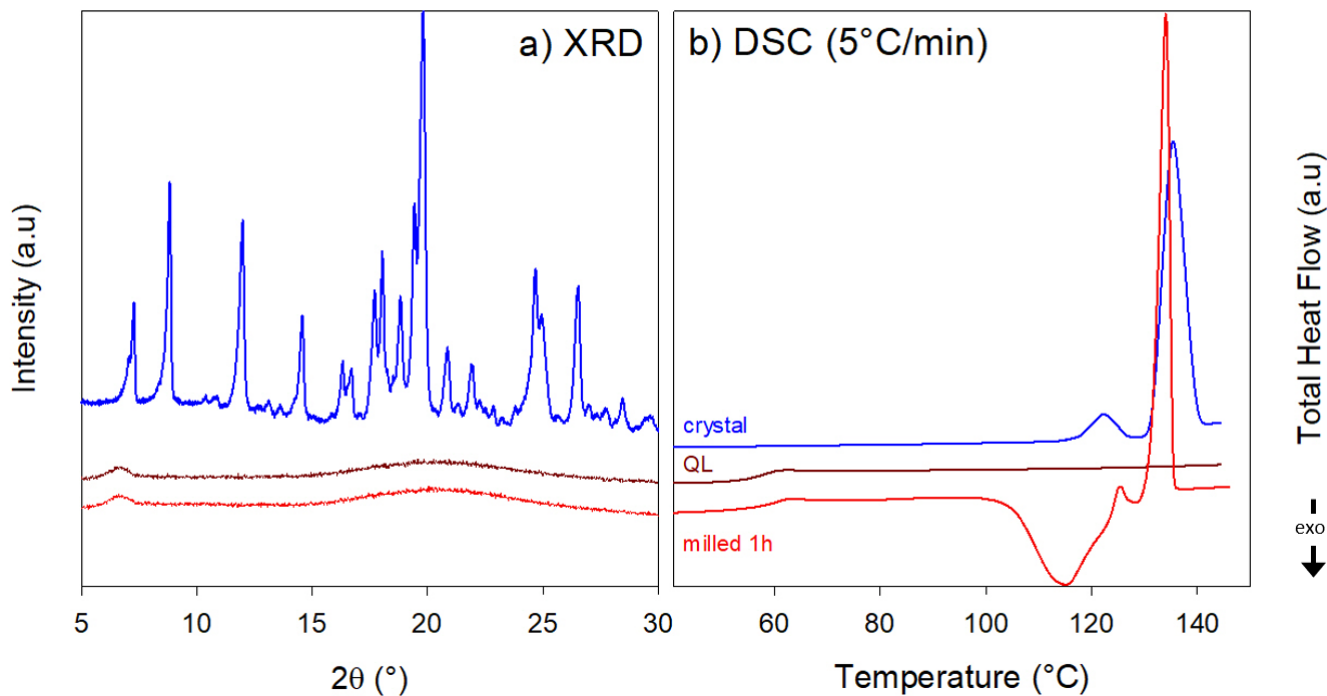
Figure 31 – a) XRD patterns of commercial Chx as received (blue curve), of the quenched liquid (brown curve) and of Chx milled for 1 hour (red curve), and b) the corresponding DSC scans (5°C/min).

The milled Chx was also analyzed using ^{1}H NMR spectroscopy, as shown in Figure 30. It must be noted that the milling time performed was longer (3 hours) than the one presented in Figure 31 in order to make sure of the robustness of the milling process on Chx.

Interestingly, the spectrum corresponding to the milled Chx is identical to that of the crystal, indicating that no degradation was induced by the milling process. It must also be noted that the additional peak at 2.08 ppm present in this spectra is attributed to an acetone residue[154] stemming from the cleaning of the NMR tubes. Those results indicate that high-energy milling is a safer amorphization route compared to the quench of the liquid which induces more or less degradation depending on the melting conditions of Chx. Furthermore, it was demonstrated, that solvent-based processes such as spray- or freeze-drying (due to the lack of an appropriate solvent[156,157], cf Appendix 1), could not be used for the amorphization of Chx. Therefore, only this amorphization process will be used for this drug in all the further experiments.

The evolution of milling-induced amorphous Chx upon heating was monitored using XRD. Therefore, the X-ray diffraction patterns of Chx milled during 1 hour were recorded upon heating from 30°C to 135°C

and are represented on Figure 32. From 30 to 80°C, no Bragg peaks are observed, which confirms that the milled material remains completely amorphous in this range of temperatures. It must be noted that the peak observed at 6.6° is due to the Anton Paar chamber used in order to record the diffractograms at the desired temperatures. From 90°C to 110 °C, some Bragg peaks develop, indicating the recrystallization process. These Bragg peaks are characteristic of Form I, indicating that the recrystallization of the milling-induced amorphous sample occurs towards initial commercial form of Chx as represented in Figure 27 (see for instance peaks marked with a ★). Further heating of the material shows the development of Bragg peaks characteristic of Form II at the expense of those characteristic of Form I, revealing a transition I →II identical to that observed upon heating of the non-milled Form I (see for instance peaks marked with a ▲ for the diffractogram at 125°C). This indicates that the small endothermic event observed on the DSC scan between the recrystallization and the melting peak is, as expected, the polymorphic transition also observed for the non-milled material. At 130°C, the Bragg peaks are broadening and decreasing in intensity until, 5°C higher, they fully disappeared and gave way to the diffusion halo of the liquid Chx.
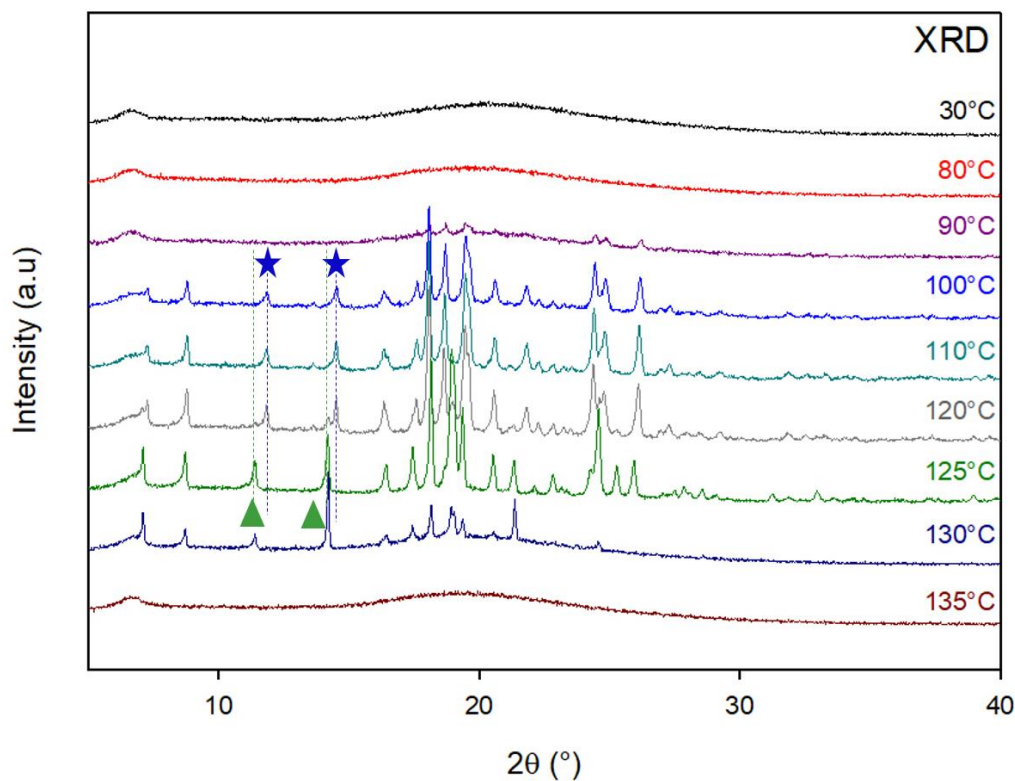
Figure 32 - X-ray diffraction patterns of Chx milled for 1h, recorded upon heating from 30 to 135°C. The temperatures at which the diffractograms were recorded are indicated on the right-hand side of each curve.

These results allowed to determine the relative stability of the two forms of Chx identified as schematized in the Gibbs free enthalpy diagram reported in Figure 33. Indeed, the milling-induced amorphous Chx recrystallizes towards Form I upon heating, which is subjected to a polymorphic transition towards Form II after further heating. As observed for crystalline Chx (Figure 29), the polymorphic transition occurs before the melting peak and is illustrated by an endothermic event which indicates that Form I and Form II of Chx are thus enantiotropically related.
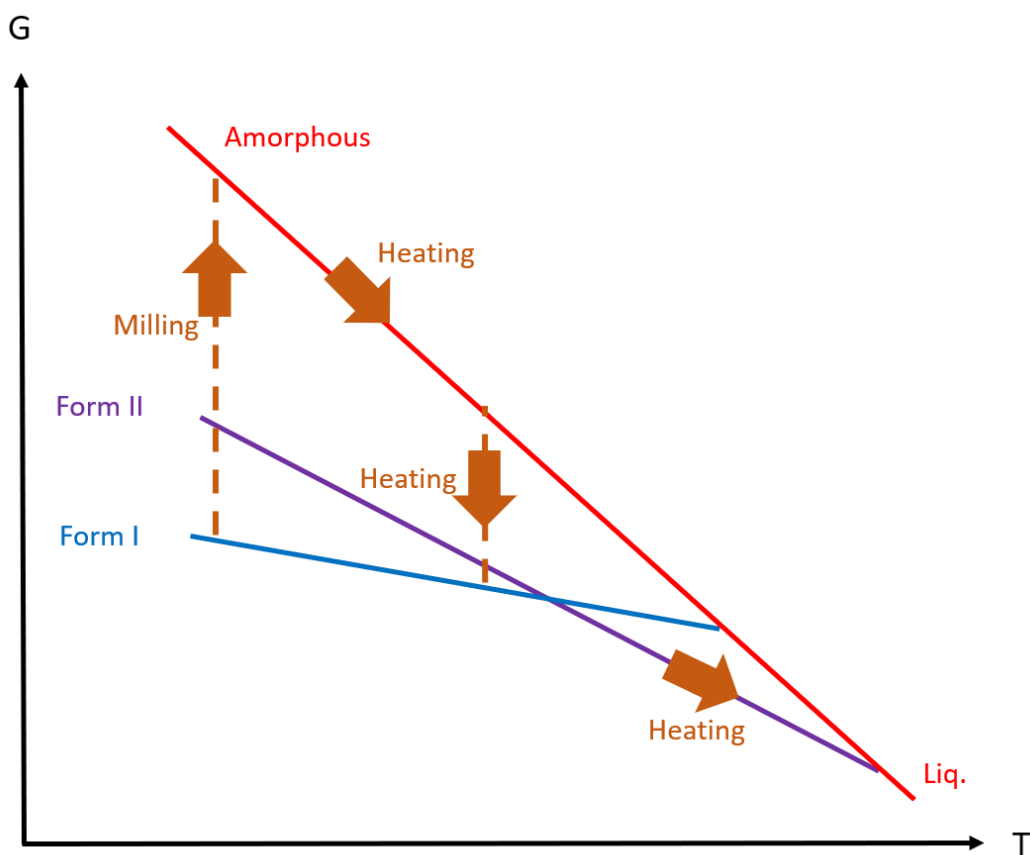
Figure 33 - Phase diagram of Chx upon milling. The arrows indicate the trajectory of Chx during the milling and the subsequent heating of Chx.

III.1.3 Amorphization kinetics upon milling

Commercial chlorhexidine was milled for several milling times (t_m) ranging from 0 min to 12 hours and the corresponding XRD patterns are reported in Figure 34. During the first 5 min, a progressive flattening and broadening of the Bragg peaks can be observed. The decrease in peak intensity indicates the progressive disappearance of the crystal and thus, the increasing fraction of amorphous material. Meanwhile, the broadening signals both the size reduction and the deformation of the remaining crystallites induced by the mechanical impacts of the milling balls. Besides, it can be observed that after 15 min of milling, the Bragg peaks totally disappeared, giving rise to a diffusion halo which indicates a complete amorphization of the material. No further evolution of the X-ray diffraction patterns can be detected for longer milling times (up to 12 hours).
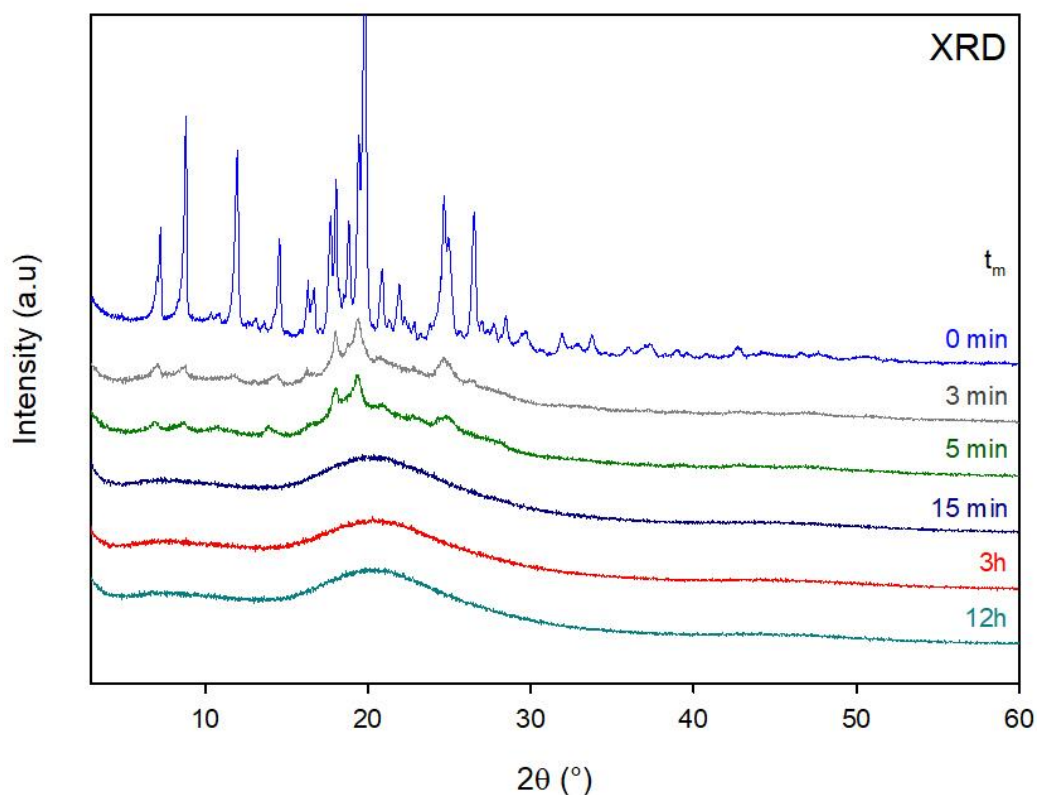
Figure 34 - XRD patterns of commercial chlorhexidine recorded after different milling times (tm) ranging from 0 min (no milling) to 12h.

The corresponding DSC heating scans (5°C/min) are reported in Figure 35. It must be noted that there are 3 additional thermograms corresponding to 1min, 1h and 24h of milling. The scans show the progressive development of a Cp jump at the glass transition temperature (Tg = 60.4°C), which reveals the progressive amorphization of the drug. The Cp jump at Tg becomes stationary from 1h of milling, which proves that the amorphization upon milling is complete after that time period.

Above Tg, the thermograms also show an exotherm of recrystallization whose evolution during milling appears to be more complex. During the first hour of milling, this exotherm develops and shifts towards higher temperatures. These two features indicate respectively that the amorphous fraction increases and becomes more and more stable. Beyond 1h of milling, the exotherm no longer shifts but progressively disappears to finally vanish after 24h of milling. This indicates that the stability of the amorphous fraction further increases after 1h of milling, eventually preventing its recrystallization upon heating. Such a physical stability is quite exceptional for a milling-induced amorphous material and was only observed in a very few cases, e.g. lactulose[26].

The polymorphic transition I → II represented by the endothermic event around 122°C, also appears to have a complex evolution. Indeed, during the first 3 min of milling, this endotherm seems to disappear while the amount of remaining Form I estimated from the enthalpy of recrystallization (21.6 J/g) remains high and close to 28.2%. This suggests that the first few minutes of milling seem to have disturbed the micro-structure of the crystal enough to prevent the polymorphic transition I → II to occur. However, from 5min to 3h of milling, the endothermic event is progressively restored in parallel with the development of the recrystallization exotherm. This strongly suggests that the recrystallization occurs toward Form I, and that this fresh Form I (which has not been milled) undergoes the polymorphic transition I → II. After 3 hours of milling, the endotherm associated with the transition I → II vanishes again due to the stabilization of the amorphous fraction which results in a decreasing recrystallization toward Form I.

The evolution of the melting peak for increasing milling time is simpler. It shows a progressive decrease from 12h of milling when the amorphous fraction produced by the milling becomes increasingly stable, and almost totally disappeared after 24h of milling. It must also be noted that the melting temperature of Form II is slightly shifted toward the low temperatures in all milled samples compared to the non-milled material. This well-known effect is due to the so-called Gibbs Thomson effect and is induced by

the strong crystallite size reduction[158] which is known to occur at the very beginning of the milling process (typically within the first few minutes[159]).
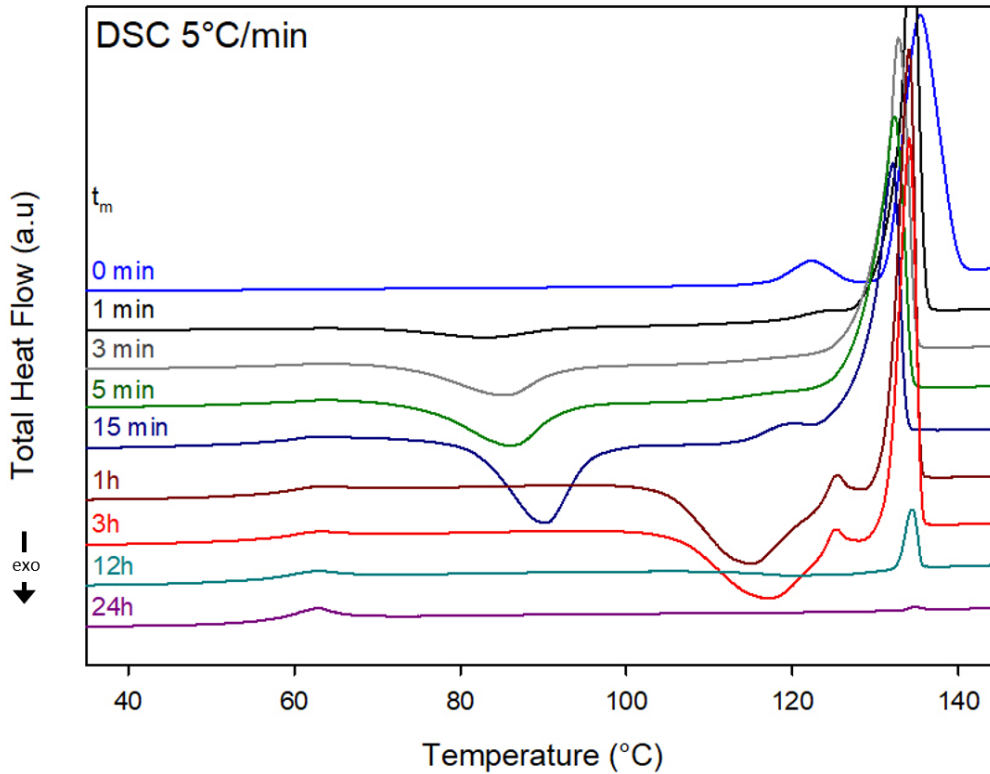
Figure 35 – DSC scans (5°C/min) of commercial Chx recorded after different milling times (tm) ranging from 0 min (no milling) to 24h.

The time evolution of the total amorphous fraction during the milling process is reported in Figure 36. It has been obtained by calculating both the fraction of amorphous Chx which recrystallizes upon heating and the one that does not. The first one was directly derived from the enthalpy of recrystallization while the second one was derived from the difference between the enthalpies of melting of the milled and non-milled material as depicted in the series of equations below.

$$X_{am}(t) = X_{am}(recryst, t) + X_{am}(not\ recryst, t) \quad (18)$$

$$X_{am}(t) = \frac{\Delta H_c^{Tc}(milled, t)}{\Delta H_m^{Tc}(crystal)} + \frac{\Delta H_m(crystal) - \Delta H_m(milled, t)}{\Delta H_m\ (crystal)} \quad (19)$$

$$\text{With } \Delta H_m^{Tc}(crystal) = \Delta H_m(crystal) - \Delta C_p * (T_m - T_c) \quad (20) \text{ (Appendix 2)}$$

With:

- Tc as average temperature of recrystallization.
- ΔH_m and ΔH_c as the melting and crystallization enthalpies, respectively.
- ΔH_m^{Tc} (crystal) as the enthalpy of melting of commercial Chx (crystalline) extrapolated at the crystallization temperature T_c.
- T_m as the temperature at which the endothermic peak of melting of the commercial Chx occurs.

The amorphization kinetics thus determined seem to obey an exponential relaxation law. The best fit of this law to the data is also reported in Figure 36 and provides a relaxation time τ = 4.6 min. This indicates that the propensity of Chx to reach the amorphous state upon milling is exceptionally high as most of pharmaceutical materials milled with identical conditions are characterized by an amorphization relaxation time close to 1h[30,92]. However, a few cases of very low relaxation times were already reported in the literature, e.g. lactulose[26] and bosentan[160].

$$X_{am} = 1 - e^{-t/\tau}$$

$$\tau = 4.6 \text{ min}$$
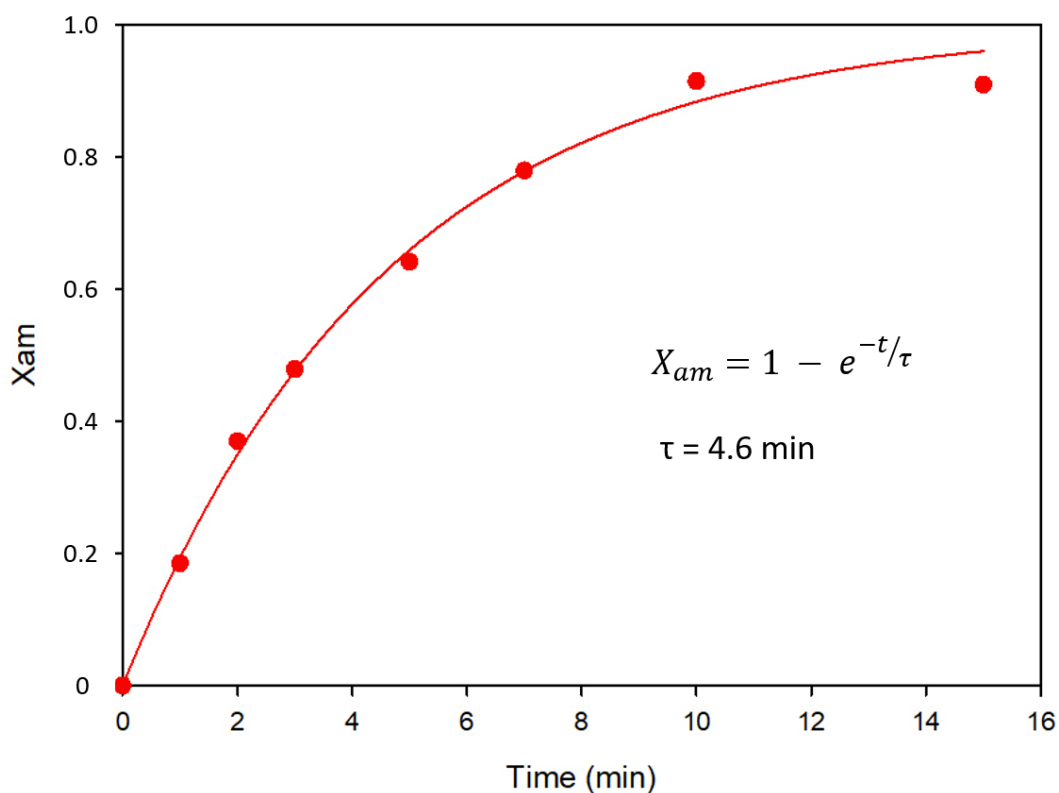
Figure 36 - Amorphization kinetics of Chx upon milling derived from the analysis of DSC scan shown in Figure 35. The red dots represent the experimental data. The red line illustrates the best fit of an exponential relaxation law to the data.

III.2 Dissolution performances

After a deep physical characterization of the commercial Chx free base and of the milled material previously highlighted, an evaluation of their dissolution performances in ultra-pure water was performed using different set ups. This investigation was proposed in order to assess the advantage of the amorphous form compared to commercial chlorhexidine.

III.2.1 Determination of the solubility limit of chlorhexidine

First of all, in order to have a good understanding of the behavior of crystalline and milling-induced amorphous chlorhexidine in water, it was necessary to evaluate their solubility limit and the time period necessary for it to be reached. To that extend, about 150mg of API, were used in order to have it in excess in the medium (ultra-pure water, 10mL). For the crystalline form of Chx, the commercial material was used as received. Indeed, as it was demonstrated that the polymorphic form (Form II) was not stable upon cooling and, as no other method was investigated, it was not produced. The amorphous form of Chx was obtained by milling commercial Chx for 3 hours. Indeed, as the previous results indicated that high-energy milling was a safer amorphization route compared to the quench of the liquid, only the milling-induced amorphous form will be evaluated for dissolution performances.

The dissolution kinetics of these powders in ultra-pure water at 37°C under non-sink conditions (large excess of Chx) are illustrated in Figure 37. The first 8 hours of dissolution are displayed on the insert of Figure 37 for more visibility. During the first 3 hours, crystalline Chx reaches a maximum of dissolution of around 167 mg/L. But at later time points (after 4 hours), this concentration decreased to about 100 mg/L and then leveled-off. In contrast, the tendency observed for the amorphous form of Chx is less clear. Indeed, after the first hour of dissolution, the concentration observed was higher than for the crystalline Chx as it reached about 150 mg/L. However, from 2 to 4 hours of dissolution, it decreased so significantly that the concentration of Chx dissolved became inferior compared to the one of crystalline Chx. Surprisingly, until 8 hours, the tendency seems to be reversing as the concentration of Chx dissolved for the amorphous form increases again and reached around 190 mg/L. Finally, at later time points (after 24 hours), as observed for crystalline Chx, the concentration of drug dissolved for the amorphous form decreases again and reached a plateau of about 100 mg/L after 72 hours.

From those results, it seems that during the dissolution of amorphous and crystalline Chx, a precipitation occurs for different time points. Therefore, an accurate ranking of the solubilities of these two forms seems rather difficult to determine.
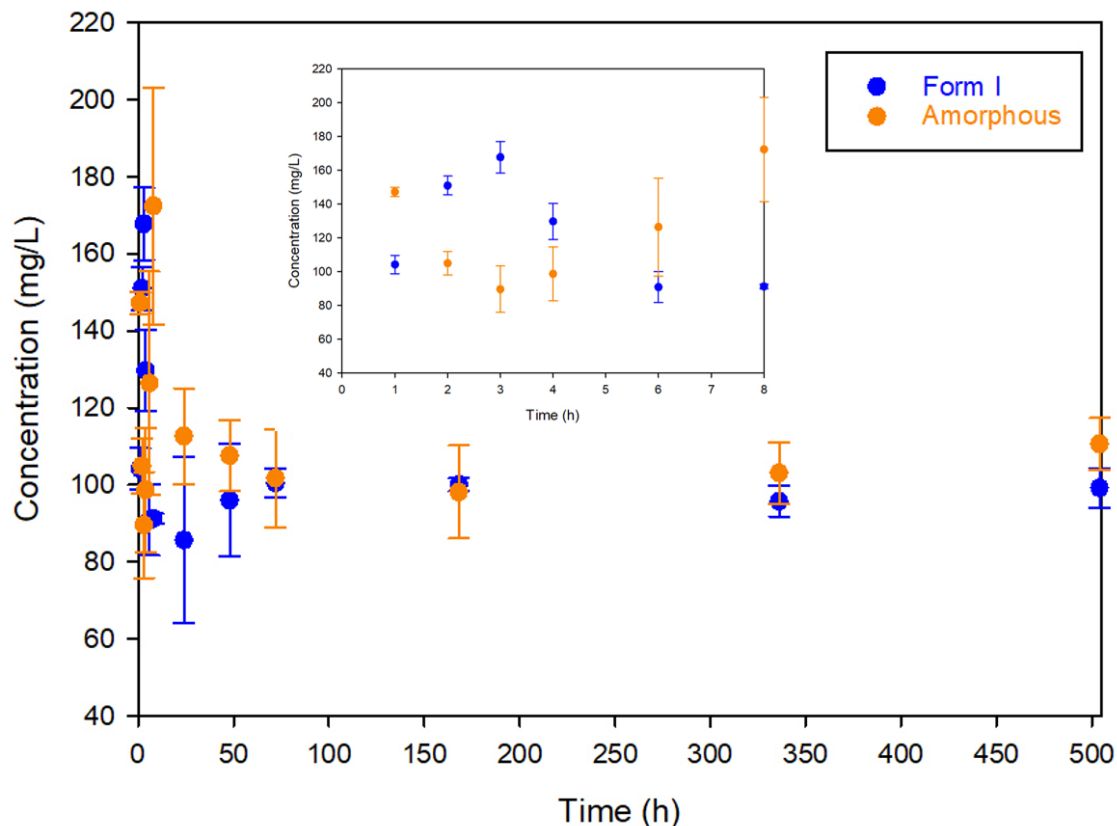
Figure 37 - Dissolution kinetics of Chx non-milled (crystal) and milled Chx for 3 hours (amorphous) in ultra-pure water at 37°C under agitation (80 rpm) and super-saturation conditions: a large excess of non-dissolved Chx was provided throughout the experiment.

In order to have a better understanding of which form of chlorhexidine precipitates during the dissolution measurements, the solids obtained at the end of the experiment (after 21 days) were separated by filtration, dried (under vacuum, at room temperature, overnight) and analyzed by XRD and TGA. Figure 38 shows the XRD pattern of the residue obtained after 21 days in water of crystalline chlorhexidine. However, it must be noted that an identical pattern was observed in the case of the residual solid obtained from the amorphous form (data not shown). Interestingly, it differs from the one of commercial Chx (crystalline) as its characteristic peaks (marked with a ★) disappeared and new peaks emerged (see for instance the peaks at 5.0° and 23.3°, marked with ●).
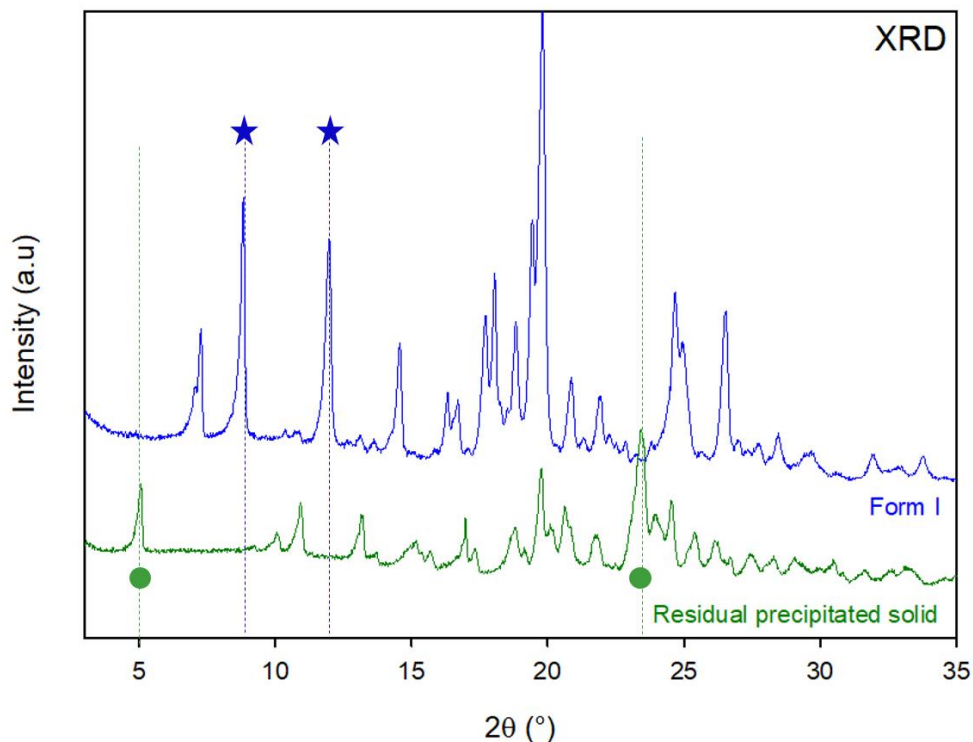
Figure 38 - XRD patterns of commercial Chx (crystal) recorded at room temperature and after 21 days spent in ultra-pure water heated to 37°C and stirred at 80rpm (purple curve) and subsequently dried under vacuum at room temperature.

The TGA scan (5°C/min) of the residue, which is reported in Figure 39, shows two distinct weight losses before the chemical degradation starts (after 150°C). The first one occurs between 20°C and 90°C and shows a mass loss close to 10.2%, which roughly corresponds to the calculated value for the loss of 3 water molecules (10.3%). The second one occurs between 80°C and 130°C and shows a mass loss of around 6.5% which is very close from the value expected for the loss of 2 water molecules (6.9%).

The evolution of the diffractogram of the recrystallized solid upon heating (5°C/min) from room temperature to 120°C, i.e. in the temperature range in which the mass losses were observed, is reported in Figure 40. It shows the progressive appearance and disappearance of some Bragg peaks and two phases can be distinguished. The first one from room temperature to 90°C leads to a distinct X-ray diffraction pattern which differs from the recrystallized residual solid and the second one from 90°C to 120°C which leads to the pattern of commercial chlorhexidine.

Therefore, all these results support the hypothesis that the crystalline chlorhexidine dissolved in water, precipitated towards a pentahydrate form, whose dehydration upon heating led firstly to a dihydrate form and then to the anhydrous commercial form of Chx.
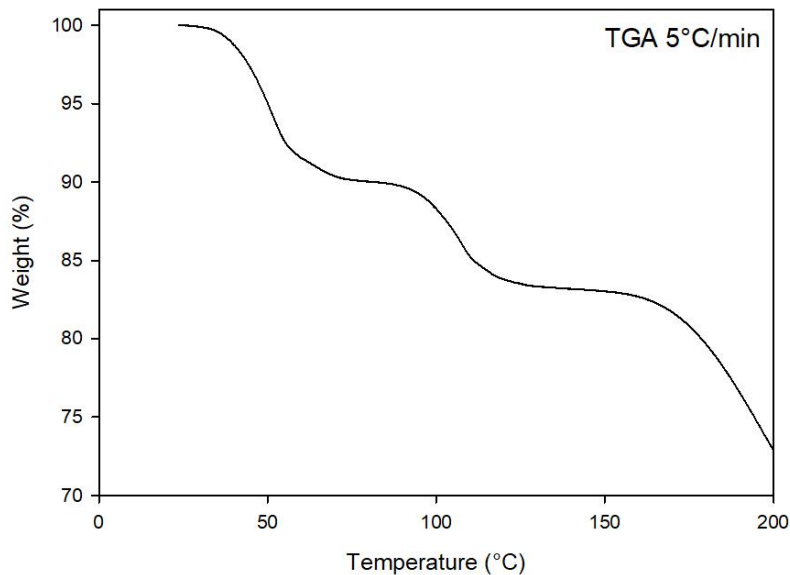
Figure 39 - TGA scan (5 °C/min) of the reprecipitated solid from the crystalline chlorhexidine during the dissolution study.
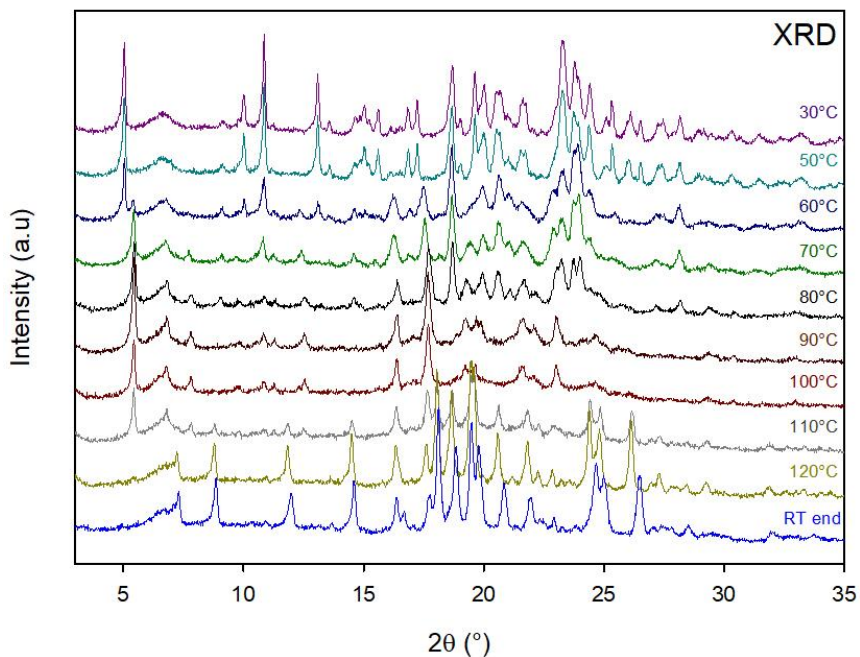
Figure 40 - XRD patterns of the solid which reprecipitated during the dissolution study of crystalline Chx in water. The samples were heated at 5°C/min followed by an isothermal of about 13 min (scan duration) at different temperatures (as indicated on the right side of each curve).

III.2.2 Powder dissolution in sink and non-sink conditions

As the dissolution in super-saturated conditions did not allow a clear distinction between crystalline and milling-induced amorphous Chx due to a rapid crystallization into a hydrate form, the dissolution in sink conditions was studied. Indeed, in this case, the amount of API is at least 3 times below its solubility limit. However, as only the solubility of the hydrate could be determined from the previous experiment, the value present in the literature[147,148] was chosen to impose the sink conditions, i.e. 80 mg/L.

Figure 41 illustrates the dissolution kinetics of crystalline and amorphous Chx in ultra-pure water in sink conditions (20mg of API in 800mL of ultra-pure water). These two forms show a biphasic dissolution profile as they show a steep slope during the first few hours, followed by a decrease in the dissolution rate until 48 hours of dissolution are reached. However, if the dissolution rates might seem to be similar during the first 4 hours of dissolution, significant gaps in the amount of chlorhexidine dissolved can be noticed and the two forms can thus be ranked as follows: Form I >> Amorphous form. Furthermore, after 48 hours of dissolution, Form I was completely dissolved whereas the amorphous form only reached around 80% of release. Form I thus shows an unexpected quicker dissolution compared to the amorphous form.

Figure 41 - Dissolution kinetics over 48 hours of the crystalline Chx (Form I) and of the amorphous form (milled 3h) in a large volume of ultra-pure water (800mL) heated at 37°C under stirring (100 rpm) and in sink conditions.

As the particles size and shape can significantly influence the dissolution of an API, SEM pictures of the powders of the two forms used for dissolution testing were taken and are depicted in Figure 42. Amorphous Chx and Form I powders both consisted of small particles. However, the amorphous particle formed aggregates whereas those of Form I were needle-shaped. Therefore, it seems that the aggregates formed by the amorphous particles are larger compared to the needle-shaped crystals of Form I. This observation can explain the propensity of crystalline Chx to dissolve quicker compared to the amorphous form.
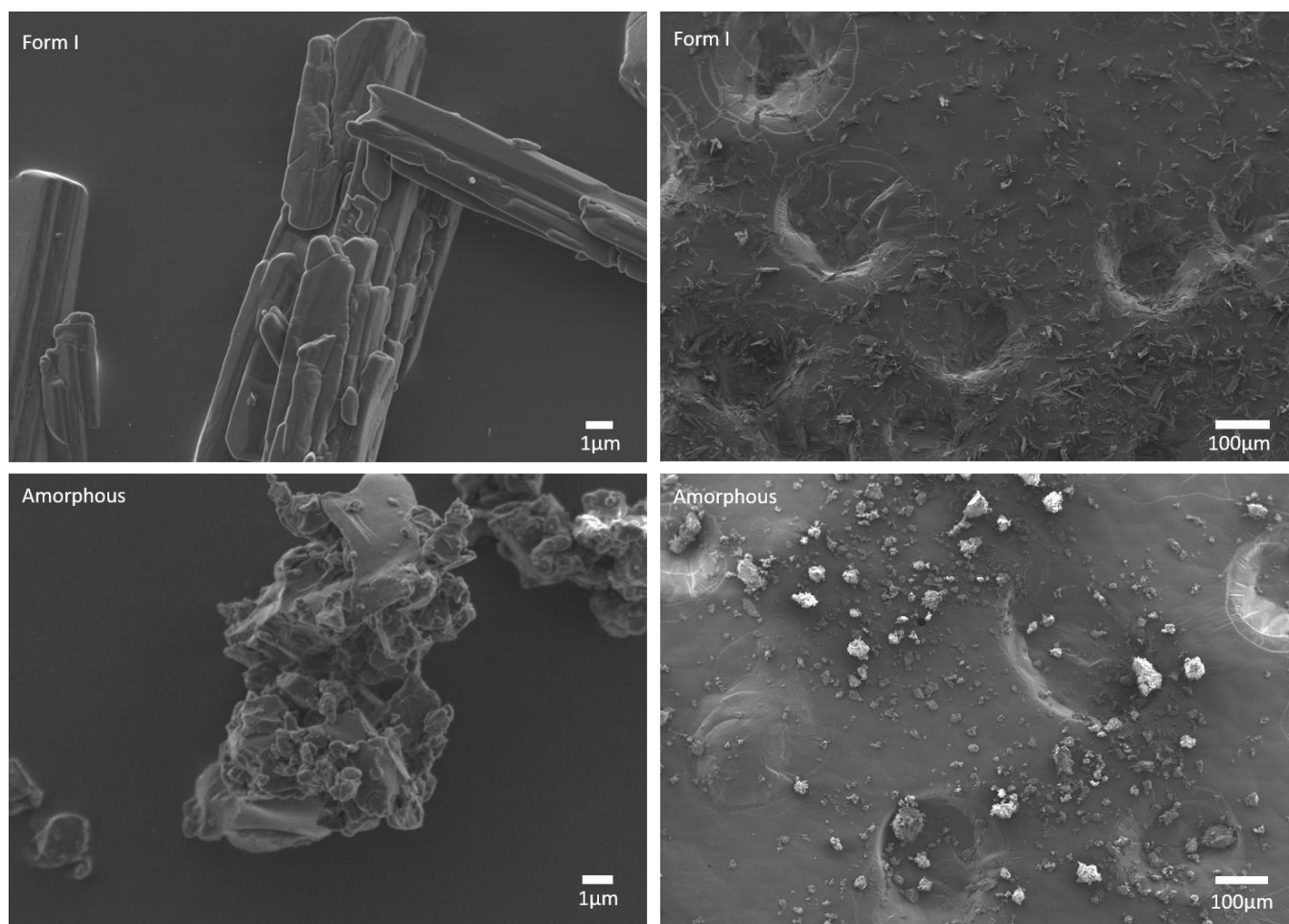
Figure 42 - SEM pictures of crystalline Chx (Form I) and milling-induced (3 hours) amorphous Chx powders used for the dissolution experiments.

Figure 43 illustrates the dissolution kinetics of the two forms previously presented in ultra-pure water in non-sink conditions as 150mg of API were used in the same amount of dissolution medium. It must be noted that in this case, according to the literature, the solubility of Form I was exceeded. Interestingly, in this dissolution set-up, Form I shows a significantly higher amount of Chx dissolved as soon as the powder comes in contact with the dissolution medium compared to the amorphous form. This behavior can be explained by the fact that, as depicted in Figure 44, the Form I particles are well dispersed in the dissolution medium whereas the amorphous particles quickly formed aggregates which stuck on the vessel wall or on the paddle.

Furthermore, in this dissolution set-up, Form I showed again the quickest dissolution compared to the amorphous form and even reached 100% of Chx dissolved after 48 hours of dissolution. In contrast, even if the amorphous form shows a higher dissolution rate during the first 4 hours as the slope seems steeper compared to Form I, a significant drop in the amount of Chx dissolved is then observed until it increased again, after 8 hours of dissolution. This strong decrease in the amount of Chx dissolved might be attributed to a recrystallization into the hydrate form as observed in section III.2.1. Besides, the solubility limit of the hydrate was evaluated to be at 100 mg/L, which corresponds to about 53% of Chx released (as illustrated in green dashes) and it also corresponds to the percentage of Chx dissolved reached for the amorphous form after 48 hours of dissolution. Interestingly, in the case of crystalline Chx, this percentage was exceeded which indicates that in this particular dissolution set-up, the transformation into the hydrate form is prevented. It can be thus assumed that this phenomenon is due to the dissolution set-up itself. Indeed, in this case, the higher volume of dissolution medium (800mL versus 10mL) accompanied with a difference in hydrodynamics induced by a paddle agitation (100rpm) compared to a horizontal shaking (80 rpm) could prevent the precipitation.

These results strongly suggest that the dissolution of the amorphous form is drastically slowed down by the formation of sticky aggregates when in contact with the dissolution medium, which has already been observed in the case of curcumin[161]. The second explanation for this decrease in the dissolution rate relies on the recrystallization of the amorphous form into the pentahydrate, less soluble, which was already observed in the case of carbamazepine[162]. Therefore, in this particular case, the amorphous form of Chx exhibits less advantages for the dissolution in water compared to its crystalline counterpart.
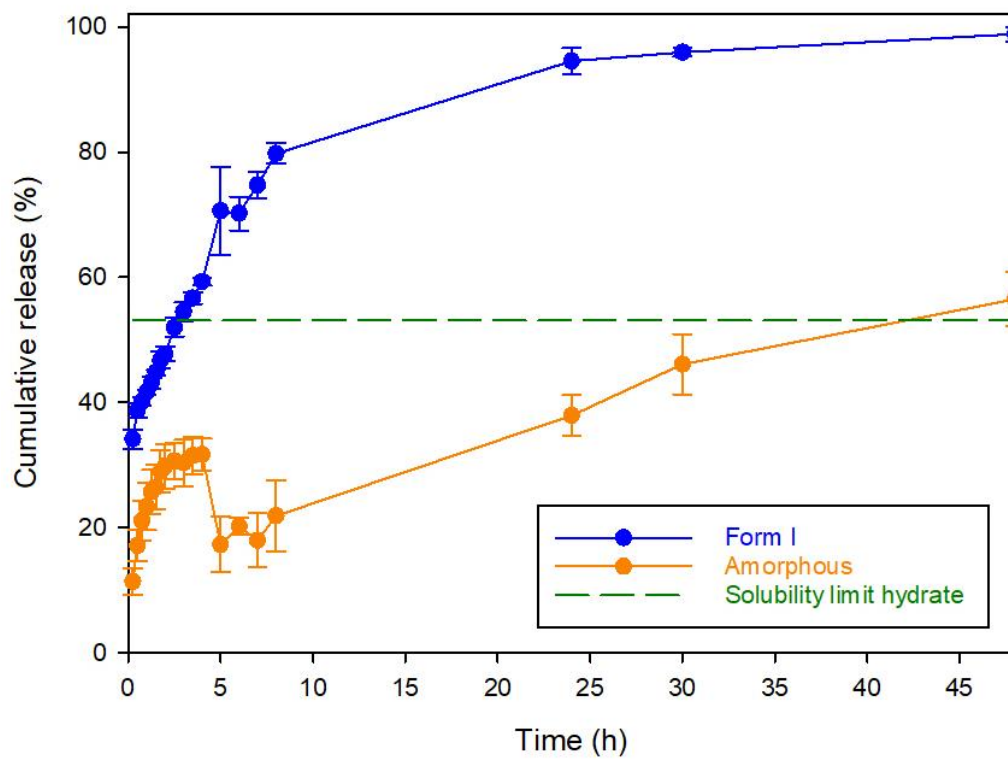
Figure 43 - Dissolution kinetics over 48 hours of the crystalline Chx (Form I) and of the amorphous form (milled 3h) in a large volume of ultra-pure water (800mL) heated at 37°C under stirring (100 rpm) and in non-sink conditions.

Form I
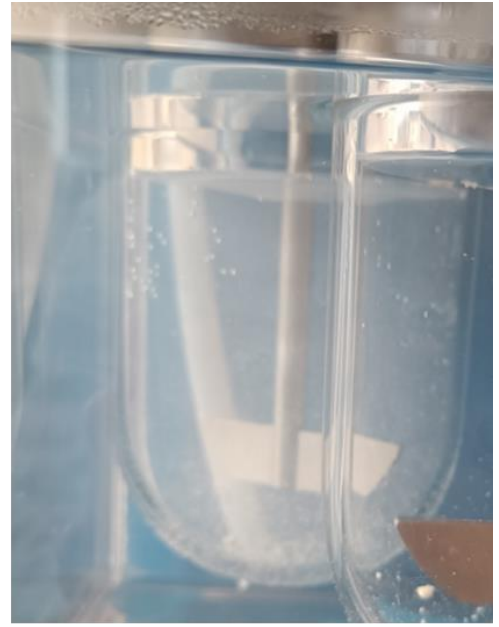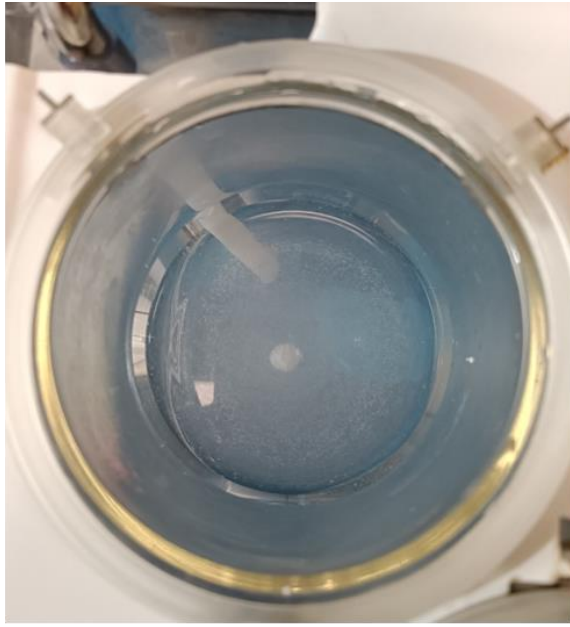
Amorphous

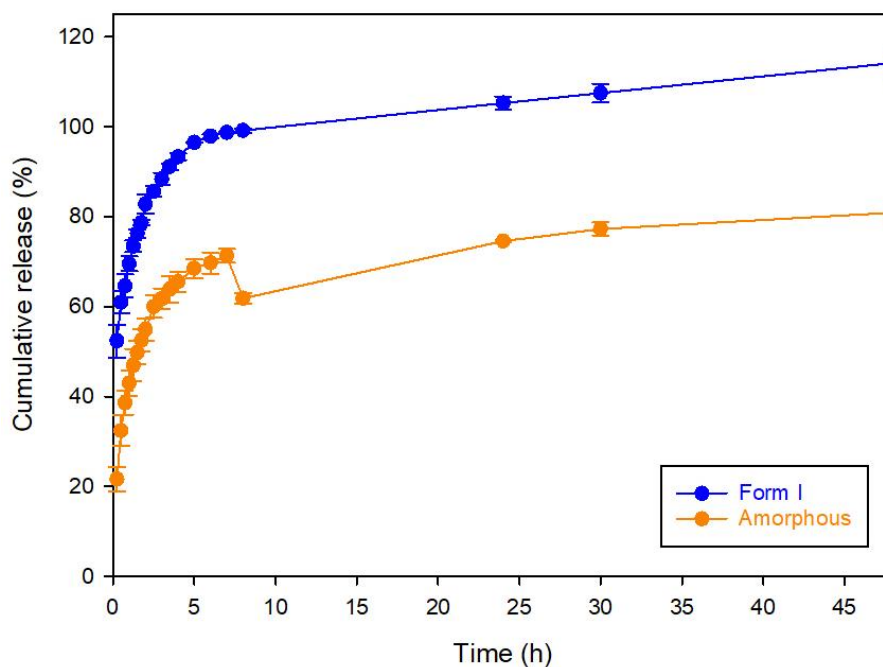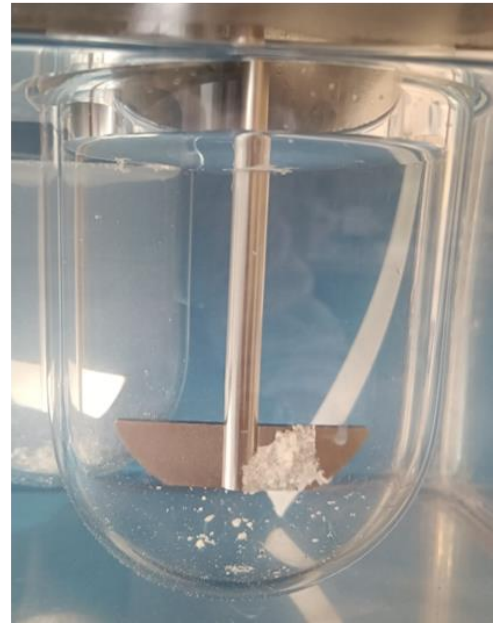*Figure 44 - Pictures after 15min of dissolution of the crystalline Chx (Form I) and of the amorphous form (milled 3h) in a large volume of ultra-pure water (800mL) heated at 37°C under stirring (100 rpm) and in non-sink conditions.*

III.2.3 Intrinsic dissolution

In order to obtain a clear determination of the dissolution rates of both Form I and the milling-induced amorphous form of Chx the intrinsic dissolution of these two forms was performed. Indeed, this method is particularly useful as it allows to hinder the influence of the particle size and shape which should have a particular interest in this case as the SEM pictures (Figure 42) revealed significant differences between the crystalline and amorphous particles.

First of all, the influence of the compaction on the physical state of the two forms was evaluated. For this study, the compacts were prepared using the exact same protocol as for the intrinsic dissolution (compaction at a 1t force). However, after the compaction step, instead of screwing the holder, the metallic plate was unscrewed and the compact was taken out of the die by strongly pressing on the punch. After this manipulation, the compact was found to be intact and was therefore analyzed using XRD. Afterwards, pieces were cut in order to perform both the DSC and the TGA analysis.

Figure 45 shows the X-ray diffraction patterns of both crystalline (Form I) and milling-induced amorphous Chx, before and after compaction. Form II of Chx is also showed for comparison. It is clear that after compaction of Form I, the Bragg peaks present on the X-ray pattern are those characteristic of Form I before compaction. However, some differences in intensities or in peak resolution can be noticed, (e.g. around 16° and around 21 and 22°) which are attributed to the preferential orientation of the crystal particles during the compaction. Regarding the milling-induced amorphous form of Chx, no Bragg peaks are visible on the X-ray diffraction pattern after compaction, which indicates that the material remained amorphous after this process. Such a stability upon compression of the amorphous form could be surprising without any stabilizing agent but it was already observed for several materials for compacts produced for intrinsic dissolution studies[163].
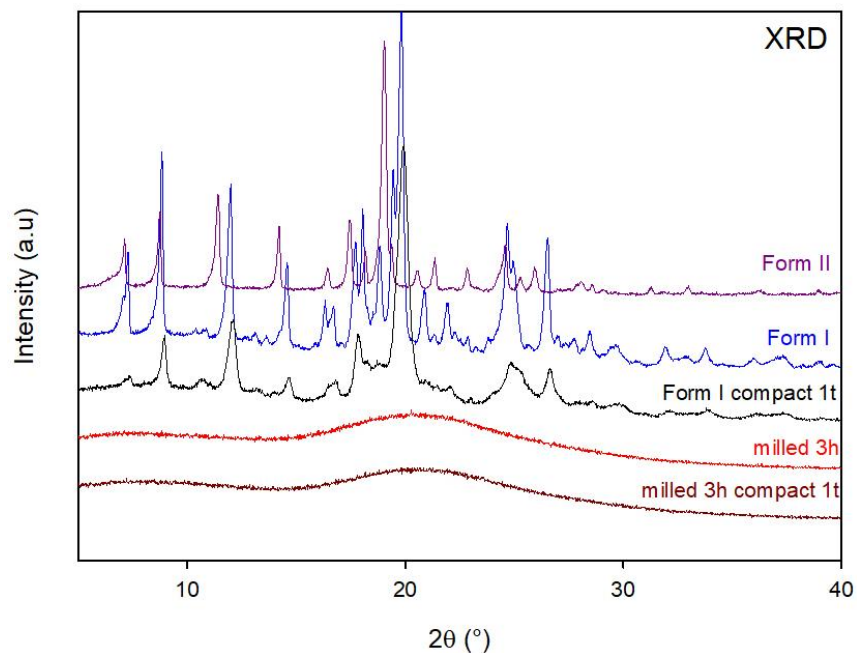
Figure 45 - X-ray diffraction patterns recorded at room temperature of crystalline (Form I) and amorphous (milled 3h) Chx before and after compaction. The purple curve corresponds to the X-ray diffraction pattern of Chx Form II obtained after the heating of Form I at 130°C.

Figure 46 shows the total heat flow signal of the corresponding DSC heating scans (5°C/min). Regarding Form I after compaction, a wide endotherm characteristic of free water departure can be observed before 80°C. Moreover, the endotherm corresponding to the polymorphic transition Form I → Form II can still be observed after compaction even though it is less prominent compared to the one observed before compaction of the drug. This seems to indicate that after compaction, less energy is necessary for the polymorphic transition to occur. This is probably due to the presence of crystal defects (deformations, dislocations…) induced by the pressure applied during compaction. Regarding the milling-induced amorphous Chx, a Cp jump suggesting a glass transition is observed (Tg = 46.7°C) and is significantly depressed compared to the one of the amorphous Chx before compaction (Tg = 60.4°C). Furthermore, further heating of the compacted amorphous material shows an exotherm of recrystallization which is also depressed compared to the one observed for the amorphous powder. This observation strongly corroborates the fact that the Cp jump observed is due to the glass transition.
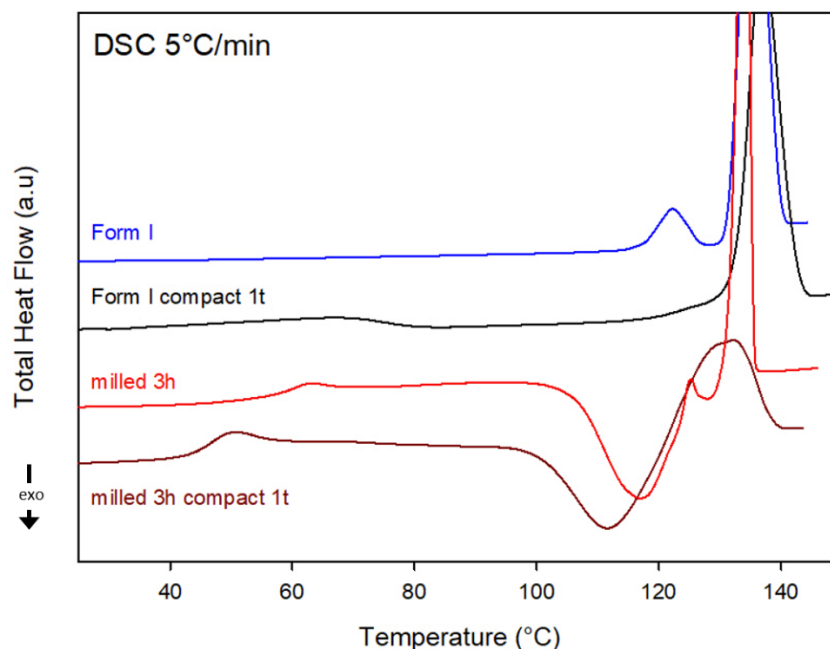
Figure 46 - DSC heating scans (5°C/min) of crystalline (Form I) and amorphous (milled 3h) Chx before and after compaction.

Figure 47 shows the DSC heating scans (5°C/min) of milling-induced amorphous Chx before compaction, directly after compaction and after compaction and a hand-milling of the compact thus obtained. For the compacted material, a first heating was performed (Run 1) followed by a quench-cooling and a subsequent heating (Run 2). The heating of the quenched liquid (Run 2) shows a Cp jump characteristic of a glass transition at a higher Tg compared to the directly compacted material (Run 1). Furthermore, when the compact is hand-milled and thus reduced back to a powder, the Cp jump seems to be at the same Tg as the one observed for the quenched liquid of the compact. Such a behaviour could be related to a lack of conductivity in the compacted material due to the thickness of the sample which would explain why this phenomenon is not observed in the case of a powder or a liquid sample. Another hypothesis would be related to an entrapment of free water absorbed during the milling process which could not be evaporated in the case of the compacted material.
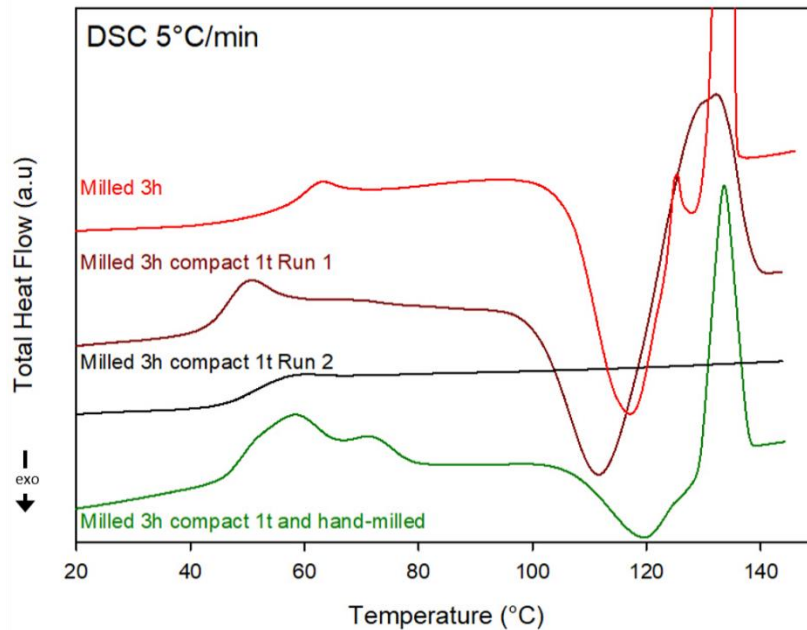
Figure 47 - DSC heating scans (5°C/min) of amorphous (milled 3h) Chx before, after compaction and after compaction and a hand-milling.

Figure 48 shows the TGA scans (5°C/min) of the milling-induced amorphous Chx before and after compaction and also after compaction followed by a hand-milling. In the milled material (non-compacted), 1.1% of weight loss is observed up to 100°C which is attributed, to the departure of free water caught by the sample during the milling. However, after compaction of this milled material, only a weight loss of 0.5% is observed in the same range of temperatures. Meanwhile, after compaction followed by hand-milling, a weight loss of 0.9% is observed in the same range of temperatures. These results suggest that the water absorbed by the milled material during milling is entrapped in the compact and thus have difficulty to evaporate upon heating. This entrapped water has a plasticizing effect which leads to the depressed Tg observed.
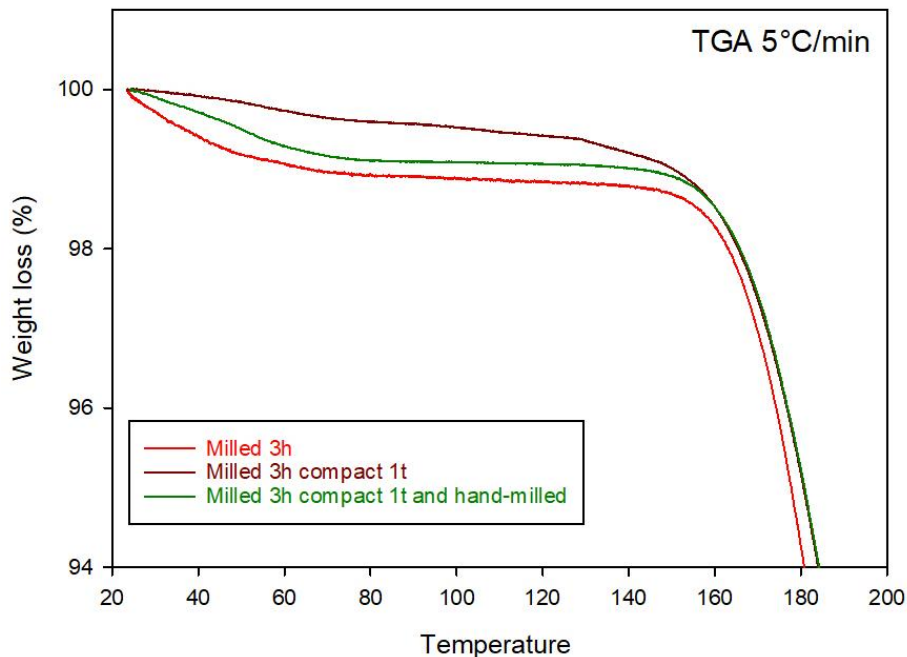
Figure 48 - TGA heating scans (5°C/min) of amorphous (milled 3h) Chx before, after compaction and after compaction and a hand-milling.

The intrinsic dissolution profiles of both Form I and amorphous Chx are illustrated in Figure 49. In order to fulfill the intrinsic dissolution conditions, as the dissolution rate corresponds to the slope of the curve obtained, the results must appear as a linear curve which usually corresponds to an amount of compact dissolved not exceeding 10%. In this case, changes in the slope can be detected and the graph can be divided into 3 different phases:

- From 0 to 2 hours: Form I shows a slightly higher dissolution rate compared to the amorphous form.
- From 2.5 to 8 hours: Form I roughly keeps the same dissolution rate whereas a decrease in the one of the amorphous form is observed.
- From 24 to 30 hours: No change is observed in the dissolution rate of the amorphous form while a decrease occurs for Form I and the slope seems to be similar to the one of the amorphous form.

In order to have a better understanding of the slope changes observed, the intrinsic dissolution profile of the hydrate form of Chx can also be found on Figure 49 for comparison. First, it must be noted that for this experiment, in order to obtain the hydrate form of Chx, the same conditions as presented in

section III.2.1 were used, except that the residual solid of Form I was collected after 7 days in water instead of 21 days. Indeed, as the crystallization into the hydrate form was observed after a few days and as the plateau corresponding to the solubility limit of the hydrate was already reached after 7 days (Figure 37), this amount of time was considered sufficient to obtain the hydrate form of Chx. It can also be noticed that the hydrate form is only detectable after 5 hours of dissolution, probably due to a longer wetting time.

In the second phase of the dissolution (from 2.5 to 8 hours), the curves of the amorphous form and of the hydrate form seem to be parallel, which thus indicates that these two forms show the same dissolution rate. This strongly suggests that the decrease in the dissolution rate observed in the amorphous form, from 2.5 hours of dissolution, is due to a recrystallization into the hydrate form of Chx. Meanwhile, Form I continues to dissolve as the initial crystalline form without any disturbance.

Interestingly, in the last phase of dissolution (from 24 to 30 hours), all the curves seem to be parallel which indicates that after 24 hours, Form I also transformed into the hydrate form of Chx which shows a lower dissolution rate.

For more precision, the dissolution rates of the three different forms during the three different stages of the intrinsic dissolution are reported in Table 6. If the values are rather small, the tendency can still clearly be identified as explained above.

The evaluation of the intrinsic dissolution rates highlighted that the amorphous form of Chx shows a slower dissolution due to a precipitation into a hydrate form of Chx, less soluble, which also occurs in the case of crystalline Chx but at later time points. However, this does not explain why the intrinsic dissolution rate of the amorphous form is also the lowest at the very beginning of the experiment. This is highly unexpected as, without any precipitation, the amorphous form should exhibit a higher dissolution rate compared to its crystalline counterpart. A hypothesis could be that the precipitation occurs already at the very beginning but slowly as it takes time for water molecules to penetrate into the compact.
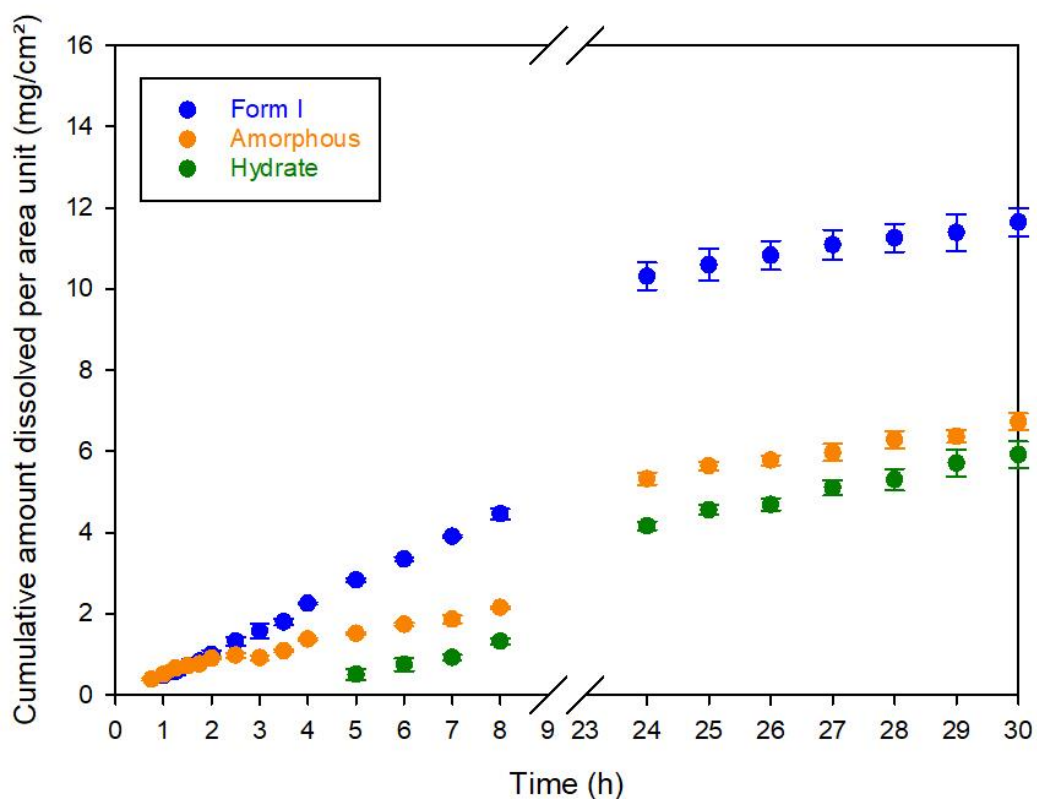
Figure 49 - Intrinsic dissolution kinetics over 30 hours of the crystalline Chx (Form I), the amorphous form (milled 3h) and the hydrate form of Chx, in ultra-pure water (400mL) heated at 37°C under stirring (50 rpm).

Table 6 – Intrinsic dissolution rates of the different forms of Chx at different stages of the dissolution. As the experiment was performed in triplicates, mean values were used for the calculations and the standard deviations of the linear fit are also reported.

Dissolution phase	Form I	Amorphous form	Hydrate
From 0 to 2 hours	0.51 ± 0.02 mg/cm²/h	0.39 ± 0.03 mg/cm²/h	NA
From 2.5 to 8 hours	0.58 ± 0.01 mg/cm²/h	0.22 ± 0.02 mg/cm²/h	0.26 ± 0.03 mg/cm²/h
From 24 to 30 hours	0.21 ± 0.01 mg/cm²/h	0.22 ± 0.01 mg/cm²/h	0.29 ± 0.01 mg/cm²/h

III.2.4 Tablet manufacturing and dissolution

In order to be closer to "real life" conditions, tablets of both crystalline (Form I) and milling-induced (3h) amorphous Chx were produced using the formulation and the method described in Chapter II, section II.4.3.

As explained, the fixed parameter for the tablet production was a hardness set to 80N (±10%). To that extend, 3 different lower punch forces were tested in triplicates and the corresponding hardness of the tablets were measured. A linear fit was then used in order to determine the lower punch force required to obtain this targeted hardness.

Even though the manual filling of the die performed is not fit for industrialization of the process, the manufacturing parameters were evaluated and compared for the two physical states of Chx investigated.

The tabletability represents the capacity of a powdered material to be transformed into a tablet for a specified strength under the effect of compaction pressure. Indeed, it is an important tablet feature to evaluate in order to ensure a sufficient mechanical strength to endure further processes such as coating, packaging or transport and a sufficient weakness to disintegrate in the human body to release the API. Typically, a mechanically strong enough tablet would show a tensile strength greater than 1.7 MPa but it also has been reported that 1MPa could be sufficient if the tablets are not subjected to heavy mechanical stresses[164]. Figure 50 illustrates the tabletability of Chx in both in its crystalline state (Form I) and in its milling-induced amorphous state. In both physical states, the tabletability seems similar and satisfactory tensile strengths were obtained for an applied pressure in a range of 75-100MPa. Therefore, in this case, the physical state of the drug does not seem to have a significant influence on the tabletability of Chx. Such a similarity in terms of tensile strength between an amorphous and its crystalline counterpart, was already observed in both the case of celecoxib[165] an investigation performed by Hancock et al.[166]. However, the latter study also revealed a higher brittleness in the case of the amorphous form which was also more susceptible to failure induced by the presence of flaws.
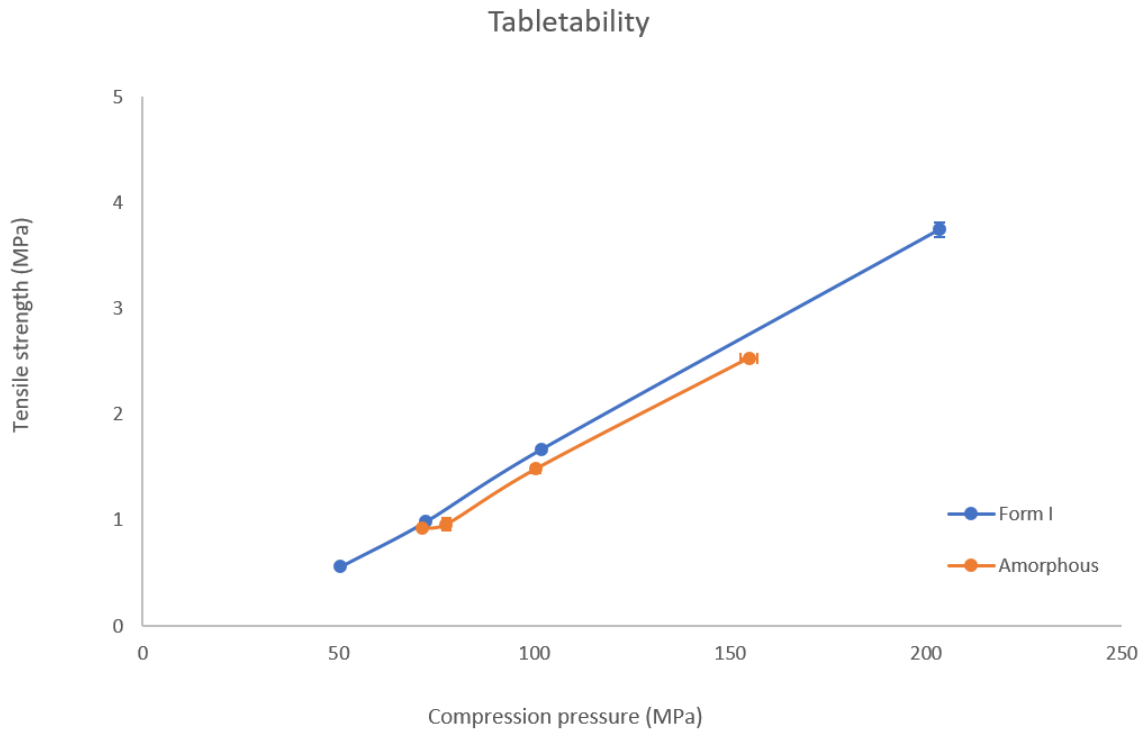
Figure 50 - Tabletability of Chx in its crystalline state (Form I) and milling-induced (3 hours) amorphous state.

The compressibility represents the ability of a powdered material to reduce its volume when a pressure is applied and is characterized by several compression equations and mathematical models. The most commonly used one is the Heckel model[167–169] which follows the Equation 21:

$$-\ln(\varepsilon) = \ln\left(\frac{1}{1-D}\right) = KP + A \qquad (21)$$

Where:

- ε represents the porosity
- D is the relative density of the compact
- P corresponds to the applied pressure (MPa)
- K corresponds to the Heckel coefficient (slope of the linear curve, in MPa^{-1}) and A is a constant (y-intercept).

The yield pressure (P_y) is calculated as the reciprocal value of the Heckel coefficient K and is used to determine the compressibility. Indeed, the smaller the P_y value, the better the compressibility of the tablet. In this work, this parameter is determined using the out-die method from the data acquired from the tablet press (positions of the lower and the upper punches) to calculate the dimensions of the tablet

after the compression phase. Figure 51 shows the compressibility of Chx in both its crystalline (Form I) and in its milling-induced amorphous state. From the linear regressions applied, the K coefficient and the corresponding P_Y were calculated and are reported in Table 7. It can be noticed that the P_Y value corresponding to the amorphous Chx is lower than the one of crystalline Chx. Therefore, the compressibility of amorphous Chx can be considered better compared to its crystalline counterpart. This lower value of yield pressure (out-of-die), and thus a higher plasticity, was also observed in the case of amorphous celecoxib[165]. Indeed, according to this study, such a behavior is to be expected as higher forces are required to initiate deformation on crystalline compacts due to the presence of the crystal lattice.
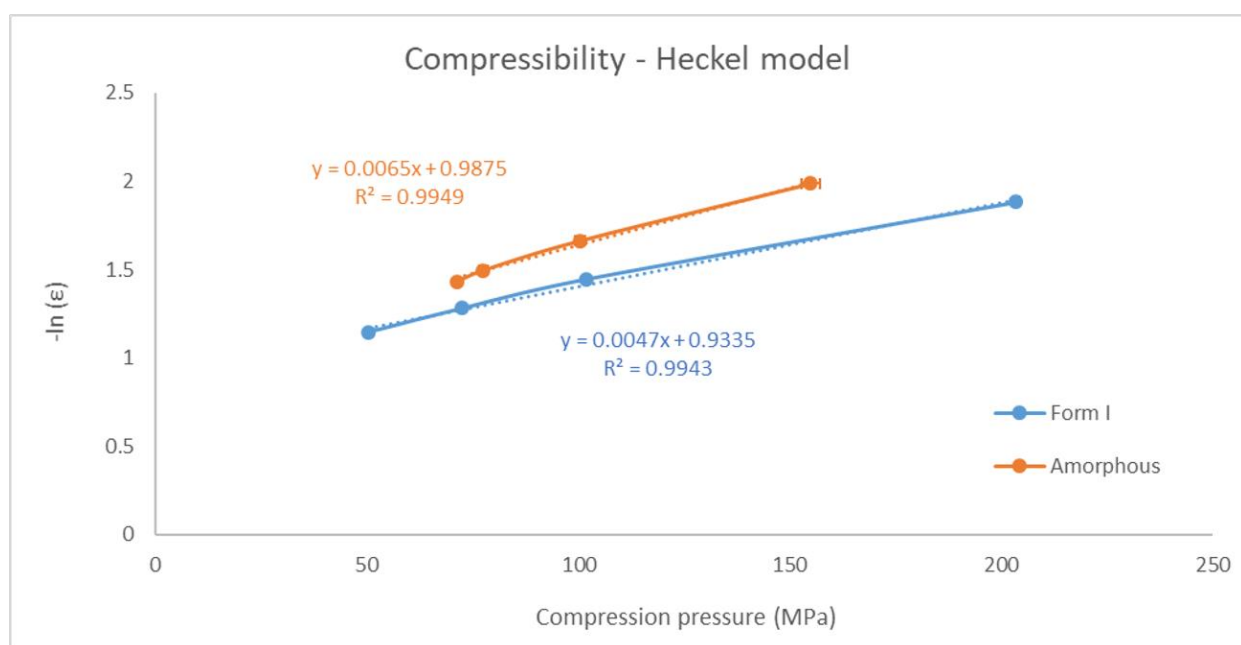
Figure 51 – Compressibility of Chx in its crystalline (Form I) and amorphous state (obtained from Form I milled 3h) using the Heckel model.

Table 7 – Numeric values of the in-die Heckel parameters.

	Form I	Amorphous
K (MPa^{-1})	0.0047	0.0065
P_Y (MPa)	212.8	153.8

In Table 8 are reported the tablets properties and related compression process parameters of the tablets produced for the targeted hardness of 80N (± 10%). Regarding the process parameters, it can be observed that the targeted hardness was reached for similar pressures applied and that the ejection forces applied to produce the tablets are exceptionally high. This means that both formulations highly tend to stick on the punch once compressed and that the lubricant added in the formulation, even though usually used and in the same proportions (Magnesium Stearate, 0.5%)[170], was not sufficient to prevent this feature. However, as the ejection force depends on the tablet dimensions, the ejection shear stress (in MPa) is usually calculated in order to perform an accurate comparison. Indeed, this ejection shear stress is calculated by dividing the peak ejection force by the area of the tablet in contact with the die wall. The lower the ejection shear stress, the lower the possibility of inducing defects such as capping or lamination on the tablets. According to the literature, the ejection shear stress of a commercial tablet should not exceed 3 MPa in order to ensure no capping nor lamination[171]. However, ejection shear stresses up to 5 MPa may be acceptable for tablets which are not subjected to large mechanical stresses on subsequent processing such as film-coating. In our case, the ejection shear stress of the formulation containing amorphous Chx is around 5MPa which remains acceptable as no further process is performed on the tablet. However, the one corresponding to crystalline Chx is around 7MPa which means that this formulation is highly prone to defects during the tableting even though none was observed during the production. However, as in this work, the tablets batches are rather small (up to 18 tablets in a row) compared to a commercial production, it appears understandable that these defects are not encountered. However, the ejection shear stress obtained for each formulation indicate that these formulations are not worth considering as such for industrial manufacturing and that they would need further optimization.

Regarding the tablet properties, the dimensions are similar for both physical states, except for a slightly higher thickness along with a higher porosity (smaller solid fraction) in the case of the formulation containing crystalline Chx. For both physical states, the tablets are disintegrating within the first few seconds which is exceptionally rapid considering the requirement of not exceeding 15min for uncoated tablets according to the pharmacopeia[172].

Table 8 – Tablet properties and related compression process parameters.

		Form I	Amorphous form (milled 3h)
Process parameters	Lower punch force (n=18, kN)	7.23 ± 0.05	7.74 ± 0.09
	Ejection force (n=18, N)	1123.4 ± 30.9	820.0 ± 20.1
	Ejection shear stress (n=18, MPa)	7.1 ± 0.2	5.4 ± 0.1
Tablet properties	Weight (n=18, mg)	498.9 ± 1.0	500.4 ± 0.6
	Diameter (n=18, mm)	11.33 ± 0.00	11.33 ± 0.01
	Thickness (n=18, mm)	4.47 ± 0.01	4.31 ± 0.01
	Solid fraction (n=18, %)	72.2 ± 0.1	77.6 ± 0.3
	Hardness (n=3, N)	78.8 ± 0.4	73.6 ± 3.7
	Tensile strength (n=3, MPa)	0.99 ± 0.00	0.96 ± 0.05
	Disintegration time (n=3, s)	17 ± 1	9 ± 2

The physical state integrity of Chx after compression was assessed only using XRD. Indeed, the DSC data proved to be unavailing as the numerous excipients present prevented from extracting reliable information. Figure 52 shows the X-ray diffraction patterns of tablets containing crystalline Chx (form I) and milling-induced amorphous Chx after production (t0) and after 4 weeks of storage at 25°C, 60%RH (t4w). These specific storage conditions were chosen according to the ICH guideline[141] for long term stability study of drug substances. However, according to this guideline, it should be performed during 12 months but due to time constraints, only 4 weeks were evaluated in this work. The X-ray diffraction patterns of both crystalline Chx in its powder form and of the tablet placebo (without API) are also represented for comparison. It can be noticed that the peak characteristic of Form I (e.g. peaks marked with a ★ at 7.3° and 8.9°) are still present in the tablets containing crystalline Chx both after production and after 4 weeks of storage. Regarding the tablets containing amorphous Chx, those characteristic peaks are absent both after production and after 4 weeks of storage which means that the Bragg peaks observed are only corresponding to the excipients as observed on the diffractogram of the placebo. It can thus be assumed that the physical state of the API was not altered during the compression process which could be expected as the same conclusion could be made after the preparation of compacts for the intrinsic dissolution. Furthermore, it can be deduced that the amorphous form is stable in the tablet over 4 weeks of storage in these conditions.
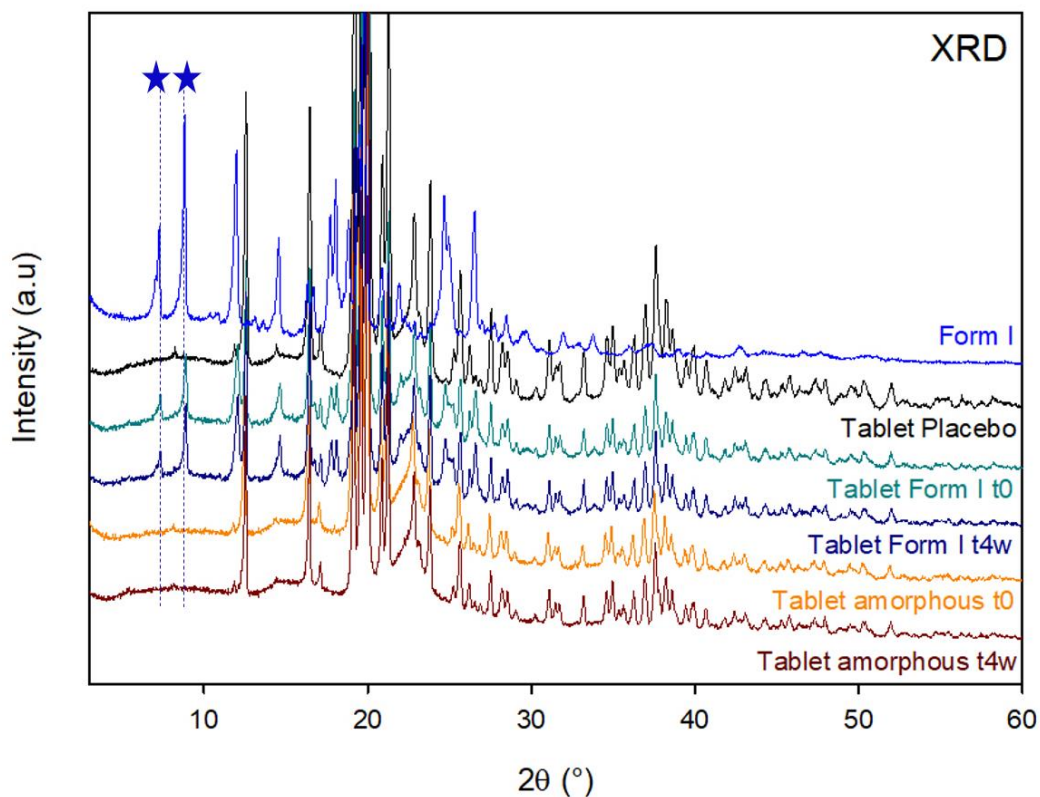
Figure 52 – X-Ray diffraction patterns of tablets of Chx non-milled (Tablet Form I) and milled 3h (Tablet amorphous) directly after production (t0) and after 4 weeks of storage at 25°C, 60% RH (t4w). The commercial form of Chx (Form I) and the tablet not containing API (Tablet Placebo) are also represented.

The tablet release of Chx in both its crystalline (Form I) and milling-induced amorphous state was evaluated both after production and after 4 weeks of storage (25°C, 60%RH) and the corresponding dissolution kinetics are illustrated in Figure 53. Directly after production, as observed in the previously presented dissolution experiments, the release of amorphous Chx is slower compared to its crystalline counterpart. Indeed, the immediate release percentage (after 15 min) is already lower and a drop can be observed after 5 hours of dissolution, which is probably due to the recrystallization of the amorphous form into the hydrate form of Chx. Interestingly, even though this drop corresponding to a recrystallization is not visible for the tablets dissolved after 4 weeks of storage, a decrease in the dissolution rate (gentler slope) is observed after 1 hour of dissolution and the same release percentage (around 80%) is reached after 48 hours of dissolution. Regarding the crystalline Chx, the release profiles directly after production and after 4 weeks of storage are very similar, with a high dissolution rate (steep

slope) during the first 8 hours of dissolution and then the amount released levels-off until it reaches approximately 85% and 90% of Chx release at t0 and at t4w, respectively.
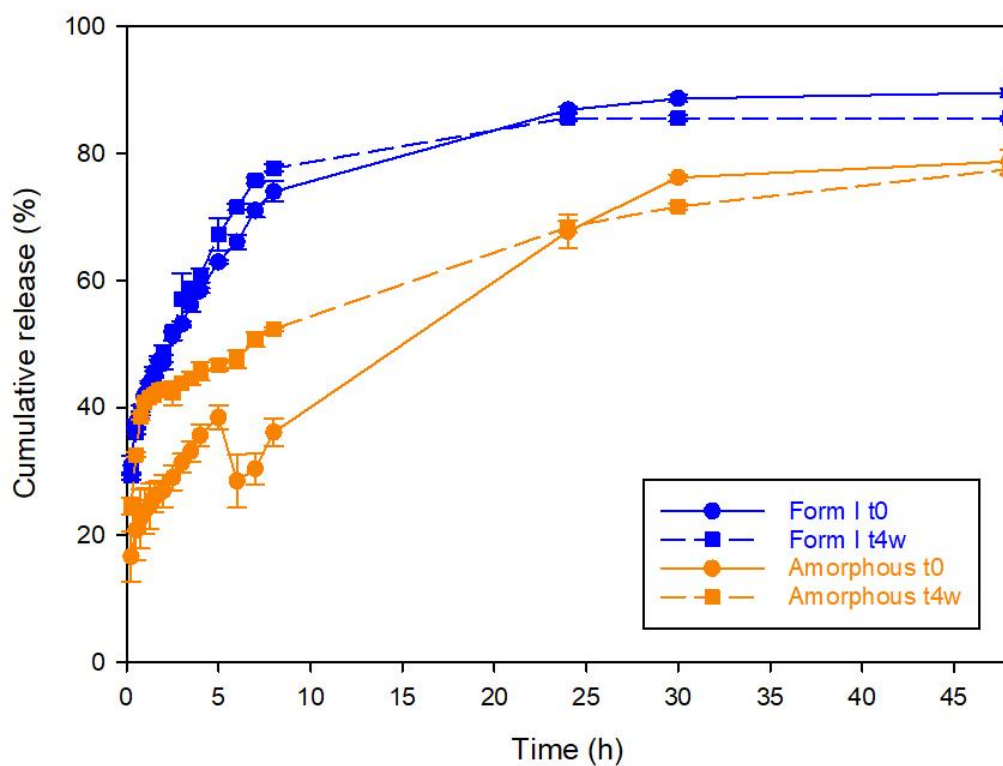
Figure 53 - Tablet dissolution of Chx crystalline (Form I) and milled 3h (amorphous) after production (t0) and after 4 weeks of storage at 25°C, 60% RH (t4w), in ultra-pure water (800mL) heated at 37°C under stirring (100 rpm).

Conclusion

In this chapter it was showed that Chx free base undergoes a polymorphic transition Form I → Form II upon heating before the melting of the drug. This transition appeared to be completely reversible as upon rapid cooling Form II transformed back into Form I. It was also proven that high-energy milling was a more suitable amorphization process for Chx free base (Form I) compared to the traditional liquid quench due to thermal degradation. The glass transition temperature was evaluated to Tg = 60.5°C and the Cp jump at Tg was ΔCp = 0.59 J/g/°C. Upon heating, amorphous Chx was found to recrystallize into its initial form (Form I) and further heating led to the polymorphic transition Form I → Form II before the melting of the drug. Either upon heating or milling, these two forms appear to be enantiotropically related and their relative stability at room temperature was ranked as follows: I >> II. The amorphization kinetics upon milling were also determined and were found to follow an exponential relaxation law with an exceptionally low relaxation time τ = 4.6 min.

Regarding the dissolution kinetics, the first set-up (super-saturated solution) revealed a drop in the amount of dissolved Chx after 24 hours of dissolution for both crystalline and amorphous Chx due to a recrystallization into a pentahydrate. The pentahydrate was characterized and its solubility limit was determined at approximately 100mg/L.

The powder dissolution in sink conditions highlighted the influence of the particle size and shape as it revealed a slower and incomplete dissolution for the amorphous Chx (~ 80%) compared to its crystalline counterpart. Meanwhile, the dissolution in non-sink conditions revealed that in this dissolution set-up, only amorphous Chx was prone to recrystallization into the hydrate form during the dissolution. Therefore, this recrystallization, along with the highlighted formation of aggregates, led to a slower and incomplete dissolution for the amorphous Chx compared to its crystalline counterpart.

The intrinsic dissolution highlighted 2 phases for both crystalline and amorphous Chx, which occurred at different time points depending on the physical state of the drug. Indeed, the dissolution rate of amorphous Chx decreased after 2.5 hours of dissolution and was found to reach the same value as the pentahydrate, whereas this same observation was made only after 24 hours of dissolution for crystalline Chx. Therefore, without the influence of the particle size and shape, crystalline Chx was still found to

reveal the fastest dissolution as it recrystallized into the hydrate form (less soluble) later compared to amorphous Chx.

Finally, the tablet manufacturing analysis of both crystalline and amorphous Chx revealed a slight advantage for the amorphous form as it showed a better compressibility (lower P_y value) and a lower ejection shear stress. Nor the compression nor the tablet storage at 25°C, 60% RH were found to have altered the physical state of the drug, which allowed to have accurate results and comparisons in both tablet properties and dissolution kinetics. In this galenic form, crystalline Chx once more showed the fastest dissolution compared to the milling-induced amorphous form both directly after production and after 4 weeks of storage at 25°C, 60%RH.

CHAPTER IV - CO-AMORPHIZATION OF CHLORHEXIDINE UPON MILLING

As demonstrated in the last chapter, milling-induced amorphous Chx is highly prone to recrystallization both upon heating and during the dissolution. Besides, it was demonstrated that amorphous Chx exhibited a slower dissolution compared to its crystalline counterpart, which was due to both aggregation and precipitation into a hydrate form, less soluble.

Furthermore, as amorphous drugs are usually not formulated as such but as an amorphous solid dispersion within a polymer matrix, polymers were added in order to stabilize the amorphous form as an attempt to enhance its dissolution performances. To that extend, two polymers were chosen, PVPK12 and Lycoat RS720 (as illustrated in Figure 54).

PVP is a widely used hydrophilic polymer for the production of amorphous solid dispersions[33,121,125,173–176], whereas the Lycoat is an excipient used for film forming and coating but it was graciously offered by Roquette, the industrial partner of this project, in order to investigate its potential application to the formulation of ASDs.
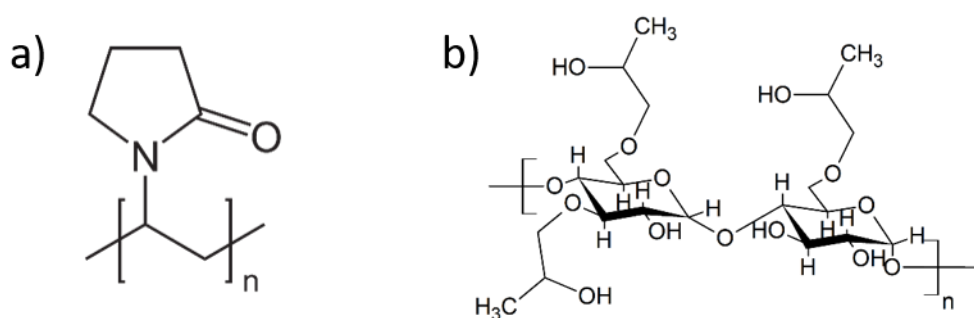
Figure 54 - illustration of the polymer molecules: a) PVP and b) Lycoat RS720

The objective of this chapter is first to investigate on the potential co-amorphization of Chx free base with these polymers and then to perform a detailed physical characterization of the different molecular alloys for various fractions of Chx in the mixture.

Secondly, for specific Chx/polymer mixtures the dissolution kinetics are determined in order to evaluate the influence of the physical state of the API in drug/polymer mixtures and to assess the advantage of the co-milled mixture compared to a physical mixture containing either amorphous or crystalline Chx.

Finally, a comparison between the two polymers is also performed in order to determine the most suitable one to enhance the dissolution performances of this API.

IV.1 Physical characterization of chlorhexidine-polymer mixtures

The objective of this section is first to investigate on the potential co-amorphization of chlorhexidine with two different polymers including PVPK12 and Lycoat RS 720 upon milling. Then, the aim is to perform a detailed physical characterization of the various molecular alloys obtained to have a clear understanding of the behavior of chlorhexidine in such a mixture.

IV.1.1   Polymers presentation

Figure 55 shows the TGA heating scans (5°C/min) of the two polymers chosen for the co-amorphization with chlorhexidine. PVPK12 and Lycoat RS 720 both show a small weight loss up to 100°C of 3% and 6% respectively, attributed to water evaporation due to their hygroscopicity. Further heating of PVPK12 revealed a drastic weight loss (about 91%) starting from 300°C due to the chemical degradation of the polymer. Lycoat RS 720 shows a strong weight loss (about 82%) starting from 250°C also due to chemical degradation of the polymer. As highlighted by the TGA scans, to avoid degradation of the polymers, 250°C and 300°C should not be exceeded during the DSC experiments for Lycoat and PVP respectively.

Figure 56 shows both the X-ray diffraction patterns (a) and the DSC heating scans (b) of both polymers. The X-ray diffractograms show diffusion halos with no Bragg peak indicating that both polymers are completely amorphous. Regarding the DSC scans, a Cp jump (ΔCp = 0.32 J/g/°C) characteristic of a glass transition can be observed for PVP at Tg = 103.7°C. For the second polymer, there is no Cp jump visible on the thermogram of Lycoat which suggests that the Tg of this polymer is in fact located above its degradation temperature. The evolution of Tg for water content varying from 0% to 30% was provided by the supplier[177].This evolution indicates that for a sample without any water content, the Tg should be located around 245°C. As our sample was analyzed in an open pan (without a lid), all the water present in the sample should have evaporated upon heating which indicates that the Tg of the dry Lycoat should be observed. As it was not the case, it implies that this Tg at 245°C is probably slightly underestimated. Nevertheless, as the Tg of milling-induced amorphous Chx was determined at Tg = 60.5°C, both polymers should act as anti-plasticizers in co-amorphous mixtures which should enhance the physical stability of amorphous Chx in such mixtures.
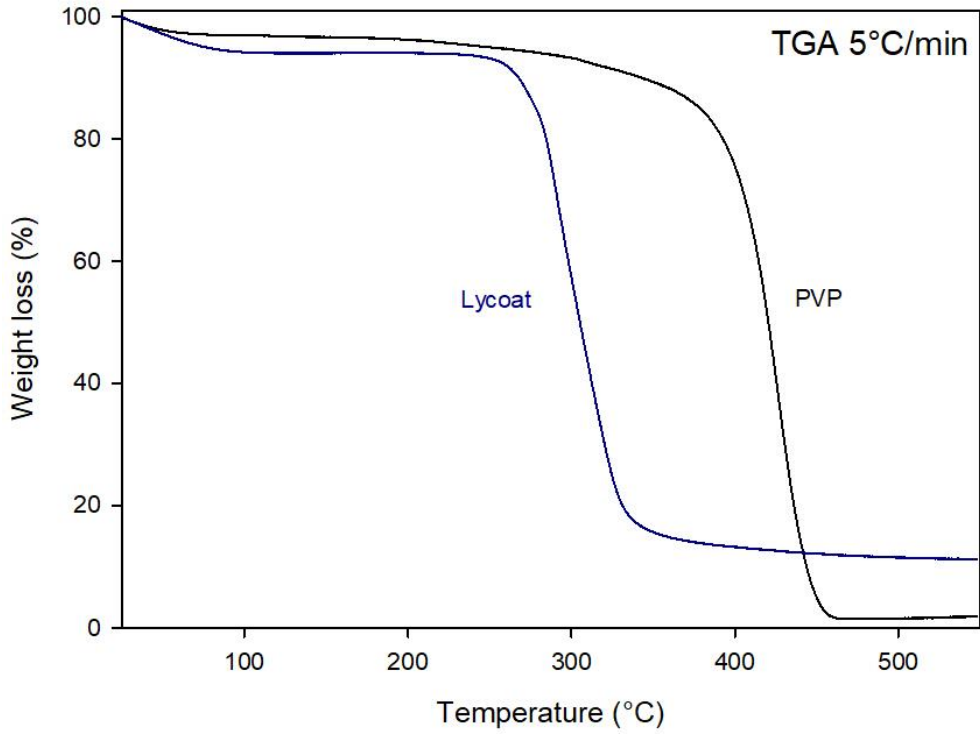
Figure 55 - TGA scans (5°C/min) of PVPK12 and Lycoat RS720.
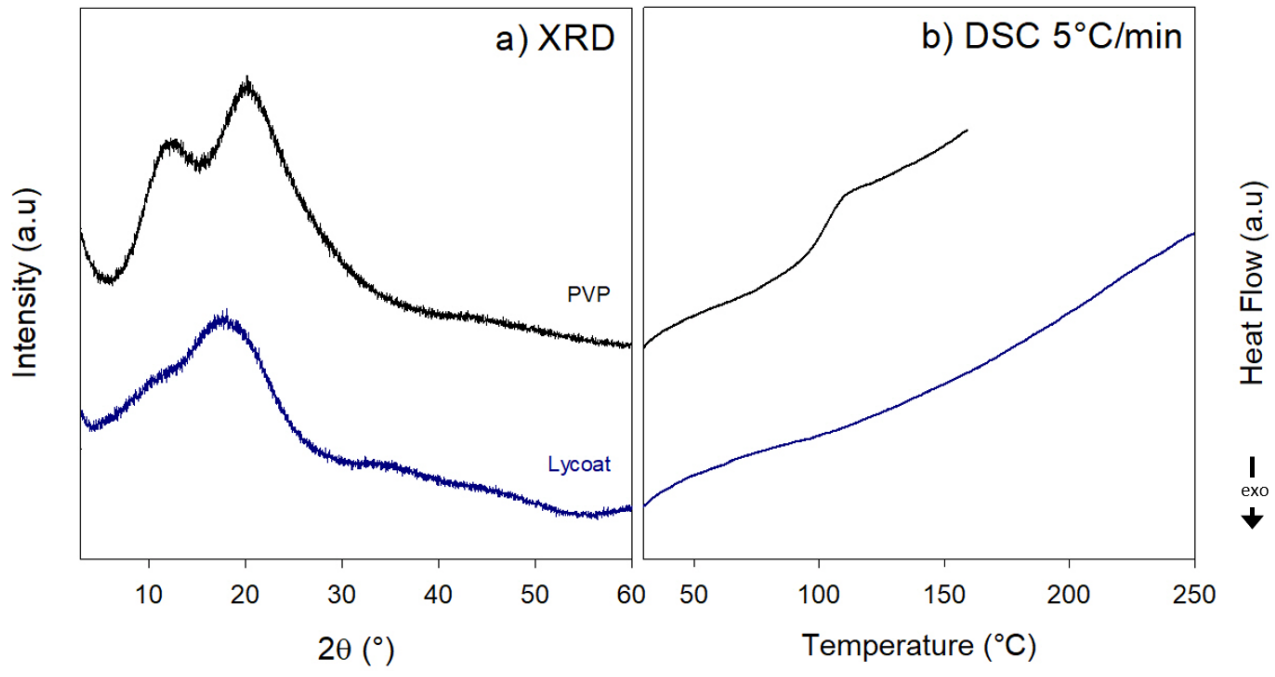
Figure 56 - a) X-ray diffraction patterns and b) DSC heating scans (5°C/min) of PVPK12 and Lycoat RS720.

IV.1.2 Co-amorphization with PVPK12

This section is focused on testing the possibility to produce amorphous molecular alloys of Chx and a widely used polymer for ASDs, PVPK12. Once the co-amorphization feasibility was proven, it was performed for various compositions of the mixture to determine the evolution of the Tg of the molecular alloy with the fraction of Chx.

(1) Co-amorphization feasibility

As the milling time chosen for the different characterizations of pure chlorhexidine in chapter III was 3 hours, the same milling time was tested for the co-amorphization with PVPK12. Figure 57 shows both the X-ray diffraction patterns (a) and the DSC heating scans (b) of a co-milled mixture of Chx and PVP (50/50, w/w). The diffractograms and thermograms corresponding to Chx milled 3h and to PVPK12 are also showed for comparison. As illustrated on the diffractogram, the co-milled mixture (3h) of Chx and PVP, only presents the diffusion halo characteristic of an amorphous form. Furthermore, the corresponding thermogram depicts only one Cp jump characteristic of an amorphous form at Tg = 87.9°C which is located between the one corresponding to pure amorphous Chx (60.5°C) and to the one of PVPK12 (102.9°C). Moreover, no endothermic peak highlighting the melting of remaining crystallites of Chx can be detected which confirms the complete amorphization of Chx during the co-milling. Therefore, it appears that this milling time is sufficient (with our specific milling conditions) to produce a homogenous co-amorphous molecular alloy of Chx and PVP.
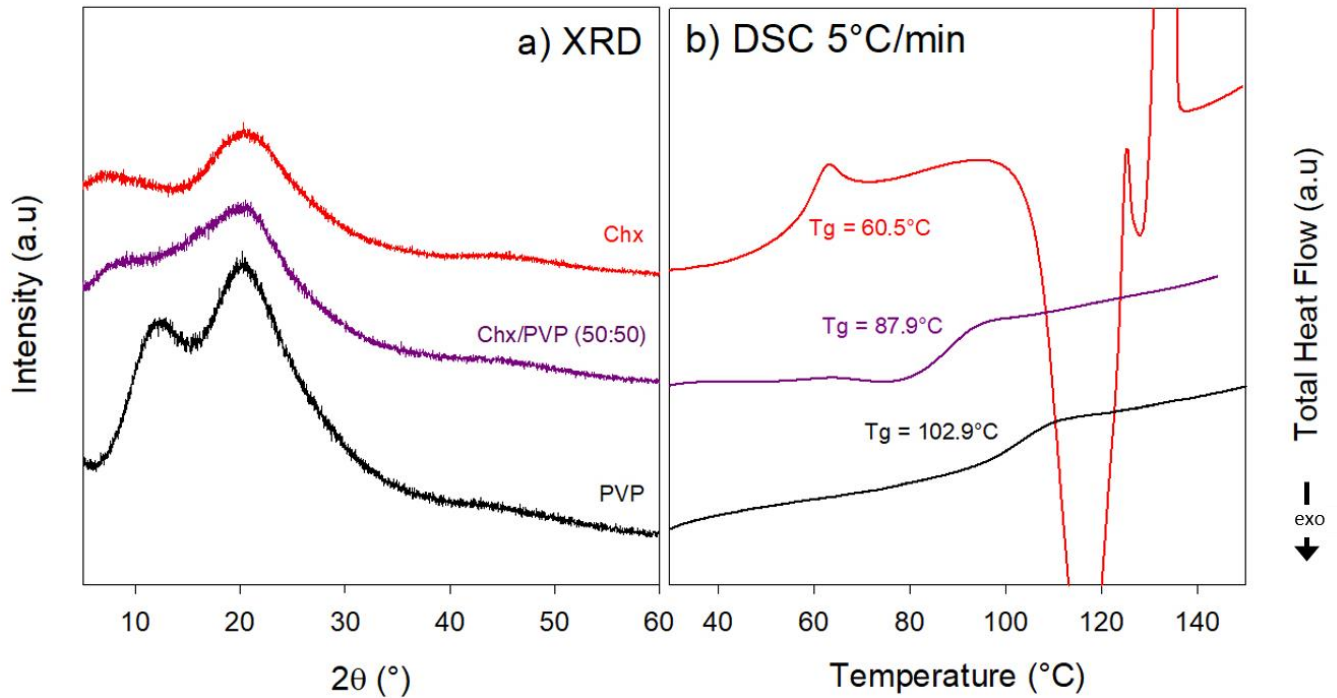
Figure 57 - X-Ray diffraction patterns (a) and DSC scans 5°C/min (b) of Chx milled for 3 hours, Chx/PVP (50/50, w/w) co-milled 3 hours and of PVPK12.

(2) Gordon-Taylor curve determination

The co-milling (3h) of Chx and PVPK12 was performed for different compositions of the mixture and the corresponding X-ray diffractions patterns are represented in Figure 58. For comparison, the X-ray patterns of both pure PVP and of pure milling induced amorphous Chx (3h) are also shown. It appears that whatever the fraction of Chx in the mixture, no Bragg peaks could be detected indicating each time, a complete amorphization of Chx during the 3 hours of milling.
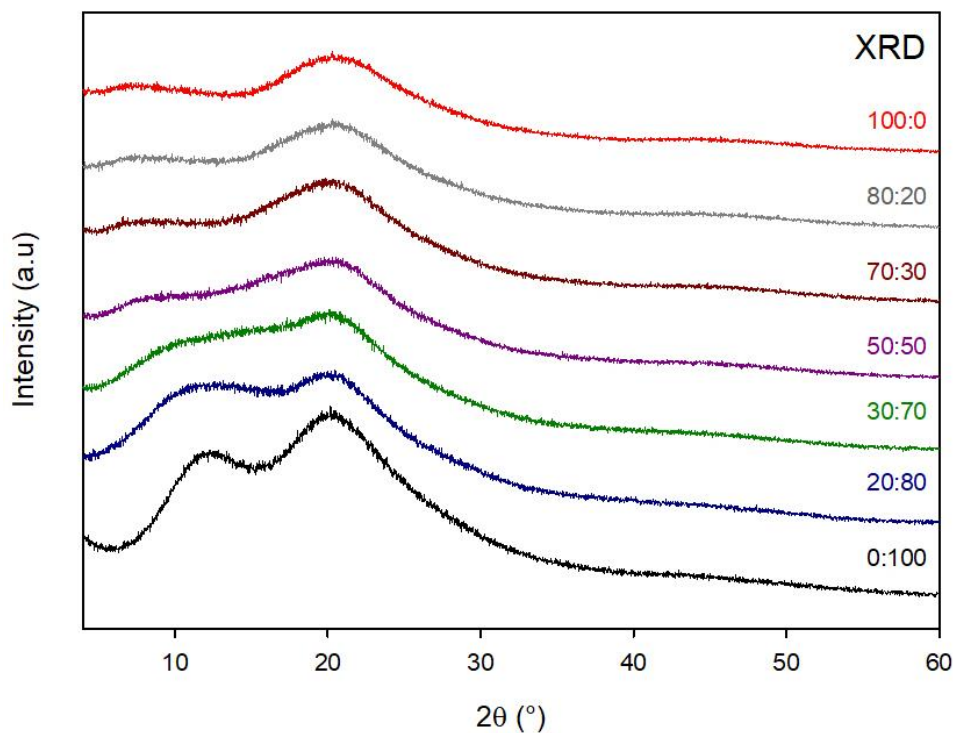
Figure 58 - X-Ray diffraction patterns of Chx/PVP mixtures of different compositions, milled for 3 hours. The compositions (Chx/PVP, w/w) are reported on the right-hand side of each curve.

The corresponding DSC scans are illustrated in Figure 59 along with 2 more compositions of the co-milled Chx/PVP mixture. It can be noticed that in each case, a single Tg is observed indicating that a homogenous co-amorphous mixture has been produced. It can also be observed that, in each case, except for the (80/20, w/w) mixture, the Cp jump at Tg is preceded by a slight exotherm which indicates the milling process has generated glasses of very high energetic level[178]. This absence of exotherm in the case of the (80/20, w/w) mixture is probably due to the fact that the Tg of the mixture is close to the milling temperature. Indeed, the glass relaxation during the milling annihilates the increase in enthalpy due to the milling. It can be noted that the same phenomenon is observed for pure Chx (red curve in Figure 59). Furthermore, with increasing the PVP fraction, the position of Tg shifts towards the higher temperatures which confirms the anticipated anti-plasticizing effect of PVPK12 in the drug/polymer mixture. It must also be noticed that contrary to pure Chx, the co-milled Chx/PVP mixture do not show any sign of recrystallization upon heating below 150°C, temperature at which, the degradation of the drug occurs. Therefore, it can be safely pointed out that the co-amorphization with PVPK12 allowed to increase the physical stability of amorphous Chx upon heating.
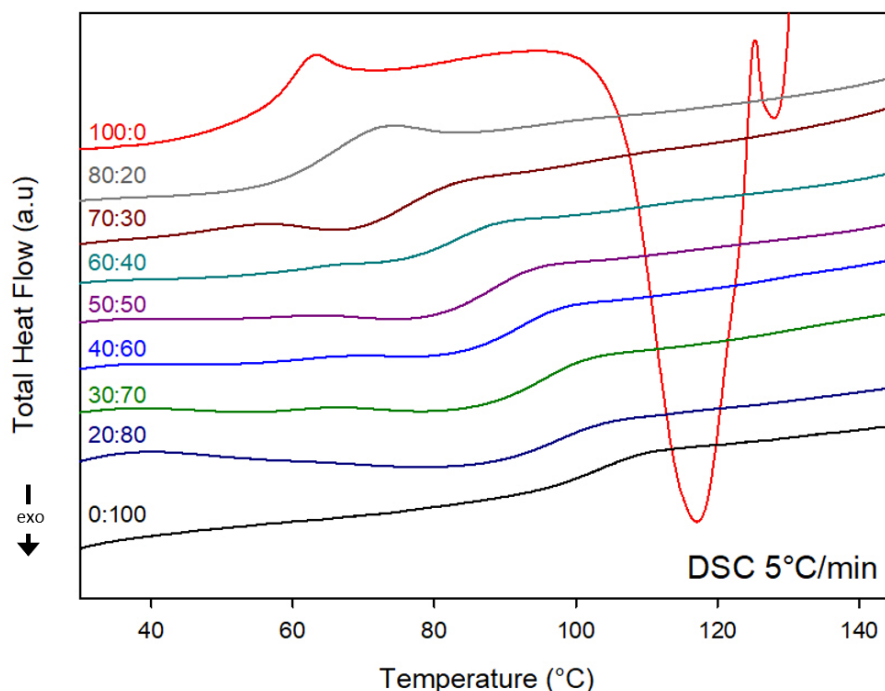
Figure 59 – DSC scans (5°C/min) of Chx/PVP mixtures of different compositions, milled for 3 hours. The compositions (Chx/PVP, w/w) are reported on the left-hand side of each curve.

The evolution of the Tg of the alloy (obtained from Figure 59) with the fraction of Chx in the mixture is reported in Figure 60. The solid line represents the best fit of the Gordon-Taylor law (Equation 15, Chapter I, section I.4.1) to the experimental data (represented in black dots). The coefficient K which defines the curvature of the evolution, was determined and the value obtained was K=1.5. The red curve corresponds to the theoretical curve of an ideal Chx/PVP mixture for which K is given by the ratio of the amplitudes of the Cp jumps at Tg of the two pure compounds[117] (Equation 16, Chapter I, section I.4.1):

$$K = \frac{\Delta Cp_{PVP}\ (0.29\ J/g/°C)}{\Delta Cp_{\ Chx}(0.47\ J/g/°C)} = 0.62$$

It can first be noticed that experimental data are not perfectly following the fit especially for Chx fractions higher than 0.6 which could be due to a significant approximation on the Tg due to the exotherm preceding the Cp jump. Furthermore, the curve obtained is the oppositely oriented compared to the theoretical one which suggests that strong interactions exist between the drug and the polymer in the amorphous alloy.
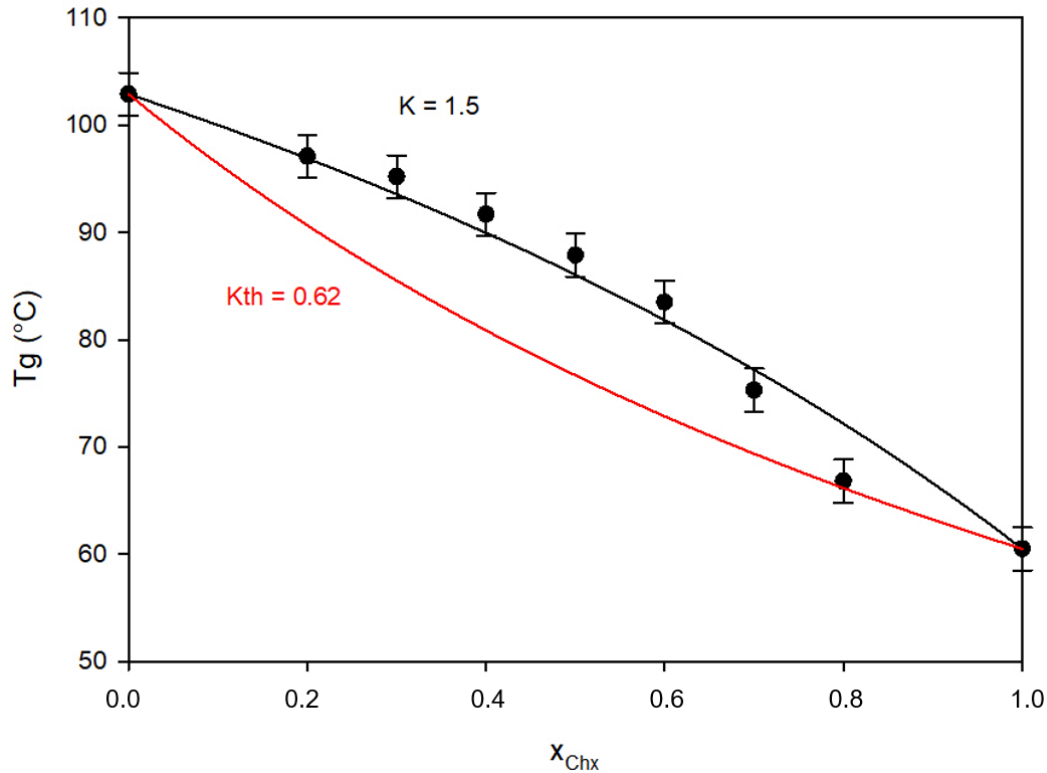
Figure 60 - Black dots represent the evolution of the Tg of the co-milled $(Chx)_x(PVPK12)_{1-x}$ binary mixtures against the Chx fraction. The black solid line represents the best fit of the Gordon Taylor equation to the experimental data and the red curve represents the theoretical Gordon-Taylor curve for an ideal mixture. It must be noted that an estimated error on the Tg of 2°C has been added in order to consider both the eventual Tg measurement error induced by the exotherm observed before the Cp jump and the eventual approximation on the composition of the mixture.

As no recrystallization could be observed upon heating, and in an attempt to suppress the exotherm preceding the Cp jump, a second heating cycle was performed on all the co-milled mixtures. The corresponding DSC scans are reported in Figure 61. These scans show the exact same tendency of a single Tg of the amorphous alloy shifting towards the higher temperatures with increasing the PVP fraction in the mixture. Furthermore, the exotherm preceding the Cp jump on the first heating cycle disappeared allowing a more accurate determination of the Tg. It can also be noticed that the thermal treatment (first heating cycle to 150°C, then cooling) did not induce any demixion as only a single glass transition is still observed. It also does not render unstable the amorphous Chx upon heating as no sign of recrystallization upon heating can still be detected during the second heating cycle.

The corresponding evolution of the Tg of the alloy is illustrated in Figure 62. Once more, the solid line represents the best fit of the Gordon-Taylor law to the experimental data (represented in black dots).

The coefficient K, was thus determined and the value obtained was K=1.4 which is very close to the value previously obtained.

It can first be noticed these results are in complete adequation with the ones previously obtained from the first heating runs which confirms that this particular mixture does not follow the classical Gordon-Taylor law. Such a deviation to the Gordon-Taylor equation was already observed in the case of monosaccharide/disaccharide or monosaccharide/trisaccharide mixtures by Seo et al[179], and explained by an influence of the size and shape of the sugar molecules. Therefore, in the case of Chx/PVP mixtures, a significant difference in the size and/or the shape of the molecules could explain the deviation observed. Furthermore, strong interactions between the drug and the polymer in the amorphous alloy could explain the opposite curvature obtained compared to the theoretical one.
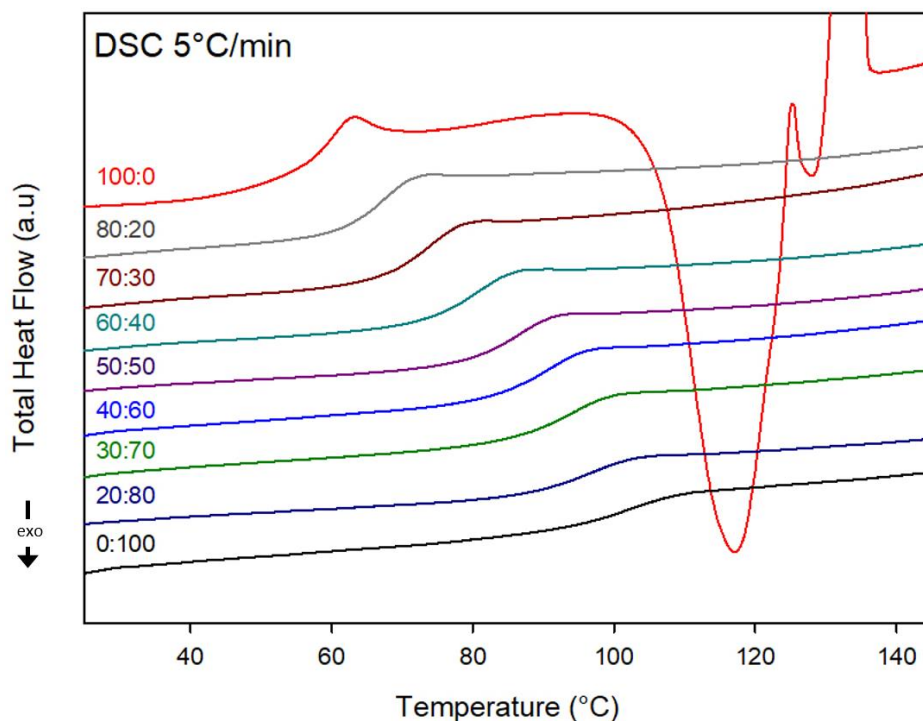
Figure 61 - DSC scans (5°C/min) of Chx/PVP mixtures of different compositions, after 3 hours of milling and subsequent heating to 150°C. The compositions (Chx/PVP, w/w) are reported on the left-hand side of each curve.
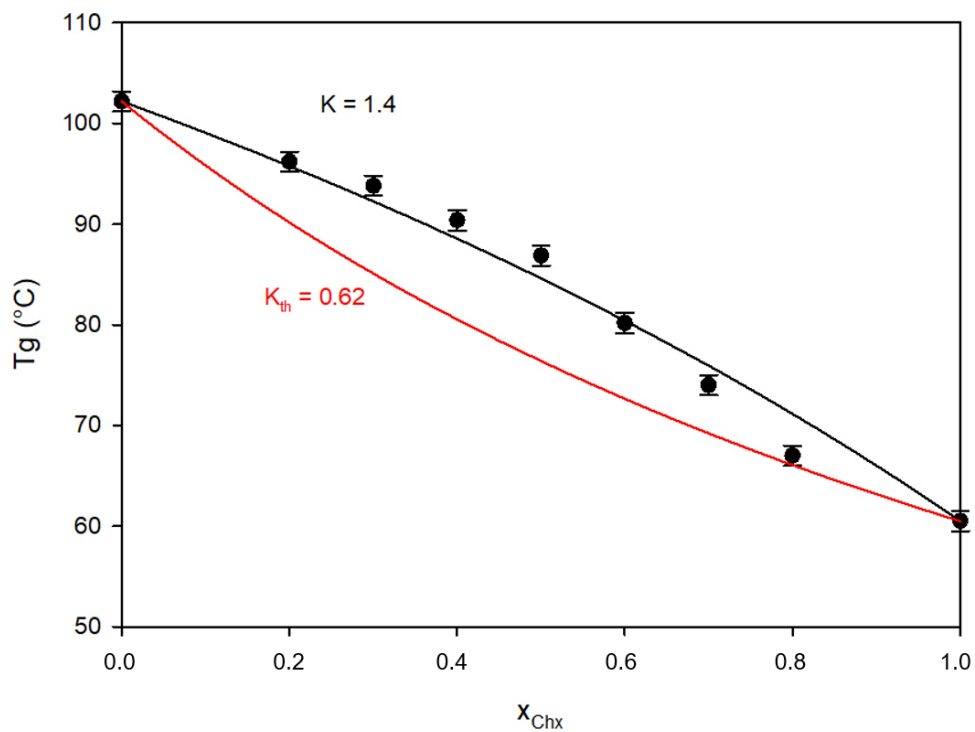
Figure 62 - Black dots represent the evolution of the Tg of the co-milled $(Chx)_x(PVPK12)_{1-x}$ binary mixtures against the Chx fraction (2nd heating cycle). The black solid line represents the best fit of the Gordon Taylor equation to the experimental data and the red curve represents the theoretical Gordon-Taylor curve for an ideal mixture. It must be noted that an estimated error on the Tg of 1°C has been added in order to consider both the eventual Tg measurement error and the eventual approximation on the composition of the mixture.

IV.1.3   Co-amorphization with Lycoat RS 720

This section is focused on testing the possibility to produce amorphous molecular alloys of Chx with a polymer proposed by the company Roquette, Lycoat RS720. Once the co-amorphization feasibility was proven, it was performed for various compositions of the mixture. Finally, the evolution of the Tg of the molecular alloy with the fraction of Chx in the mixture was evaluated.

(1) Co-amorphization feasibility

Contrary to the case of PVPK12, the milling time chosen for the co-amorphization of Chx and Lycoat was of 12 hours (cf. Chapter VI, section VI.1.2). Figure 63 shows both the X-ray diffraction patterns (a) and the DSC heating scans (b) of a co-milled mixture of Chx and Lycoat (50/50, w/w). The diffractograms and thermograms corresponding to Chx milled 3h and to Lycoat are also showed for comparison. As illustrated on the diffractogram, the co-milled mixture (12h) of Chx and Lycoat, only presents the diffusion halo characteristic of an amorphous form. Furthermore, the corresponding thermogram depicts only one Cp jump characteristic of an amorphous form at Tg = 104.1°C which is higher compared to the one of pure amorphous Chx.

Therefore, it appears that 12 hours of milling time is sufficient to produce a homogenous co-amorphous molecular alloy of Chx and Lycoat. However, as the Tg of the Lycoat is higher than 150°C, it is not excluded that a Tg corresponding to a mixture enriched in Lycoat could be present at a temperature higher than 150°C which unfortunately cannot be observed due to the degradation of Chx above 150°C.
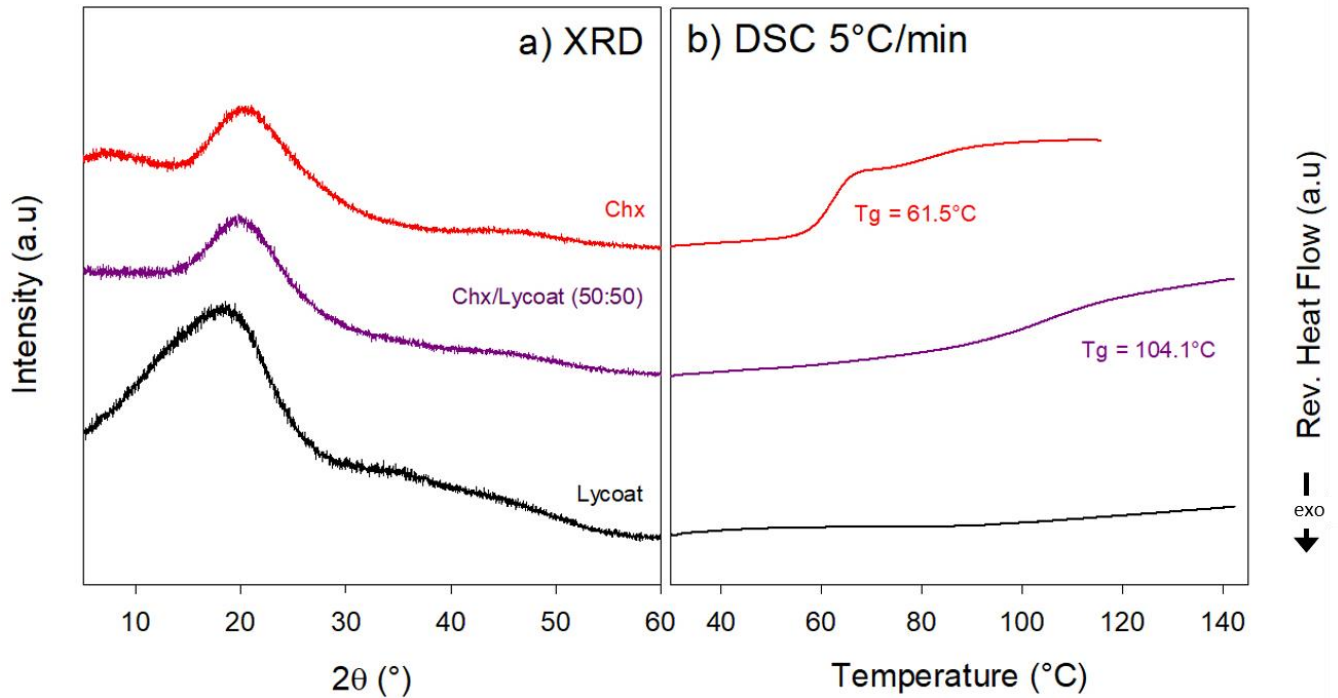
Figure 63 - X-Ray diffraction patterns (a) and DSC scans 5°C/min (b) of Chx milled for 3 hours, Chx/Lycoat (50/50, w/w) co-milled 12 hours and of Lycoat.

(2) Gordon-Taylor curve

The co-milling (12h) of Chx and Lycoat was performed for different compositions of the mixture and the corresponding X-ray diffractions patterns are represented in Figure 64. For comparison, the X-ray patterns of both pure PVP and of pure milling induced amorphous Chx (3h) are also shown. It appears that whatever the fraction of Chx in the mixture, no Bragg peaks could be detected indicating each time, indicating a complete amorphization of Chx after the 12 hours of milling.
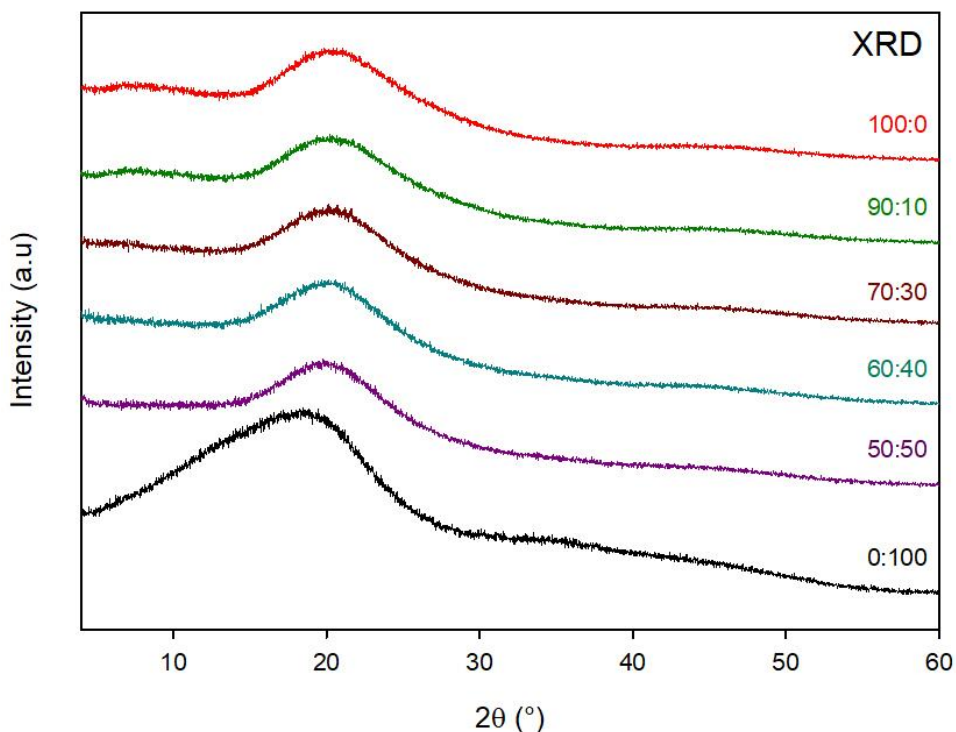
Figure 64 - X-Ray diffraction patterns of Chx/Lycoat mixtures of different compositions, milled for 12 hours. The compositions (Chx/Lycoat, w/w) are reported on the right-hand side of each curve.

Figure 65 shows the DSC heating scan (reversible signal) of the mixture Chx/Lycoat (80/20, w/w) recorded after 12h of milling. It clearly shows two Cp jumps at 65.8°C and 97.2°C. It must be noted that this double Cp jump was observed for mixtures with a Chx concentration greater that 70%. In order to determine if this is due to a heterogeneity of the co-amorphous mixture, a second heating cycle was directly performed after a cooling to room temperature of the sample. This second heating corresponds to run 2 in Figure 65. It revealed a single Cp jump at Tg = 66.6°C which indicates that the amorphous alloy produced after a prior heating to 150°C is homogenous.

Clearly the single Cp jump in run 2 corresponds to the first Cp jump seen in run 1. Moreover, the heat flow corresponding to run 1 is lower compared to the one of run 2 before the end of the first Cp jump. While just above the 1st Cp jump, the heat flow slowly regains the Cp level of run 2. Such a behavior is typical of powders which presents a lack in thermal conductivity. The heat flow is generally lower below Tg but when Tg is reached, the powder melts, the sample flattens, the thermal conductivity increases and the heat flow finally reaches its expected value. Therefore, it can be safely assumed that the second

Cp jump does not correspond to a glass transition, but to a microstructural change of the sample which goes from a finely divided powder to a bulk droplet[180]. As no recrystallization is observed during the first heating cycle, the reversible heat flow signal of the second heating cycle will be chosen for further experiments.
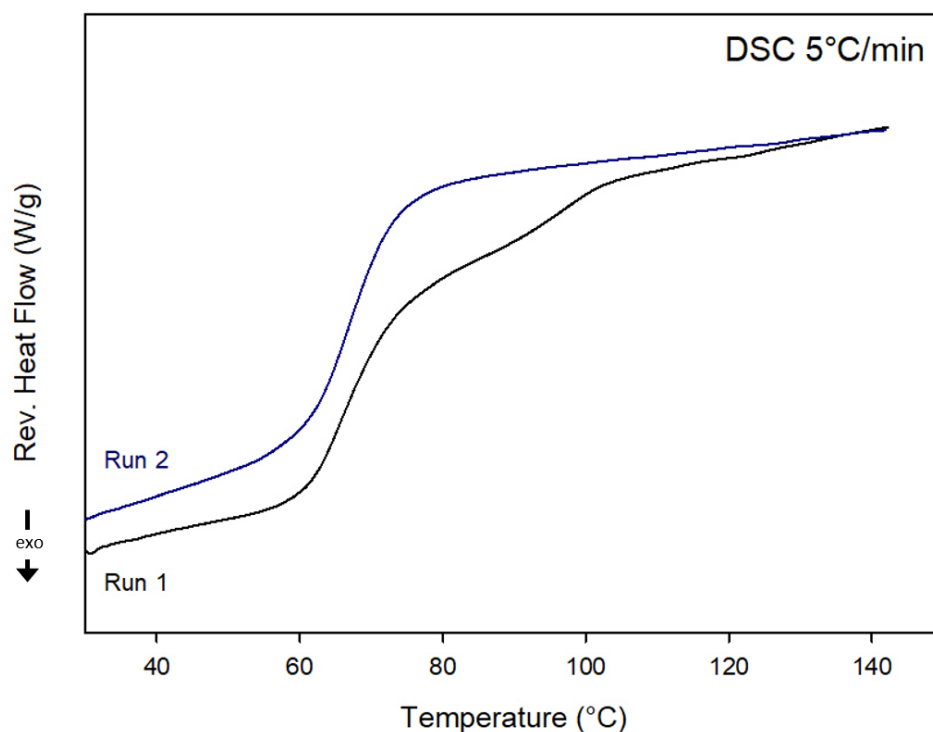
Figure 65 – DSC heating scans of a co-milled (12h) Chx/Lycoat (80/20, w/w) mixture directly after milling (Run 1) and after subsequent heating to 150°C and cooling (Run 2).

Several Chx/Lycoat co-milled (12h) mixtures of different compositions were produced and analyzed using the DSC. The corresponding thermograms (second heating cycle) are reported in Figure 66. In each case, a single Tg is observed and with increasing the Lycoat fraction, the position of this Tg shifts towards the higher temperatures which shows the expected anti-plasticizing nature of Lycoat in the drug/polymer mixture. It must be noted that for all mixtures, the fraction of Chx is higher than 50%. Indeed, as the Tg of the Lycoat is very much higher than 150°C, for lower fractions of Chx, the Tg of the mixture was also higher than 150°C and thus, it could not be observed due to the degradation of Chx above 150°C.

Furthermore, as observed in the case of the co-milled Chx/PVP mixtures, no sign of recrystallization upon heating can be detected before 150°C, temperature at which, the degradation of the drug occurs. Therefore, it can be safely pointed out that the co-amorphization with Lycoat also allowed to increase the physical stability of amorphous Chx upon heating.
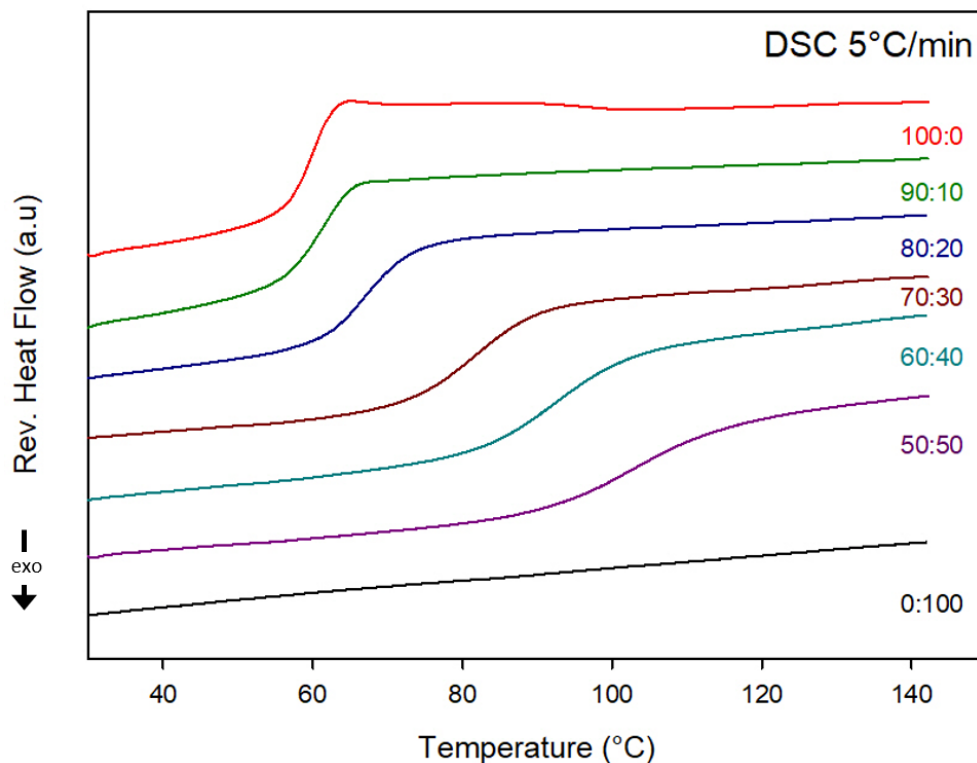
Figure 66 - DSC scans (5°C/min) of Chx/Lycoat mixtures of different compositions, after 12 hours of milling and subsequent heating to 150°C. The compositions (Chx/PVP, w/w) are reported on the right-hand side of each curve. Pure Chx was milled for 3 hours only and Lycoat is non-milled.

The evolution of the Tg of the amorphous alloy (obtained from Figure 66) is illustrated in Figure 67. Compared to the case of PVPK12, the fit with the Gordon-Taylor equation was not performed. Indeed, a crucial data is missing as the Tg of the experimental Tg of the Lycoat could not be observed. However, it will be performed later in this manuscript, in Chapter VI section VI.1.2, using riboflavin/Lycoat mixtures.

Even though, the fit was not performed, it can be noticed that the curve seems to have the same particularity (S-shaped curve) as the one obtained for the Chx/PVP mixtures which indicates that there could be a significant difference in the size and/or the shape of the molecules which could explain the deviation observed.
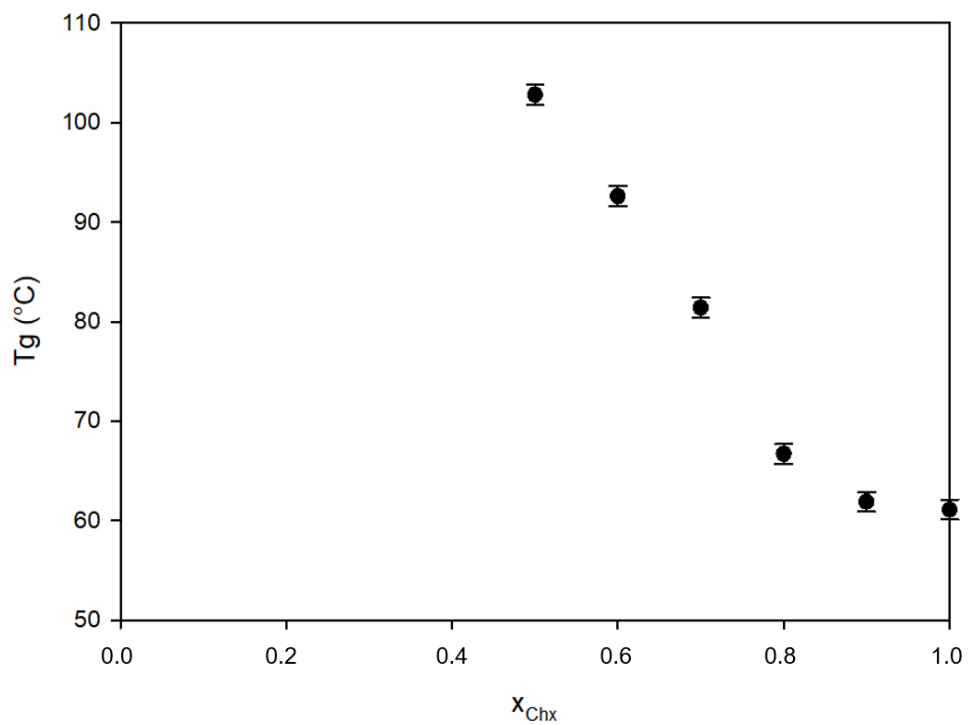
Figure 67 - Evolution of the Tg of the co-milled (Chx)$_x$(Lycoat)$_{1-x}$ binary mixtures against the Chx fraction (2nd heating cycle). It must be noted that an estimated error on the Tg of 1°C has been added in order to consider both the eventual Tg measurement error and the eventual approximation on the composition of the mixture.

IV.2 Dissolution performances of chlorhexidine-polymer mixtures

After a deep physical characterization of the chlorhexidine/polymer alloys previously highlighted, an evaluation of their dissolution performances in ultra-pure water was performed using different set ups. As it was demonstrated in the previous chapter that milling-induced amorphous Chx showed slower dissolution kinetics compared to its crystalline counterpart, an investigation regarding the enhancement of the solubility of amorphous Chx with the addition of a polymer was therefore conducted. Indeed, this investigation aimed to evaluate the influence of the physical state of the API in drug/polymer mixtures and to assess the advantage of the co-milled mixture compared to a physical mixture containing either amorphous chlorhexidine or crystalline chlorhexidine. A comparison between the two polymers was also performed in order to determine the most suitable one to enhance the dissolution performances of this API.

IV.2.1 Influence of the addition of PVPK12 on the dissolution performances of chlorhexidine

After a succinct presentation of the different Chx/PVP mixtures chosen for this study, the dissolution performances of Chx were evaluated using different experimental set-ups including the powder dissolution in sink and in non-sink conditions, the intrinsic dissolution and the tablet dissolution.

(1) Presentation of the mixtures chosen for the dissolution

In order to both evaluate the influence of the physical state of the API in drug/polymer mixtures and to assess the advantage of the co-milled mixture in terms of dissolution performances, three different Chx/PVP (70:30, w/w) mixtures were chosen:

- A physical mixture (PM) of crystalline Chx Form I and PVP named Chx/PVP PM
- A physical mixture of amorphous Chx (obtained by milling Form I for 3 hours) and PVP named ChxM3h/PVP PM

- A co-amorphous mixture of Chx and PVP obtained by co-milling Form I and PVP for 3 hours, named Chx/PVP CM3h

Figure 68 shows the DSC scans (5°C/min) of these 3 mixtures along with the ones of pure milling-induced amorphous Chx and of pure PVPK12 for comparison. Please note that as the X-ray diffractograms did not show anything particular or unexpected, the corresponding data are not shown in this manuscript.

As expected, the thermogram of the physical mixture of crystalline Chx and PVP shows only one small Cp jump at the Tg corresponding to pure PVP followed by the two endotherms (polymorphic transition and melting) observed in the thermogram of pure crystalline Chx. It should be expected to observe both the Tgs of pure milling-induced amorphous Chx and of PVP on the thermogram corresponding to the physical mixture containing milling-induced amorphous Chx. However, only the Tg of pure amorphous Chx can be observed due to an exothermic event corresponding to the recrystallization of amorphous Chx which masks this Tg. Furthermore, it can be noticed that the further heating of this mixture shows the same events as observed in the thermogram of pure milling-induced amorphous Chx. On the contrary, as observed in the previous section, the co-milled mixture shows a single Tg (between the ones of the pure compounds) and is stable upon heating as no recrystallization sign can be detected up to 150°C. Therefore, and as expected, in order to stabilize milling-induced amorphous Chx upon heating, the presence alone of the polymer is not sufficient and the amorphous API must be molecularly dispersed in the polymer matrix.
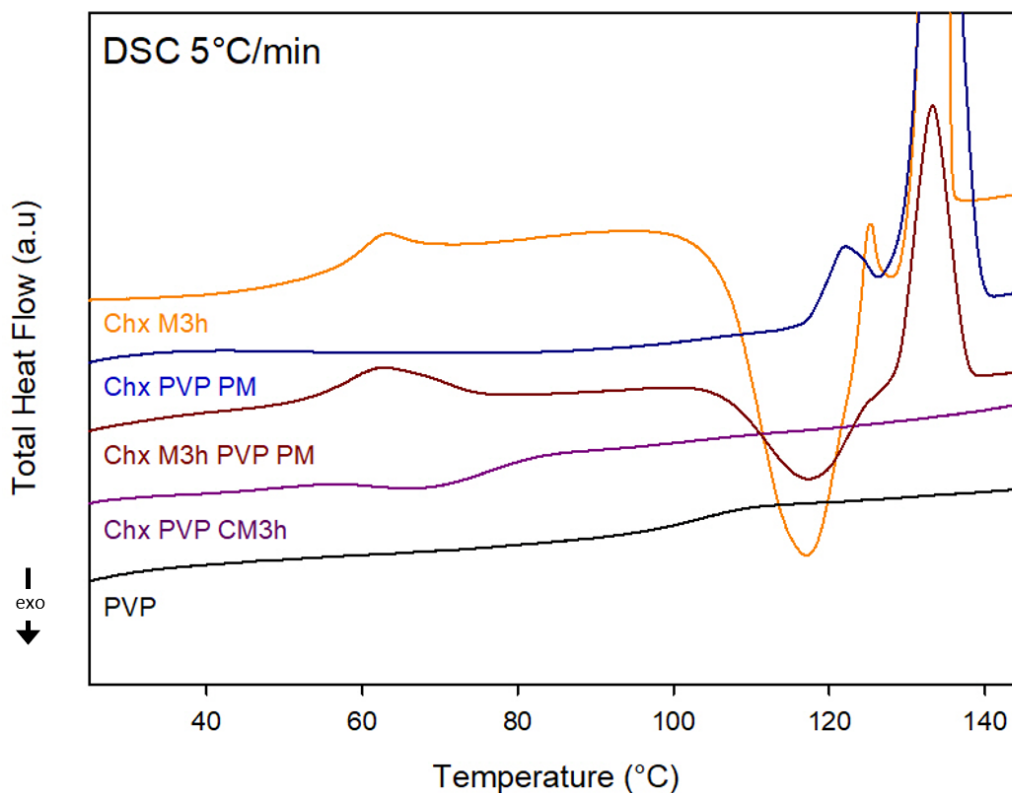
Figure 68 - DSC scans 5°C/min of pure PVP K12 (black), of milling-induced (3h) amorphous Chx (orange) and of a the 3 different Chx/PVP mixture (70:30) (w/w); a physical mixture of crystalline Chx and PVP (blue), a physical mixture of milling-induced (3h) amorphous Chx and PVP (brown) and a co-amorphous mixture of Chx and PVP obtained by co-milling for 3h.

(2) Determination of the solubility limit of Chx in presence of PVP

In order to evaluate an eventual improvement of the solubility of Chx in the presence of PVP (physical mixture), the dissolution kinetics of a physical mixture of Chx and PVP (70/30, w/w) in water were evaluated with an amount of around 150mg of API in order to have it in large excess in the medium (10mL). Figure 69 illustrates the corresponding dissolution kinetics along with the ones of crystalline Chx (presented in Chapter III, section III.2.1, Figure 37), for comparison. During the first 6 hours, crystalline Chx in the physical mixture reaches a maximum of dissolution of approximately 370 mg/L. But at later time points (after 24 hours), this concentration decreases until it reaches a plateau at around 150mg/L. In the case of pure Chx, a maximum of dissolution of around 167mg/L is reached during the first 3 hours and this concentration decreases later on (after 4 hours) to about 100mg/L and then levels-off. As the maximum of dissolution of Chx in the presence of PVP is around 2.5 times higher than the one observed

for pure Chx, it can be thus assumed that the presence alone of PVP in the solution improves the dissolution of Chx in water. Furthermore, the decrease in concentration for pure crystalline Chx was attributed to the precipitation into a pentahydrate, less soluble. It can be assumed that the decrease in concentration observed for the solution containing PVP is due to the same precipitation. However, as this decrease occurs 3 hours later, compared to the solution of pure Chx, it can be assumed that the polymer chains hamper the precipitation which explains the delay observed. Moreover, as the plateau reached is 1.5 times higher in the presence of PVP compared to the case of pure Chx, it can imply that the solubility of this alleged hydrate form is enhanced in the presence of PVP. Unfortunately, due to time constraints, the experiments (X-ray diffraction of the residual solid) allowing the confirmation of this hypothesis could not be performed.
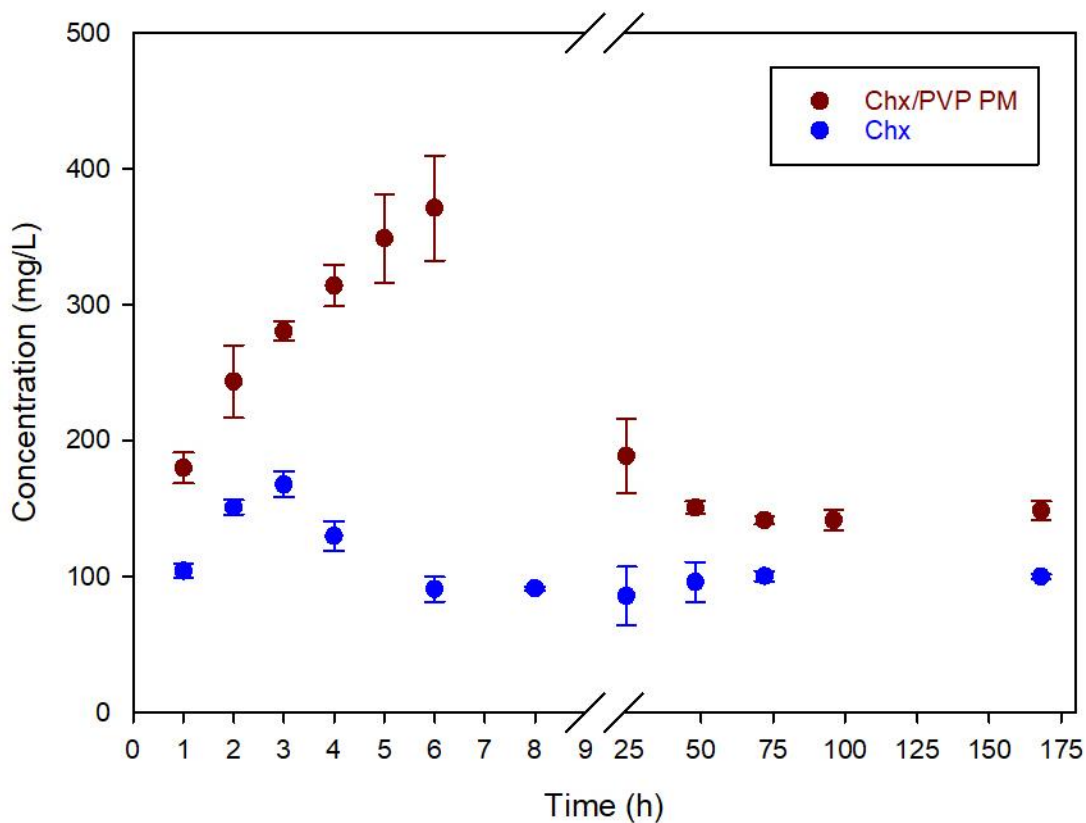
Figure 69 - Dissolution kinetics of Chx (crystal) and of a physical mixture of crystalline Chx and PVP (70/30, w/w), in ultra-pure water at 37°C under agitation (80 rpm) and super-saturation conditions: a large excess of non-dissolved Chx was provided throughout the experiment.

(3) Powder dissolution in sink and non-sink conditions

Figure 70 illustrates the dissolution kinetics of the different Chx/PVP mixtures previously presented in ultra-pure water (800mL) in sink conditions, i.e. for an amount of API at least 3 times below its solubility limit (i.e. 20mg in this case). However, similarly to the case of pure Chx, as the solubility of crystalline Chx could not be determined with absolute certainty, the value present in the literature[147,148] was chosen to impose the sink conditions, i.e. 80 mg/L.

The 3 mixtures show a biphasic dissolution profile as they show a steep slope during the first few hours, followed by a decrease in the dissolution rate until 48 hours of dissolution are reached. The first difference which can be noticed between the 3 mixtures concerns the significant gap in the amount of Chx dissolved observed in the first 4 hours of dissolution. Indeed, after 15min of dissolution, the amount of Chx dissolved in the physical mixture containing crystalline Chx already reached 83.5% whereas it reached only 30.4% and 39.4% in the physical mixture containing amorphous Chx and in the co-milled mixture respectively. However, after 5 hours of dissolution, the amount of Chx dissolved in the co-milled mixture reached the same level as the physical mixture containing crystalline Chx (considering the significant standard deviation obtained) meanwhile the concentration of Chx dissolved in the physical mixture containing amorphous Chx decreased. Nevertheless, after 24 hours of dissolution, the concentration of Chx in the physical mixture containing amorphous Chx increases again so that after 48 hours dissolution, all the mixtures reached approximately 100% of Chx dissolved. Considering the amount of Chx dissolved in the medium, the 3 mixtures seem to rank as follows:

- During the first 4 hours: Chx/PVP PM >> ChxM3h/PVP PM ~ Chx/PVP CM3h
- Between 5 hours and 24 hours: Chx/PVP PM ~ Chx/PVP CM3h > ChxM3h/PVP PM
- After 24 hours: Chx/PVP PM ~ Chx/PVP CM3h ~ ChxM3h/PVP PM

During the first 4 hours, this ranking can be explained by the fact that, as observed with the SEM pictures of crystalline and amorphous Chx (Chapter III, section III.2.2, Figure 42), the milling-induced amorphous Chx particles tend to form aggregates of a larger size compared to the needle-shaped particles of the crystal. Therefore, the aggregates forming in the mixtures containing amorphous Chx require more time to be dissolved compared to the crystalline particles.

Figure 70 - Dissolution kinetics over 48 hours of the different Chx/PVP mixtures in a large volume of ultra-pure water (800mL) heated at 37°C under stirring (100 rpm) and in sink conditions.

Figure 71 illustrates the dissolution kinetics of the same 3 mixtures in non-sink conditions as 150mg of API were used in the same amount of dissolution medium. It must be noted that in case, the solubility of Form I should be exceeded.

After 15min of dissolution, the amount of Chx dissolved in the mixture containing crystalline Chx is 10% higher compared to the one in the mixtures containing amorphous Chx. This observation can be explained by the fact that, as depicted in Figure 72, particles of the mixture containing crystalline Chx are well dispersed in the dissolution medium whereas the particles of the mixtures containing amorphous Chx quickly formed aggregates which require a longer time to dissolve. Nevertheless, the amount of Chx dissolved in the 3 mixtures already reached the same level (around 40%) after the first hour of dissolution.

After 2.5 hours of dissolution, the dissolution rate observed for the mixtures containing amorphous Chx decreases whereas the one observed for the mixture containing crystalline Chx seems to remain constant. Furthermore, a significant drop in the amount of Chx dissolved in the physical mixture containing amorphous Chx is also observed after 5 hours of dissolution. This could be due to the

precipitation of the amorphous Chx into a hydrate as observed in the case of pure amorphous Chx. In this case, it can be assumed that the presence of PVP alone in the solution is not sufficient to protect amorphous Chx from recrystallization, as observed in the case of the super-saturated solution in Chx also containing PVP (Figure 69). However, in the case of the co-milled mixture, even though the dissolution is slowed down, such a drop is not observed which indicates that having the amorphous Chx molecularly dispersed in the PVP matrix allowed at least to restrict the recrystallization of amorphous Chx.

After 24 hours of dissolution, the amount of Chx dissolved in the physical mixture containing crystalline Chx reached a plateau at approximately 95% of Chx released. Comparatively, in the mixtures containing amorphous Chx, the amount of Chx dissolved was still increasing after that timepoint until it reached, after 48 hours of dissolution, around 75% and 85% in the physical mixture and in the co-milled mixture respectively. It can be noticed that the solubility limit of the Chx dissolved in the presence of PVP, evaluated at 150mg/L (Figure 69), corresponds to 80% of Chx released (as illustrated in black dashes). Therefore, as the same percentage was reached (after 48 hours) in the case of the physical mixture containing amorphous Chx, it can be deduced that the recrystallization observed for amorphous Chx led to the same form of Chx as observed in the case of the super-saturated solution of crystalline Chx and PVP (physically mixed). However, as the percentage reached (after 48 hours) for the co-milled mixture was slightly higher, it can be assumed that amorphous Chx remained in the solution. Interestingly, in the case of the mixture containing crystalline Chx, this percentage was exceeded which indicates that in this particular dissolution set-up, the transformation into an alleged hydrate form is prevented. As the same observation was made for the dissolution of pure Chx, it can be assumed that this phenomenon is due to the dissolution set-up itself. Indeed, in this case, the higher volume of dissolution medium (800mL versus 10mL) accompanied with a difference in hydrodynamics induced by a paddle agitation (100rpm) compared to a horizontal shaking (80 rpm) could prevent the precipitation.

Figure 71 - Dissolution kinetics over 48 hours of the different Chx/PVP mixtures in a large volume of ultra-pure water (800mL) heated at 37°C under stirring (100 rpm) and in non-sink conditions.

Chx/PVP PM

ChxM3h/PVP PM
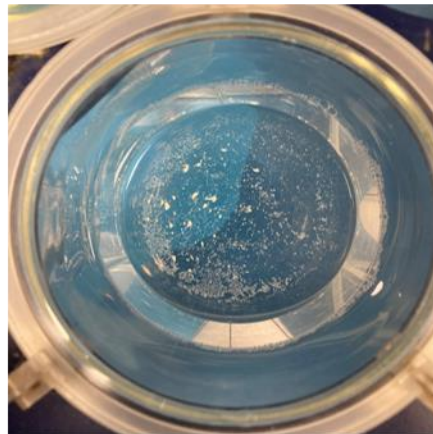
Chx/PVP CM3h
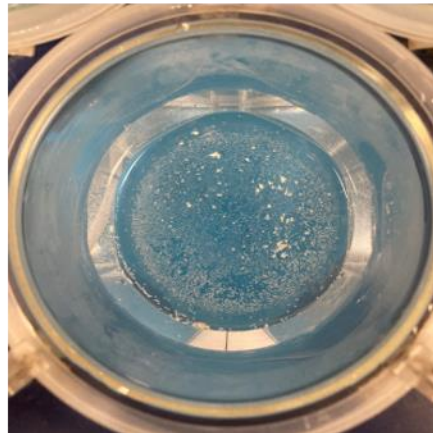
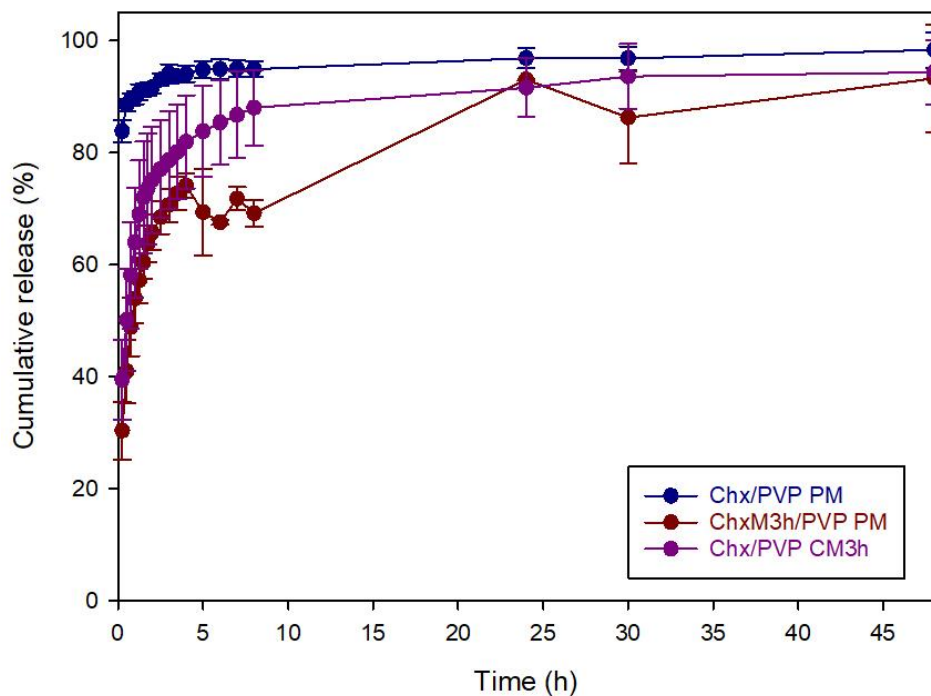*Figure 72 – Pictures after 15min of dissolution of the different Chx/PVP mixtures in a large volume of ultra-pure water (800mL) heated at 37°C under stirring (100 rpm) and in non-sink conditions.*

(4) Intrinsic dissolution

In order to prevent both the influence of the particles size and shape and the formation of aggregates, the intrinsic dissolution of the physical mixture containing crystalline Chx and of the co-milled mixture was performed. Unfortunately, due to time constraints, the intrinsic dissolution of the physical mixture containing amorphous Chx could not be performed. Nevertheless, with a clear determination of the intrinsic dissolution rate for both mixtures, the influence of the physical state of Chx can be evaluated.

First of all, as the physical integrity of the physical state of Chx upon compression of the pure API was demonstrated in the previous chapter, no physical characterization was performed on the compacts produced with the different Chx/PVP mixtures.

Figure 73 illustrates the intrinsic dissolution profiles of the two mixtures previously mentioned. As observed in the case of pure Chx, due to the changes of slope observed, the graph can be divided into 3 different phases:

- From 0 to 4 hours: The physical mixture with crystalline Chx seem to exhibit a slightly higher dissolution rate compared to the one of the co-milled mixture.
- From 5 to 8 hours: The physical mixture with crystalline Chx roughly keeps the same dissolution rate whereas a decrease in the one of the co-milled mixture is observed.
- From 24 to 30 hours: No change is observed in the dissolution rate of the co-milled mixture while a decrease occurs for the physical mixture containing crystalline Chx but the slope seems still be slightly steeper compared to the one of the co-milled mixture.

For more precision, the dissolution rates of the three different forms during the three different stages of the intrinsic dissolution are reported in Table 9. If the values are rather small, the tendency can still clearly be identified as explained above.

Interestingly, compared to the value obtained for pure crystalline Chx (cf Table 6), the dissolution rates in each phase of the physical mixture containing crystalline Chx, are higher which confirms the accelerated dissolution due to an enhanced solubility of crystalline Chx in the presence of PVP. Regarding, the dissolution rates obtained for the co-milled mixture, it must be noted that the value obtained during the first phase is also higher compared to the one of pure amorphous Chx (cf Table 6).

Furthermore, the dissolution rates obtained for the second and third phases of the co-milled mixture are very similar to the ones obtained for the hydrate of Chx (cf Table 6). Therefore, it seems appropriate to deduce that a precipitation occurred after 4 hours of dissolution in the case of the co-milled mixture probably leading to a hydrate form of Chx. However, compared to pure amorphous Chx, this precipitation occurred 2 hours later. It can thus be confirmed that having the amorphous API molecularly dispersed in the PVP matrix allows to hinder the precipitation. Interestingly, the dissolution rate obtained for the physical mixture containing crystalline Chx in the third phase is higher than the one obtained for the hydrate which thus implies that the precipitation was in this case, even more hindered.

However, the fact that the intrinsic dissolution rate of the co-milled mixture is also the lowest at the very beginning of the experiment is still highly unexpected. Indeed, without any precipitation, the amorphous form should exhibit a higher dissolution rate compared to its crystalline counterpart. Therefore, similarly to the case of the pure amorphous Chx, a hypothesis could be that the precipitation occurs already at the very beginning but slowly as it takes time for water molecules to penetrate into the compact.
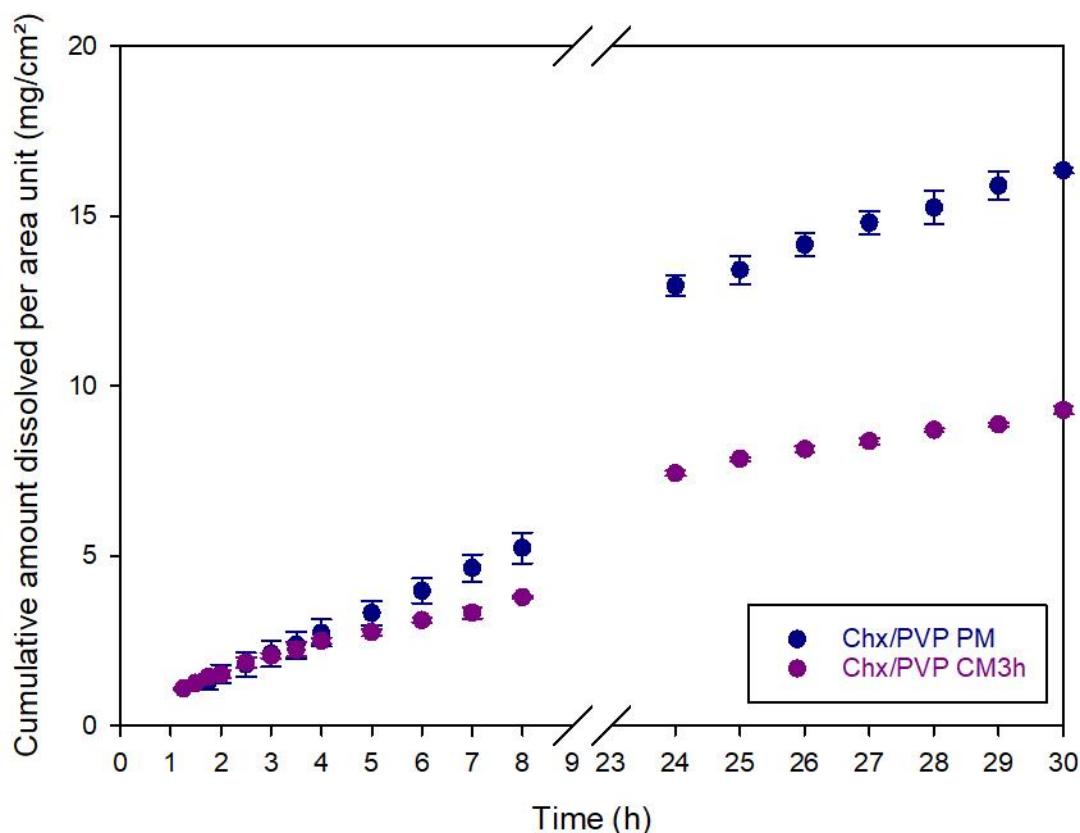
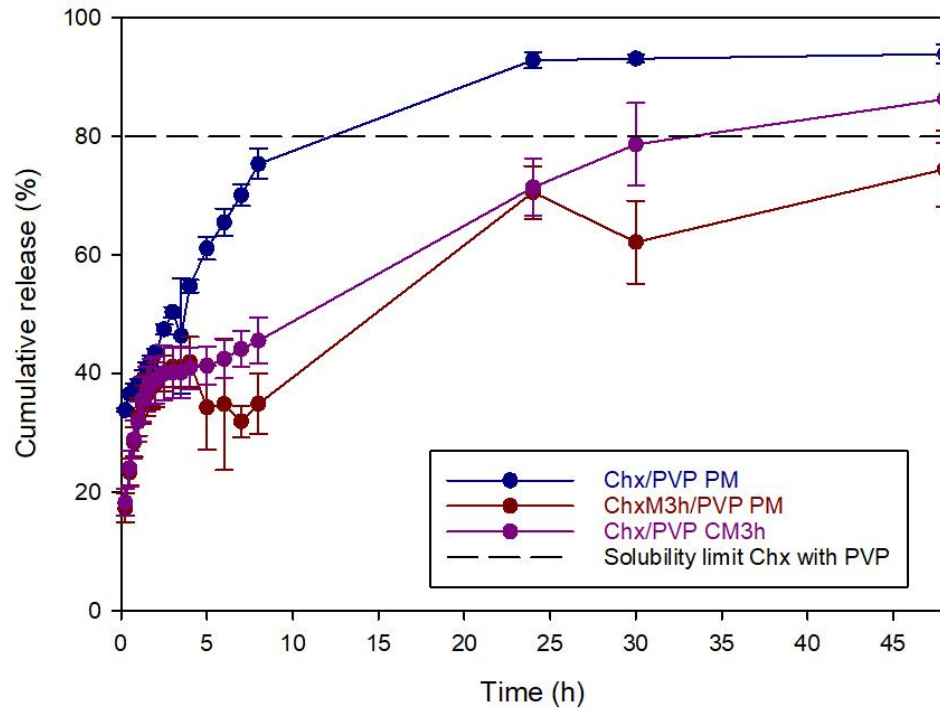*Figure 73 – Intrinsic dissolution kinetics over 30 hours of two different Chx/PVP mixtures in ultra-pure water (400mL) heated at 37°C under stirring (50 rpm).*

Dissolution phase	Chx/PVP PM (crystalline Chx)	Chx/PVP CM3h (co-amorphous)
From 0 to 4 hours	0.63 ± 0.02 mg/cm²/h	0.50 ± 0.02 mg/cm²/h
From 5 to 8 hours	0.64 ± 0.01 mg/cm²/h	0.33 ± 0.03 mg/cm²/h
From 24 to 30 hours	0.58 ± 0.02 mg/cm²/h	0.29 ± 0.01 mg/cm²/h

(5) Tablet manufacturing and dissolution

In order to be closer to "real life" conditions, tablets of the 3 mixtures were produced using the formulation and the method described in Chapter II, section II.4.3.

As explained, the fixed parameter for the tablet production was a hardness set to 80N (±10%). To that extend, 3 different lower punch forces were tested in triplicates and the corresponding hardness of the tablets were measured. A linear fit was then used in order to determine the lower punch force required to obtain this targeted hardness.

Even though the manual filling of the die performed is not fit for industrialization of the process, the manufacturing parameters were evaluated and compared for the 3 different mixtures. However, during the first attempt for the production of tablets from the physical mixture containing crystalline Chx, powder sticking was observed on the punches leading to lamination. This issue in the manufacturing was due to an absence of prior mixing of the physical mixture Chx/PVP. Therefore, the formulation had to be produced again and the batches at different lower punch forces were performed once more. However, as different forces had already been tested on the previous mixture, a range of forces was already identified to obtain the targeted hardness. Unfortunately, due to the fact that the forces tested on the new formulation were too close, the tabletability and the compressibility of the physical mixture containing crystalline Chx could not be evaluated.

Figure 74 illustrates the tabletability of both the physical mixture containing amorphous Chx and the co-milled mixture. As explained in the previous chapter, a mechanically strong enough tablet would show a tensile strength greater than 1.7 MPa but it also has been reported that 1MPa could be sufficient if the tablets are not subjected to heavy mechanical stresses[164]. In both mixtures, the tabletability seems similar and satisfactory tensile strengths were obtained for an applied pressure in a range of 70-100MPa.

Therefore, in this case, having the amorphous drug molecularly dispersed in the polymer matrix or only physically mixed with the polymer, does not have a significant impact on the tabletability.
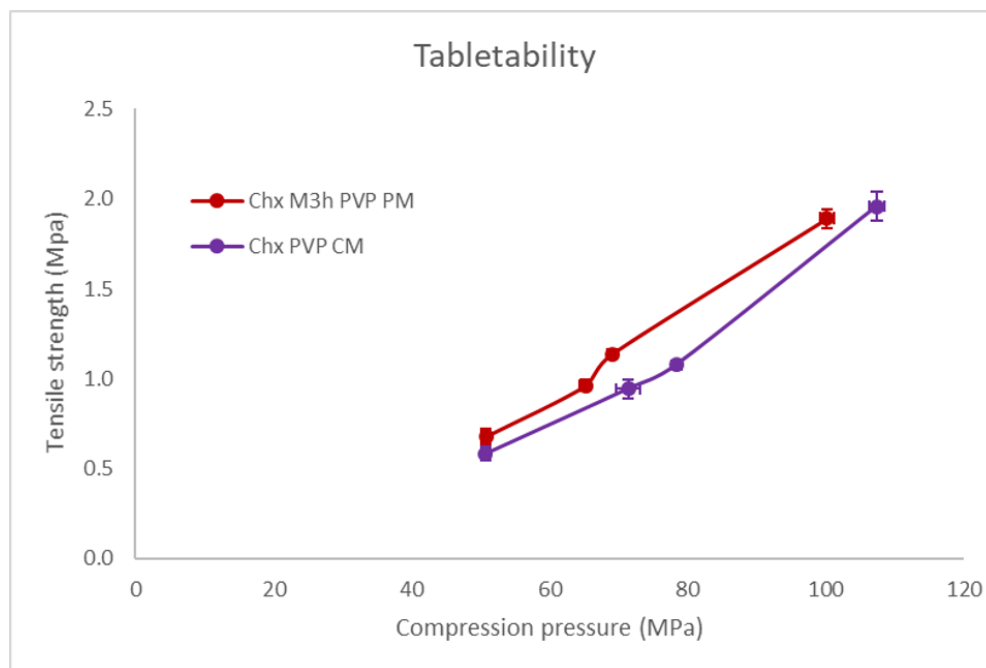
Figure 74 - Tabletability of two different Chx/PVP mixtures: physical mixture containing milling-induced (3h) amorphous Chx and a co-milled (3h) mixture.

As described in the previous chapter, the Heckel-model is used to evaluate the compressibility of the two mixtures (Chapter III, section III.2.4, equation 21) and the P_y is deduced. Indeed, the smaller the P_y value, the better the compressibility of the tablet. In this work, this parameter is determined using the out-die method from the data acquired from the tablet press (positions of the lower and the upper punches) to calculate the dimensions of the tablet after the compression phase.

Figure 75 shows the compressibility of the two mixtures containing amorphous Chx. From the linear regressions applied, the K coefficient and the corresponding P_y were calculated and are reported in Table 10. It can be noticed that the P_y value of the physical mixture containing amorphous Chx is slightly lower compared to the one of the co-milled mixture. Therefore, the formulation shows a slightly better compressibility when the amorphous materials are physically mixed compared to when the amorphous Chx is molecularly dispersed in the polymer matrix.
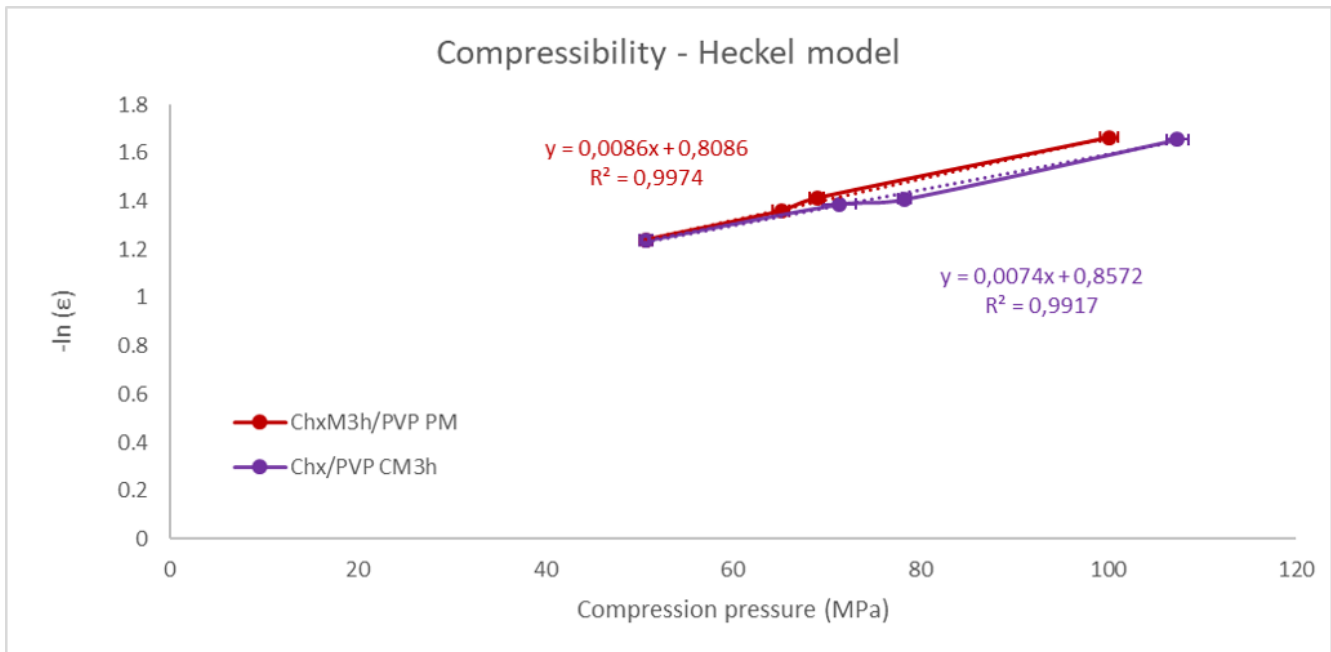
Figure 75 - Compressibility of two different Chx/PVP mixtures: physical mixture containing milling-induced (3h) amorphous Chx and a co-milled (3h) mixture.

Table 10 - Numeric values of the in-die Heckel parameters.

	ChxM3h/PVP PM	Chx/PVP CM3h
K (MPa^{-1})	0.0086	0.0074
P$_y$ (MPa)	116.3	135.1

In Table 11 are reported the tablets properties and related compression process parameters of the tablets produced for the targeted hardness of 80N (± 10%). Regarding the process parameters, it can be observed that the targeted hardness was reached for similar forces applied and that the ejection forces applied to produce the tablets are exceptionally high. This means that each formulation highly tend to stick on the punch once compressed and that the lubricant added in the formulation, even though commonly used and in the usual proportions (Magnesium Stearate, 0.5%)[170], was not sufficient to prevent this feature. However, as the ejection force depends on the tablet dimensions, the ejection shear stress (in MPa) is usually calculated in order to perform an accurate comparison. As presented in the previous chapter, the ejection shear stress of a commercial tablet should not exceed 3 MPa in order to ensure no capping nor lamination[171]. However, ejection shear stresses up to 5 MPa may be acceptable

for tablets which are not subjected to large mechanical stresses on subsequent processing such as film-coating. In our case, each formulation exhibits an ejection shear stress higher than 5MPa which means they are highly prone to defects during the tableting. Nevertheless, lamination was only observed in the case of the formulation containing crystalline Chx but it was due to the fact that no prior mixing of Chx and PVP was performed before addition to the other excipients. Once, it was properly physically mixed, these defects were not observed anymore. However, as in this work, the tablets batches are rather small (up to 18 tablets in a row) compared to a commercial production, it appears understandable that these defects are not encountered. However, the ejection shear stress obtained for each formulation indicate that these formulations are not worth considering as such for industrial manufacturing and would require further optimization.

Regarding the tablet properties, the dimensions, the porosity and tensile strength are similar for the 3 formulations.

Table 11 - Tablet properties and related compression process parameters.

		Chx/PVP PM	ChxM3h/PVP PM	Chx/PVP CM3h
Process parameters	Lower punch force (n=18, kN)	6.37 ± 0.11	6.51 ± 0.09	7.13 ± 0.13
	Ejection force (n=18, N)	1432.0 ± 52.5	1413.4 ± 72.9	1048.5 ± 71.7
	Ejection shear stress (n=18, MPa)	8.7 ± 0.3	8.8 ± 0.5	6.5 ± 0.4
Tablet properties	Weight (n=18, mg)	496.3 ± 1.6	500.9 ± 1.9	498.7 ± 0.9
	Diameter (n=18, mm)	11.36 ± 0.02	11.36 ± 0.02	11.34 ± 0.00
	Thickness (n=18, mm)	4.63 ± 0.01	4.55 ± 0.00	4.53 ± 0.01
	Solid fraction (n=18, %)	73.5 ± 0.4	74.3 ± 0.4	75.1 ± 0.2
	Hardness (n=3, N)	75.4 ± 1.5	78.1 ± 2.5	76.1 ± 4.2
	Tensile strength (n=3, MPa)	0.91 ± 0.02	0.96 ± 0.03	0.94 ± 0.05

The physical state integrity of Chx after compression was assessed only using XRD. Indeed, the DSC data proved to be unavailing as the numerous excipients present prevented from extracting reliable information. Figure 76 and Figure 77 shows the X-ray diffractions patterns of the tablets containing the 3 different Chx/PVP mixtures previously presented, directly after production and after 4 weeks of storage at 25°C, 60% RH, respectively. The X-ray diffraction patterns of both crystalline Chx in its powder form and of the tablet placebo (without API) are also represented for comparison, in both figures. It can be noticed that the peak characteristic of Form I (e.g. peaks marked with a ★ at 7.3° and 8.9°) are still present in the tablet containing crystalline Chx (Chx/PVP PM) directly after production but they are not

observed after 4 weeks of storage. However, other peaks characteristic of Form I (e.g. peaks marked with a ★ at 15°, 18°, 25° and 27°), are still observed, which confirms that Chx remained as the crystalline Form I during the storage. As observed in the case of the compact of Chx Form I (Chapter III, section III.2.3, Figure 45), some differences in intensities can be noticed compared to the tablet analyzed directly after production, which can be attributed to the preferential orientation of the crystal particles during the compression. Regarding the tablets containing amorphous Chx, all those characteristic peaks are absent both after production and after 4 weeks of storage which means that the Bragg peaks observed are only corresponding to the excipients as observed on the diffractogram of the placebo. It can thus be assumed that the physical state of the API was not altered during the compression process and that the amorphous form, either only physically mixed with PVP or molecularly dispersed in the polymer matrix is stable in the tablet over 4 weeks of storage in these conditions. This stability of the amorphous form during storage was expected as it was also stable when the formulation did not contain PVP.
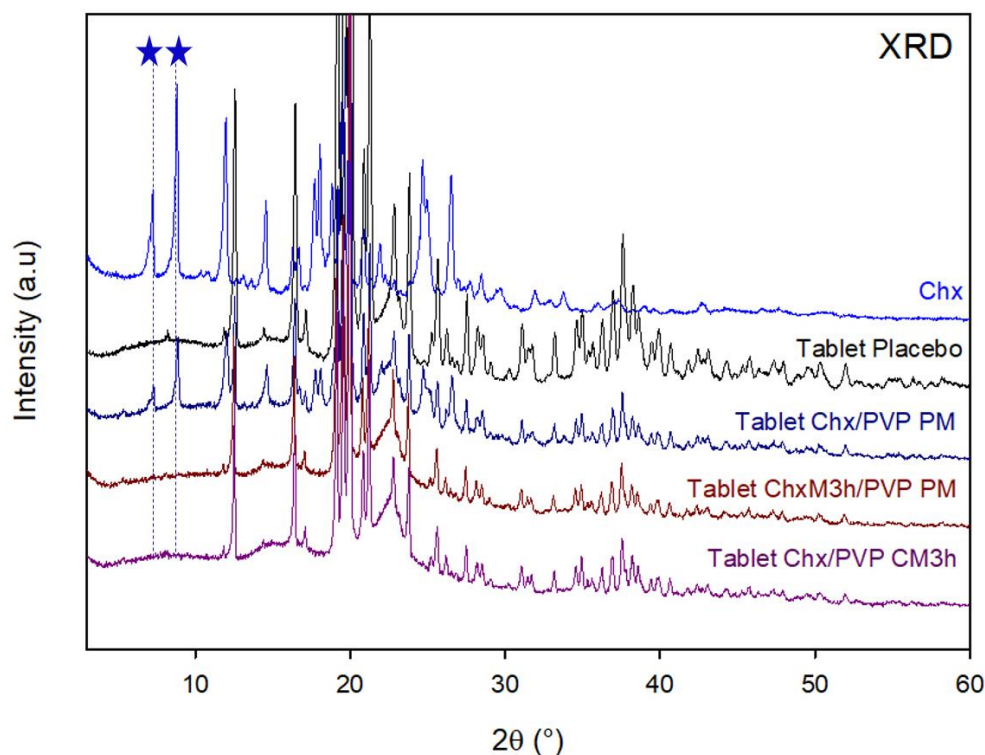
Figure 76 - X-Ray diffraction patterns of tablets containing the 3 different Chx/PVP mixtures directly after production. The commercial form of Chx (Form I) and the tablet not containing API (Tablet Placebo) are also represented.
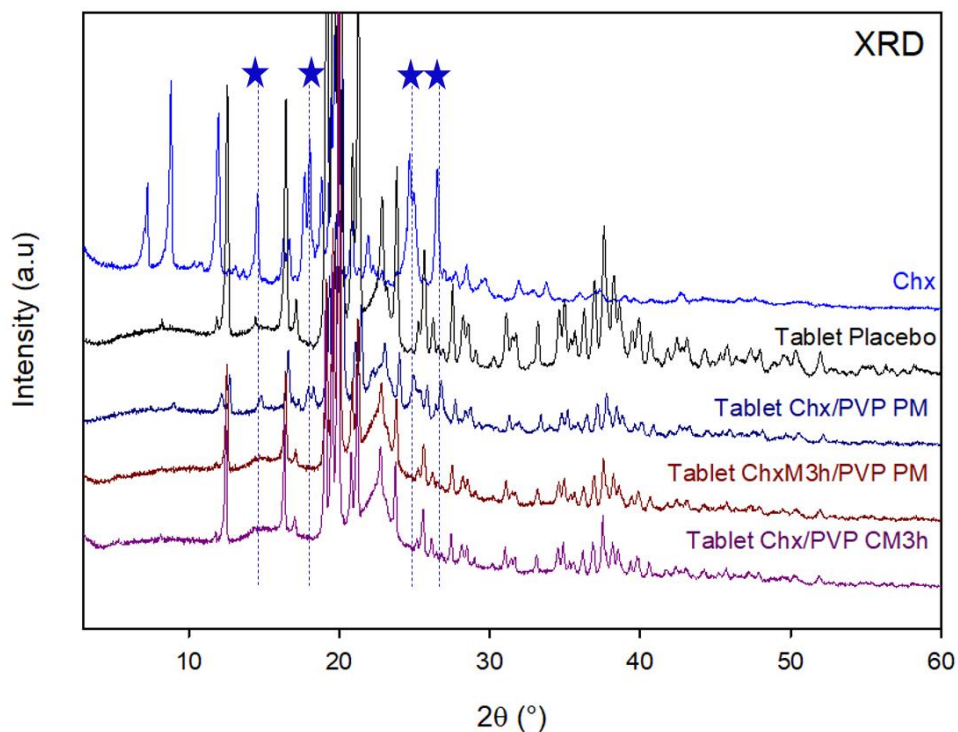
Figure 77 - X-Ray diffraction patterns of tablets containing the 3 different Chx/PVP mixtures after 4 weeks of storage at 25°C, 60% RH. The commercial form of Chx (Form I) and the tablet not containing API (Tablet Placebo) are also represented.

The Chx release in tablets corresponding to each Chx/PVP mixture was evaluated both after production and after 4 weeks of storage (25°C, 60%RH) and the corresponding dissolution kinetics are illustrated in Figure 78 and Figure 79, respectively.

For the dissolution kinetics directly after production, as observed in the case of the powder dissolution in non-sink conditions, after 15min of dissolution, the amount of Chx dissolved in the tablet containing crystalline Chx is higher (40%) compared to the one in the tablets containing amorphous Chx (around 10%).

Furthermore, after 2.5 hours of dissolution, a decrease in the dissolution rate is observed for tablets containing amorphous Chx whereas the one observed for tablets containing crystalline Chx appears to remain constant. As observed in the case of the powder dissolution in non-sink conditions, it would be expected to observe a drop in the percentage of Chx released for the tablets containing the physical mixture of amorphous Chx and PVP. However, a drop is indeed observed but exclusively for the tablets containing crystalline Chx. As this phenomenon was not observed during the powder dissolutions (pure

crystalline Chx or Chx/PVP PM, non-sink conditions) nor during the tablet's dissolution of pure crystalline Chx, the probability of it happening in these conditions was extremely low. However, as it was observed in the case of the super-saturated solution, this probability still existed and it could have been triggered by external factors.

Moreover, after 48 hours of dissolution the percentage of Chx released in the tablets containing the crystalline Chx reaches approximately 80% which corresponds to the solubility limit of the Chx dissolved in the presence of PVP. Therefore, it can be deduced that the precipitation observed for led to the same form of Chx as observed in the case of the super-saturated solution of crystalline Chx and PVP (physically mixed). For the tablets containing amorphous Chx, it seems to be more complex. Indeed, even though, no drop suggesting a precipitation is observed in the case of the co-milled mixture, the final percentage reached is also 80%. This suggests that, a precipitation also seems to occur but less promptly and that it also led to the same form of Chx as observed in the case of the super-saturated solution of crystalline Chx and PVP (physically mixed). Regarding the tablets containing the physical mixture of amorphous Chx and PVP, the final percentage reached is slightly higher than 80% but a decrease in the dissolution rate was still observed. This suggests that, unexpectedly, the precipitation also seems to occur but it must not be total as more Chx can be dissolved.
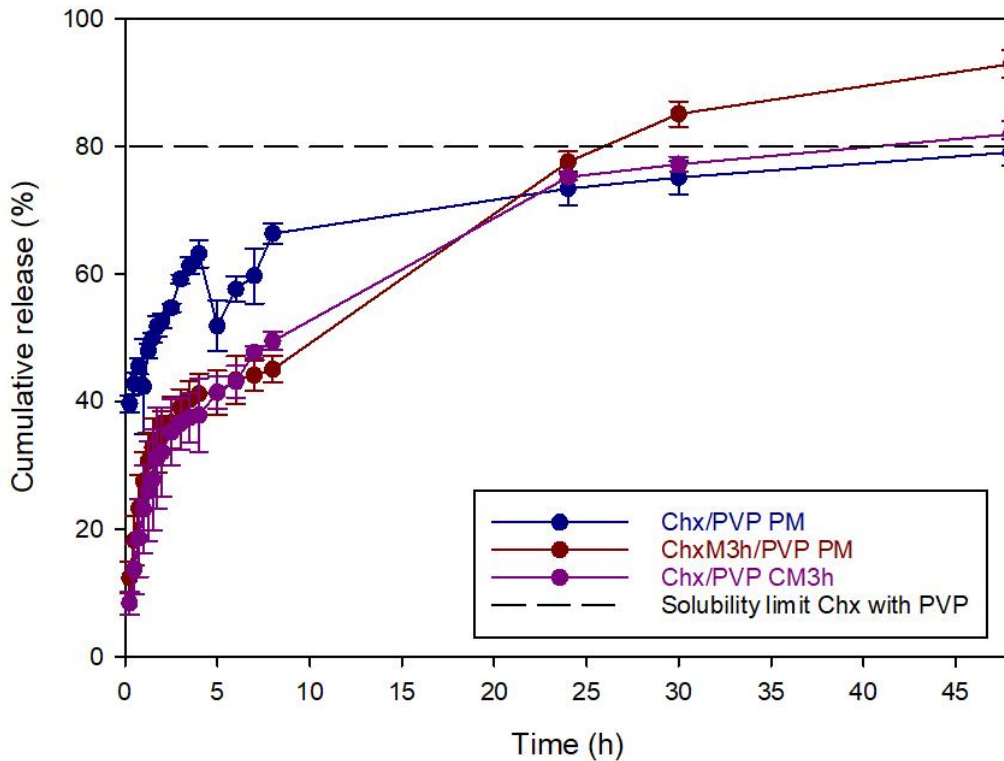
Figure 78 – Tablet dissolution (after production) over 48 hours of the different Chx/PVP mixtures in ultra-pure water (800mL) heated at 37°C under stirring (100 rpm).

For the dissolution kinetics after 4 weeks of storage, the same observation can be made after 15min of dissolution as the amount of Chx dissolved in the tablet containing crystalline Chx is higher compared to the one in the tablets containing amorphous Chx. However, interestingly, after 1 hour of dissolution the percentage of Chx released for the tablet containing the co-milled mixture reached the one observed in the tablet containing crystalline Chx (around 40%).

Compared to the dissolution kinetics after production, the release profiles are slightly different. Indeed, the drop observed in the Chx released percentage in the case of the tablets containing crystalline Chx is not observed. However, a decrease in the dissolution rate is observed after 8 hours of dissolution and, after 48 hours, the percentage reached is slightly above 80%. This suggests that the precipitation observed previously still occurred but less promptly and that it probably also led to the same form of Chx as observed in the case of the super-saturated solution of crystalline Chx and PVP (physically mixed).

The tablets containing amorphous Chx share the same tendencies, even though the percentage of Chx released remains higher in the case of the co-milled mixture during the entire dissolution. Indeed, a significant decrease in the dissolution rate is observed after 5 hours of dissolution and, after 48 hours, the percentage reached is around 80%. This suggests that the precipitation observed previously also occurred but less promptly and that it probably also led to the same form of Chx as observed in the case of the super-saturated solution of crystalline Chx and PVP (physically mixed).
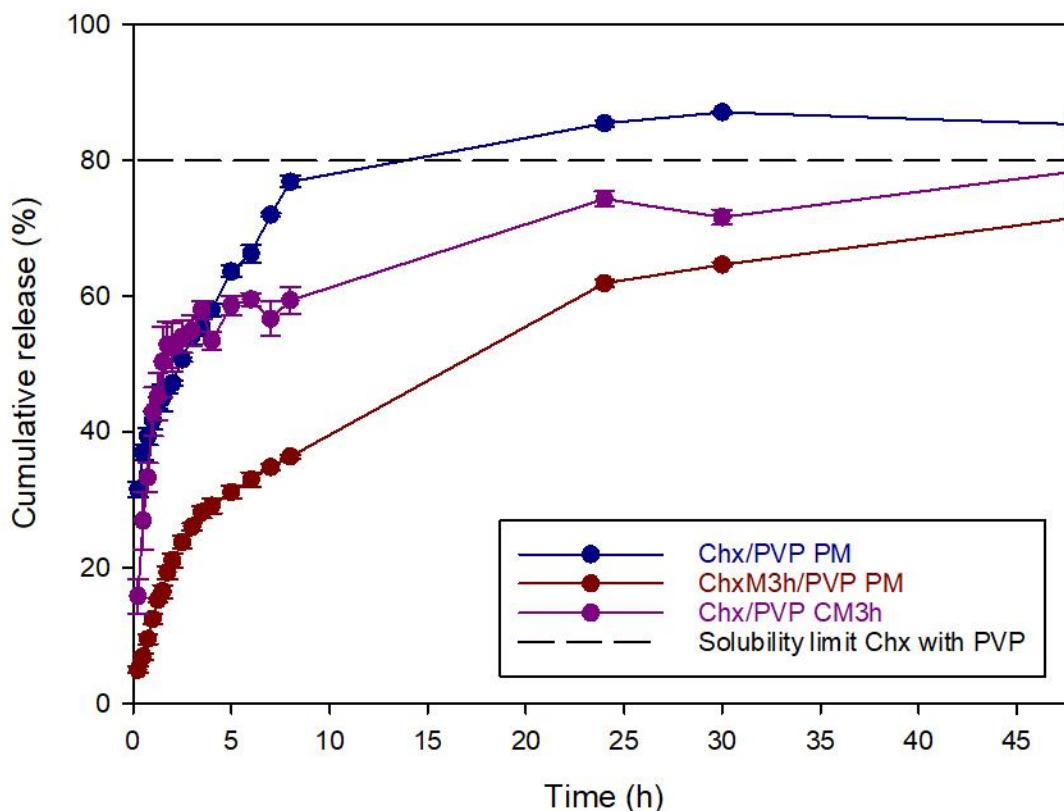
Figure 79 - Tablet dissolution (after 4 weeks of storage, 25°C, 60% RH) over 48 hours of the different Chx/PVP mixtures in ultra-pure water (800mL) heated at 37°C under stirring (100 rpm).

IV.2.2 Influence of the addition of Lycoat RS 720 on the dissolution performances of chlorhexidine

After a succinct presentation of the different Chx/Lycoat mixtures chosen for this study, the dissolution performances of Chx were evaluated using different experimental set-ups including the powder dissolution in sink and in non-sink conditions, the intrinsic dissolution and the tablet dissolution.

(1) Presentation of the mixtures chosen for the dissolution

In order to both evaluate the influence of the physical state of the API in drug/polymer mixtures and to assess the advantage of the co-milled mixture in terms of dissolution performances, three different Chx/Lycoat (70:30, w/w) mixtures were chosen:

- A physical mixture (PM) of crystalline Chx Form I and Lycoat named Chx/Lyc PM
- A physical mixture of amorphous Chx (obtained by milling Form I for 3 hours) and Lyc named ChxM3h/Lyc PM
- A co-amorphous mixture of Chx and PVP obtained by co-milling Form I and Lyc during 12 hours, named Chx/Lyc CM12h

Figure 80 shows the DSC scans (5°C/min, total heat flow) of these 3 mixtures along with the ones of pure milling-induced amorphous Chx (3h and 12h of milling) and of pure Lycoat for comparison. Please note that as the X-ray diffractograms did not show anything particular or unexpected, the corresponding data are not shown in this manuscript. As expected, as the Tg of Lycoat is above 150°C, it cannot be observed in the thermograms corresponding to the physical mixtures containing either crystalline or amorphous Chx. Indeed, the thermogram corresponding to the physical mixture with amorphous only exhibits the Tg of pure Chx, as observed in the pure drug milled 3h. Besides, further heating of the physical mixture with amorphous Chx shows an exothermic peak of recrystallization followed by the endotherm of melting. However, compared to pure amorphous Chx, milled 3h, the exothermic peak appears less prominent which suggests that a higher fraction of Chx remained amorphous upon heating in the presence of Lycoat. Furthermore, the corresponding endotherm of melting is also less intense compared to the one observed for the physical mixture containing crystalline Chx which confirms the hypothesis of a partial recrystallization of the amorphous Chx.

Regarding the co-milled mixture, the results are more complex, as encountered in section IV.1.3. Indeed, due to a wide exotherm from 60°C to around 100°C, no clear Cp jump characteristic of a glass transition seems discernable. Besides, a wide exotherm seems to be present after 120°C which would suggest a recrystallization as it was proven previously that the co-milled mixture (12 hours) was completely amorphous. Therefore, for more clarity, Figure 81 shows the reversible signal of this co-milled mixture after two successive heating cycles (run 1 and run 2). For run 1, a broad Cp jump characteristic of a glass transition is observed but for run 2, the Cp jump is narrower. It seems clear that the Cp jump in run 2 correspond to the Cp jump seen in run 1. Moreover, the heat flow corresponding to run 1 is lower compared to the one of run 2 before the end of the Cp jump. While just above the Cp jump, the heat flow slowly regains the Cp level of run 2. Such a behavior is typical of powders which presents a lack in thermal conductivity, as observed previously. Therefore, as the Cp jumps occur at the same Tg for both runs, there seem to be no recrystallization in the total heat flow during the first heating cycle. As expected, in order to stabilize completely the milling-induced amorphous Chx upon heating, the presence alone of the polymer is not sufficient and the amorphous API must be molecularly dispersed in the polymer matrix.
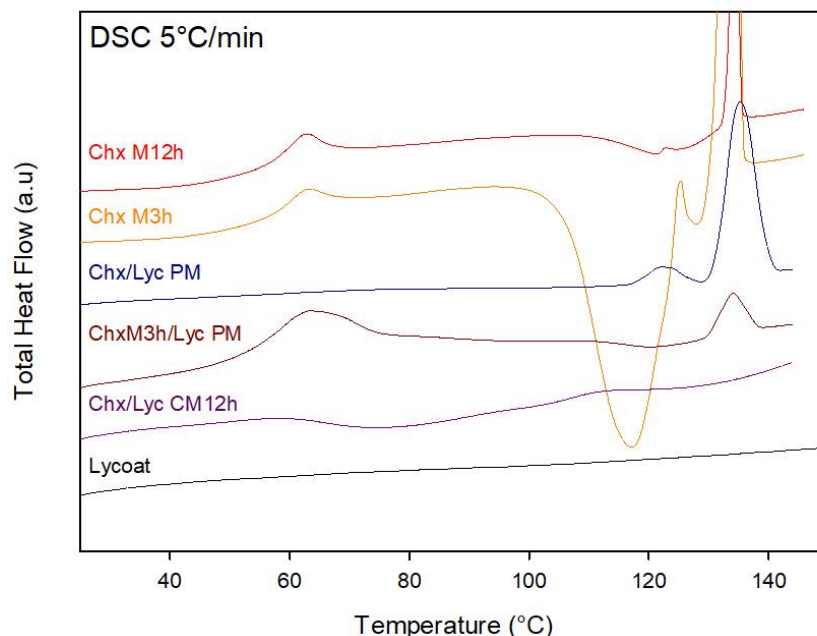
Figure 80 - DSC scans 5°C/min (total heat flow) of pure Lycoat (black), of milling-induced amorphous Chx (3h, orange and 12h, red) and of a the 3 different Chx/Lycoat mixture (70:30) (w/w); a physical mixture of crystalline Chx and Lycoat (blue), a physical mixture of milling-induced (3h) amorphous Chx and Lycoat (brown) and a co-amorphous mixture of Chx and Lycoat obtained by co-milling for 12h.
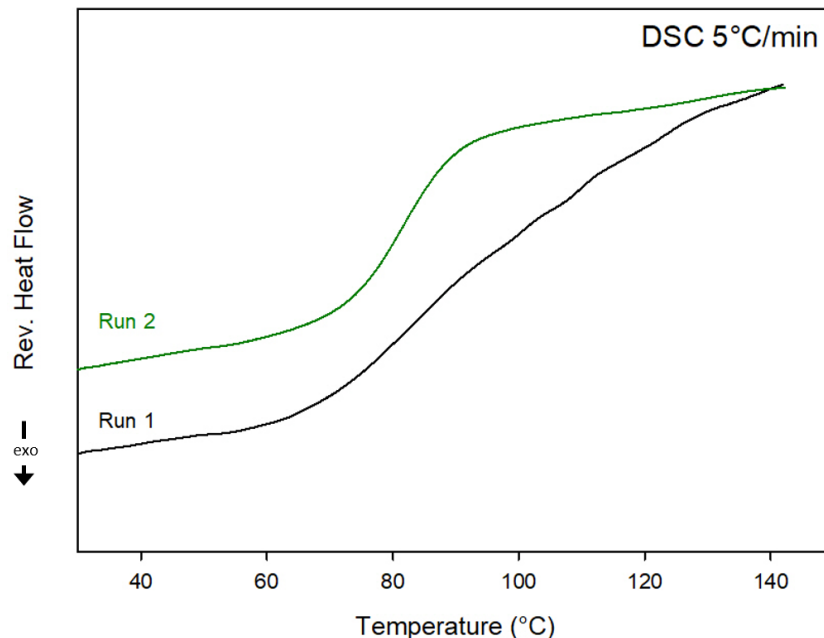
Figure 81 - DSC scans 5°C/min (reversing signal) of the co-milled (12h) mixture Chx/Lycoat during the first heating cycle (run 1) and during the second heating cycle (run 2).

(2) Determination of the solubility limit of Chx in presence of Lycoat

In order to evaluate an eventual improvement of the solubility of Chx in the presence of Lycoat (physical mixture), the dissolution kinetics of a physical mixture of Chx and Lycoat (70/30, w/w) in water were evaluated with an amount of around 150mg of API in order to have it in large excess in the medium (10mL). Figure 82 illustrates the corresponding dissolution kinetics along with the ones of crystalline Chx (presented in Chapter III, section III.2.1, Figure 37), for comparison. During the first 6 hours, crystalline Chx in the physical mixture reaches a maximum of dissolution of approximately 320 mg/L. But at later time points (after 24 hours), this concentration decreases until it reaches a plateau at around 100mg/L. In the case of pure Chx, a maximum of dissolution of around 167mg/L is reached during the first 3 hours and this concentration decreases later on (after 4 hours) to about 100mg/L and then levels-off. As the maximum of dissolution of Chx in the presence of Lycoat is around 2 times higher than the one observed for pure Chx, it can be thus assumed that the presence alone of Lycoat in the solution improves the dissolution of Chx in water. Moreover, the decrease in concentration for pure crystalline Chx was attributed to the precipitation into a pentahydrate, less soluble. It can thus be assumed that the decrease in concentration observed for the solution containing Lycoat is due to the same precipitation.

140

Furthermore, the plateau is reached at the same value in the presence of Lycoat compared to the case of pure Chx, which indicates that this hypothesis could be valid. Unfortunately, due to time constraints, the experiments (X-ray diffraction of the residual solid) allowing the confirmation of this hypothesis could not be performed. However, as this decrease occurs 3 hours later, compared to the solution of pure Chx, it can be assumed that the polymer chains hamper the precipitation which explains the delay observed.
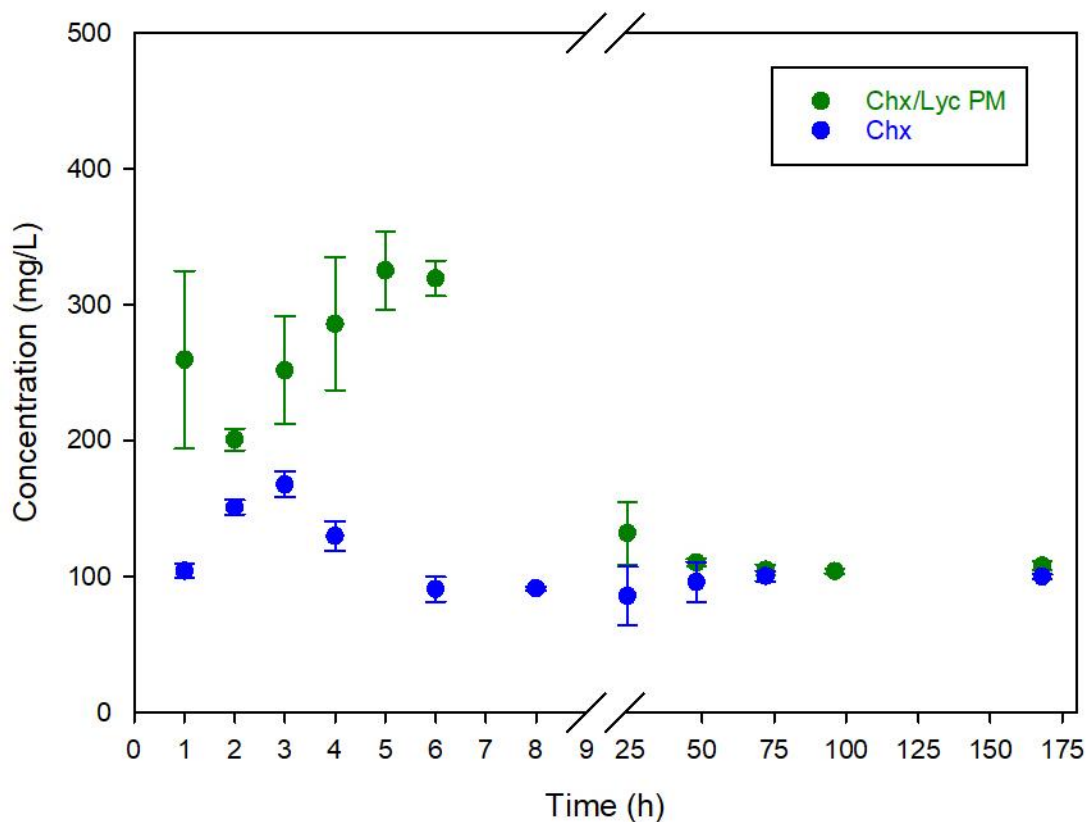
Figure 82 - Dissolution kinetics of Chx (crystal) and of a physical mixture of crystalline Chx and Lycoat (70/30, w/w), in ultra-pure water at 37°C under agitation (80 rpm) and super-saturation conditions: a large excess of non-dissolved Chx was provided throughout the experiment.

(3) Powder dissolution in sink and non-sink conditions

Figure 83 illustrates the dissolution kinetics of the different Chx/Lycoat mixtures previously presented in ultra-pure water (800mL) in sink conditions, i.e. for the same amount of API as used in the case of Chx/PVP mixtures.

The 3 mixtures show a biphasic dissolution profile as they show a steep slope during the first few hours, followed by a decrease in the dissolution rate until the amount of Chx dissolved levels-off and reaches a plateau. The first difference which can be noticed between the 3 mixtures concerns the significant gap in the amount of Chx dissolved observed in the first hour of dissolution. Indeed, after 15min of dissolution, the amount of Chx dissolved in the physical mixture containing crystalline Chx already reached 75.8% whereas it reached only 25.7% and 43.9% in the physical mixture containing amorphous Chx and in the co-milled mixture respectively. However, after 1 hour of dissolution, the curve corresponding to the co-milled mixture catches up with the one of the physical mixture containing crystalline Chx and the release profiles of these two mixtures remain similar until the end of the 48 hours of dissolution. Regarding, the physical mixture containing amorphous Chx, the curve remains below the others which suggests a slower dissolution. However, due to the significant standard deviations obtained, it can be considered as rather similar. Furthermore, after 48 hours of dissolution, all the mixtures approximately released 90 to 110% of Chx which confirms that all the dissolution profiles are rather similar in sink conditions for the 3 mixtures.

Figure 83 - Dissolution kinetics over 48 hours of the different Chx/Lycoat mixtures in a large volume of ultra-pure water (800mL) heated at 37°C under stirring (100 rpm) and in sink conditions.

Figure 84 illustrates the dissolution kinetics of the same 3 mixtures in non-sink conditions as 150mg of API were used in the same amount of dissolution medium. It must be noted that in this case, the solubility of Form I should be exceeded.

As encountered during the dissolution in sink conditions, the release profiles of the physical mixture containing crystalline Chx and of the co-amorphous mixture (obtained by co-milling), are similar during the first 5 hours of dissolution. However, a gap in the amount of Chx released can be noticed between the mixtures containing amorphous Chx and the one containing crystalline Chx, even though it is less pronounced in the case of the co-milled mixture. This difference can be explained, once again, by the propensity of the amorphous mixtures to quickly form aggregates, as illustrated in Figure 85.

After 5 hours of dissolution, the dissolution rate of the co-amorphous mixture slows down and the amount of Chx released seems slightly lower compared to the one of the physical mixture containing crystalline Chx until the end of the 48 hours of dissolution. However, due to the high standard deviations observed for this mixture, the release profiles can be considered rather similar. Regarding the physical

143

mixture containing amorphous Chx, the curve remains below the others which suggests a slower dissolution. Furthermore, a drop in the amount of Chx released is observed after 5 hours of dissolution which, again, can be attributed to a precipitation and explains the slower dissolution observed until the end of the experiment.

However, it can be noticed that after 48 hours of dissolution, due to the high standard deviations observed, the mixtures containing amorphous Chx seem to reach the same amount of Chx released (around 95%) whereas the one containing crystalline Chx is slightly higher than 100%. Furthermore, it can be noticed that all mixtures reached a higher percentage of Chx released compared to the one corresponding to the solubility limit of the precipitated solid of Chx in the super-saturated solution of crystalline Chx and Lycoat physically mixed. In the case of the physical mixture containing crystalline Chx, it seems expected as no sign of precipitation is observed on the release profile. However, regarding the two mixtures containing amorphous Chx, no convincing explanation has yet been found.

Figure 84 - Dissolution kinetics over 48 hours of the different Chx/Lycoat mixtures in a large volume of ultra-pure water (800mL) heated at 37°C under stirring (100 rpm) and in non-sink conditions.
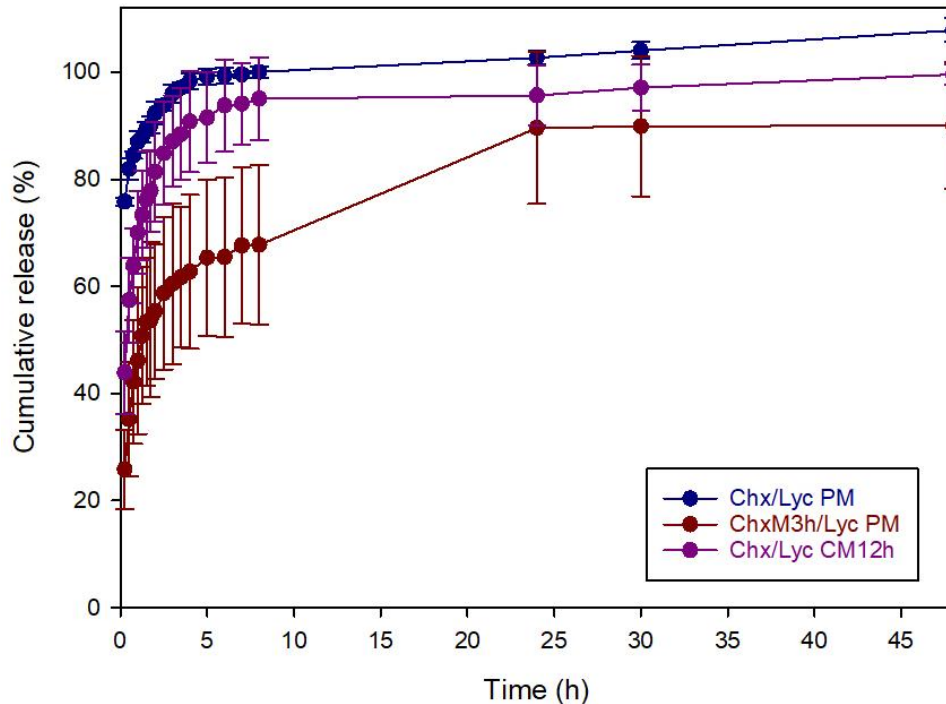
Chx/Lyc PM

ChxM3h/Lyc PM
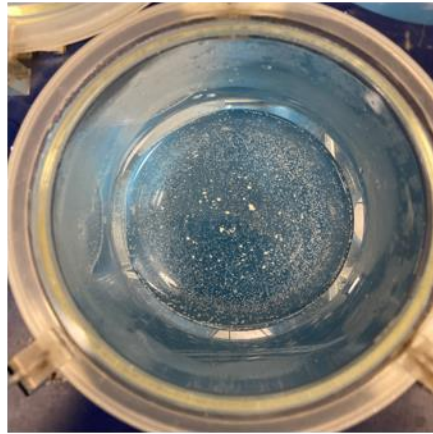
Chx/Lyc CM12h
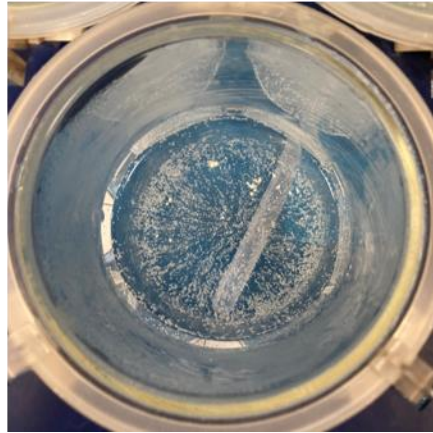
Figure 85 - Pictures after 15min of dissolution of the different Chx/Lycoat mixtures in a large volume of ultra-pure water (800mL) heated at 37°C under stirring (100 rpm) and in non-sink conditions.

(4) Intrinsic dissolution

In order to prevent both the influence of the particles size and shape and the formation of aggregates, the intrinsic dissolution of the physical mixture containing crystalline Chx and of the co-milled mixture was performed. Unfortunately, due to time constraints, the intrinsic dissolution of the physical mixture containing amorphous Chx could not be performed. Nevertheless, with a clear determination of the intrinsic dissolution rate for both mixtures, the influence of the physical state of Chx can still be evaluated.

First of all, as the physical integrity of the physical state of Chx upon compression of the pure API was demonstrated in the previous chapter, no physical characterization was performed on the compacts produced with the different Chx/Lycoat mixtures.

Figure 86 illustrates the intrinsic dissolution profiles of the two mixtures previously mentioned. As observed in the case of pure Chx, due to the changes of slope observed, the graph can be divided into 2 different phases:

- From 0 to 8 hours: The physical mixture with crystalline Chx exhibits a higher dissolution rate compared to the one of the co-milled mixture.
- From 24 to 30 hours: Both mixtures exhibit a decrease in dissolution rate but the one of the physical mixture with crystalline Chx remains higher compared to the one of the co-milled mixture.

For more precision, the dissolution rates of the three different forms during the three different stages of the intrinsic dissolution are reported in Table 12. If the values are rather small, the tendency can still clearly be identified as explained above.

Interestingly, compared to the value obtained for pure crystalline Chx (see Table 6), the dissolution rates in each phase of the physical mixture containing crystalline Chx, are higher, which confirms the accelerated dissolution due to an enhanced solubility of crystalline Chx in the presence of Lycoat. Regarding the dissolution rates obtained for the co-milled mixture, it must be noted that the value obtained during the first phase is also slightly higher compared to the one of pure amorphous Chx. Furthermore, the dissolution rates obtained for the second phase of the co-milled mixture is very similar to the one obtained for the hydrate of Chx after 24 hours of dissolution. Therefore, it seems appropriate

to deduce that a precipitation occurred after 8 hours of dissolution in the case of the co-milled mixture, probably leading to a hydrate form of Chx. However, compared to pure amorphous Chx, this precipitation occurred at least 6 hours later. It can thus be confirmed that having the amorphous API molecularly dispersed in the Lycoat matrix allows to hinder the precipitation. Interestingly, the dissolution rate obtained for the physical mixture containing crystalline Chx in the second phase, is still higher than the one obtained for the hydrate which thus implies that the precipitation was prevented or at least significantly hindered due to the presence of Lycoat.

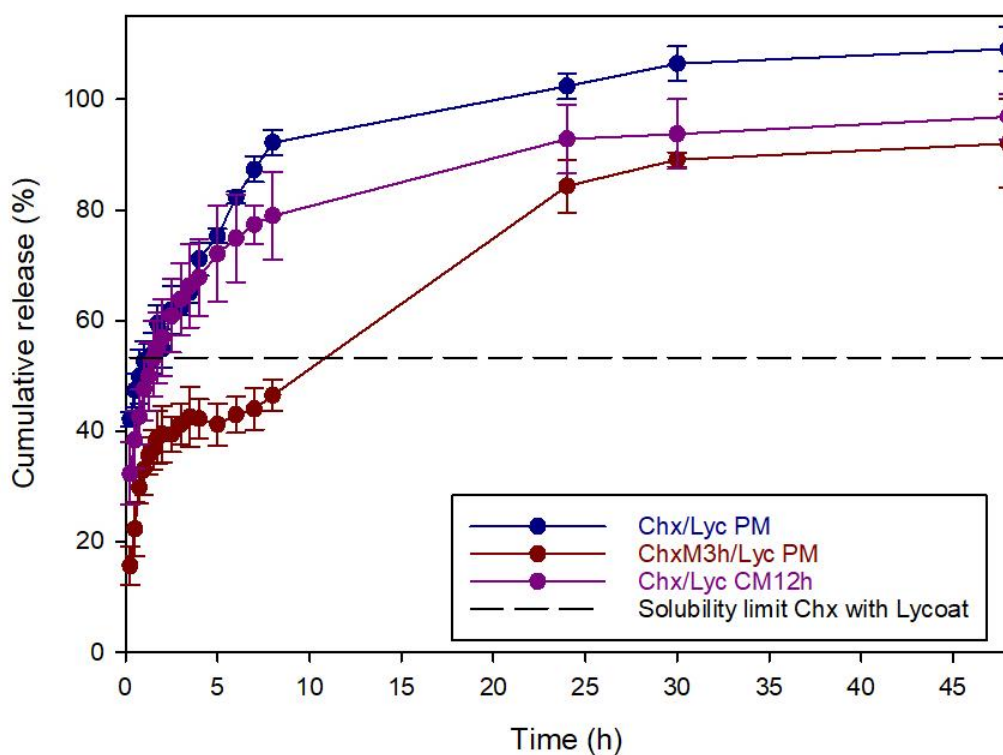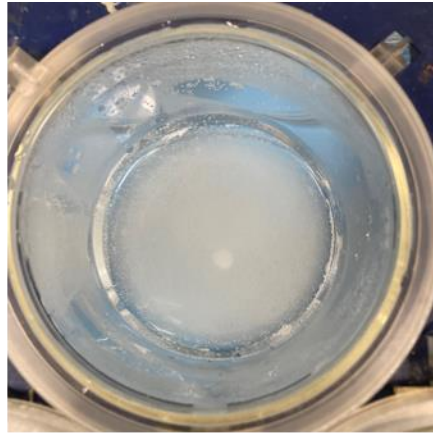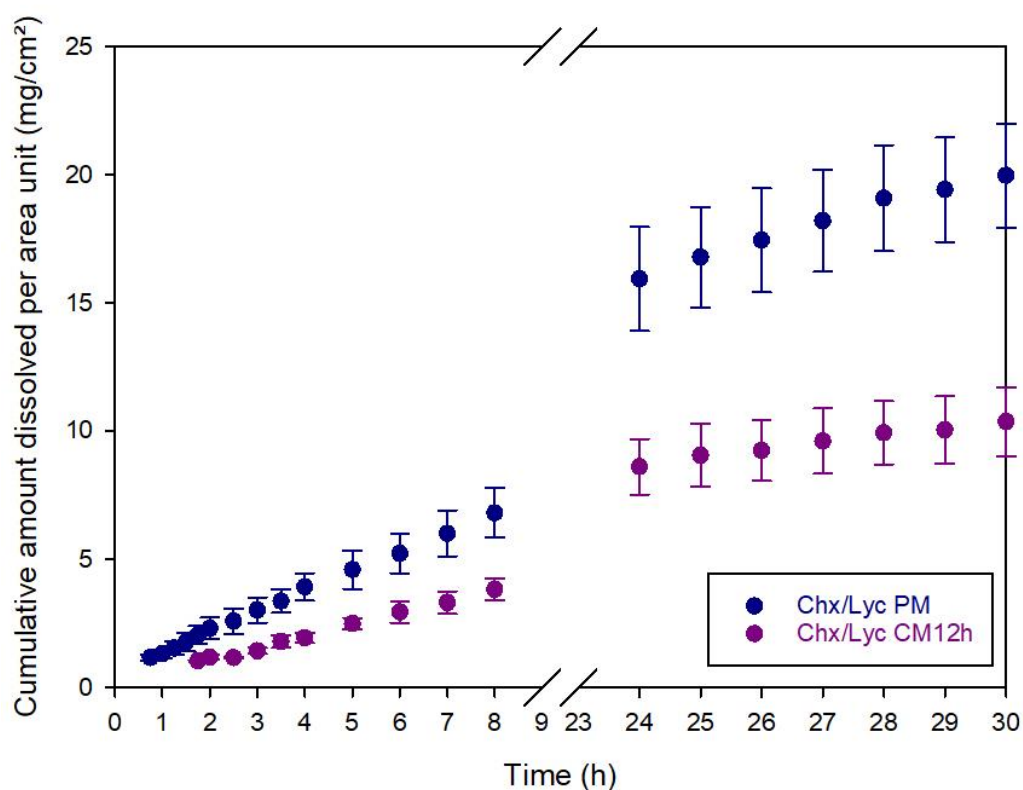*Figure 86 - Intrinsic dissolution kinetics over 30 hours of two different Chx/Lycoat mixtures in ultra-pure water (400mL) heated at 37°C under stirring (50 rpm).*

Table 12 - Intrinsic dissolution rates of the 2 Chx/Lycoat mixtures at different stages of the dissolution. As the experiment was performed in triplicates, mean values were used for the calculations and the standard deviations of the linear fit are also reported.

Dissolution phase	Chx/Lyc PM (crystalline Chx)	Chx/Lyc CM12h (co-amorphous)
From 0 to 8 hours	0.77 ± 0.01 mg/cm²/h	0.46 ± 0.01 mg/cm²/h
From 24 to 30 hours	0.67 ± 0.03 mg/cm²/h	0.28 ± 0.02 mg/cm²/h

(5) Tablet manufacturing and dissolution

In order to be closer to "real life" conditions, tablets of the 3 mixtures were produced using the formulation and the method described in Chapter II, section II.4.3.

As explained, the fixed parameter for the tablet production was a hardness set to 80N (±10%). To that extend, 3 different lower punch forces were tested in triplicates and the corresponding hardness of the tablets were measured. A linear fit was then used in order to determine the lower punch force required to obtain this targeted hardness.

Even though the manual filling of the die performed is not fit for industrialization of the process, the manufacturing parameters were evaluated and compared for the 3 different mixtures.

Figure 87 illustrates the tabletability of the three different mixtures. As explained previously, a mechanically strong enough tablet would show a tensile strength greater than 1.7 MPa but it also has been reported that 1MPa could be sufficient if the tablets are not subjected to heavy mechanical stresses[164]. In each mixture, the tabletability seems similar and satisfactory tensile strengths were obtained for an applied pressure in a range of 70-100MPa. Therefore, in this case, neither the physical state of the API, nor having the amorphous drug molecularly dispersed in the polymer matrix compared to having it only physically mixed with the polymer, have a significant impact on the tabletability. This conclusion was expected as the same observation was made in both the cases of the pure drugs and of the Chx/PVP mixtures.
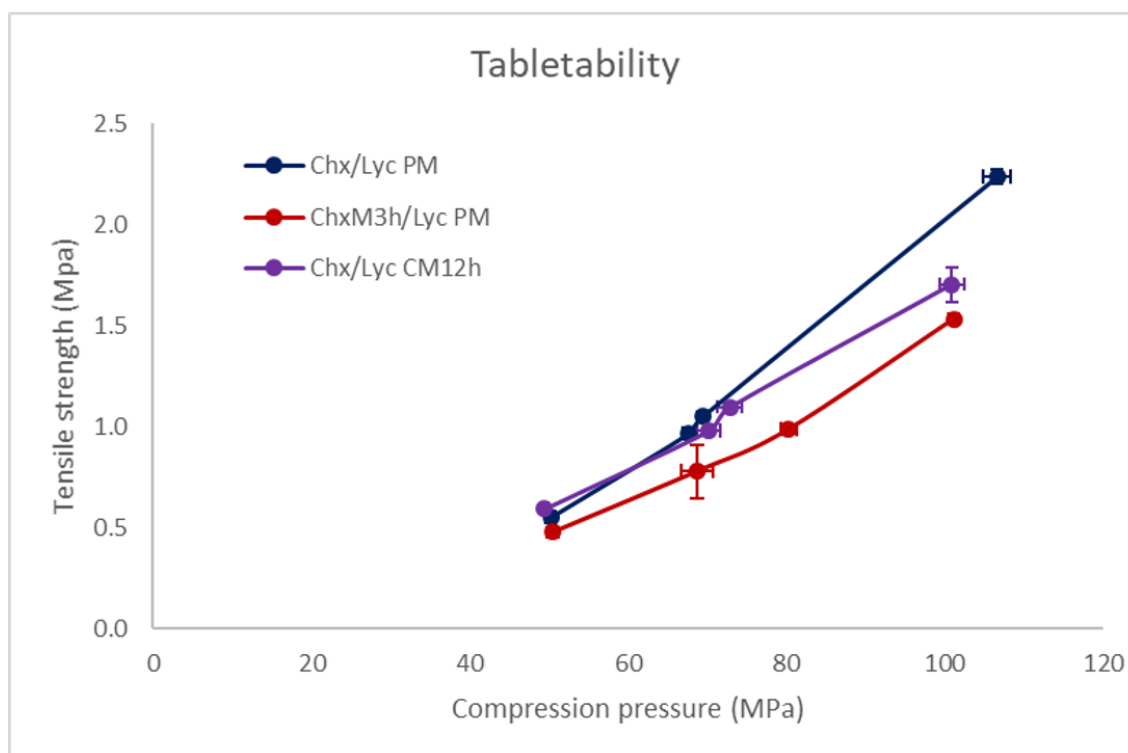
Figure 87 - Tabletability of the 3 different Chx/Lycoat mixtures.

As previously described, the Heckel-model is used to evaluate the compressibility of the two mixtures (Chapter III, section III.2.4, equation 21) and the P_y is deduced. Indeed, the smaller the P_y value, the better the compressibility of the tablet. In this work, this parameter is determined using the out-die method from the data acquired from the tablet press (positions of the lower and the upper punches) to calculate the dimensions of the tablet after the compression phase.

Figure 88 shows the compressibility of the two mixtures containing amorphous Chx. From the linear regressions applied, the K coefficient and the corresponding P_y were calculated and are reported in Table 13. It can be noticed that the 3 mixtures, in terms of P_y values, can be ranked as follows Chx/Lyc CM12h > Chx/Lyc PM > ChxM3h/Lyc PM. Therefore, it appears that the formulation demonstrating the best compressibility is the one containing the physical mixture of amorphous Chx and Lycoat. This was expected as, in the case of pure Chx, the formulation containing amorphous Chx also demonstrated the best compressibility. Furthermore, as observed in the case of the Chx/PVP mixtures, the formulation containing the physical mixture of amorphous Chx and Lycoat shows a better compressibility compared to the co-milled mixture.
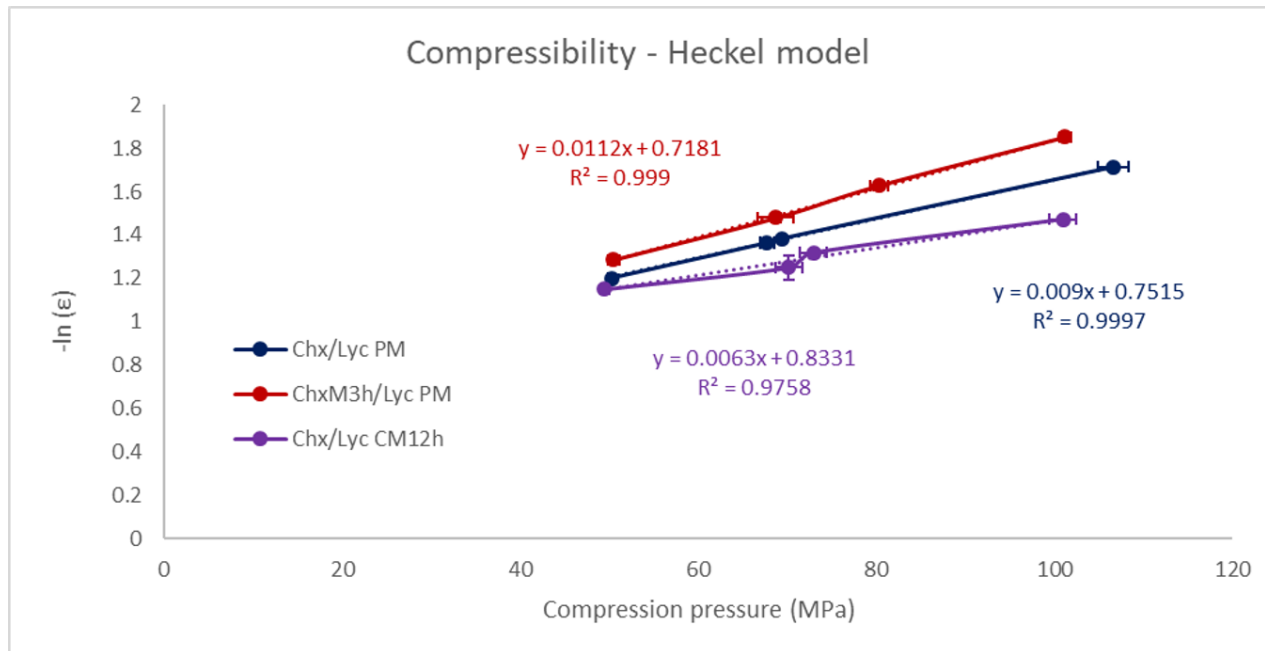
Figure 88 - Compressibility of the 3 different Chx/Lycoat mixtures.

Table 13 -Numeric values of the in-die Heckel parameters.

	Chx/Lyc PM	ChxM3h/Lyc PM	Chx/Lyc CM12h
K (MPa^{-1})	0.009	0.0112	0.0063
P$_y$ (MPa)	111.1	89.3	158.7

In Table 14 are reported the tablets properties and related compression process parameters of the tablets produced at the targeted hardness of 80N (± 10%). Regarding the process parameters, it can be observed that the targeted hardness was reached with forces ranging from 6.7 to 8 kN, and that the ejection forces applied to produce the tablets are exceptionally high except in the case of the co-milled mixture. This means that both formulations containing the physical mixtures, highly tend to stick on the punch once compressed and that the lubricant added in the formulation, even though commonly used and in the usual proportions (Magnesium Stearate, 0.5%)[170], was not sufficient to prevent this feature. However, as the ejection force depends on the tablet dimensions, the ejection shear stress (in MPa) is usually calculated in order to perform an accurate comparison. As presented in the previous chapter, the ejection shear stress of a commercial tablet should not exceed 3 MPa in order to ensure no capping

nor lamination[171]. However, ejection shear stresses up to 5 MPa may be acceptable for tablets which are not subjected to large mechanical stresses on subsequent processing such as film-coating. In our case, only the formulation containing crystalline Chx exhibits an ejection shear stress higher than 5MPa which means it is highly prone to defects during the tableting. Nevertheless, such defects were not observed during the tablet production. However, as in this work, the tablets batches are rather small (up to 18 tablets in a row) compared to a commercial production, it appears understandable that these defects are not encountered. Regarding the one corresponding to the formulation containing amorphous Chx, the ejection shear stress is between 3MPa and 5MPa which remains acceptable as no further process is performed on the tablet. The ejection shear stress of the formulation containing the co-milled mixture (0.9MPa) does not exceed 3MPa which should ensure the prevention of such defects during manufacturing. Therefore, the best formulation, in terms of manufacturing purposes, seems to be the one containing the co-milled mixture of Chx and Lycoat.

Regarding the tablet properties, the dimensions, the porosity and tensile strength are similar for the 3 formulations. However, a slightly higher thickness was observed for the tablets containing crystalline Chx. It can be noticed that the tablets containing the physical mixture of amorphous Chx, also the less porous, exhibited a slightly highest disintegration time compared to the others, but none of the tablets exceeded the time limit of 15min imposed by the pharmacopeia for uncoated tablets[172].

Table 14 -Tablet properties and related compression process parameters.

		Chx/Lyc PM	ChxM3h/Lyc PM	Chx/Lyc CM12h
Process parameters	Lower punch force (n=18, kN)	6.77 ± 0.09	8.02 ± 0.13	7.29 ± 0.10
	Ejection force (n=18, N)	1073.0 ± 22.3	719.4 ± 18.8	140.8 ± 4.3
	Ejection shear stress (n=18, MPa)	6.6 ± 0.1	4.7 ± 0.1	0.9 ± 0.0
Tablet properties	Weight (n=18, mg)	499.7 ± 1.5	500.2 ± 1.7	501.6 ± 2.8
	Diameter (n=18, mm)	11.34 ± 0.00	11.34 ± 0.01	11.34 ± 0.00
	Thickness (n=18, mm)	4.61 ± 0.01	4.33 ± 0.01	4.41 ± 0.01
	Solid fraction (n=18, %)	74.4 ± 0.2	80.4 ± 0.3	73.3 ± 0.4
	Hardness (n=3, N)	79.4 ± 1.4	76.2 ± 1.5	86.2 ± 1.1
	Tensile strength (n=3, MPa)	0.97 ± 0.02	0.99 ± 0.02	1.1 ± 0.02
	Disintegration time (n=3, s)	39 ± 9	168 ± 88	25.7 ± 2

The physical state integrity of Chx after compression was assessed only using XRD. Indeed, once again, the DSC data proved to be unavailing as the numerous excipients present prevented from extracting reliable information. Figure 89 shows the X-ray diffractions patterns of the tablets containing the 3 different Chx/Lycoat mixtures previously presented, directly after production. The X-ray diffraction patterns of both crystalline Chx in its powder form and of the tablet placebo (without API) are also represented for comparison. Unfortunately, due to time constraints, the stability over 4 weeks of storage at 25°C, 60%RH of the tablets containing the Chx/Lycoat mixtures could not be performed.

It can be noticed that the peak characteristic of Form I (e.g. peaks marked with a ★ at 7.3° and 8.9°) are still present in the tablet containing crystalline Chx (Chx/Lyc PM) directly after production. Regarding the tablets containing amorphous Chx, those characteristic peaks are absent which means that the Bragg peaks observed are only corresponding to the excipients as observed on the diffractogram of the placebo. It can thus be assumed that the physical state of the API was not altered during the compression process which could be expected the same conclusion could be made after the preparation of compacts for the intrinsic dissolution.
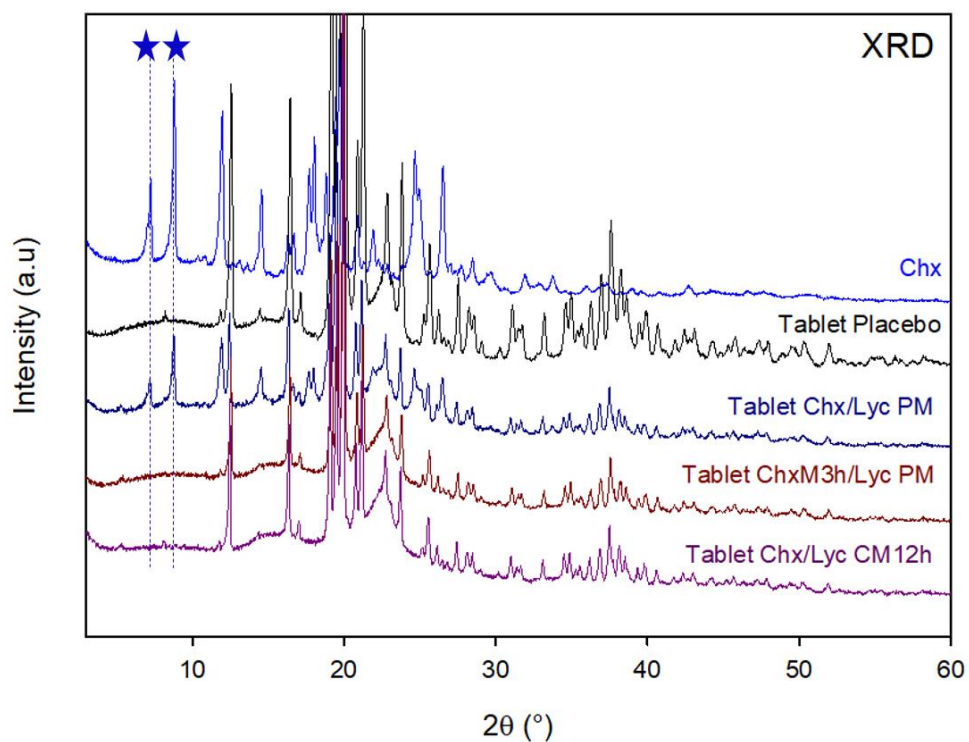
Figure 89 - X-Ray diffraction patterns of tablets containing the 3 different Chx/Lycoat mixtures directly after production. The commercial form of Chx (Form I) and the tablet not containing API (Tablet Placebo) are also represented.

Figure 90 illustrates the dissolution kinetics of the tablets corresponding to the same 3 mixtures. It can be noticed that the release profiles of the mixtures containing amorphous Chx are very similar during the entire dissolution. When compared to the mixture containing crystalline Chx, a gap in the amount of Chx released can be noticed directly after 15 min of dissolution. This difference can be explained, as encountered during the powder dissolution in non-sink conditions, by the propensity of the amorphous mixtures to quickly form aggregates.

After 1.5 hours of dissolution, in the case of the physical mixture containing amorphous Chx and after 3.5 hours of dissolution in the case of the co-milled mixture, a decrease in the dissolution rate is observed. As previously encountered, such a behavior can be attributed to a precipitation and explains the slower dissolution observed until 24 hours of dissolution.

After 24 hours of dissolution, all release profiles seem rather similar and all mixtures reach the same percentage of Chx dissolved after 48 hours of dissolution, i.e around 80%. Furthermore, it can be noticed this percentage is higher compared to the one corresponding to the solubility limit of the precipitated solid of Chx in the super-saturated solution of crystalline Chx and Lycoat physically mixed. In the case of the physical mixture containing crystalline Chx, it seems expected as no sign of precipitation is observed on the release profile. However, regarding the two mixtures containing amorphous Chx, as encountered in the case of powder dissolution in non-sink conditions, no convincing explanation has yet been found.
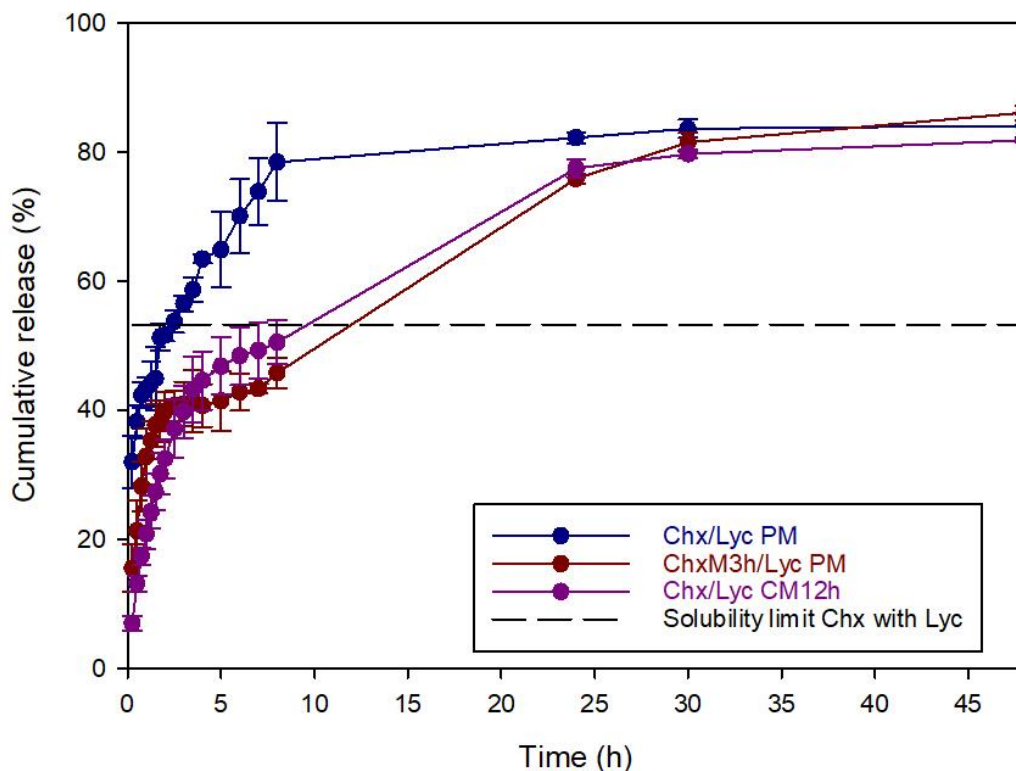
Figure 90 - Tablet dissolution (after production) over 48 hours of the different Chx/Lycoat mixtures in ultra-pure water (800mL) heated at 37°C under stirring (100 rpm).

IV.2.3   Comparison between PVPK12 and Lycoat RS 720

The determination of the solubility limit of Chx in a super-saturated solution with either PVP (Figure 69) or Lycoat (Figure 82) revealed a rather similar propensity of the two polymers to enhance the solubility of crystalline Chx in water, at least during the first 6 hours. However, after 24 hours of dissolution, none of the polymers prevented the precipitation of Chx in solution. Nevertheless, the plateau reached in the case of the solution containing PVP was higher compared to the one reached with Lycoat. Therefore, it can be assumed that the precipitated solid is more soluble in water in presence of PVP.

Regarding the powder dissolution, no significant difference was observed in the sink conditions. However, in the non-sink conditions, if the physical mixture of amorphous Chx and PVP exhibits a significant drop in percentage of Chx released after 5 hours of dissolution (Figure 71), the corresponding mixture with the Lycoat only shows a decrease in dissolution rate (Figure 84). Furthermore, the co-milled

mixture with the PVP shows a significant decrease in the dissolution rate at the same time-point whereas the one with the Lycoat does not. Therefore, it seems that the Lycoat allows a faster release during the first few hours of dissolution and that it is more promising regarding the inhibition of recrystallization of the amorphous Chx. Nevertheless, after 48 hours of dissolution, no significant difference can be noticed between the two polymers as all mixtures show similar results.

The tablet manufacturing parameters analysis revealed higher ejection shear stress for each formulation containing PVP (Table 11) compared to the ones containing Lycoat (Table 14). Furthermore, only the formulation containing the co-milled mixture of Chx and Lycoat exhibited an ejection shear stress allowing an insurance of non-defective tablets during the manufacturing. By comparison of the P_y values the formulation containing the physical mixture of amorphous Chx and Lycoat (Table 13) showed a better compressibility compared to the corresponding one with PVP (Table 10). However, the formulation containing the co-milled mixture with PVP showed a better compressibility compared to the corresponding one with Lycoat.

The tablet dissolution (after production) revealed, unexpectedly, a drop in concentration attributed to a precipitation in the case of the tablet containing the physical mixture of crystalline Chx and PVP (Figure 78) which was not observed in the corresponding tablet with Lycoat (Figure 90). In the case of the tablets containing amorphous Chx, similar release profiles were observed for the tablets containing either PVP or Lycoat, with a decrease in dissolution rate after 5 hours of dissolution but no drop in cumulative release was revealed. Nevertheless, after 48 hours of dissolution, no significant difference can be noticed between the two polymers as all mixtures show similar results, except for the tablet containing the physical mixture of amorphous Chx and PVP which showed a higher percentage of Chx released.

Conclusion

In this chapter, it was showed that both polymers are suitable for a co-amorphization with Chx free base using high-energy milling. Furthermore, as expected, both polymers were found have an anti-plasticizing effect on the drug as the Tgs of the corresponding co-amorphous mixtures shifted towards higher temperatures with an increasing fraction of polymer. For a Chx/polymer (50/50, w/w) mixture, the Tg observed in the case of Lycoat was higher (104.1°C) compared to the one observed in the case of PVP (87.9°C). This was expected as the Tg of Lycoat is supposed to be higher than the one of PVP but it indicates that upon storage, the kinetic stability of the amorphous Chx in the co-milled mixture with Lycoat should be even more ensured.

Moreover, in the case of the co-milled mixtures, both polymers were found to prevent amorphous Chx from recrystallization upon heating which was neither avoidable during the heating of the pure milling-induced amorphous API nor in the case of the milling-induced amorphous API physically mixed with the polymer. However, in the case of the physical mixture of amorphous Chx and Lycoat, the recrystallization upon heating seemed less pronounced, and therefore probably not total, compared to the one observed in the corresponding mixture with PVP. Therefore, if both polymers can be considered suitable for the formulation of ASDs with Chx, the Lycoat seems to have higher stabilizing properties on the milling-induced amorphous Chx upon heating.

Regarding the evolution of the Tg against the composition of the co-milled mixture and its comparison with an ideal mixture, only the Chx/PVP mixtures could be accurately fitted to with the Gordon-Taylor equation as the Tg of the Lycoat could not be observed. This study showed a significant deviation (S-shaped curve) with an opposite curvature compared to the theoretical curve (K = 1.5 VS K_{th} = 0.62) therefore revealing both an influence of the difference of size and shape between the API and the polymer and the presence of strong interactions between the two materials.

Concerning the dissolution kinetics in water, the dissolution of a super-saturated solution of crystalline Chx physically mixed with the polymer, revealed a rather similar propensity of both polymers to enhance the solubility of the API during the first 6 hours. Indeed, the maximum concentration reached was approximately 371 ± 39 mg/L with PVP and 320 ± 13 mg/L with the Lycoat. However, after 24 hours of

dissolution, none of the polymers prevented the precipitation of Chx in solution. In the corresponding experiment with pure Chx in either its crystalline or amorphous state, the same sign of precipitation was observed and the plateau of concentration reached was the same as the one reached by the solution with Lycoat. As it was demonstrated for the pure API that the precipitation was due to a transformation into a hydrate form, less soluble, it could be assumed that the precipitation occurring in both solution containing a polymer also leads to a hydrate form of Chx. However, as the plateau reached in the case of the solution containing PVP was higher compared to the one reached with Lycoat, it can be assumed that the precipitated solid is more soluble in water in the presence of PVP.

For the powder dissolution, no significant difference was observed in the sink conditions. However, in the non-sink conditions, a faster release during the first few hours of dissolution, was observed for the mixtures containing amorphous Chx. Furthermore, the Lycoat showed a higher propensity regarding the inhibition of recrystallization of the amorphous Chx during the dissolution. Nevertheless, after 48 hours of dissolution, no significant difference can be noticed between the two polymers as all mixtures show similar results.

In terms of tablet manufacturing, a higher ejection shear stress was obtained for each formulation containing PVP (between 6.5 and 8.8 MPa) compared to the ones containing Lycoat ($\leq$ 6.6 MPa). Furthermore, only the formulation containing the co-milled mixture of Chx and Lycoat exhibited an ejection shear stress (< 1MPa) allowing an insurance of non-defective tablets during the manufacturing. The comparison of the P_y values revealed a better compressibility for the formulation containing the physical mixture of amorphous Chx and Lycoat (P_y = 89 MPa) compared to the corresponding one with PVP (P_y = 116 MPa). However, the formulation containing the co-milled mixture with PVP (P_y = 135 MPa) showed a better compressibility compared to the corresponding one with Lycoat (P_y = 158 MPa).

The tablet dissolution (after production) revealed similar release profiles for the formulations containing amorphous Chx, thus highlighting no significant influence of the polymer in this case. However, the tablet containing the physical mixture of crystalline Chx and PVP clearly showed a slower dissolution during the first 24 hours of dissolution, compared to the corresponding formulation with Lycoat. Indeed, it revealed an unexpected drop in concentration attributed to a precipitation. Nevertheless, after 48 hours of dissolution, no significant difference can be noticed between the two polymers as all mixtures show

similar results (plateau around 80% of Chx released), except for the tablet containing the physical mixture of amorphous Chx and PVP which showed a higher percentage of Chx released (around 93%).

Unfortunately, the influence of the polymer after 4 weeks of storage on neither the physical integrity of the API in the tablet nor its dissolution performances can be evaluated. Indeed, due to time constraints, the stability study on the tablets containing Lycoat could not be performed. However, as the amorphous remained stable upon storage in the tablets with PVP, at least the same stability would be expected for the tablets containing the co-milled mixture with Lycoat as the Tg of the mixture is higher than the one corresponding to the Chx/PVP co-milled mixture. Regarding the dissolution kinetics after storage of the tablets containing PVP, differences could be noticed compared to the ones obtained directly after production. Indeed, a faster dissolution was observed for the tablet containing crystalline Chx after the storage as no sign precipitation was observed which was more consistent with the results obtained during the power dissolutions. Furthermore, unexpectedly, the dissolution of the tablets corresponding to the co-milled mixture was also faster after storage whereas the one corresponding the one corresponding to the physical mixture with amorphous Chx was in fact, slower.

CHAPTER V - SOLID-STATE AMORPHIZATION OF RIBOFLAVIN UPON MILLING

The accepted version of the manuscript can be found in Appendix 5.

Riboflavin free base, also known as vitamin B2 (as illustrated in Figure 91), is essential for cell growth and is general used in parenteral nutrition[181]. Even though considered as a water-soluble vitamin[182], its solubility in water at 30°C was only reported estimated to approximately 80mg/L[156]. Evidence of polymorphism was briefly mentioned in the literature along with different hydrates [183,184]. However so far, to the best of our knowledge, only the crystalline structure of the commercial form (Form I) could be determined and was found to be orthorhombic (space group P212121) [185].
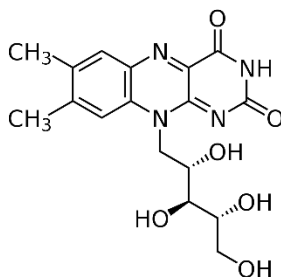
Figure 91 - Illustration of the riboflavin molecule.

Regarding its amorphous form, very little seems to be known as, to our knowledge, no successful amorphization process was reported on the pure API and its glass transition temperature is currently unknown. Indeed it appears to neither be obtained by heating-based techniques, because of a pronounced chemical degradation upon melting[186], nor by spray- or freeze-drying due to the lack of an appropriate solvent [156,157].

Therefore, this API seems to make a good candidate for an attempt of amorphization directly in the solid-state. Using the same thought process as for Chx, an exploration of the physical states of Rf was performed by mechanical milling.

The first part of this chapter will be dedicated to the physical characterization of commercial Rf and of an investigation of its amorphization upon milling. The behavior upon heating of the amorphous form thus produced will also be deeply explored.

Then, in order to assess the advantage of the amorphous form compared to its crystalline forms (stable crystal and metastable polymorphic forms), an evaluation of their dissolution kinetics in ultra-pure water are conducted using different set ups including powder dissolution and intrinsic dissolution.

V.1 Physical characterization of riboflavin

The objective of this section is to assess the possibility to obtain amorphous riboflavin using high-energy planetary milling on the crystal. This investigation is focused on a deep physical characterization in order to understand in detail the effect of this process on riboflavin.

V.1.1 Effect of milling on the physical state of riboflavin

Figure 92 illustrates the X-ray diffraction pattern of commercial riboflavin (blue curve) recorded at room temperature. It shows well defined Bragg peaks, which are characteristic of a crystalline state and their positions correspond to the one which structure was recently determined by Guerain et al[185]. It must be noted that the slight diffusion halo observed is due to the signal of the Lindemann capillary containing the sample.
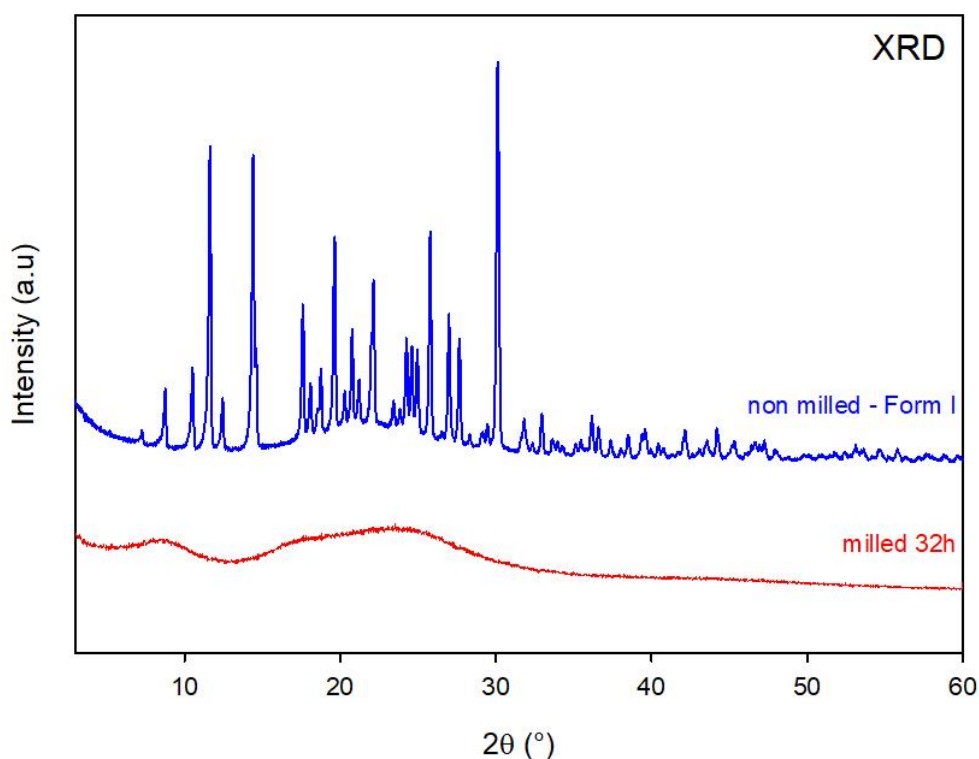
Figure 92 - XRD patterns of commercial riboflavin (blue curve) and of the milled riboflavin (red curve) recorded at room temperature.

Figure 93 shows the TGA scan of commercial riboflavin (black curve) recorded at a heating rate of 5°C/min. It shows a considerable weight loss (about 70%) starting above 250 °C, revealing a significant thermal degradation of the API. Figure 93 also shows the heating DSC scan (blue curve) of riboflavin placed in a high-pressure pan, hermetically sealed (Run 1). This scan reveals a sharp endothermic peak around 290 °C, which superimposes on a wide exothermic peak. The endotherm corresponds to the melting of Form I, while the exotherm is due to the chemical degradation highlighted by TGA. However, as the degradation seems to start slightly before the melting, it can be noted that the degradation must not be due to the melting process itself. The superimposition of those two events prevents from the accurate determination of the melting temperature of riboflavin as well as its melting enthalpy.
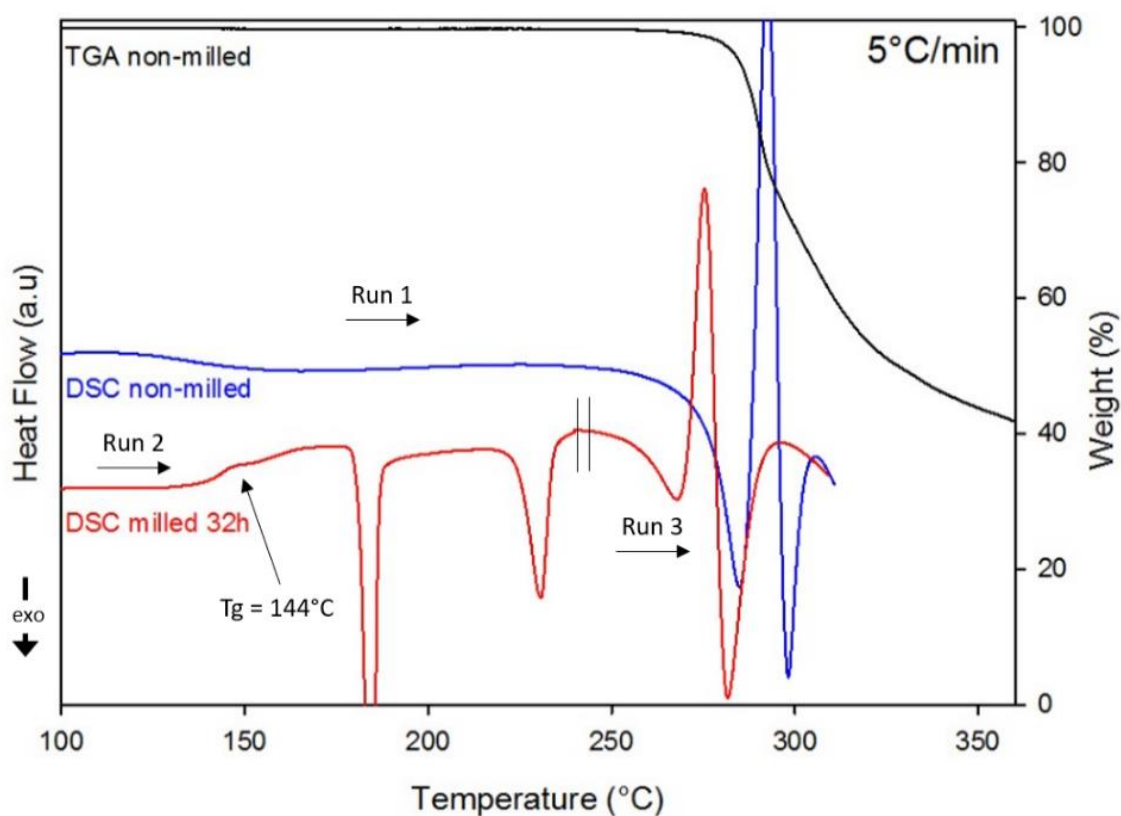
Figure 93 - TGA (black curve) and DSC (Run 1, blue curve) scans of commercial riboflavin as well as the DSC scan of the milled riboflavin (Runs 2 and 3, red curve). The symbol (//) separates run 2 (using a standard open aluminum pan) from run 3 (using a hermetically sealed pan). The heating rate was set to 5°C/min for all scans.

Figure 94 represents the ^{1}H NMR spectra of both commercial (Form I) and melted riboflavin, after dissolution in DMSO. The two spectra show significant differences, as many new peaks appeared after the melting (e.g. between 2.0 to 2.3 ppm, between 3.8 to 4.2 ppm, between 7.1 to 7.8 ppm and at 11.3 ppm), which is a characteristic of chemical degradation. All those results confirm the non-ability to obtain the amorphous state of riboflavin through the traditional quench of the melt. Furthermore, it was demonstrated, that neither solvent-based processes such as spray- or freeze-drying (due to the lack of an appropriate solvent[156,157], cf Appendix 3) nor heat-based technique such as HME (cf Appendix 4), could be used for the amorphization of Rf. In order to safely produce amorphous riboflavin, the high energy milling process was therefore tested.
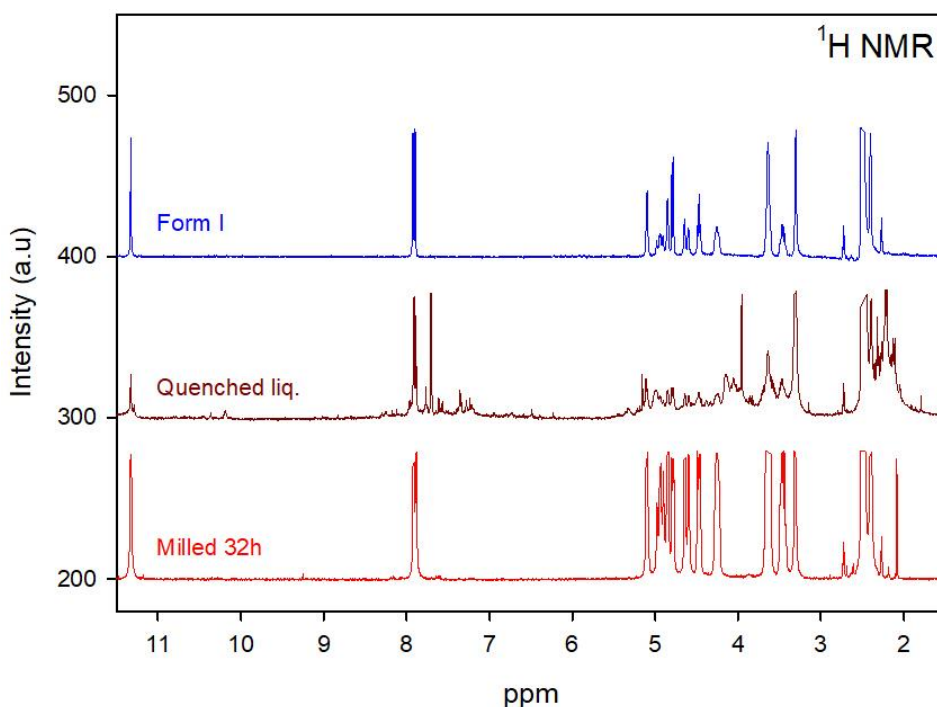
Figure 94 – ^{1}H NMR spectra of commercial riboflavin (Form I), quenched from the melt and milled for 32 hours. To better see the small peaks and avoid anarchic superimposition of the different spectra, the highest peaks have been clipped.

The red curve in Figure 92 shows the XRD pattern of riboflavin form I after 32 hours of milling. It can be noticed that all the Bragg peaks disappeared, giving rise to a diffusion halo characteristic of an amorphous form. The red curve in Figure 93 shows the corresponding heating DSC scans (5 °C/min). It must be noted that run 2 was recorded using open pans (from 45 to 240 °C) and run 3 using a hermetically closed, high-pressure pan (from 240°C to the end). The latter pan was used to protect the DSC cell from contamination by the degradation products generated upon melting. Runs 2 and 3 are separated by the 2 vertical slashes. Run 2 shows a Cp jump (ΔCp = 0.68 J/g/°C), characteristic of a glass transition at Tg = 144°C which proves that a direct "crystal to glass transformation" occurred during the milling process.

Finally, the red curve in Figure 94 shows the ^{1}H NMR spectrum of the milled riboflavin. It appears to be identical with the spectrum of the form I and no signs of degradation were detected compared to the spectrum of the quenched liquid. However, one peak appeared at 2.09 ppm but it is attributed to an acetone residue[154], stemming from the cleaning of the NMR tube. High-energy milling thus appears to be an appropriate approach to successfully and safely produce amorphous riboflavin.

V.1.2 Polymorphism

Further heating of the amorphous riboflavin obtained by milling (run 2, red curve, Figure 93) reveals two exothermic peaks. The first one occurs at around 185°C (ΔH_1 = 58.2 J/g) and is characteristic of a recrystallization. As illustrated in Figure 96, the milling-induced amorphous Rf was heated to 200°C (black curve, run 1), subsequently cooled and heated again to 250°C (blue curve, run 2). It can be noticed that after the prior heating to 200°C and subsequent cooling (Run 2), no Cp jump can be observed anymore upon heating. This indicates that the first exothermic event corresponds to a complete recrystallization of the amorphous Rf.

The diffractogram of the milled material subsequently heated to 200°C, and then recorded at room temperature (i.e. just above the first exotherm), is reported in Figure 95 (black curve). It shows well defined Bragg peaks, characteristic of a crystalline state. Furthermore, it can be noted that these peaks are clearly different from the ones characteristic of Form I (e.g. peaks marked with a ★ or ◆ in Figure 95). This indicates that the recrystallization occurred at 185°C toward another crystalline form of riboflavin, called "Form III"[184].
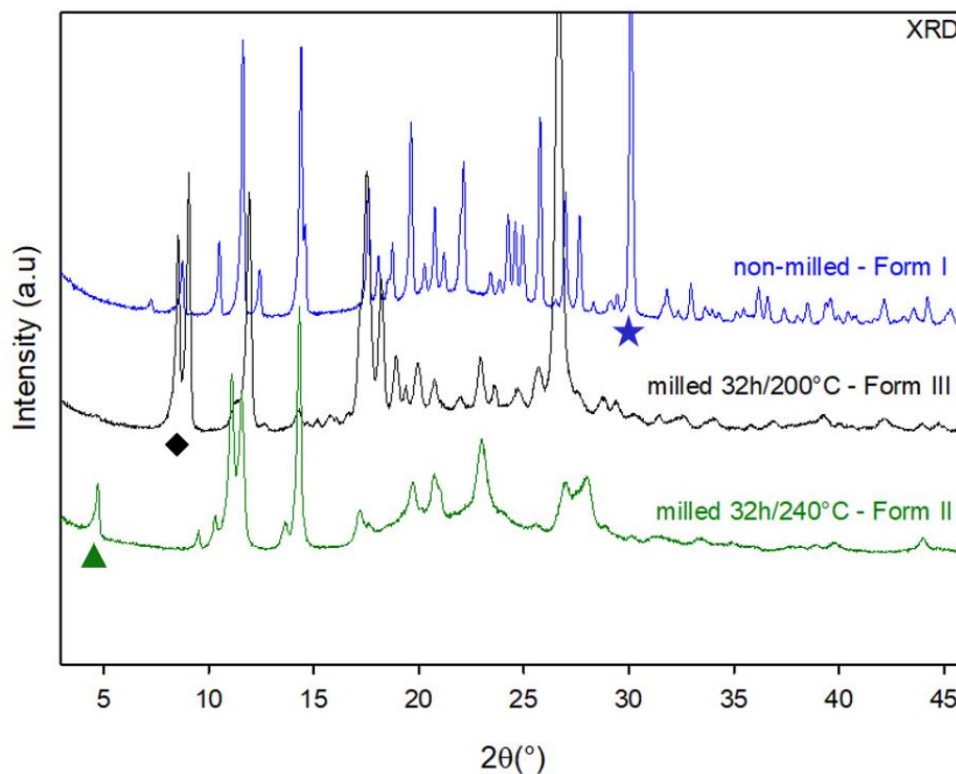
Figure 95 - XRD patterns of riboflavin Form I recorded at room temperature before and after mechanical and thermal treatments. From top to bottom: before milling (Form I, blue curve); after 32 hours of milling and subsequent heating to 200°C (Form III, black curve) and after 32 hours of milling and subsequent heating to 240°C (Form II, green curve).

The second exotherm in run 2 (red curve in Figure 93) occurs at around 230°C (ΔH_2 = 34.1 J/g) and is characteristic of a "crystal to crystal" transformation. As observed in Figure 96, the prior heating of the milling-induced amorphous Rf until complete recrystallization followed by a rapid cooling, still leads to this exotherm of "crystal to crystal" transformation upon heating.
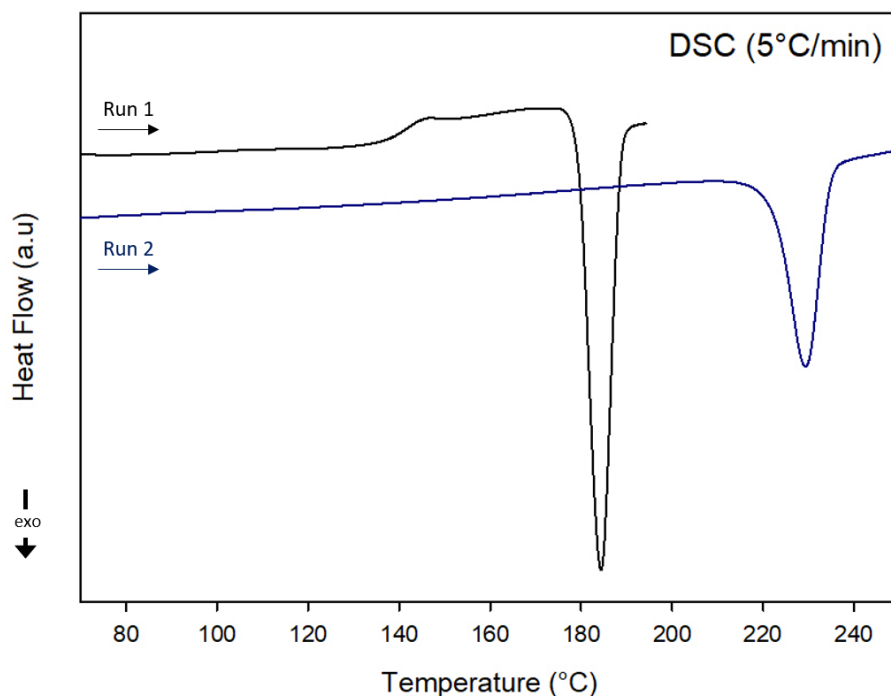
Figure 96 - DSC heating scans (5°C/min) of Rf milled 32h before and after several thermal treatments. Run 1 corresponds to the heating up to 200°C and Run 2 corresponds to the heating of the sample first subjected to a heating to 200°C and subsequent cooling to room temperature (40°C/min).

The diffractogram of the milled material recorded at room temperature after subsequent heating to 240°C (i.e. just above the second exotherm), is also reported in Figure 95 (green curve). It shows again well-defined Bragg peaks, which are different from those of Forms I and III (e.g. peaks marked with a ★, ◆ or ▲ in Figure 95). This confirms that the second exotherm is due to a polymorphic transformation, and put into evidence a further polymorphic form of riboflavin, called "Form II"[184]. Above 240 °C, run 3 (red curve in Figure 93) shows an endothermic peak due to the melting of Form II which is superimposed with an exothermic peak due to the degradation of riboflavin already seen in run 1. It can be noticed that the melting of Form II is depressed compared to the melting of Form I.

166

Figure 97 shows the ^{1}H NMR spectra of both Form II (green curve) and Form III (black curve). They appear to be identical with the spectrum of Form I. However, as for the milled material, an additional peak can be noticed at 2.09 ppm but it is attributed to an acetone residue[154], stemming from the cleaning of the NMR tube. Furthermore, no sign of riboflavin degradation was observed, which indicates that the polymorphic forms of riboflavin can be safely produced by the described milling and subsequent heating procedures.
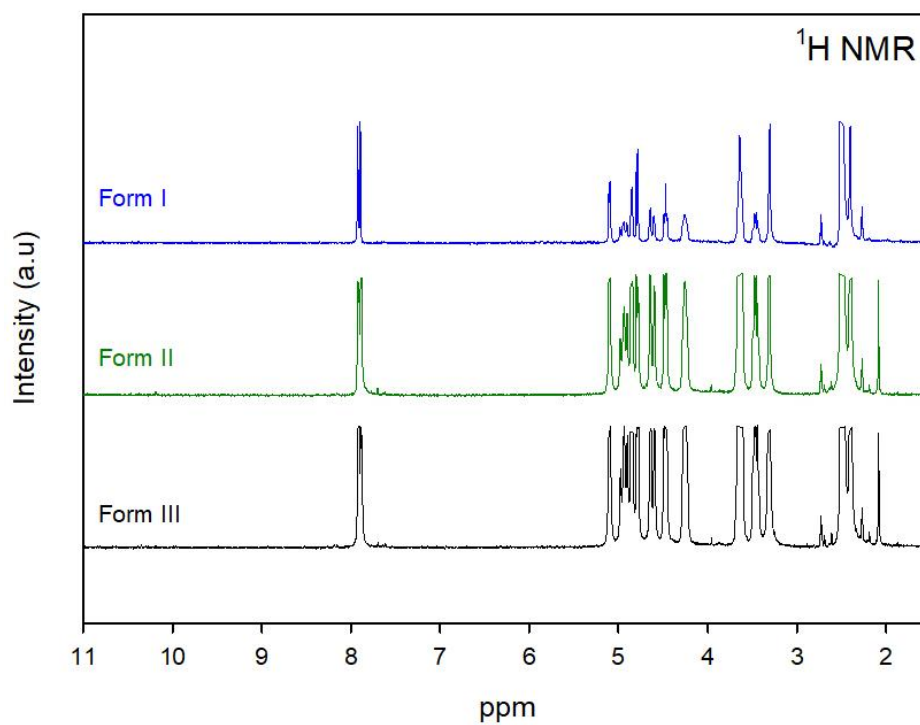
Figure 97 - ^{1}H NMR spectra of riboflavin Form I, Form II and Form III. To better see the small peaks and avoid anarchic superimposition of the different spectra, the highest peaks have been clipped.

The stability at room temperature over time was evaluated using XRD for Forms II and III as illustrated in Figure 98 and in Figure 99, respectively. No significant change can be noticed in the Bragg peaks of either form II or III, which indicate that their physical state was not altered over the 17 days of storage, at RT (humidity not controlled), in the capillary used for the first analysis. It can thus be assumed that in those storage conditions, the polymorphic forms of Rf are relatively stable, at least during 17 days.
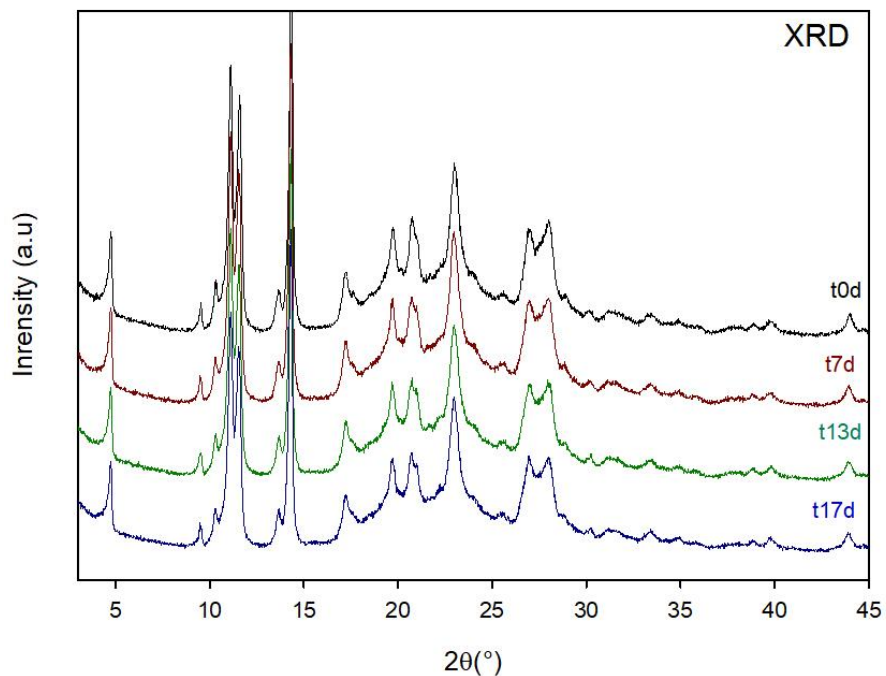
Figure 98 - XRD patterns of riboflavin Form II recorded at room temperature before and after storage at room temperature in the capillary used for the first analysis (t0d). The storage times are indicated on the right-hand side of each curve.
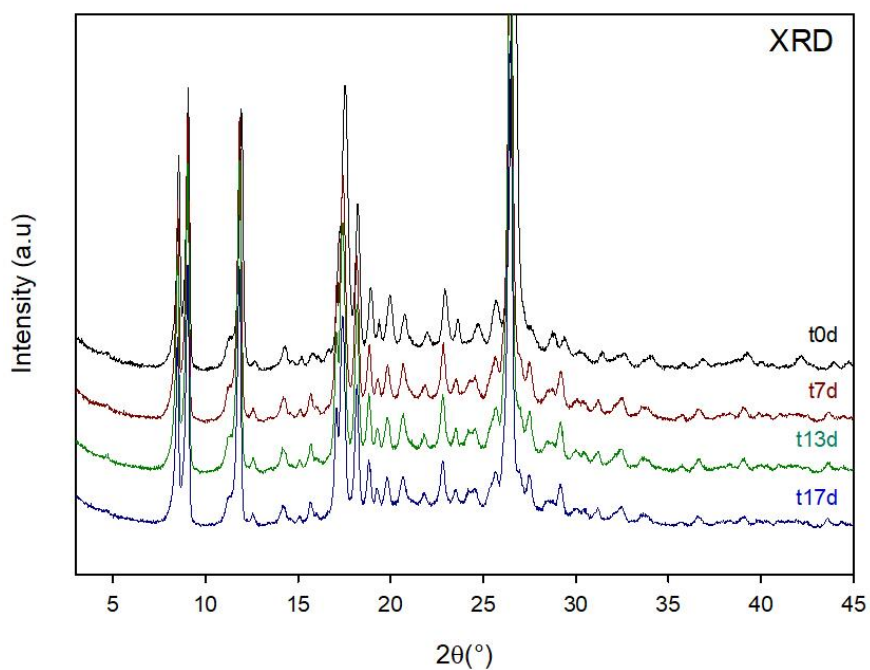
Figure 99 - XRD patterns of riboflavin Form III recorded at room temperature before and after storage at room temperature in the capillary used for the first analysis (t0d). The storage times are indicated on the right-hand side of each curve.

V.1.3 Influence of the milling time on the recrystallization behavior of amorphous riboflavin

Commercial riboflavin (Form I) was milled for different milling times (t_m) ranging from 0 min to 32 h and the corresponding XRD patterns are reported in Figure 100. From 0 min to 3 hours, a progressive flattening and broadening of the Bragg peaks can be observed. The decrease in peak heights indicates the increasing fraction of amorphous material. Meanwhile, the broadening signals both the size reduction and the deformation of the remaining crystallites induced by the mechanical impacts of the milling balls. Besides, it can be observed that after 6 hours of milling, the Bragg peaks totally disappeared, indicating a complete amorphization of the material. No further evolution of the X-ray diffraction patterns can be detected for longer milling times (up to 32 h).
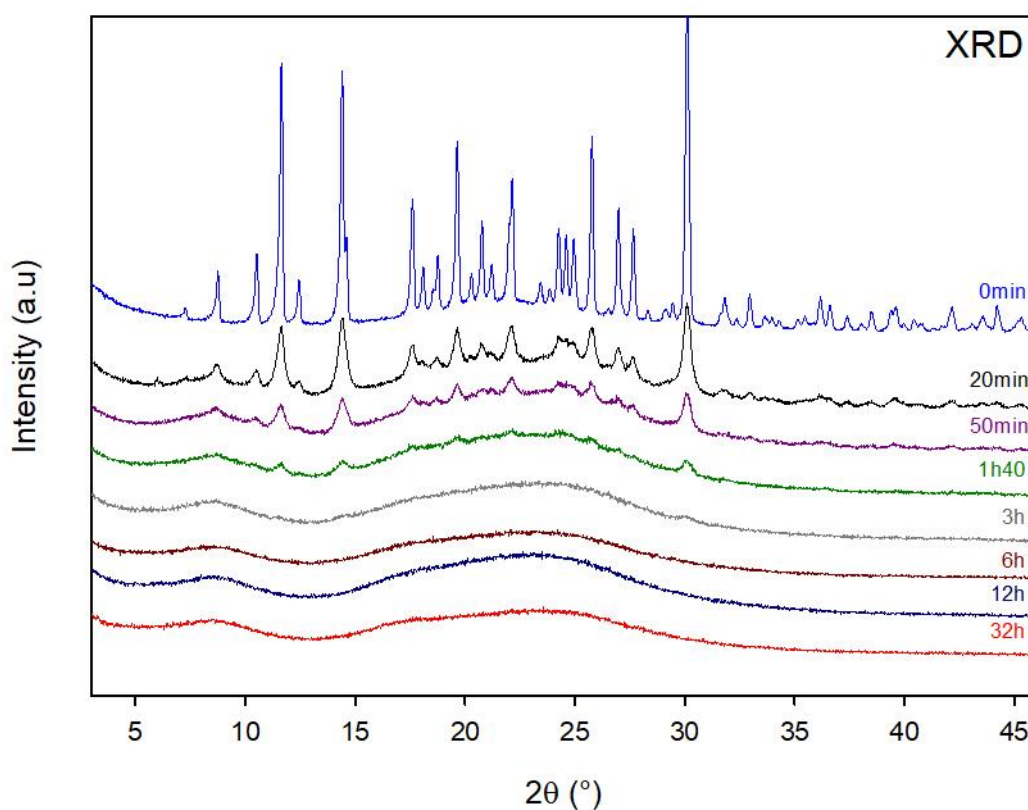
Figure 100 - XRD patterns of riboflavin Form I recorded after different milling times ranging from 0 to 32 h. The milling times are reported on the right-hand side of each curve.

The corresponding heating DSC scans (5 °C/min) are illustrated in Figure 101. They show the progressive development of a Cp jump at the glass transition temperature (Tg = 144°C), followed by a crystallization exotherm. The Cp jump becomes stationary from 6h milling, which confirms that the amorphization upon milling is complete after that time period. However, the evolution of the exotherm appears to be more complex. Indeed, it shows in particular a shift from 160 to 180 °C, which reveals an increasing stability of the amorphous fraction for increasing milling times. Moreover, noticeable modifications of the thermograms are still observed for milling times longer than 6 hours. In particular, a second exotherm develops after the recrystallization. It is already detectable after 3 and 6h of milling through a shouldering on the right-hand side of the recrystallization exotherm and then shifts toward higher temperatures up to 230 °C after 32 h of milling. This exothermic peak clearly corresponds to the polymorphic transformation "Form III → Form II" identified in section 3.2. This indicates, as already observed in the case of sulindac[187], that the structural composition of the recrystallized fraction depends on the milling time. To analyze this point in more detail, the structure of the recrystallized material has been investigated by XRD.
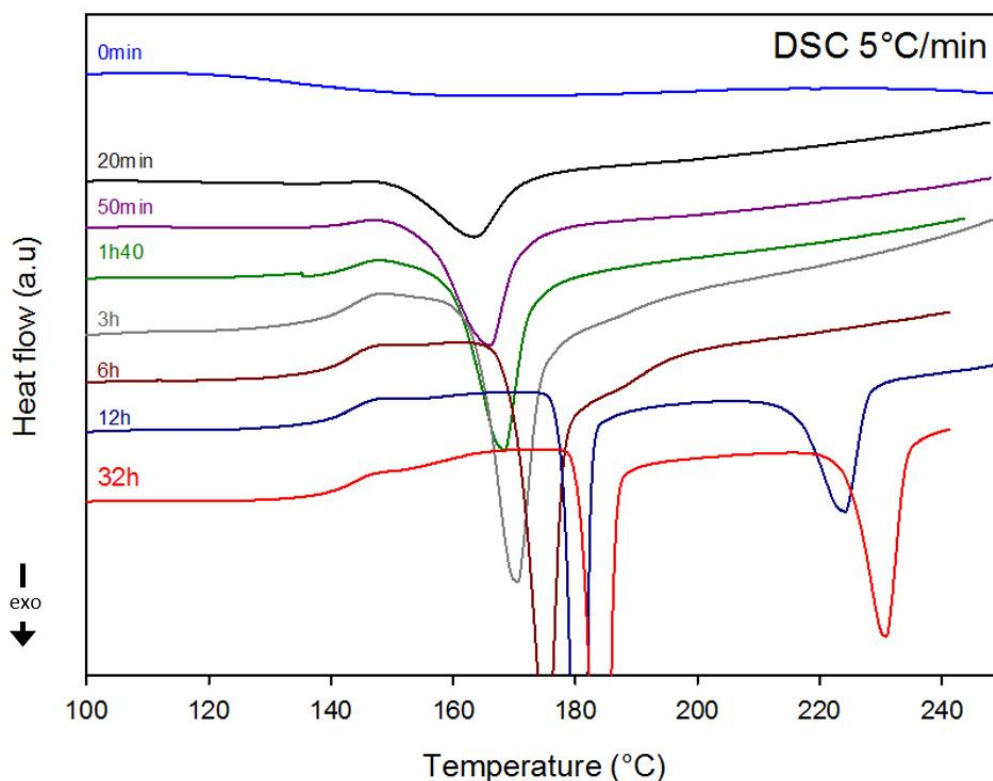
Figure 101 - DSC scans (5 °C/min) of riboflavin Form I recorded after different milling times ranging from 0 to 32 h. The milling times are reported on the left-hand side of each curve.

Figure 102 shows XRD patterns of riboflavin recorded at room temperature after milling for 50 min, 6, 12 or 32 h and subsequent heating (5 °C/min) to 210, 176, 195 and 200 °C, respectively (i.e. after recrystallization of the milled material seen in Figure 101). It shows that for 50 min milling and heating to 210 °C, the X-ray diffraction pattern of the recrystallized material only shows the Bragg peaks of Form I, while Bragg peaks characteristic of Forms II and III cannot be detected. This indicates that, for short milling times, the portion of riboflavin which has been transformed into an amorphous state (Figure 101) recrystallizes entirely towards the initial Form I. This can be explained by the presence of remaining crystallites of Form I after 50 min milling, which act as seeds for the recrystallization of Form I upon heating. This could also be due to a local order of the amorphous fraction reminiscent of the initial Form I, which would be favorable to a recrystallization towards this form. Interestingly, complete amorphization upon milling for milling times > 6 hours and subsequent heating leads to the crystallization of different polymorphic forms.

Indeed, as it can be seen in Figure 102, the X-ray diffraction patterns of the samples, which had been milled for 6, 12 or 32 h, followed by heating to 176, 195 and 200 °C, do not show the Bragg peaks of Form I. Instead, they show the Bragg peaks of the Forms II and III. Moreover, with increasing milling time, the Bragg peaks characteristic of Form III become more pronounced, while those of Form II decrease and finally disappear after 32 hours of milling. This indicates that riboflavin is completely amorphous upon milling for more than 6 hours and recrystallizes as a mixture of Forms II and III, with a proportion of Form III which increases with longer milling time. Such a behavior could be due to the apparent stabilization of amorphous riboflavin with increasing milling times, shifting the recrystallization range toward higher temperatures, at which the nucleation and growth rates of Form III could be higher than those of Form II.
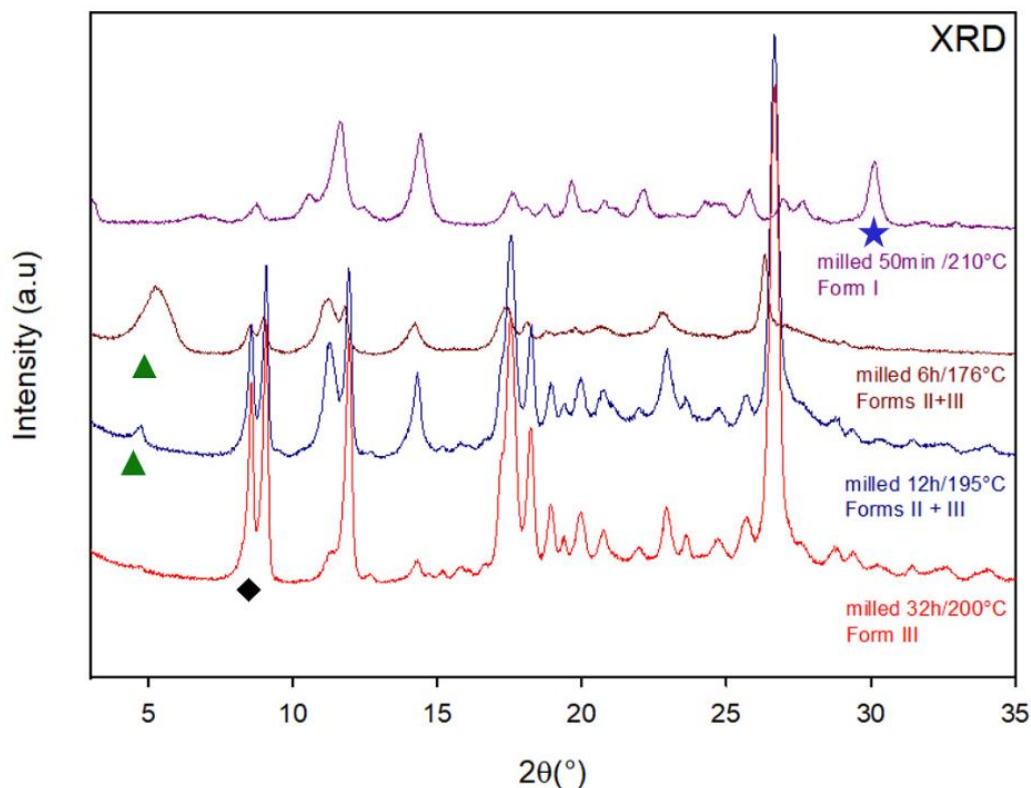
Figure 102 - XRD patterns recorded at room temperature of riboflavin, which had been milled for 50 min, 6, 12 or 32 h, and subsequently heated (5 °C/min) to 210, 176, 195 or 200°C, respectively.

V.1.4 Phase diagram of riboflavin

In order to determine the relative stability of the different forms of riboflavin, it is necessary to rank their melting temperatures. However, as showed on runs 1 and 3 in Figure 93, the melting temperatures of Forms I and II cannot be accurately determined due to the strong degradation accompanying the melting process. Furthermore, as also showed in the run 2 of Figure 93, the melting of Form III cannot be observed as it is preceded by the polymorphic transformation "Form III → Form II". To overcome these difficulties, the three forms have been analyzed by flash DSC at a heating rate of 300 °C/s. Such a high heating rate is expected to avoid the transformation "Form III → Form II" in order to observe the melting of Form III, and to strongly limit the degradation accompanying the melting process. The corresponding scans are reported in Figure 103 and do not show any trace of the transformation "Form III → Form II", nor noticeable degradation. It appears that the melting temperatures of the three forms are ranked as follows: Tm(I)>Tm(III)>Tm(II).
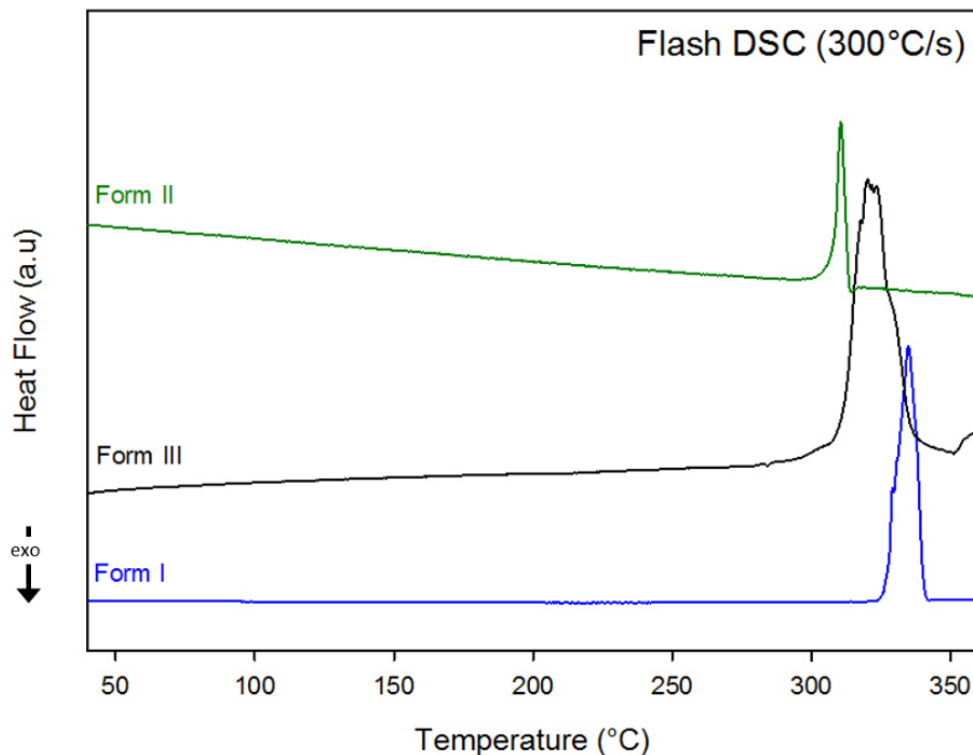
Figure 103 - Flash DSC scans (300°C/s) of riboflavin Form I, Form II and Form III.

Moreover, the exothermic character of the transformation "Form III → Form II" observed in run 2 in Figure 93 indicates that the entropy of Form III is higher than that of Form II. As a result, these two forms are enantiotropically related as schematized in the Gibbs free enthalpy diagram reported in Figure 104. It must be noted that this diagram is not to scale as, due to the close range of the different melting temperatures, there might not be such a difference in Gibbs energy for the polymorphic forms. Furthermore, Form I is monotropically related to Forms II and III and appears to be the most stable solid state at any temperature.
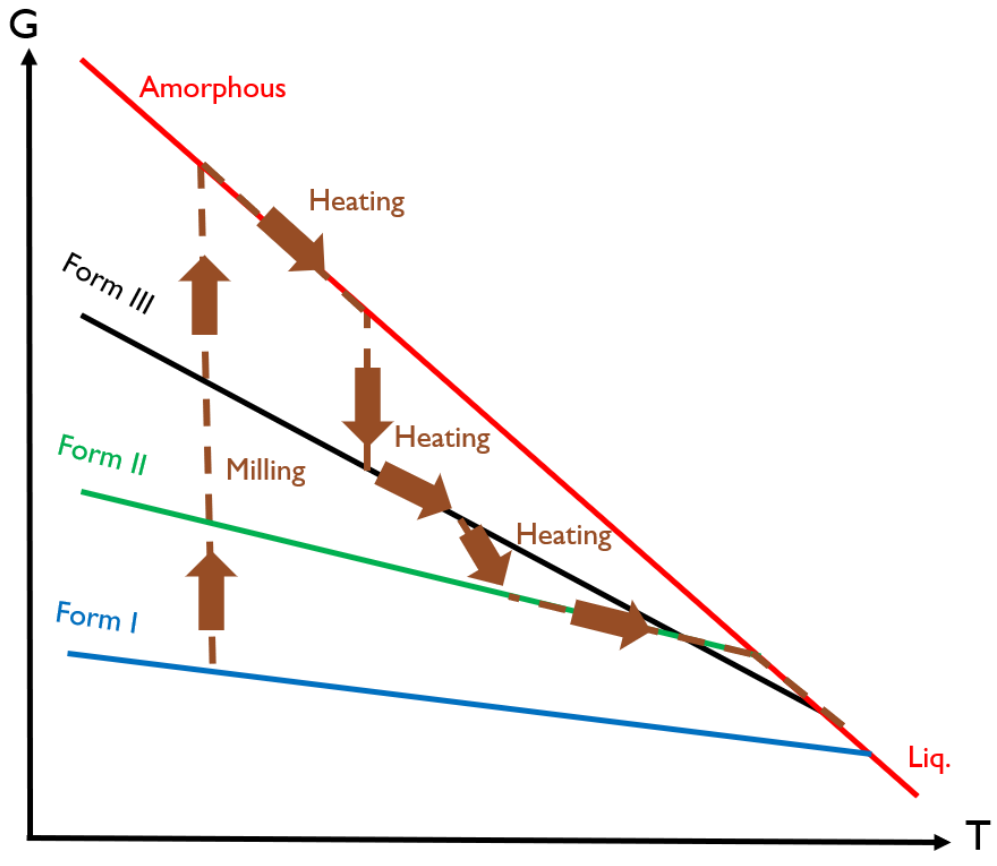
Figure 104 - Phase diagram of riboflavin. The arrows indicate the trajectory of riboflavin during the milling and subsequent heating of Form I.

V.2 Dissolution performances

After a deep physical characterization of the different forms of riboflavin previously highlighted, an evaluation of their dissolution performances in ultra-pure water was performed using different set ups. This investigation was proposed in order to assess the advantage of the amorphous form or of the metastable polymorphic forms compared to commercial riboflavin.

V.2.1 Determination of the solubility limit of riboflavin

First of all, in order to have a good understanding of the behavior of the different forms of riboflavin in water, it was necessary to determine their solubility limit and to evaluate the time frame in which it was reached. To that extend, sufficient sample quantities were required (about 150 mg) as for this experiment, an excess of API is required. Form I was used as received. The amorphous form was obtained by milling of Form I for 32 hours in the high energy planetary mill. Samples of Forms III and II were produced as follows: milling of Form I for 32 hours in the planetary mill, followed by heating in a DSC (5°C/min) Tzero open pan (no lid) to 200 and 250 °C, respectively. This procedure was repeated several times in order to produce the required quantity. The obtained samples were in a form of pellets, which is why they were slightly hand milled and the obtained powders were then pooled.

The dissolution kinetics of these powders in ultra-pure water at 37 °C under non-sink conditions (excess of solid riboflavin) are illustrated in Figure 105. Amorphous riboflavin clearly led to the highest dissolution within the first four hours: up to around 1860 mg/L. But at later time points (after 24 h), this concentration decreased to about 330 mg/L, and then leveled-off. In contrast, Form I was much less soluble (around 90 mg/L) and reached its plateau concentration within the first few hours. Forms II and III reached intermediate concentrations of dissolved riboflavin during the first four hours: about 450 mg/L. But the latter decreased again, reaching plateau values of approximately 350 and 300 mg/L, respectively, after about 7 days. This lowest solubility observed for Form I is consistent with the highest melting point observed by flash DSC (Figure 103).
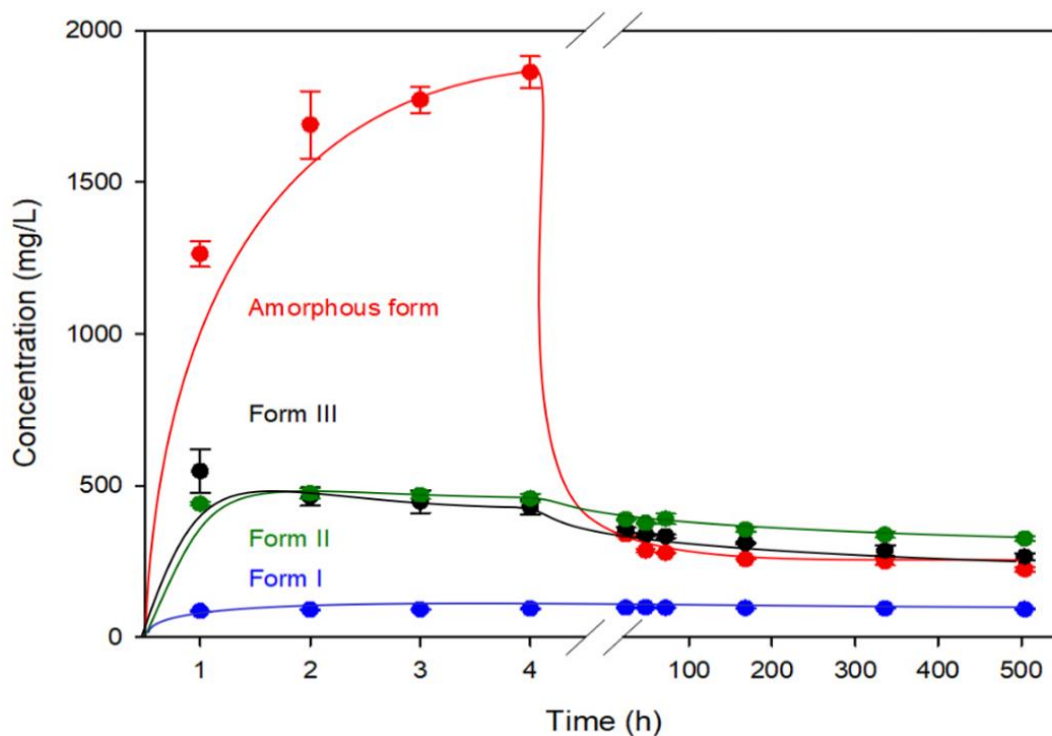
Figure 105 - Dissolution kinetics of the different forms of riboflavin in ultra-pure water at 37°C under agitation (80 rpm) and super-saturation conditions: A large excess of non-dissolved riboflavin was provided throughout the experiments. a guide for the eyes was added for each curve.

From the above results, it appears that the solubility of the different physical forms of Riboflavin can be ranked as follows: amorphous form >> Forms III ≈ Form II > Form I. This ranking matches the Gibbs free enthalpy diagram proposed in the previous section (Figure 104) but it also gives a precision on the close energy levels of Forms II and III as their solubilities are very similar. In addition, for the amorphous form, and also for Forms II and III to a lesser extent, a precipitation occurs between 4 and 24 hours, leading to an effective decrease of the concentration of riboflavin in the solution. Interestingly, the final concentration remains higher than the solubility of Form I which suggests that the precipitation occurs toward a new crystalline form.

To better understand which riboflavin form crystallizes during the dissolution measurements, the solids obtained after 7 days were separated by filtration, dried (under vacuum, room temperature, overnight) and analyzed by XRD and TGA.

Figure 106 shows the XRD pattern of the residue obtained after 7 days in water of amorphous riboflavin. Interestingly, it differs from those of Forms I, II and III (see for instance the peak at 4.3 ° marked with a ●), but seems to be similar to that of a dihydrate reported in the literature[184]. It must be noted that this X-ray pattern corresponds to the residual solid obtained from the amorphous riboflavin but identical diffractograms were observed for Forms II and III (data not shown).
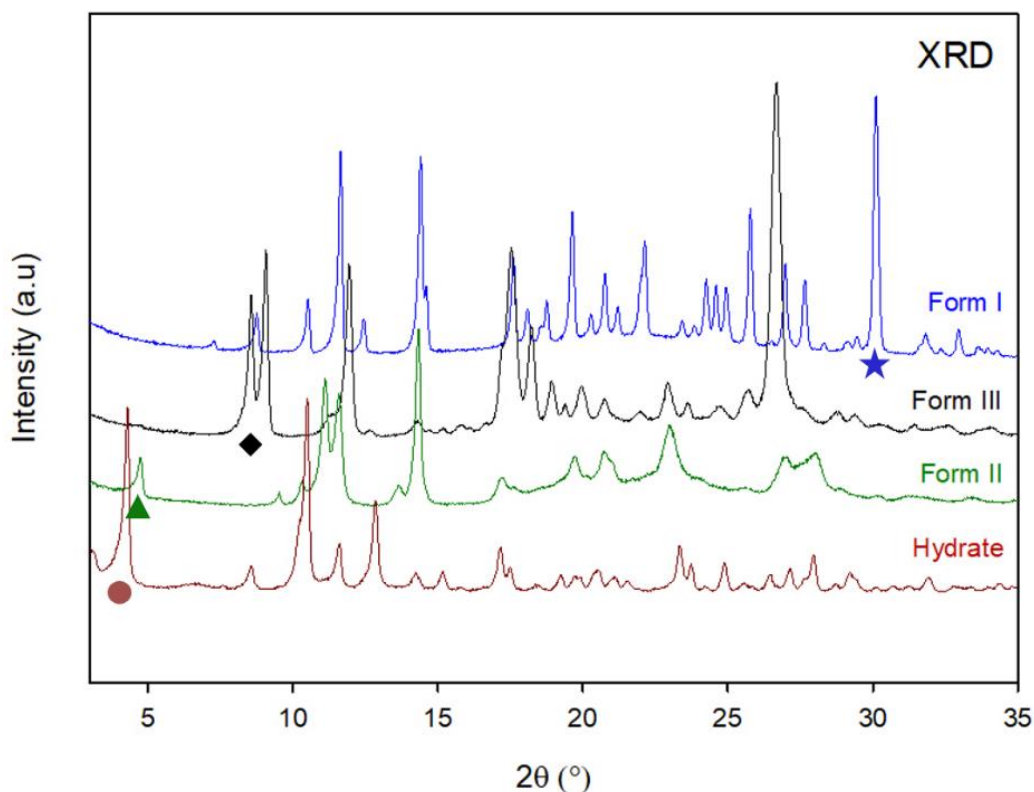
Figure 106 – XRD patterns of riboflavin form I recorded at room temperature before and after several treatments. From top to bottom: before milling (Form I, blue curve); after 32 hours of milling and subsequent heating to 200°C (Form III, black curve), after 32 hours of milling and subsequent heating to 240°C (Form II, green curve) and after 32 hours of milling followed by 7 days spent in ultra-pure water heated to 37°C and stirred at 80rpm (brown curve) subsequently dried under vacuum at room temperature.

The TGA scan (5 °C/min) of the residue, which is reported in Figure 107, shows a mass loss close to 6% between 20 and 80 °C, while a mass loss of 9.2 % would be expected for the dehydration of a dihydrate. The difference may be attributed to a slight dehydration occurring during the vacuum drying prior to TGA analysis.
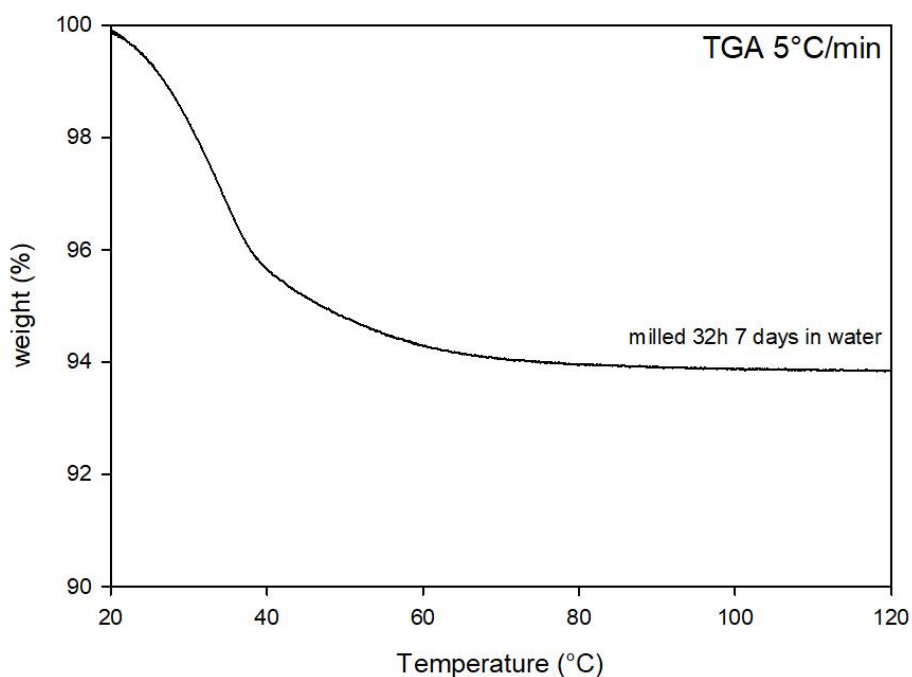
Figure 107 - TGA scan (5 °C/min) of the reprecipitated solid from the amorphous riboflavin during the dissolution study.

The evolution of the diffractogram of the recrystallized solid upon heating (5 °C/min) to 60 °C – i.e. in the temperature range in which the water loss was observed – is reported in Figure 108. It shows the progressive appearance and disappearance of some Bragg peaks, which ultimately leads to the X-ray diffraction pattern characteristic of Form II. All these results indicate that the amorphous riboflavin, dissolved in water, recrystallized toward a dihydrate form, whose dehydration upon heating led to the metastable anhydrous Form II. The precipitation of the same dihydrate form upon dissolution of amorphous riboflavin and Forms II and III can explain the similar plateau values observed at late time points for these different forms.
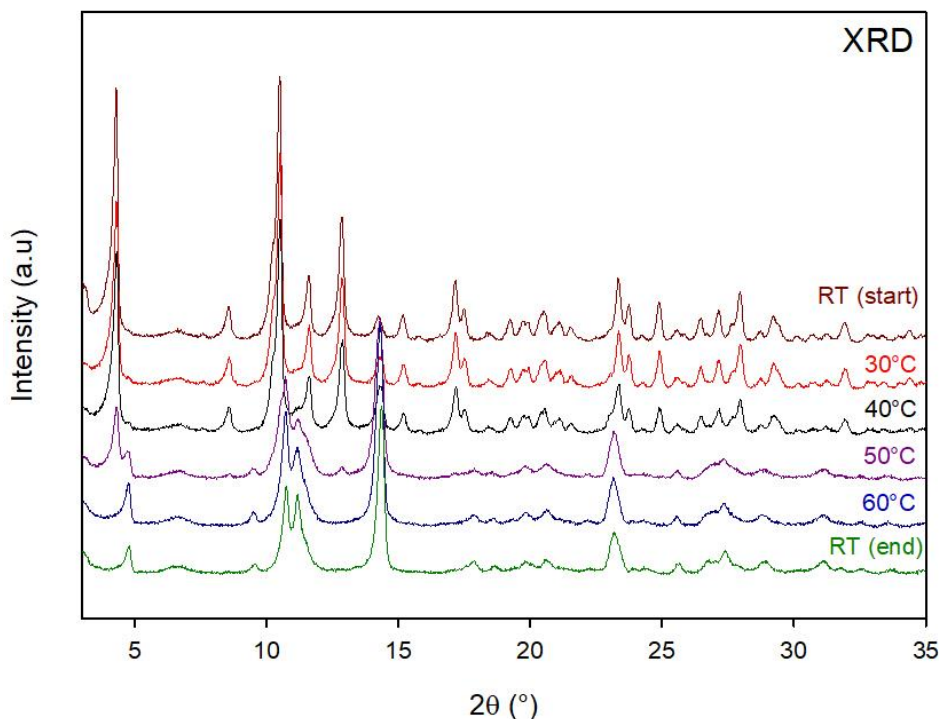
Figure 108 - XRD patterns of the solid which reprecipitated during the dissolution study of amorphous riboflavin in water. The samples were heated at 5 °C/min followed by an isothermal of about 13 min (scan duration) at different temperatures (as indicated).

V.2.2 Powder dissolution in sink and non-sink conditions

Compared to the solubility experiment presented in the previous section, Forms II and III were prepared differently. Indeed, as the heating in the DSC pan was very time consuming, a tubular oven was used instead. More precisely, around 700mg of amorphous riboflavin (previously milled for 32 hours) was spread and wrapped in aluminum foil which was placed inside the oven and heated to the required temperature. Afterwards, the aluminum was recovered and the powder was gently milled using a pestle as it tends to form aggregates upon heating, and the powder was collected.

Figure 109 illustrates the dissolution kinetics of the different forms of riboflavin in ultra-pure water in sink conditions, i.e. for an amount of API at least 3 times below its solubility limit.

All the forms show a biphasic dissolution profile as they show a steep slope followed by a decrease in the dissolution rate until reaching 100% of riboflavin dissolved after 24 hours of dissolution. However, if the dissolution rates seem to be similar between the amorphous form and forms I and III, Form II shows

a significantly slower dissolution rate. Furthermore, during the first hour (highlighted on the insert in Figure 109), significant gaps in the amount of riboflavin dissolved can be noticed between the different forms, which seem to be ranking as follows: Form I > Amorphous form > Form III >> Form II. Concerning the metastable forms, this ranking once again matches the Gibbs free enthalpy diagram previously stated (Figure 104). On the contrary, Form I shows an unexpected quicker dissolution which, in addition, does not match the dissolution kinetics of the solubility experiment.

Figure 109 - Dissolution kinetics over 24 hours of the different forms of riboflavin in a large volume of ultra-pure water (800mL) heated at 37°C under stirring (100 rpm) and in sink conditions. The insert highlights the first hour of this same experiment.

As the particles size and shape can significantly influence the dissolution of the API, SEM pictures of the different powders used for dissolution testing were taken and are depicted in Figure 110. Amorphous riboflavin and Form I powders consisted of tiny particles. The amorphous particles formed aggregates while those of Form I were needle-shaped. In contrast, the particles of Form II and Form III were much larger, because they were prepared by manual milling (versus planetary milling). But at higher magnification, also in these cases, tiny needle-shaped crystals could be observed. The particles of Form I thus appears to be the smallest compared to the ones of the metastable forms, which explains the fact that their dissolution is quicker.
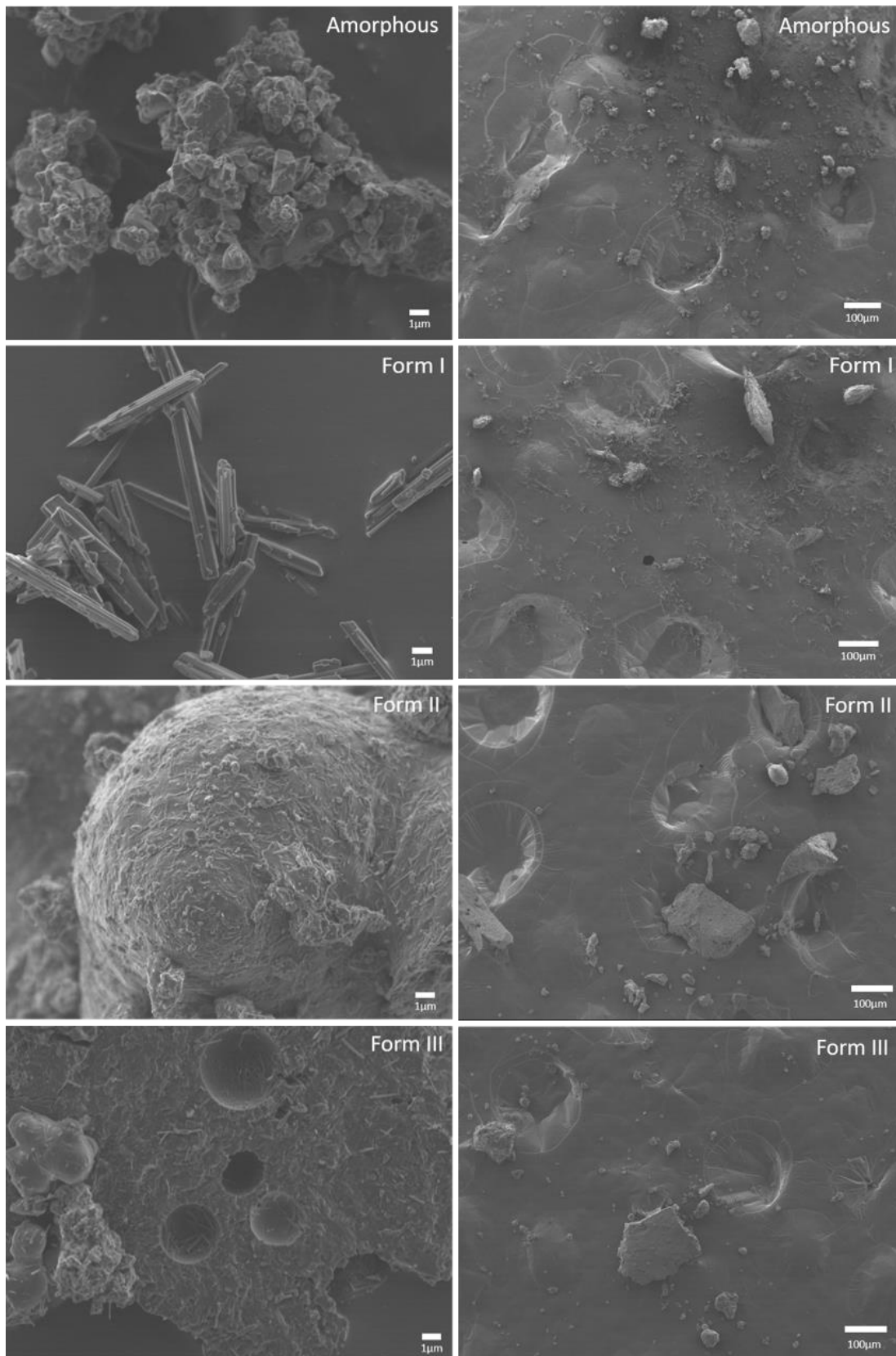
Figure 110 - SEM pictures of the different riboflavin powders used for dissolution measurements.

This indicates that, in the previous case of a super-saturated solution (Figure 105), the ratio of the small needle-shaped crystals of either form II or III was higher compared to the powder dissolution in sink conditions that it hindered the effect of the particle size, whereas it was not sufficient in this dissolution set up.

Figure 111 illustrates the dissolution kinetics of the different forms of riboflavin in ultra-pure water in non-sink conditions. It must be noted that in this case, only the solubility limit of Form I was exceeded, which explains why it only reached 43% as it approximately corresponds to this limit. In this dissolution set up, only the amorphous form reached 100% of riboflavin dissolved after 24 hours of dissolution. Regarding the amount of riboflavin dissolved during the first few minutes, the different forms can be ranked as follows: Amorphous form > Form III > Form II > Form I, which is consistent with the Gibbs free enthalpy diagram. In comparison with the sink conditions, the small size of the particles of Form I was not sufficiently impactful to allow it to surpass the dissolution rates of the polymorphic forms. Interestingly, after 20 minutes, Form III shows a drop in the amount of riboflavin dissolved which would be characteristic of a recrystallization. This could be due to the fact that according to the Gibs free enthalpy diagram, Form III is the less stable polymorphic form. In addition, it seems to drop until it reaches the curve of Form II, which could suggest that it could transform into Form II during the dissolution in non-sink conditions. Thus, it would mean that the recrystallization of the metastable forms into the hydrate form of riboflavin, in the same time frame, must occur only in the case of a super-saturated solution. Finally, in this dissolution set-up, the advantage of the amorphous form is clearly demonstrated compared to the other crystalline forms.
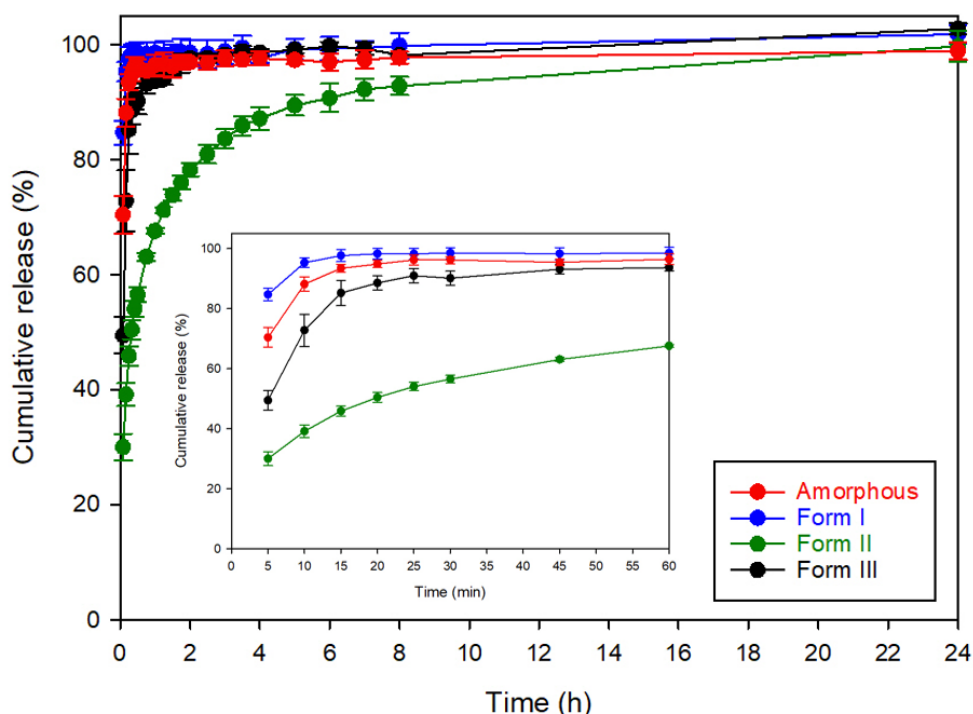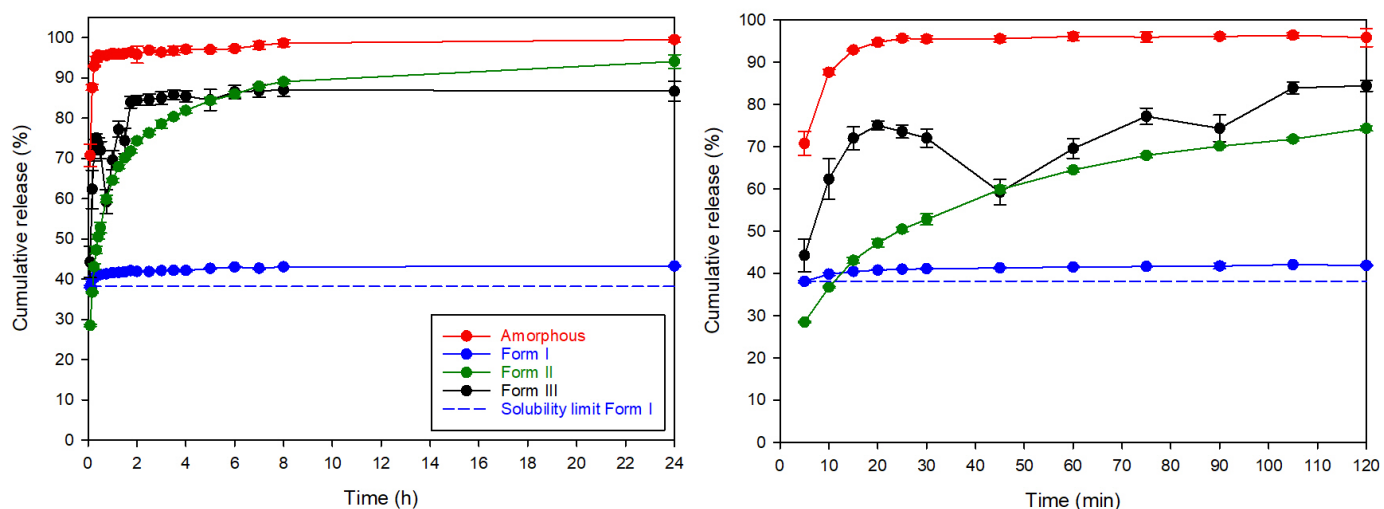
Figure 111 - Dissolution kinetics of the different forms of riboflavin in a large volume of ultra-pure water (800mL) heated at 37°C under stirring (100 rpm) and in non-sink conditions. The figure on the left shows the 24 hours of experiment and the figure on the right highlights the first two hours of this same experiment.

V.2.3 Intrinsic dissolution

In order to hinder the influence of the particle size and shape, the intrinsic dissolution set up was used on all the forms of riboflavin.

First of all, the influence of the compaction on the physical state of the different forms was evaluated. For this study, the compacts were prepared using the exact same protocol as for the intrinsic dissolution (compaction at a 2t force). However, after the compaction step, instead of screwing the holder, the metallic plate was unscrewed and the compact was taken out of the die by strongly pressing on the punch. After this manipulation, the compact was found to be intact and was therefore analyzed using XRD. Afterwards, pieces were cut in order to perform both the DSC and the TGA analysis.

Figure 112 and Figure 113 show the X-ray diffraction patterns before and after compaction of both crystalline (Form I) and milling-induced amorphous Rf and of its polymorphic forms (II and III), respectively. It is clear that after compaction of Form I, the Bragg peaks present on the X-ray pattern are those characteristics of Form I before compaction. However, some differences in intensities or in peak resolution can be noticed (e.g. around 18°, around 21° and around 25°), which are attributed to the preferential orientation of the crystal particles during the compaction. The same observations can be noticed for Forms II and III which show the Bragg peaks characteristic of their respective forms after

compaction. Regarding the milling-induced amorphous form of Rf, no Bragg peaks are visible on the X-ray diffraction pattern after compaction, which indicates that the material remained amorphous after this process. Such a stability upon compression of the amorphous form could be surprising without any stabilizing agent but it was already observed in the case of Chx and for other materials compacted for intrinsic dissolution studies[163].
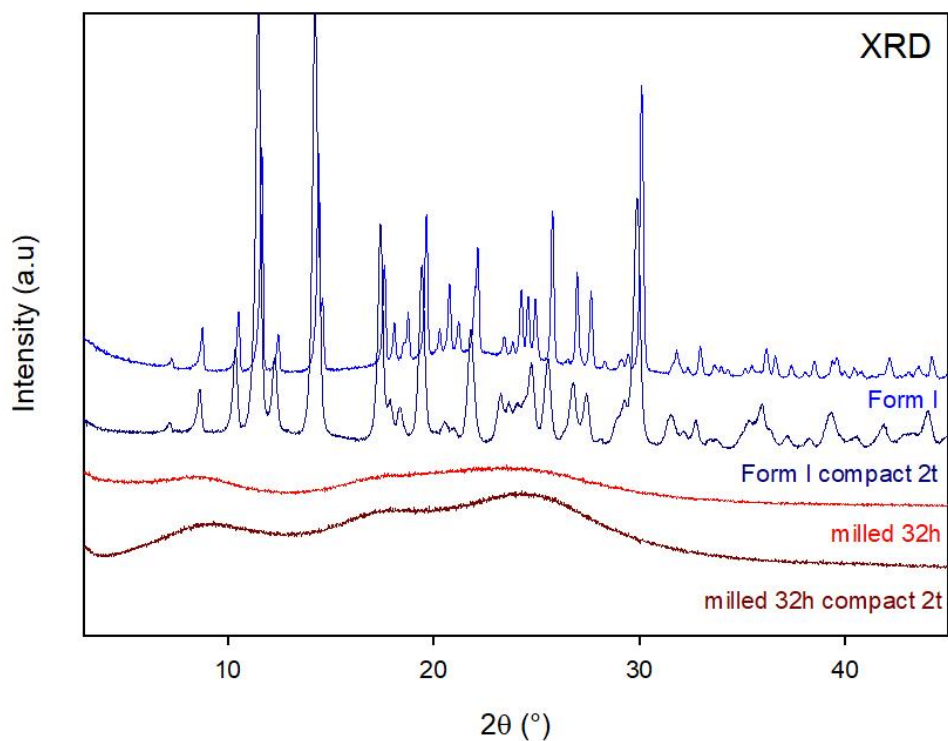
Figure 112 - X-ray diffraction patterns recorded at room temperature of crystalline (Form I) and amorphous (milled 32h) Rf before and after compaction.
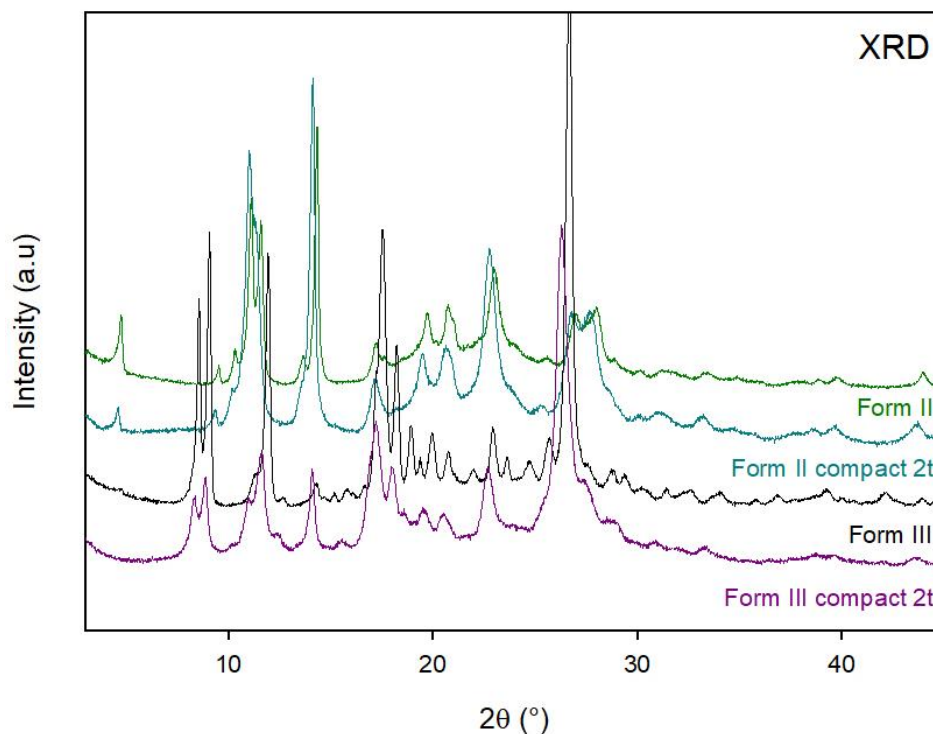
Figure 113 - X-ray diffraction patterns recorded at room temperature of the polymorphic forms of Rf (II and III) before and after compaction.

Figure 114 shows the DSC heating scans of milling-induced amorphous riboflavin before compaction, after compaction and after compaction followed by hand-milling. As nothing in particular was observed during the heating of the crystalline forms of Rf, only the data corresponding to the amorphous form is showed in this section. After compaction, a Cp jump suggesting a glass transition is observed (Tg = 124°C) and is significantly depressed compared to the one of the amorphous Rf before compaction (Tg = 144°C). Furthermore, as the same 20°C depression is observed for the recrystallization exotherm, it strongly corroborates the fact that the Cp jump observed is due to the glass transition. As mentioned in the case of Chx, (Chapter III, section III.2.3), such a behavior could either be due to a lack of conductivity in the compacted material due to the thickness of the sample or to an entrapment of free water absorbed during the milling process which could not be evaporated in the case of the compacted material.

It can also be noticed that the recrystallization pattern is different compared to the non-compacted milled material. Indeed, two exotherms are observed, suggesting a recrystallization in two steps, first of the surface and secondly of the volume[30], which would indicate a lack of thermal conductivity in the compact. However, despite heating up to a temperature higher than Tg but lower than the recrystallization exotherm onset, the Tg of the compact remained 20°C depressed compared to the non-

185

compacted milled material (data not showed). This observation strongly suggests that even if the Tg was reached, the molecular mobility did not increase sufficiently to allow the compact to be in a liquid/glassy state and thus to restore the conductivity.

Finally, the compact of amorphous Rf was hand-milled and heated using the DSC. The corresponding scan represented in Figure 114 shows a Cp jump characteristic of a glass transition at Tg = 141°C which is similar to the one of the non-compacted milled material.

Figure 115 shows the TGA scans (5°C/min) of the milling-induced amorphous Rf before and after compaction and also after compaction followed by a hand-milling. In the milled material (non-compacted), 4.2% of weight loss is observed up to 100°C, which is attributed to the departure of free water caught by the sample during the milling. However, after compaction of this milled material, only a weight loss of 0.3% is observed in the same range of temperatures. Meanwhile, after compaction followed by hand-milling, a weight loss of 3.2% is observed in the same range of temperatures. These results suggest that the water absorbed by the milled material is entrapped in the compact and thus have difficulty to evaporate upon heating, which would explain the depressed Tg observed.
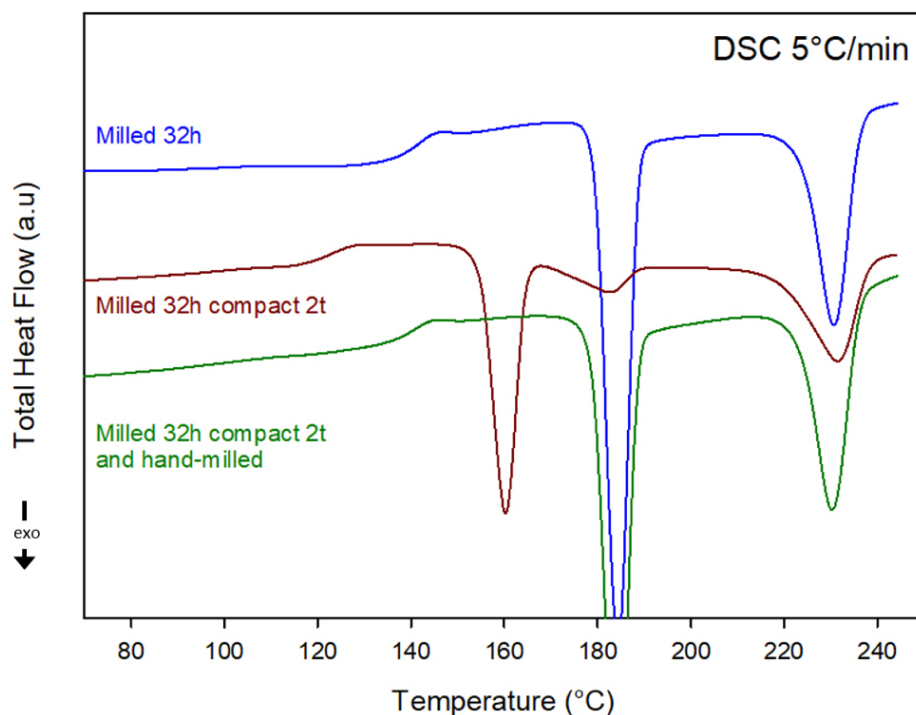
Figure 114 - DSC heating scans (5°C/min) of amorphous (milled 32h) Rf before, after compaction and after compaction and hand-milling.
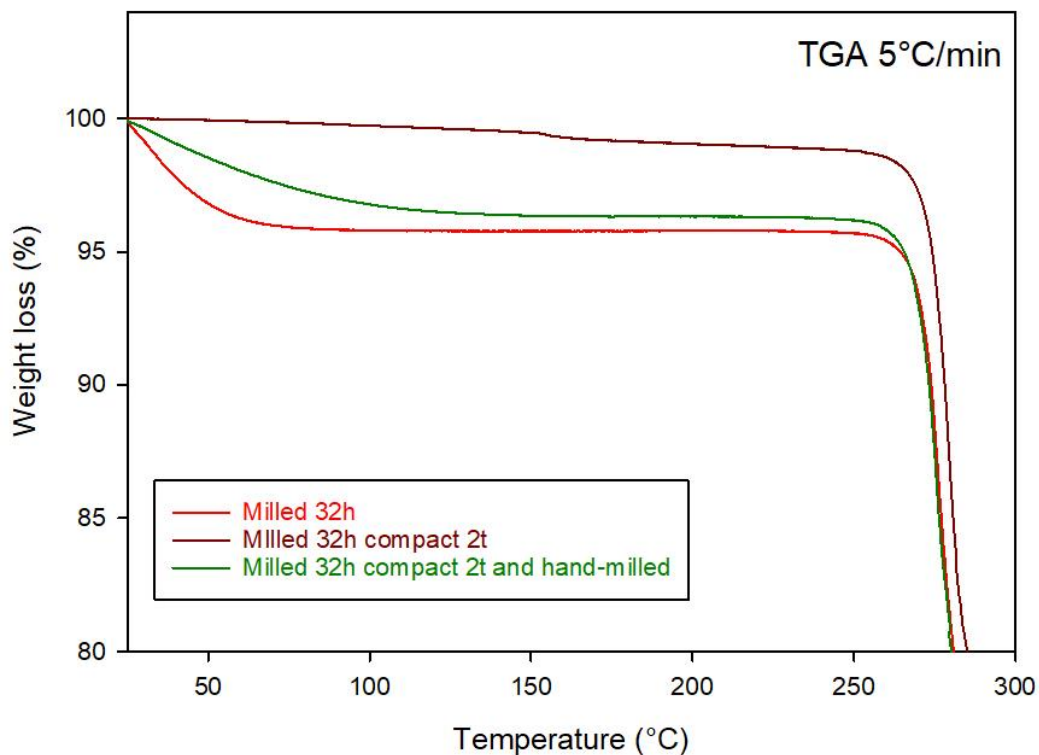
Figure 115 - TGA heating scans (5°C/min) of amorphous (milled 32h) Rf before, after compaction and after compaction and hand-milling.

The dissolution profiles of all forms are illustrated in Figure 116, except for Form III which could not be represented. Indeed, this form (all triplicates) did not hold into a compact as soon as it came in contact with the dissolution media, which made the measurements inaccurate and thus impossible to determine its dissolution rate. Indeed, as observed in the case of paracetamol[188], different polymorphic forms are not all suitable for direct compression due to lower resistance to mechanical stress. It must also be noted that in order to fulfill the intrinsic dissolution conditions, the results must appear as a linear curve which usually results in an amount of compact dissolved not exceeding 10%. In this particular case, the amorphous form was the limiting factor as it no more respected this condition after 3 hours of dissolution.
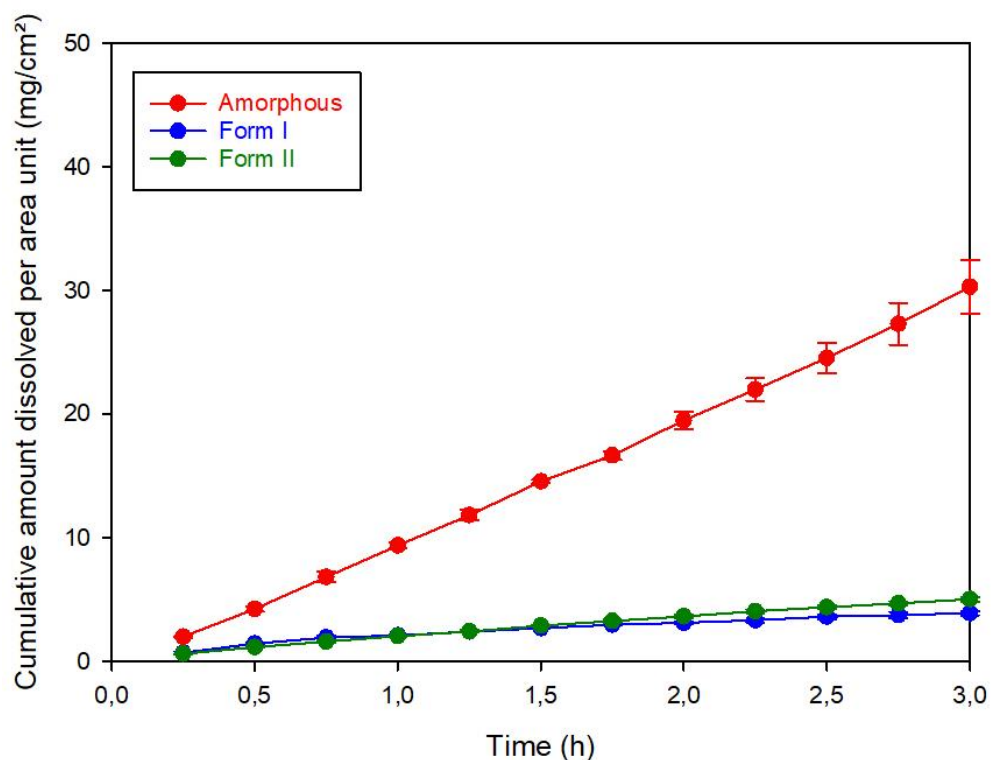
Figure 116 - Dissolution kinetics of the intrinsic dissolution of the different forms of riboflavin in ultra-pure water (400mL) heated at 37°C under stirring (50 rpm).

Interestingly, as soon as the particle size and shape have no influence, Form I and II show an almost identical dissolution rate as it was evaluated to 1.1 ± 0.07 mg/cm²/h and 1.6 ± 0.03 mg/cm²/h, respectively. In comparison, the amorphous form increased the dissolution rate of riboflavin of almost a tenfold as it reaches 10.2 ± 0.08 mg/cm²/h. It is thus clear that in this dissolution set up as well, the amorphous form shows a significant advantage compared to the crystalline forms.

Conclusion

In this chapter it was showed that amorphous riboflavin could be obtained for the first time by solid state amorphization of the crystalline Form I using high energy ball milling. The glass transition temperature (Tg = 144°C) and the Cp jump at Tg (ΔCp= 0.68 J/g/°C) could, hence, accurately and for the first time be determined. Upon heating, amorphous riboflavin was found to show a rich pattern of physical transformations, which enlightens the polymorphism of this vitamin. It shows in particular a recrystallization toward Form III, followed by a polymorphic transformation toward Form II occurring at 230°C (ΔH$_2$ = 34.1 J/g). These two forms appear to be enantiotropically related and the relative stability of the three polymorphs at room temperature appears to rank as the following: I > II > III.

Regarding the dissolution kinetics, the first set up (super-saturated solution) revealed the following order in the dissolution rates during the first 4 h: amorphous>Forms III ≈ Form II>Form I. After 4 h, a drop in the amount of dissolved riboflavin occurred for the amorphous and metastable crystalline forms due to a recrystallization toward a dihydrate. However, the plateau values were still above the solubility of Form I, revealing definitely the faster dissolution of the metastable forms (II, III and amorphous) over the stable crystalline Form I.

The dissolution kinetics in the sink conditions highlighted the influence of the particle size and shape as it revealed another order in the dissolution rates over the first hour: Form I > Amorphous form > Form III >> Form II. However, after 24 hours of dissolution, all the forms reached 100% of riboflavin dissolved. Meanwhile, the dissolution in the non-sink conditions was not as affected by the particle size and shape as similarly to the super-saturated solution experiment, the amorphous form showed a significant faster dissolution and the dissolution rates ranked as follows: Amorphous form > Form III > Form II > Form I. This order showed a complete adequation with the Gibbs free enthalpy diagram designed.

Finally, the intrinsic dissolution method allowed to confirm the fastest dissolution of the amorphous form compared to the crystalline forms. However, no distinction in the dissolution rate could be made between forms I and II. In addition, it allowed to gain knowledge on the ability of the different forms to hold in the form of a compact during the dissolution experiment. Between all the forms, only form III, the least stable polymorph, disintegrated as soon as it came in contact with the dissolution medium.

CHAPTER VI –

CO- AMORPHIZATION OF

RIBOFLAVIN UPON MILLING

As demonstrated in the last chapter, milling-induced amorphous Rf is highly prone to recrystallization upon heating. As amorphous are usually not formulated as such, polymers were added in order to stabilize the amorphous form and to enhance even greatly the dissolution performances of Rf.

To that extend, the same polymers as presented in Chapter IV, were selected for this purpose, i.e PVPK12 and Lycoat RS 720. In this particular case, due to the high glass transition temperature of Rf (Tg = 144°C), PVPK12 will have a plasticizing effect on the API whereas the Lycoat will keep its anti-plasticizing role.

The objective of this chapter is first to investigate on the potential co-amorphization of Rf free base with these polymers and then to perform a detailed physical characterization of the different molecular alloys for various fractions of Rf in the mixture.

Secondly, for specific Rf/polymer mixtures the dissolution kinetics are determined in order to evaluate the influence of the physical state of the API in drug/polymer mixtures and to assess the advantage of the co-milled mixture compared to a physical mixture containing either amorphous or crystalline Rf.

Finally, a comparison between the two polymers is also performed in order to determine the most suitable one to enhance the dissolution performances of this API.

VI.1 Physical characterization of riboflavin-polymer mixtures

The objective of this section is first to investigate on the potential co-amorphization of riboflavin with two different polymers including PVPK12 (plasticizer) and Lycoat RS 720 (anti-plasticizer) and then to perform a detailed physical characterization of the various molecular alloys obtained to have a clear understanding of the behavior of riboflavin in such a mixture.

VI.1.1 Co-amorphization with a plasticizing polymer, the case of PVPK12

This section tests the possibility to produce amorphous molecular alloys of Rf and PVPK12, which appears here to act as a plasticizing excipient since its glass transition temperature is lower than the one of Rf. First of all, the suitable milling protocol was determined in order to perform the co-amorphization of riboflavin and PVPK12 for different fractions of riboflavin in the mixture. Then, the evolution of the Tg of the molecular alloy with the composition was evaluated and the solubility of riboflavin in the polymer was determined.

(1) Milling time required for complete co-amorphization

Figure 117a shows the X-ray diffraction patterns of physical mixtures of riboflavin and PVP K12 (50:50, w/w) recorded after several co-milling times including 0, 3, 10 and 12 hours. For comparison, the X-ray patterns of pure PVP and of pure amorphous riboflavin (obtained by milling Form I during 12 hours) are also shown. Before milling, the diffractogram of the physical mixture shows Bragg peaks related to the crystalline Form I of riboflavin, which superimpose to a small halo of diffusion due both to the amorphous PVP and to the Lindemann's capillary. Upon milling the Bragg peaks progressively vanish until complete disappearance after 12 hours of milling. This indicates that riboflavin has been totally amorphized by the milling process.
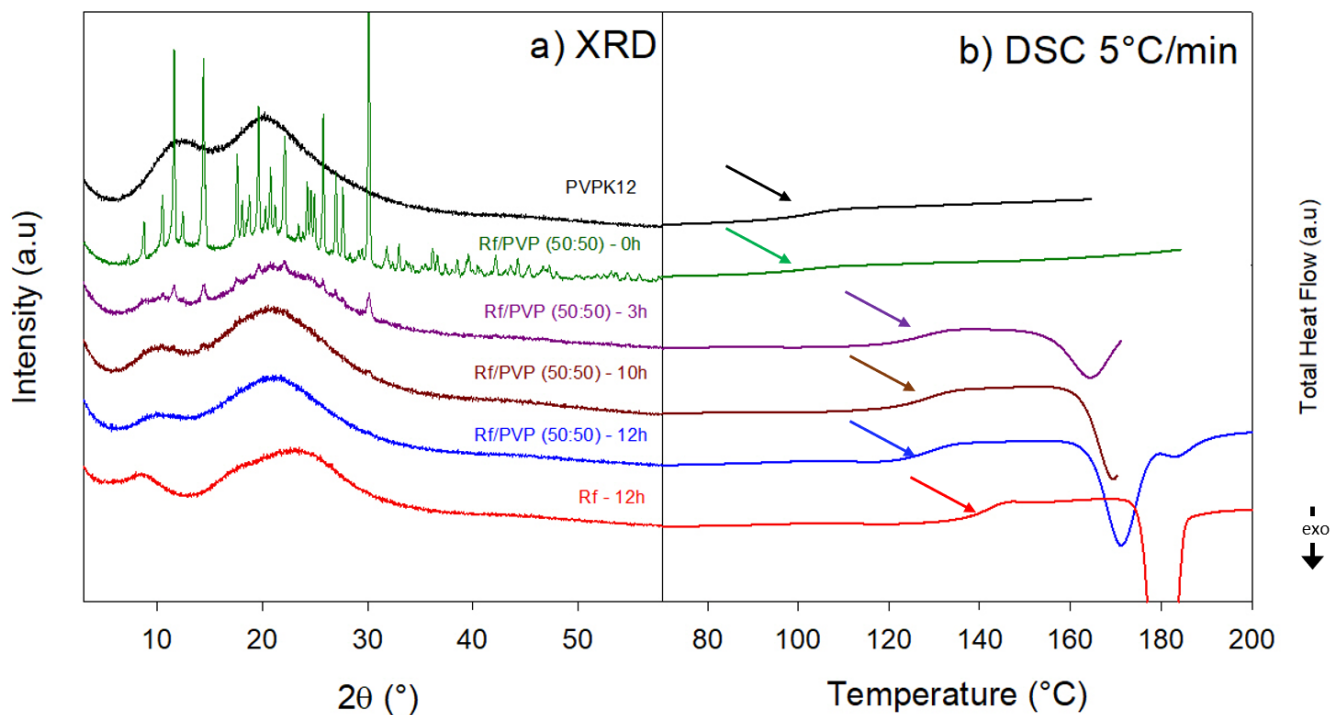
Figure 117 - a) XRD patterns, and b) DSC scans (5°C/min) of pure PVP K12 (black), of pure Rf milled for 12 hours (red) and of a Rf/PVP mixture (50:50) (w/w) recorded after several milling times (0h, green; 3h, purple; 10h, brown and 12h, blue). The arrows indicate the position of the Tg on each curve.

Figure 117b shows the corresponding DSC heating scans (5°C/min). Before milling, the scan of the physical mixture only shows the glass transition of pure PVP (Tg = 103.4°C). For increasing milling times, a single Cp jump is observed, with a position which shifted towards the higher temperatures. This reveals a progressive and homogeneous co-amorphization of the drug and the polymer and confirms the expected plasticizing effect of PVP whose glass transition temperature is much lower than that of Rf. It can be noticed that the Tg value obtained after 3, 10 and 12 hours of co-milling are very close (around 129°C) indicating that most of the co-amorphization process occurs during the first 3 hours of the 12 hours milling process. However, it can be noticed the exotherm of recrystallization, in the case of the mixture co-milled 3h, seems to occur at a slightly lower temperature compared to both mixtures co-milled during either 10 or 12h. This observation indicates that the molecular mobility in the mixture co-milled 3h is higher at a given temperature compared to the mixtures co-milled 10 or 12h. However, it seems more difficult to point out differences between the mixture co-milled 10h and the one co-milled 12h using the DSC, even though the XRD clearly revealed a complete co-amorphization only for the

mixture co-milled 12h. These results are a clear example of the need to combine these complementary techniques, as already reported in the literature[189].

It must also be noted that the fully co-amorphized sample obtained after 12 hours of milling shows a strong recrystallization above Tg. The enthalpy of recrystallization (ΔH = 32.2 J/g), when compared to that of pure amorphous riboflavin (ΔH = 58.2 J/g – cf section V.1.2), corresponds to approximately 55% of recrystallized Rf. As the mixture contained 50% of Rf, this means that all of the Rf in the mixture recrystallized. It can thus be deduced that the co-milled material is highly supersaturated and already suggests that the solubility of riboflavin in the PVP is quite weak.

(2) Evolution of the Tg for various compositions of the Rf/PVP mixture

The co-milling of riboflavin and PVPK12 was performed for different compositions of the mixture. Figure 118 shows the X-Ray diffraction patterns of Rf/PVP mixtures of several compositions recorded after 12 hours of co-milling. For comparison, the X-ray patterns of pure PVP and of pure amorphous riboflavin (obtained by milling Form I during 12 hours) are also shown. It appears that for all the mixtures containing 50% of riboflavin or more, no Bragg peaks could be detected, indicating a complete amorphization of riboflavin during the 12 hours milling. However, it can be noticed that for 10%, 20% and 40% of riboflavin in the mixture, very small Bragg peaks are still visible on the diffractogram (e.g. at 30°). This indicates that after the co-milling applied, very small crystallites of riboflavin remained in the mixture and that 12 hours of milling is thus not sufficient to amorphize completely mixtures containing less than 40% of Rf. Such a behavior could be explained by the fact that for small fractions of riboflavin in the mixture, the drug is imbedded into the polymer. As a result, the PVP endures most of the impacts induced by the milling balls and absorbs shocks on the remaining crystallites, thus slowing down the amorphization kinetics of riboflavin.
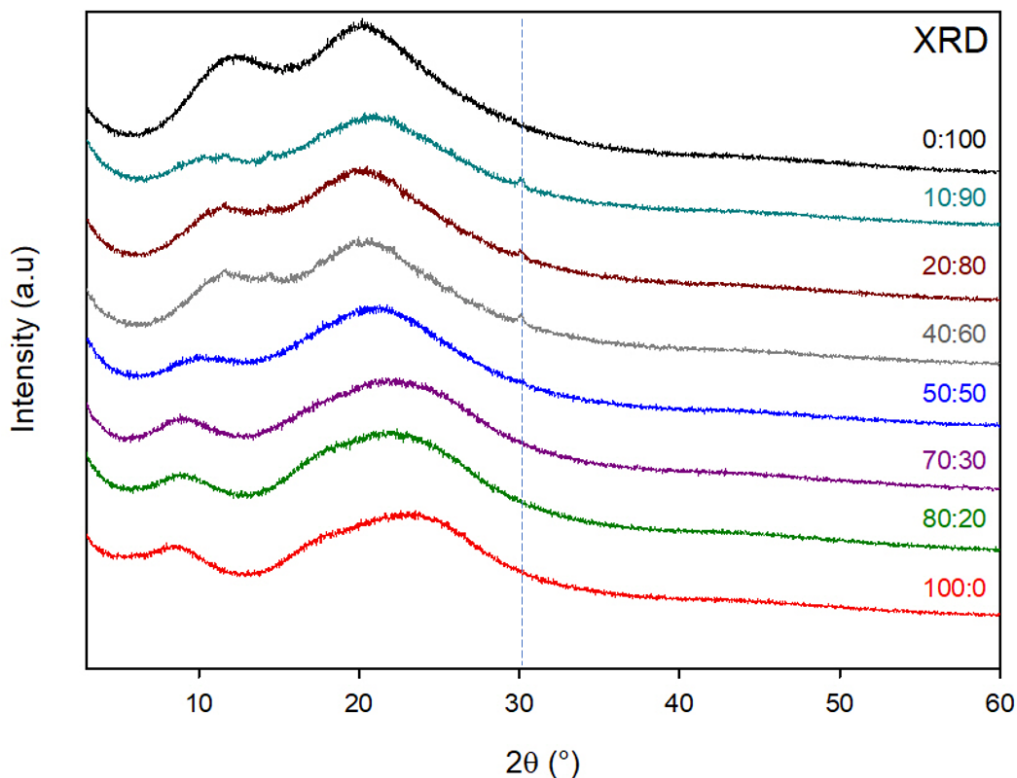
Figure 118 - X-Ray diffraction patterns of Rf/PVP mixtures of different compositions, milled for 12 hours. The compositions (Rf/PVP, w/w) are reported on the right-hand side of each curve. Pure PVPK12 (black) and pure amorphous Rf (obtained by 12h milling, red) are also reported for comparison. The vertical dashed line marks the position of the most intense Bragg peak of crystalline Rf.

The DSC scans corresponding to the mixtures containing 50% or more of riboflavin co-milled during 12 hours are reported in Figure 119. For comparison, the scans of pure PVP and of pure amorphous riboflavin (12 hours of milling) are also shown. It can be noticed that in each case, a single Tg is observed indicating that a homogenous co-amorphous mixture has been obtained. We can also notice that the Cp jump at Tg is preceded by slight and broad exotherm which indicates that milling has produced glasses of very high enthalpic level[178]. Furthermore, with increasing the riboflavin fraction, the position of this Tg shifts towards the higher temperatures which reconfirms the anti-plasticizing effect of riboflavin in the drug/polymer mixture. It must be noticed that for each composition of the mixture, an exotherm of recrystallization can be observed after the Tg. This indicates that despite the co-amorphization with PVP, and thus having amorphous Rf molecularly dispersed in the polymer matrix, the amorphous riboflavin is still not stable upon heating. Moreover, with increasing the PVP fraction, the Tg of the co-milled mixture

decreases which allows an increase in the molecular mobility and thus diminishes the physical stability. However, it can be noticed that Tgs of the co-milled mixtures remain relatively high (> 120°C) which suggests that Rf could remain kinetically stable in the amorphous state.
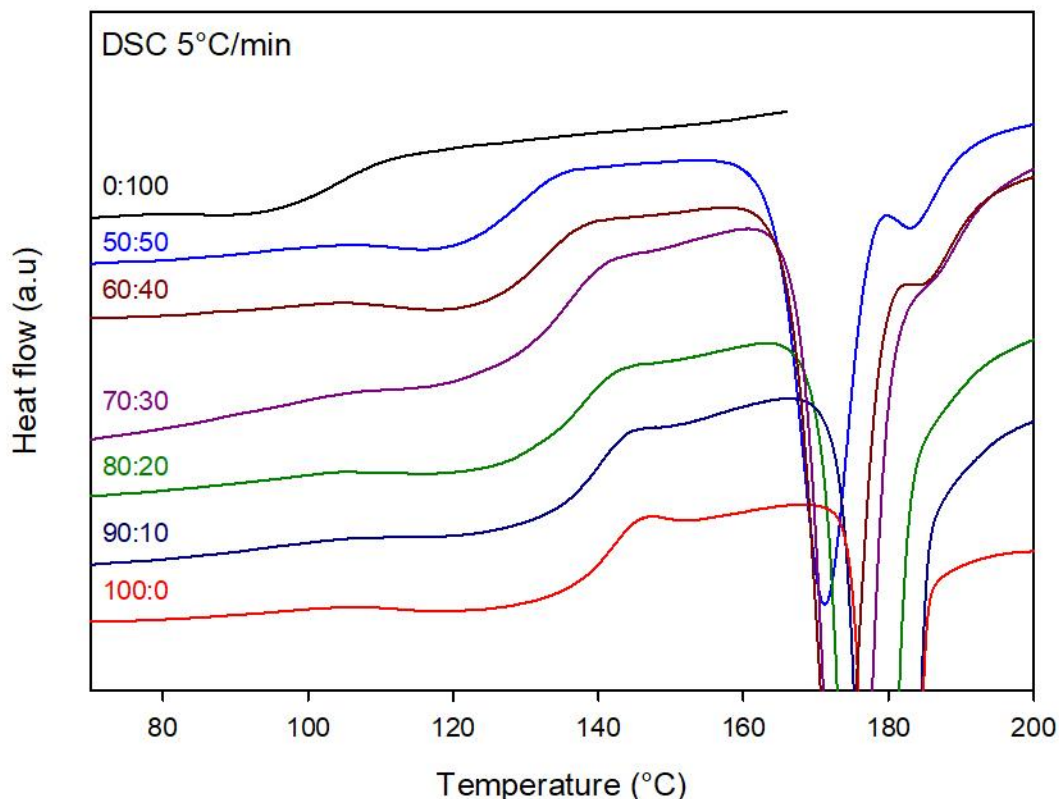
Figure 119 – DSC scans (5°C/min) mixtures of Rf/PVP mixtures of different compositions, milled for 12 hours. The compositions (Rf/PVP, w/w) are reported on the left-hand side of each curve. Pure PVPK12 (black) and pure amorphous Rf (obtained by 12h milling, red) are also reported for comparison.

The evolution of the Tg of the alloy (obtained from Figure 119) with the composition is reported in Figure 120. The solid line represents the best fit of the classical Gordon-Taylor law[117] (Equation 15, Chapter I, section I.4.1) to the experimental data (represented in black dots) and a rather good agreement was obtained. The coefficient K which defines the curvature of the evolution, was determined and the value obtained was K = 0.54. The red dashed line corresponds to the theoretical curve of an ideal Rf/PVP mixture for which K is given by the ratio of the amplitudes of the Cp jumps at Tg of the two pure compounds[117]: (Equation 16, Chapter I, section I.4.1):

$$K = \frac{\Delta Cp_{PVP} \ (0.36 \ J/g/°C)}{\Delta Cp \ _{Rf}(0.62 \ J/g/°C)} = 0.58$$

This fit appears to be very close to the experimental data obtained. This suggests that the interactions between the riboflavin molecules and PVP are minimal or even inexistent in the amorphous alloy.
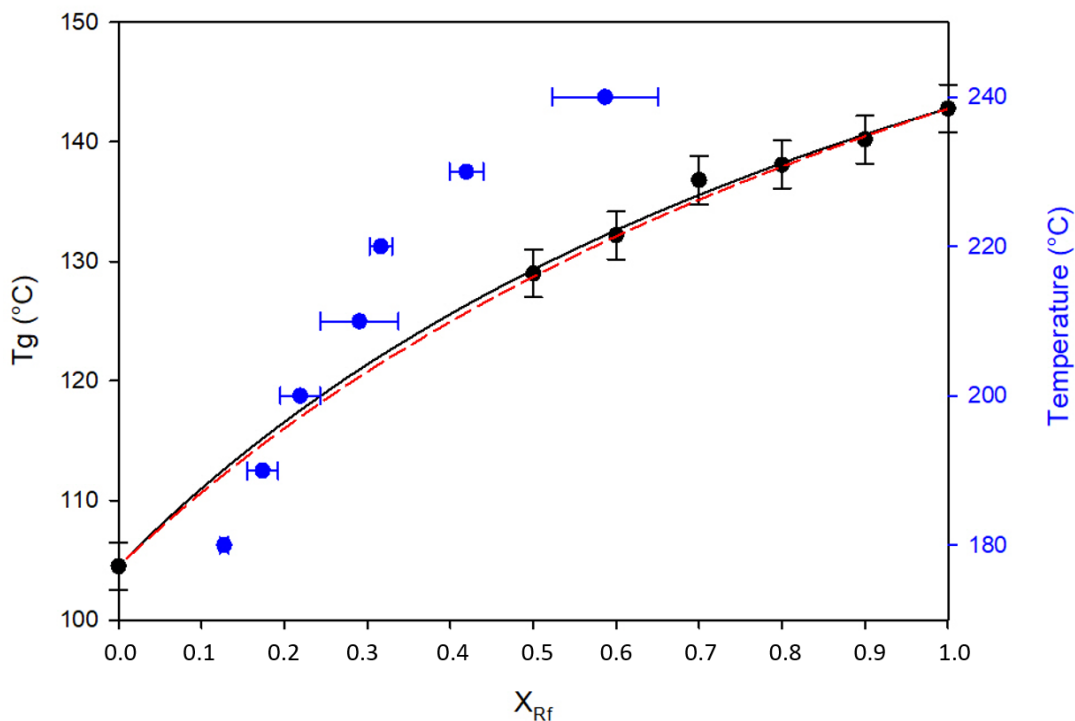
Figure 120 - Black dots represent the evolution of the Tg of the co-milled $(Rf)_x(PVPK12)_{1-x}$ binary mixtures against the Rf fraction x (right axis). The black solid line represents the best fit of the Gordon Taylor equation to the experimental data and the dashed red curve represents the theoretical fit of the Gordon Taylor equation for an ideal mixture. It must be noted that an estimated error on the Tg of 2°C has been added in order to consider both the eventual Tg measurement error induced by the exotherm observed before the Cp jump and the eventual approximation on the composition of the mixture. The blue dots indicate the experimentally measured solubility of Rf in PVPK12 at different temperatures (right y-axis).

(3) Determination of the solubility of riboflavin in PVPK12

To experimentally determine the solubility of Rf in PVP at different temperatures, a specific thermal treatment was applied on a physical mixture of Rf and PVP as shown in Figure 121. The Rf/PVP mixture (e.g. 80:20, w/w) was repeatedly scanned (5 °C/min) by DSC. For each heating, the final temperature was increased by 10 °C compared to the previous one and a 20min annealing was performed to allow the dissolution of Rf into PVP in order to reach equilibrium solubility at this temperature. After each annealing, the sample was cooled down to 20 °C as fast as possible to avoid any recrystallization of the fraction of Rf dissolved in PVP during the previous annealing.
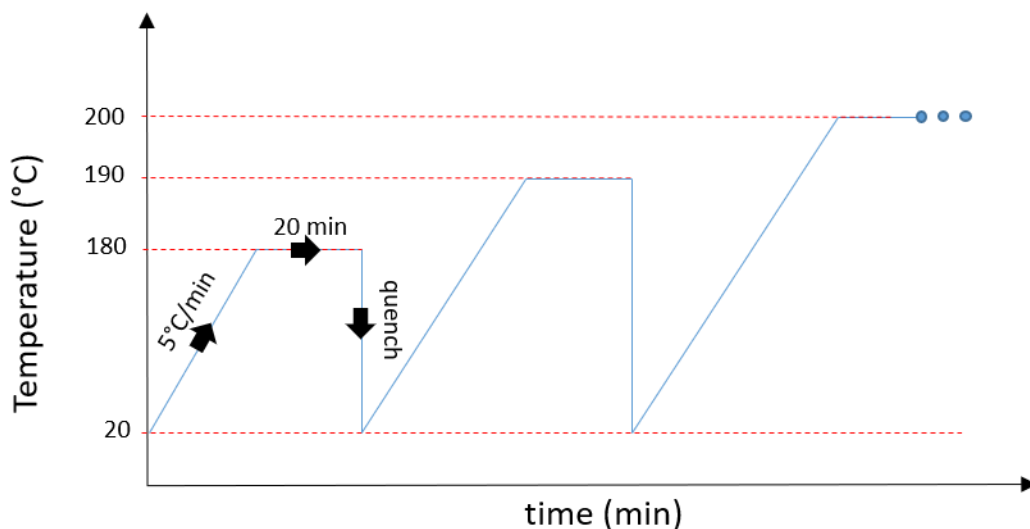
Figure 121 - Scheme of the thermal treatment used to determine the solubility curve of riboflavin in PVP.

This experiment was conducted for three different compositions of the physical mixture (e.g. 60:40, 70:30 and 80:20, w/w) to assess the reproducibility. Figure 122 shows the DSC scans recorded after the annealing performed at different temperatures ranging from 180 °C to 240 °C for the sample 80:20 (w/w). All thermograms show a Cp jump corresponding to the glass transition of the molecular dispersion ("glass solution"). This Cp jump shifts towards higher temperatures for increasing annealing temperatures which reveals an increasing dissolution of Rf into the PVP matrix. It has been checked that longer annealing stages do not lead to higher glass transition temperatures which proves that the 20 mins annealing performed at each temperature is long enough to reach the equilibrium solubility at this temperature.

By measuring the Tg, and using the Gordon-Taylor fit showed in Figure 120 as a calibration curve, the solubility of riboflavin in PVPK12 at each annealing temperature could be determined. These solubility points are also reported in Figure 120 (blue curve and blue y-axis). According to these results, the solubility of the riboflavin in PVPK12 appears to be very poor as it barely reaches 13% at 180°C, which indicates that it is even more extremely poor at room temperature. Therefore, the co-amorphous mixtures studied are unstable as they are highly super-saturated. However, as previously mentioned, these mixtures exhibit high glass transition temperatures which should lead to a kinetic stability.
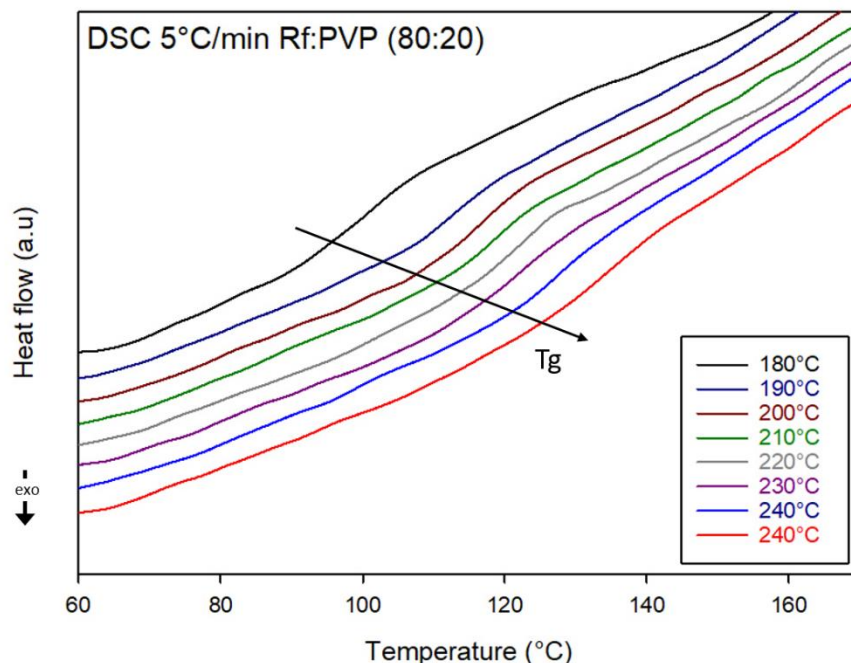
Figure 122 - heating DSC scans (5°C/min) of a physical mixture of riboflavin and PVKK12 80:20 (w/w) recorded after successive 20 min. annealing at increasing temperatures as sketched in figure 121. The annealing temperatures are reported on the right-hand side of the figure.

VI.1.2 Co-amorphization with an anti-plasticizing polymer, the case of Lycoat RS 720

This section tests the possibility to produce amorphous molecular alloys of Rf and Lycoat RS720 which appears here to act as an anti-plasticizing excipient. The same milling time as used for Rf/PVPK12 mixtures was applied. Then, the evolution of the Tg of the molecular alloy was evaluated and the Tg of the polymer was determined. Finally, a focus was performed on 3 different mixtures in order to investigate on the behavior of riboflavin in such the mixture.

(1) Co-amorphization of Rf/Lycoat mixtures

As it was demonstrated in the previous section that 12 hours of milling were sufficient to obtain a homogenous co-amorphous mixture of riboflavin and PVPK12, the same milling time was applied for the different mixtures containing riboflavin and Lycoat. Figure 123 shows the X-Ray diffraction patterns of Rf/Lycoat mixtures of several compositions recorded after 12 hours of co-milling. For comparison, the X-ray patterns of pure Lycoat (non-milled) and of pure amorphous riboflavin (12 hours of milling) are also shown. It can be noticed that for each composition of the mixture (from 20% of riboflavin to 80%), no Bragg peaks can be detected on the X-ray diffraction patterns which indicates the complete amorphization of riboflavin in each mixture. This situation contrasts with the case of PVP, for which the co-amorphization was not total for Rf concentration smaller than 50%. It thus appears, that the coamorphization of Rf is easier with lycoat than with PVP.
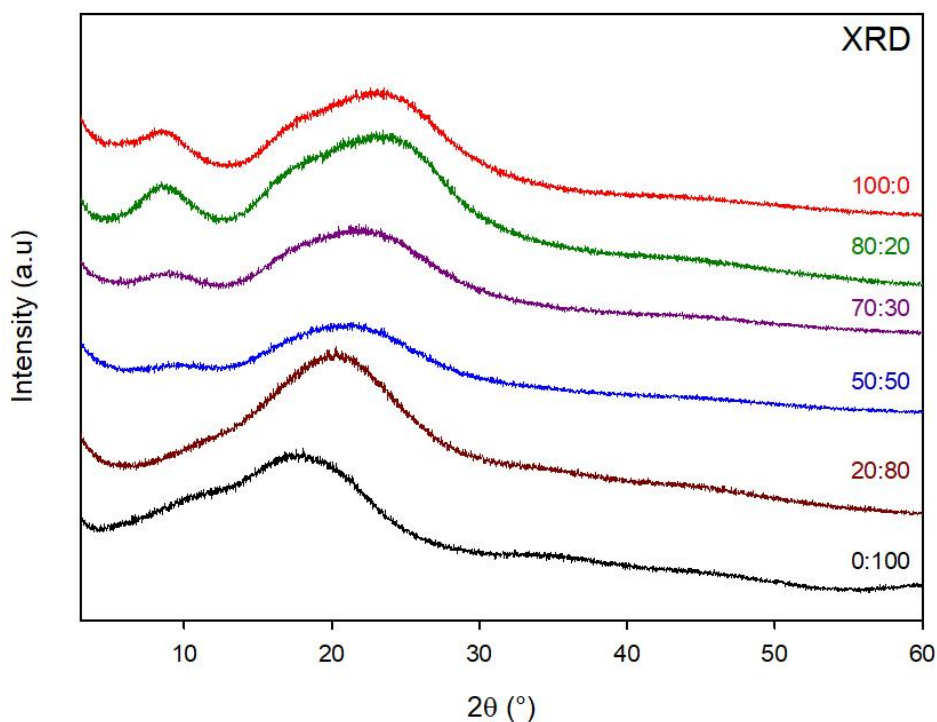
Figure 123 - X-Ray diffraction patterns for different compositions of the Rf/Lycoat co-milled (12 hours) mixtures. The compositions (w/w) are reported on the right-hand side of each curve. Pure Lycoat (black) and pure milling-induced (12h) amorphous Rf (red) are also reported for comparison.

Figure 124 shows the DSC scans corresponding to the co-milled (12h) mixtures for Rf concentrations ranging from 20 to 80 %. For comparison, the scans of pure Lycoat (non-milled) and of pure milling-induced (12h) amorphous riboflavin are also shown. It can be noticed that in each case, a single Tg is observed indicating that a homogenous co-amorphous mixture has been produced. Nevertheless, as the Tg of the Lycoat cannot be observed due to its value above 250°C (cf Chapter IV, section IV.1.1, Figure 56), it cannot be not excluded that a second Tg could be present. Furthermore, for decreasing riboflavin fractions, the position of this Tg shifts towards the higher temperatures which confirms the anti-plasticizing effect of Lycoat in the drug/polymer mixture. For each composition of the mixture, an exotherm of recrystallization can be observed above Tg. Indeed, for example, the mixture Rf/Lycoat (70/30, w/w) exhibits an enthalpy of recrystallization (ΔH = 42.3 J/g) which, when compared to the one of pure amorphous Rf (ΔH = 58.2 J/g – cf section V.1.2), corresponds to approximately 73% of recrystallized Rf. As the mixture contained 70% of Rf, this means that all of the Rf in the mixture recrystallized. It can thus be deduced that the co-milled material is highly supersaturated and already suggests that the solubility of riboflavin in the Lycoat is quite weak. It must be noticed that the recrystallization is not clearly observed for 30% and 20% of riboflavin in the mixture as the maximum temperature reached during the heating was not high enough.
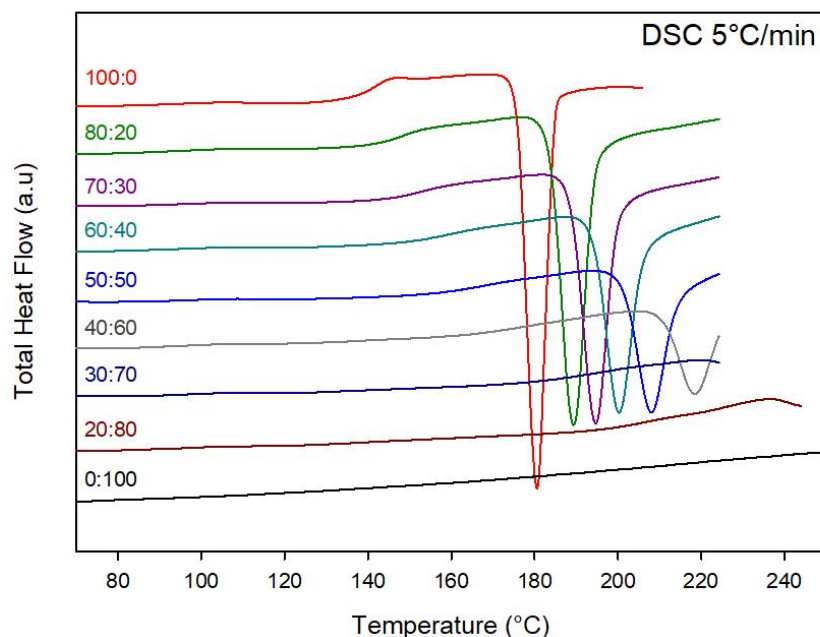
Figure 124 - DSC scans (5°C/min), Total Heat Flow, of Rf/Lycoat mixtures of different compositions co-milled for 12 hours. The compositions (w/w) are reported on the left-hand side of each curve. Pure Lycoat (black) and pure milling-induced (12h) amorphous Rf (red) are also reported for comparison.

(2) Evolution of the Tg for various compositions of the Rf/Lycoat mixtures and estimation of the Tg of the Lycoat

The aim of this section is to obtain an estimation of the Tg of the Lycoat by using the Gordon-Taylor equation. To that extend, a single fit involving the two sets of experimental data (Rf/Lycoat alloy and Chx/Lycoat alloy) was performed. Indeed, a single fit allows a better approximation of the Tg compared to two performed on each set of experimental data.

First the Tgs of the co-milled Rf/Lycoat mixture were determined for various compositions. This determination was performed using the reversing heat flow signal as illustrated in Figure 125. Indeed, for more accuracy, as the data will be combined with the set of data obtained for the Chx/Lycoat mixtures (cf Chapter IV, section IV.1.3), the same signal had to be used.
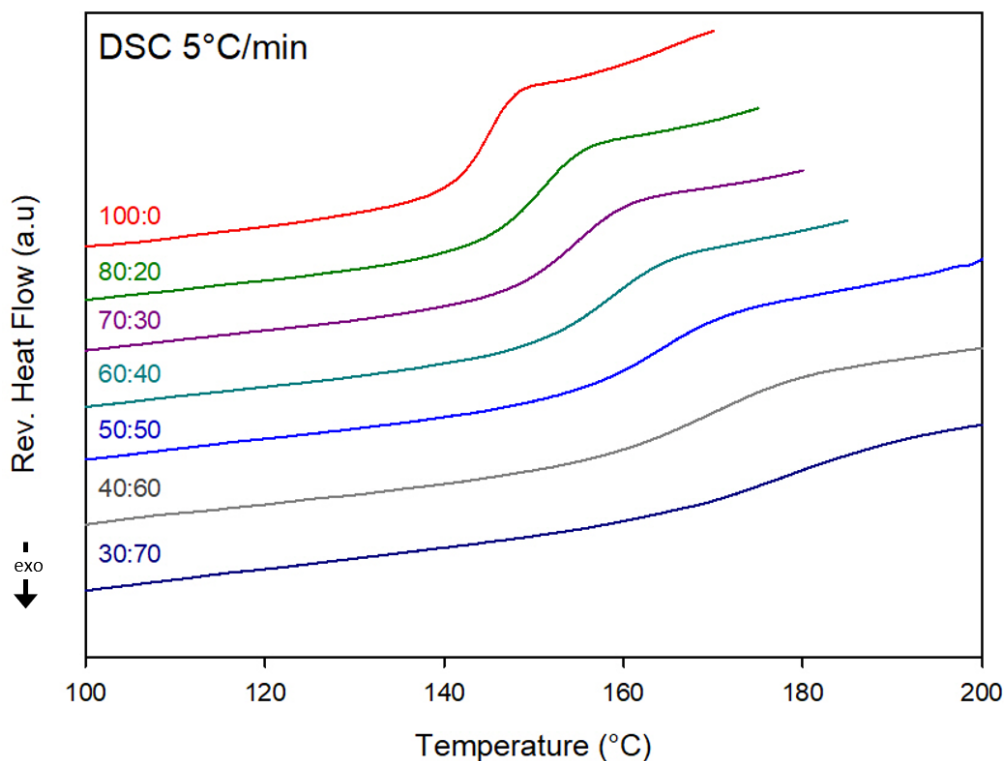
Figure 125 - DSC scans (5°C/min), reversing Heat Flow, of Rf/Lycoat mixtures of different compositions co-milled for 12 hours. The compositions (w/w) are reported on the left-hand side of each curve.

The evolution of the Tg of the alloy (obtained from Figure 125) with the composition is reported in Figure 126 along with the revolution of the Tg of the Chx/Lycoat alloy (obtained from Figure 66 in Chapter IV, section IV.1.3). As explained in Chapter IV, the Tg the Lycoat cannot be observed upon heating using the DSC as it is located above its degradation temperature. Moreover, as the amplitude of the Cp jump at Tg cannot be measured, it was impossible to obtain the theoretical Gordon Taylor curve for the Rf/Lycoat. It was thus, impossible to evaluate the presence of interactions between the two components.

The single fit to the combination of the two sets of data allowed an estimation of the Tg of the Lycoat at 301.9 ± 69.9 °C. According to the standard deviation obtained, the value estimated by the provider (Tg = 245°C) is within the range of values that were obtained using this fit.
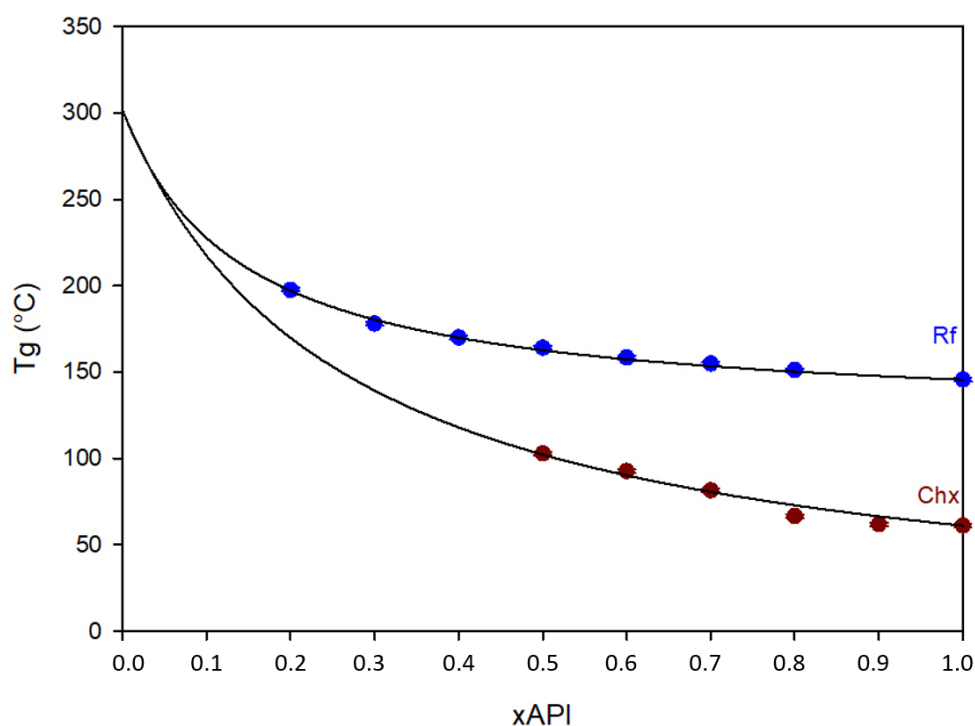
Figure 126 - Evolution of the Tg of the co-milled (API)$_x$(Lycoat)$_{1-x}$ binary mixtures against the API fraction x (Rf – blue dots and Chx – brown dots). It must be noted that an estimated error on the Tg of 1°C has been added in order to consider the eventual approximation on the composition of the mixture. The black solid lines represent the best fit of the Gordon Taylor equation to the two sets of experimental data.

VI.2 Dissolution performances of riboflavin-polymer mixtures

After a deep physical characterization of the riboflavin/polymer alloys previously highlighted, an evaluation of their dissolution performances in ultra-pure water was performed using different set ups. This investigation was proposed in order to evaluate the influence of the physical state of the API in such mixtures and to assess the advantage of the co-milled mixture compared to a physical mixture containing either amorphous riboflavin or crystalline riboflavin. A comparison between the two polymers was also performed in order to determine the most suitable one to enhance the dissolution performances of this API.

VI.2.1 Influence of the addition of PVPK12 on the dissolution performances of riboflavin

After a succinct presentation of the different Rf/PVP mixtures chosen for this study, the dissolution performances of Rf were evaluated using different experimental set-ups including the powder dissolution in sink and in non-sink conditions and the intrinsic dissolution.

(1) Presentation of the mixtures chosen for the dissolution

In order to both evaluate the influence of the physical state of the API in drug/polymer mixtures and to assess the advantage of the co-milled mixture in terms of dissolution performances, three different Rf/PVP (70:30, w/w) mixtures were chosen:

- A physical mixture (PM) of crystalline Rf Form I and PVP named Rf I/PVP PM
- A physical mixture of amorphous Rf (obtained by milling Form I for 32 hours) and PVP named RfM32h/PVP PM
- A co-amorphous mixture of Rf and PVP obtained by co-milling Form I and PVP during 12 hours, named Rf I/PVP CM12h.

Figure 127 shows the DSC scans (5°C/min) of these 3 mixtures along with the ones of pure milling-induced amorphous Rf and of pure PVPK12 for comparison. Please note that as the X-ray diffractograms did not show anything particular or unexpected, the corresponding data are not shown in this manuscript.

As expected, the thermogram of the physical mixture of crystalline Rf and PVP shows only one small Cp jump at the Tg corresponding to pure PVP. Regarding the physical mixture of milling-induced amorphous Rf and PVP, as expected, both the Tgs of pure amorphous Rf and of PVP are observed whereas the co-milled mixture exhibits a single Tg. Furthermore, it can be noticed that the further heating of this mixture shows the same events as observed in the thermogram of pure milling-induced amorphous Rf. On the contrary, as highlighted previously, the co-milled mixture exhibits only one exotherm of recrystallization followed by a shouldering, which corresponds to the pattern observed for Rf milled 6h (Chapter V, section V.1.3, Figure 101). Furthermore, as the second endotherm attributed to the polymorphic transformation is not observed, it can be assumed that the shouldering observed for the co-milled mixture corresponds to this polymorphic transformation.
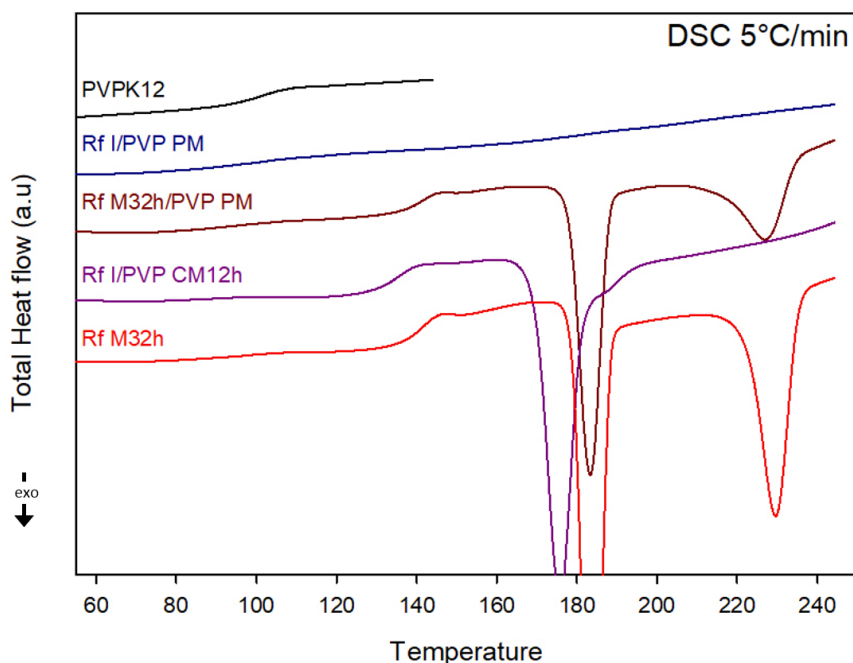
Figure 127 - DSC scans 5°C/min (total heat flow) of pure PVP K12 (black), of pure amorphous Rf (obtained by milling the crystal for 32h, red curve) and of a the 3 different Rf/PVP mixture (70:30) (w/w); crystalline Rf and PVP physically mixed (dark blue), amorphous Rf (obtained by milling the crystal for 32 hours) and PVP physically mixed (brown) and co-amorphous mixture of Rf and PVP obtained by co-milling for 12 hours crystalline Rf and amorphous PVP (purple).

(2) Powder dissolution in sink and non-sink conditions

Figure 128 illustrates the dissolution kinetics of the different riboflavin/PVP mixtures in ultra-pure water in sink conditions, i.e. for an amount of API at least 3 times below its solubility limit.

All the mixtures show a biphasic dissolution profile as they present a steep slope and then level-off until reaching approximately 100% of riboflavin dissolved after 24 hours of experiment. It can be noticed that considering the standard deviation values, even if the physical mixture containing amorphous riboflavin seem to show a slower dissolution for the first 2 hours, the difference with the two other mixtures is not significant.
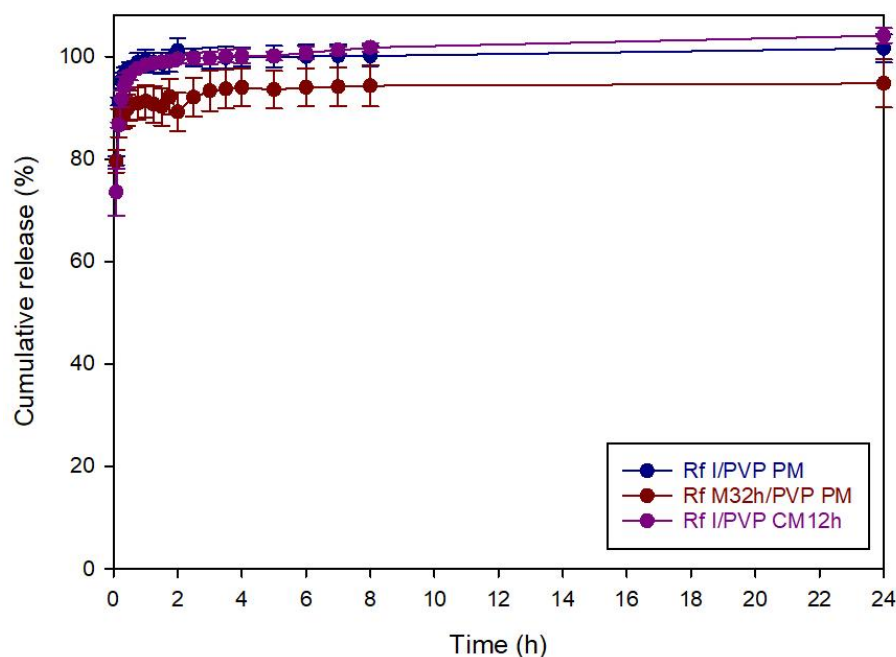
Figure 128 - Dissolution kinetics over 24 hours of the different riboflavin/PVP mixtures in a large volume of ultra-pure water (800mL) heated at 37°C under stirring (100 rpm) and in sink conditions.

Figure 129 shows the corresponding dissolution kinetics in ultra-pure water in non-sink conditions. It must be noted that in this case, only the solubility limit of Form I was exceeded which explains why the Rf I/PVP physical mixture only reached about 45% of release as it approximately corresponds to this limit. Regarding the two mixtures containing amorphous riboflavin, no significant difference can be observed and the two of them reached 100% after approximately 3 hours of dissolution. This seems to indicate that there is no clear advantage for using the co-milled mixture.
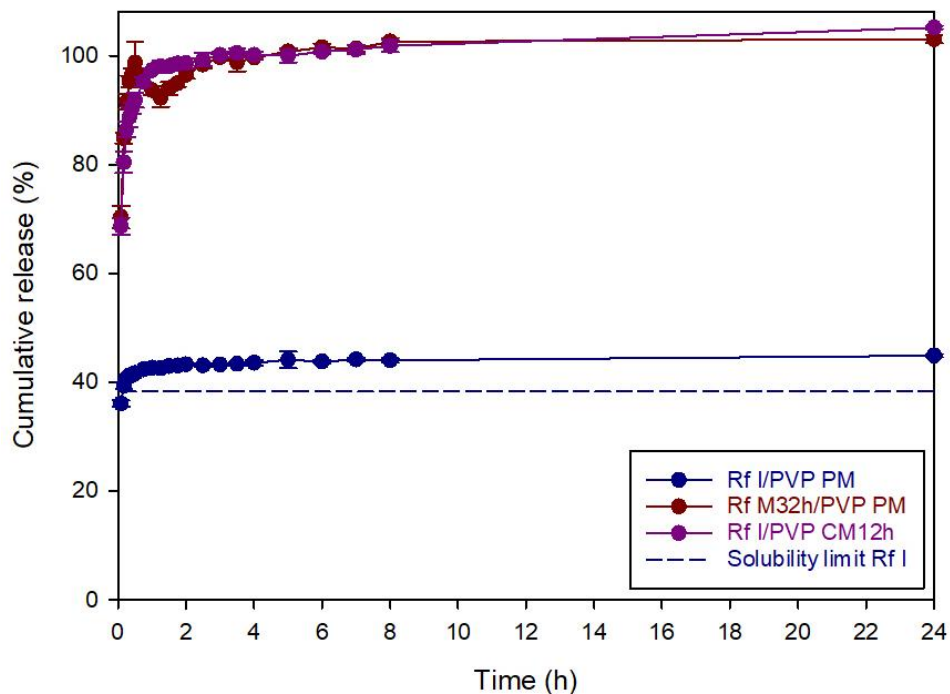
Figure 129 - Dissolution kinetics over 24 hours of the different riboflavin/PVP mixtures in a large volume of ultra-pure water (800mL) heated at 37°C under stirring (100 rpm) and in non-sink conditions.

(3) Intrinsic dissolution

First of all, as the physical integrity of the physical state of Rf upon compression of the pure API was demonstrated in the previous chapter, no physical characterization was performed on the compacts produced with the different Rf/PVP mixtures.

Figure 130 represents the intrinsic dissolution profiles of the three different riboflavin/PVP mixtures. It must be noted that after two hours of dissolution the curves of the mixtures containing amorphous riboflavin were no longer linear which made then inaccurate the determination of the intrinsic

dissolution rate. As expected, as similarly observed for the API, the mixture containing crystalline riboflavin shows the slowest dissolution rate i.e. 1.0 ± 0.07 mg/cm²/h. However, the mixtures containing amorphous riboflavin show a significant advantage as the dissolution rate was almost 10 times higher. Moreover, these results highlight a slight advantage for having the amorphous riboflavin molecularly dispersed in the polymer as the co-milled mixture showed a dissolution rate of 8.6 ± 0.14 mg/cm²/h compared to 7.5 ± 0.13 mg/cm²/h for the physical mixture.

Figure 130 - Dissolution kinetics of the intrinsic dissolution of the riboflavin/PVP mixtures in ultra-pure water (400mL) heated at 37°C under stirring (50 rpm).

VI.2.2 Influence of the addition of Lycoat RS 720 on the dissolution performances of riboflavin

After a succinct presentation of the different Rf/Lycoat mixtures chosen for this study, the dissolution performances of Rf were evaluated using intrinsic dissolution.

(1) Presentation of the mixtures chosen for the dissolution

In order to both evaluate the influence of the physical state of the API in drug/polymer mixtures and to assess the advantage of the co-milled mixture in terms of dissolution performances, three different Rf/Lycoat (70:30, w/w) mixtures were chosen:

- A physical mixture (PM) of crystalline Rf Form I and Lycoat named Rf I/Lyc PM
- A physical mixture of amorphous Rf (obtained by milling Form I for 32 hours) and Lycoat named RfM32h/Lyc PM
- A co-amorphous mixture of Rf and PVP obtained by co-milling Form I and Lycoat during 12 hours, named Rf I/Lyc CM12h

Figure 131 shows the DSC scans (5°C/min) of these 3 mixtures along with the ones of pure milling-induced amorphous Rf and of pure Lycoat for comparison. Please note that as the X-ray diffractograms did not show anything particular or unexpected, the corresponding data are not shown in this manuscript.

It can be noticed that the physical mixture containing amorphous riboflavin and Lycoat exhibits the same recrystallization pattern as pure amorphous riboflavin (milled 12 or 32h, Chapter V, section V.1.3, Figure 101), whereas the co-milled mixture shows only one exotherm of recrystallization. Regarding the Tg positions, the physical mixture containing crystalline riboflavin does not show any sign of Tg as the one of Lycoat cannot be observed and for the same reason, the physical mixture containing amorphous riboflavin shows only the Tg of pure amorphous Rf. Finally, the co-milled mixture of Rf and Lycoat shows a single Tg, slightly superior compared to one of pure amorphous riboflavin.
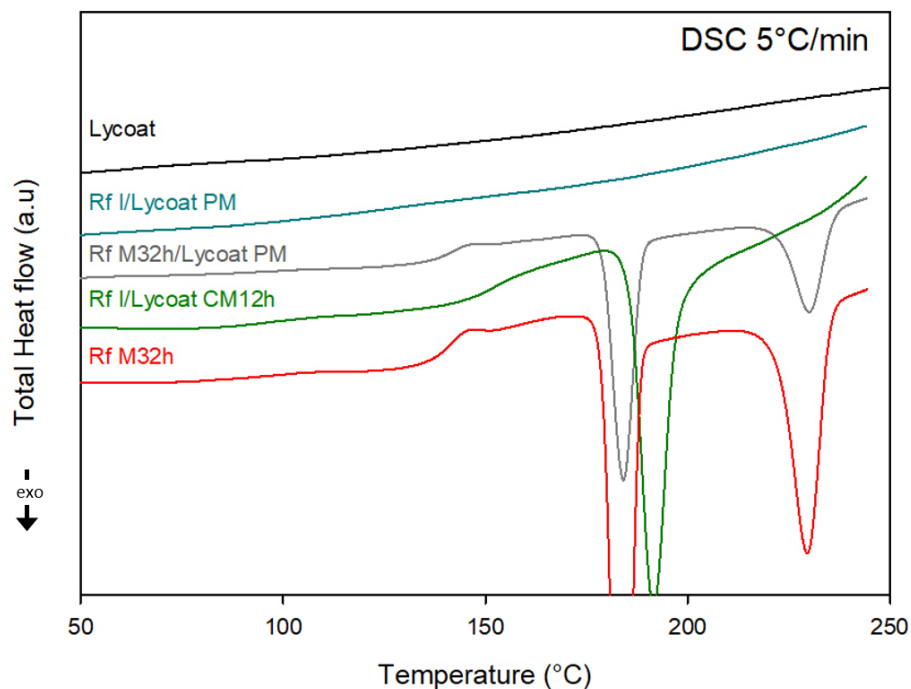
Figure 131 – DSC scans (5°C/min), Total Heat flow, of pure Lycoat (black), of pure crystalline Rf (blue) and of a the 3 different Rf/Lycoat mixture (70:30) (w/w); crystalline Rf and Lycoat physically mixed (dark blue), amorphous Rf (milled 32h) and Lycoat physically mixed (brown) and co-amorphous mixture of Rf and Lycoat co-milled 12 hours (purple).

(2) Intrinsic dissolution

As the powder dissolution of the Rf/PVP mixtures showed no clear difference for between the two mixtures containing amorphous riboflavin, only the intrinsic dissolution was performed for the Rf/Lycoat mixtures.

First of all, as the physical integrity of the physical state of Rf upon compression of the pure API was demonstrated in the previous chapter, no physical characterization was performed on the compacts produced with the different Rf/Lycoat mixtures.

It must be noticed that just as previously explained with the PVP case, the dissolution rate was calculated for the first 2 hours of dissolution due to the slope change afterwards for the mixtures containing amorphous riboflavin.

Figure 132 illustrates the dissolution profiles of the three Rf/Lycoat mixtures. As observed for the PVP case, the physical mixture containing crystalline Rf and Lycoat shows the slowest dissolution rate i.e. 1.6 ± 0.09 mg/cm²/h. As expected, the mixtures containing amorphous riboflavin show a great advantage as the dissolution rates were significantly enhanced.

Interestingly, in this case, the co-milled mixture shows a more noticeable benefit compared to the physical mixture containing amorphous Rf. Indeed, the dissolution rate of the co-milled mixture was evaluated to 12.5 ± 0.49 mg/cm²/h whereas it was 8.4 ± 0.17 mg/cm²/h for the physical mixture.
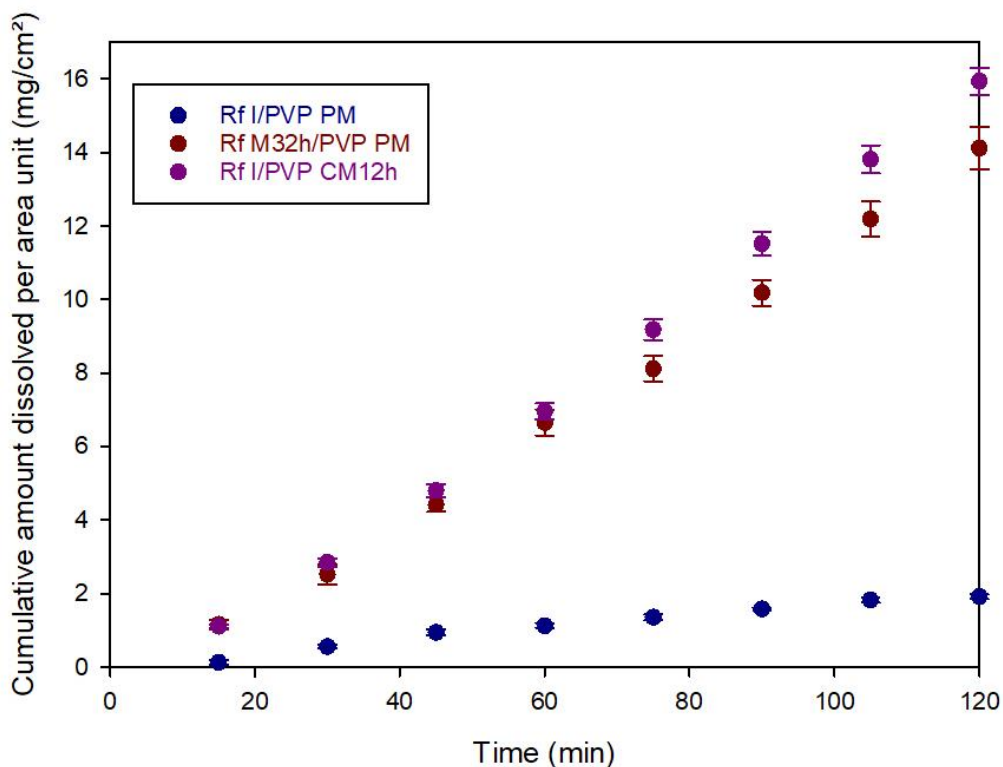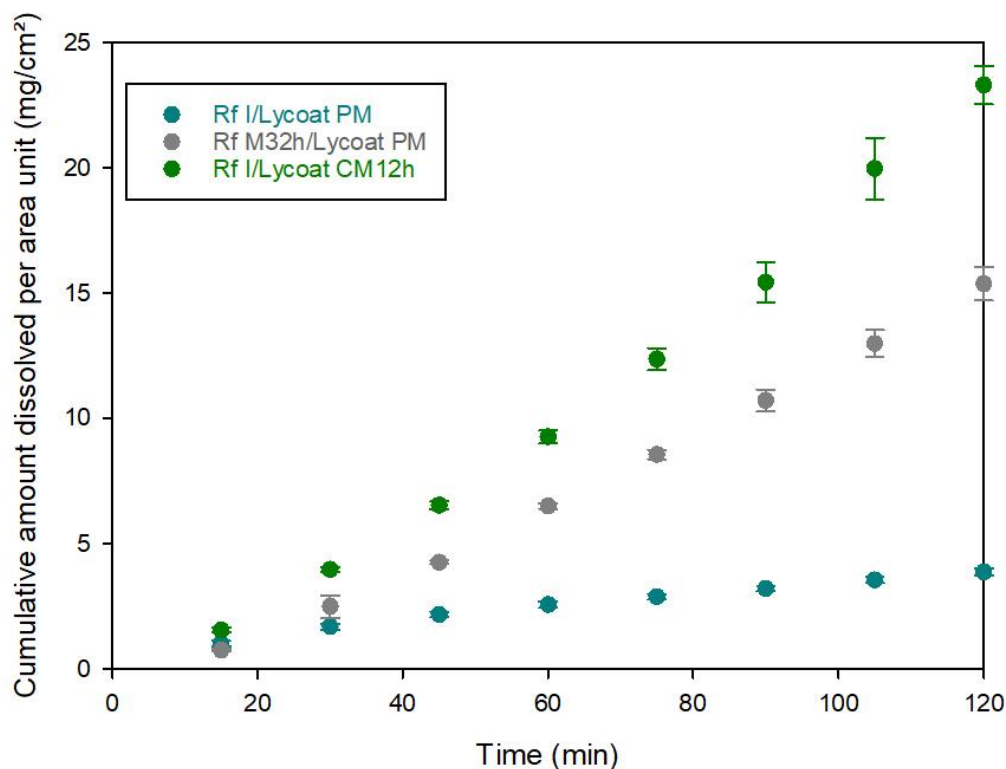

Figure 132 - Dissolution kinetics of the intrinsic dissolution of the riboflavin/Lycoat mixtures in ultra-pure water (400mL) heated at 37°C under stirring (50 rpm).

VI.2.3   Comparison between PVPK12 and Lycoat RS 720

As the influence of the physical state of riboflavin were investigated for three different mixtures containing either PVPK12 or Lycoat RS 720, it was also important to compare the polymers together in order to determine which polymer was the most suitable for this API. To that extend, a comparison was made with the pure amorphous Rf on one hand and with the pure crystalline Rf on the other hand to evaluate whether the polymer addition had a positive or a negative influence on the dissolution rate of the API.

Regarding the influence of the addition of the polymer on the dissolution rate of crystalline Rf, Figure 133 shows the intrinsic dissolution kinetics of the physical mixtures containing crystalline Rf compared to the pure crystal. It can be noticed that in both cases, the addition of the polymer presents a slight benefit in terms of amount of API dissolved. However, regarding the dissolution rates, no significant difference can be highlighted between the physical mixtures containing either Lycoat or PVP and the pure crystalline Rf as they were evaluated to 1.6 ± 0.09 mg/cm²/h, 1.0 ± 0.07 mg/cm²/h and to 1.1 ± 0.07 mg/cm²/h respectively.
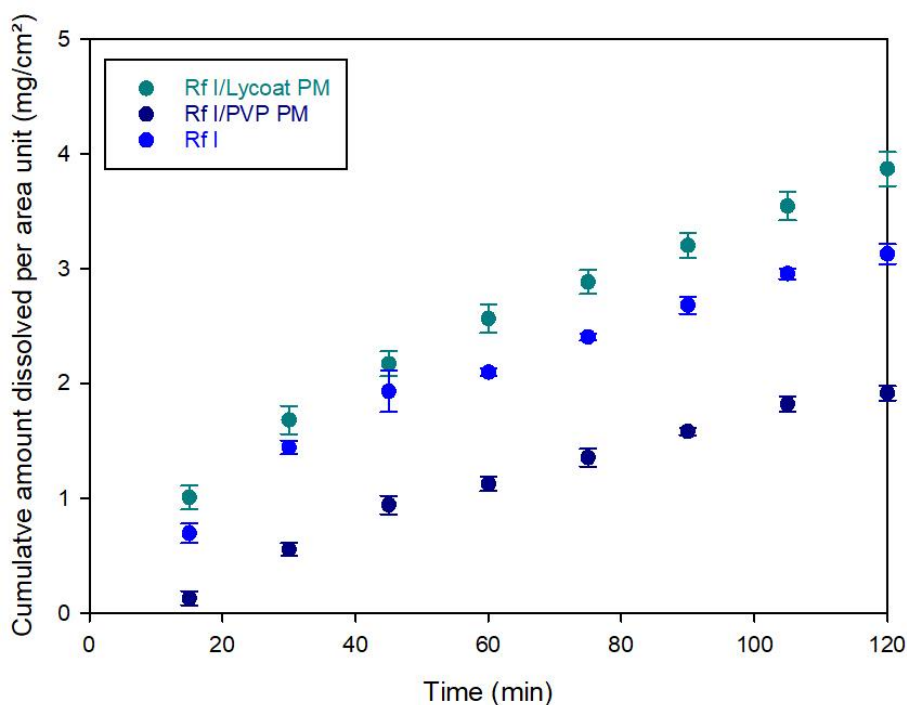
Figure 133 - Dissolution kinetics of the intrinsic dissolution of the riboflavin (crystalline)/polymer physical mixtures and of pure crystalline riboflavin in ultra-pure water (400mL) heated at 37°C under stirring (50 rpm).

Figure 134 shows the comparison in the intrinsic dissolution kinetics between the physical mixtures containing amorphous Rf (milled 32h) and the pure amorphous Rf (milled 32h). For both PVPK12 and Lycoat RS 720, the addition of the polymer seems to slightly decrease the dissolution rate of the API. Indeed, it was evaluated to 7.5 ± 0.13 mg/cm²/h and to 8.4 ± 0.17 mg/cm²/h for the mixture containing PVPK12 and Lycoat RS 720 respectively and to 10.2 ± 0.08 mg/cm²/h for pure amorphous Rf.
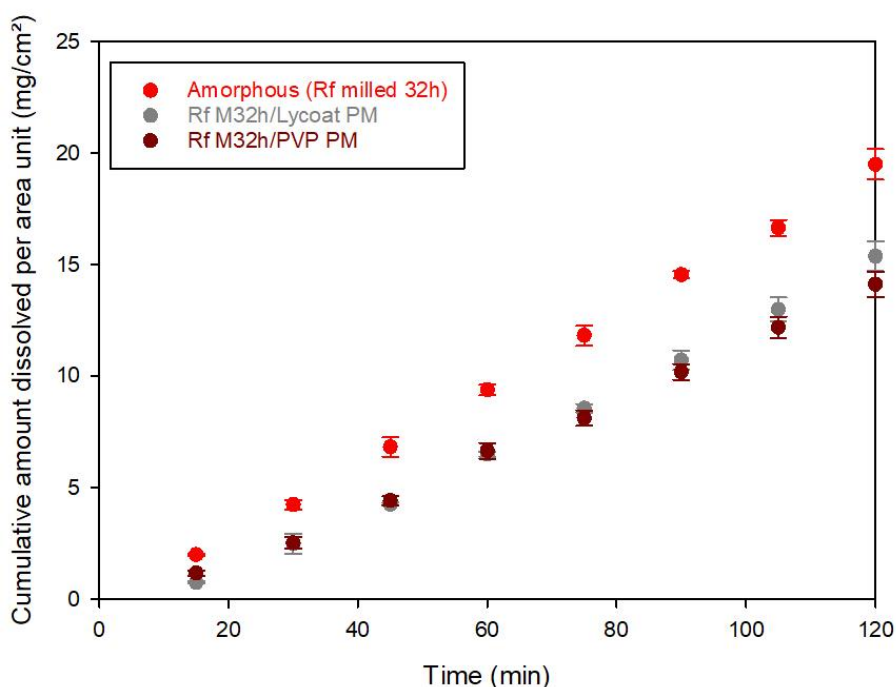
Figure 134 - Dissolution kinetics of the intrinsic dissolution of the riboflavin (amorphous, milled 32h)/polymer physical mixtures and of pure amorphous riboflavin (milled 32h) in ultra-pure water (400mL) heated at 37°C under stirring (50 rpm).

However, for the co-milled mixtures, illustrated in Figure 135, the conclusions are slightly different. Indeed, if the addition of PVPK12 still seems to slow down the dissolution of the API, the addition of Lycoat RS 720 shows a similar curve compared to the pure amorphous Rf with a slight improvement after 1h of dissolution. In terms of dissolution rates, a decrease is observed for the co-milled mixture containing PVPK12 whereas an increase is observed for the one containing Lycoat RS 720 compared to the pure amorphous API as they were evaluated to 8.6 ± 0.14 mg/cm²/h, to 12.5 ± 0.49 mg/cm²/h and to 10.2 ± 0.08 mg/cm²/h respectively.
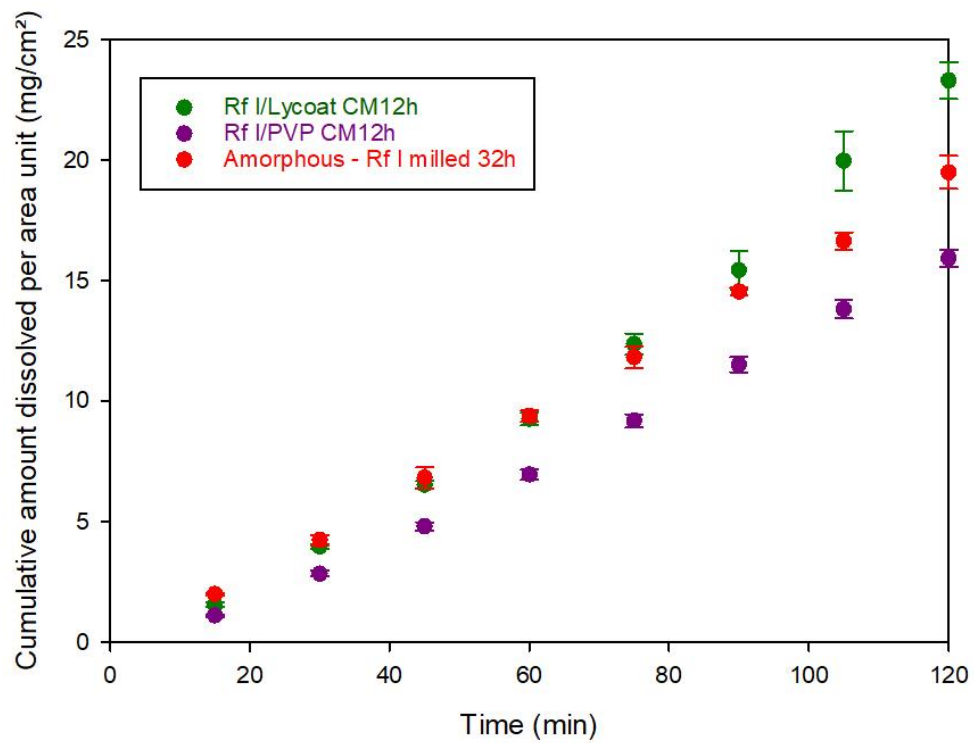
Figure 135 - Dissolution kinetics of the intrinsic dissolution of the riboflavin/polymer co-milled (12 hours) mixtures and of pure amorphous riboflavin (milled 12 hours) in ultra-pure water (400mL) heated at 37°C under stirring (50 rpm).

Conclusion

In this chapter, it was showed that is was possible to successfully obtain co-amorphous molecular alloys of Rf/polymer with either PVPK12 and Lycoat RS 720 for different compositions of the mixture using high-energy ball milling. If the addition of PVP induced a plasticizing effect compared to Lycoat which presented the opposite effect. Neither of the polymer could prevent the recrystallization of amorphous Rf upon heating.

Besides, the evaluation of the Tg for both the Rf/PVP and the Rf/Lycoat alloys was evaluated and, in both cases, it fitted the Gordon-Taylor equation. In the case of PVPK12, this curve was found to show a rather good similarity with the theoretical curve indicating that there were probably very few chemical interactions between the API and the polymer. Furthermore, in the case of Lycoat, for which the Tg could not be determined using the DSC, a fit combining the experimental data obtained with Chx and with Rf allowed an estimation of the Tg of the polymer which was approximately 301°C. The solubility of the Rf in the PVPK12 was also determined and was found to be very poor (approximately 13% at 180°C) indicating that the molecular alloys produced can only exist in supersaturation conditions.

Finally, in order to evaluate the influence of the physical state of riboflavin when a polymer addition is performed, for both polymers, three different mixtures were physically characterized and their dissolution performances were evaluated. For both polymers, the physical mixture containing crystalline Rf showed the slowest dissolution rate and the co-milled mixture presented a slight advantage compared to the physical mixture containing amorphous Rf.

However, the results showed that, considering crystalline Rf, the addition of PVPK12 seemed to decrease the amount of API dissolved even though similar dissolution rates were observed. Regarding the comparison with pure amorphous Rf, PVPK12 seemed to slow down the dissolution of the amorphous API in both the physical and the co-milled mixtures. In the case of Lycoat, even though it seemed to slow down the dissolution of the amorphous API in the case of the physical mixture, the co-milled mixture presented a slight advantage as it showed an increase in the dissolution rate.

In conclusion, Lycoat RS 720 seems to be the most suitable polymer for the production of Rf ASDs using co-milling as it both allows an increase of the Tg and thus, of the physical stability during storage, and an improvement in the dissolution rate compared to pure amorphous Rf.

General conclusion and perspectives

The main objective of this thesis project was to produce amorphous solid dispersions (ASDs) of poorly-soluble drugs and to compare the solubility, as well as the physical stability, of the APIs thus formulated with those of the pure APIs in different forms, i.e crystalline, metastable polymorphs and amorphous form.

For this work, two model drugs are chosen including chlorhexidine free base (Chx) and riboflavin free base (Rf). Indeed, as those drugs are very-poorly soluble and crystalline, the aim was to enhance their solubility by producing formulations in the amorphous state. However, before preparing an optimized formulation, it is of the most importance to have a good understanding of the physical characteristics of the drug and of the influence of the amorphization process on the latter. Then, the aim was to evaluate the dissolution performances of the drug in both its crystalline and amorphous state for different experimental set-ups.

The next step consisted in stabilizing the drug in its amorphous state in a formulation. To that extend, the drug was molecularly dispersed in a polymer matrix by co-milling of a physical mixture of the crystalline drug and the polymer. Therefore, two polymers were chosen including polyvinylpyrrolidone (PVP) as it is widely used in the production of ASDs and Lycoat RS720, a starch-based polymer graciously offered by our industrial partner, Roquette.

Furthermore, in order to assess the advantage of having an amorphous drug molecularly dispersed in the polymer in terms of drug release, three different mixtures were tested for each polymer including:

- A physical mixture of crystalline drug and polymer
- A physical mixture of milling-induced amorphous drug and polymer
- A co-amorphous mixture of drug and polymer obtained by co-milling.

It was demonstrated that these specific drugs are both prone to thermal degradation and practically insoluble in most organic solvents. Therefore, neither heat-based nor solvent-based amorphization processes could be used. It was thus decided to perform the amorphization directly in the solid state and to that extend, high-energy milling was selected.

Chlorhexidine free base

During the physical characterization of Chx free base, it was demonstrated that it undergoes a polymorphic transition Form I → Form II upon heating before the melting of the drug. This transition appeared to be completely reversible as upon rapid cooling Form II transformed back into Form I.

It was also proven that high-energy milling was a more suitable amorphization process for Chx free base (Form I) compared to the traditional liquid quench due to thermal degradation. The glass transition temperature was evaluated to Tg = 60.5°C and the Cp jump at Tg was ΔCp = 0.59 J/g/°C. Upon heating, amorphous Chx was found to recrystallize into its initial form (Form I) and further heating led to the polymorphic transition Form I → Form II before the melting of the drug. However, such a recrystallization did not occur upon heating of quenched melt. Either upon heating or milling, these two forms appear to be enantiotropically related and their relative stability at room temperature was ranked as follows: I >> II. The amorphization kinetics upon milling were also determined and were found to follow an exponential relaxation law with an exceptionally low relaxation time τ = 4.6 min.

Regarding the dissolution kinetics, the first set-up (super-saturated solution) revealed a drop in the amount of dissolved Chx after 24 hours of dissolution for both crystalline and amorphous Chx due to a recrystallization into a pentahydrate. The pentahydrate was characterized and its solubility limit was determined at approximately 100mg/L.

The evaluation of the dissolution kinetics in the case of the powder dissolution, the intrinsic dissolution or the tablet dissolution revealed a slower dissolution for the amorphous Chx compared to its crystalline counterpart. Such an unexpected behavior of the amorphous form was proven to be due to both the formation of aggregates and to the precipitation into the hydrate form, less soluble, during the dissolution. Interestingly, the precipitation into the hydrate form was also observed during the dissolution of crystalline Chx but only in the case of the intrinsic dissolution. As it also occurred in the case of the super-saturated solution, such a difference in behavior was attributed to the parameters used for the dissolution set-ups i.e. the dissolution medium volume and the stirring technique itself which could induce a difference in hydrodynamics. As the dissolution in water revealed systematically a slower dissolution for the amorphous form compared to its crystalline counterpart, it should be

interesting to perform the same experiments using a more biorelevant dissolution medium for comparison.

Regarding the tablet manufacturing, the amorphous form revealed a better behavior. Indeed, it showed a better compressibility (lower P_y value) and a lower ejection shear stress. However, as both formulations were not worth considering as such for industrial manufacturing, it would be interesting to perform further optimization of the formulations. For instance, with an addition of an external lubricant, or of a glidant to improve the flowability or by investigating the use of other excipients and corresponding proportions. Nor the compression nor the tablet storage at 25°C, 60% RH were found to have altered the physical state of the drug, which allowed to have accurate results and comparisons in both tablet properties and dissolution kinetics.

As an attempt to enhance the stability of the amorphous form upon heating and during the dissolution, a co-amorphization with two polymers was performed using high-energy milling. As expected, both polymers were found to have an anti-plasticizing effect on the drug as the Tgs of the corresponding co-amorphous mixtures shifted towards higher temperatures with an increasing fraction of polymer. Furthermore, as the Tg of Lycoat is higher than the one of PVP, higher Tgs of the co-milled mixtures were observed when using Lycoat. This indicated that upon storage, the kinetic stability of the amorphous Chx in the co-milled mixture with Lycoat should be even more ensured.

Moreover, in the case of the co-milled mixtures, both polymers were found to prevent amorphous Chx from recrystallization upon heating which was neither avoidable during the heating of the pure milling-induced amorphous API nor in the case of the milling-induced amorphous API physically mixed with the polymer. However, in the case of the physical mixture of amorphous Chx and Lycoat, the recrystallization upon heating seemed less pronounced, and therefore probably not total, compared to the one observed in the corresponding mixture with PVP. Therefore, if both polymers can be considered suitable for the formulation of ASDs with Chx, the Lycoat seemed to have higher stabilizing properties on the milling-induced amorphous Chx upon heating.

Regarding the evolution of the Tg against the composition of the co-milled mixture and its comparison with an ideal mixture, only the Chx/PVP mixtures could be accurately fitted with the Gordon-Taylor equation as the Tg of the Lycoat could not be observed. This study showed a significant deviation (S-

shaped curve) with an opposite curvature compared to the theoretical curve (K = 1.5 VS K_{th} = 0.62) therefore revealing both an influence of the difference of size and shape between the API and the polymer and the presence of strong interactions between the two materials.

Concerning the dissolution kinetics in water, the dissolution of a super-saturated solution of crystalline Chx physically mixed with the polymer, revealed a rather similar propensity of both polymers to enhance the solubility of the API during the first 6 hours. Indeed, the maximum concentration reached was approximately 371 ± 39 mg/L with PVP and 320 ± 13 mg/L with the Lycoat. However, after 24 hours of dissolution, none of the polymers prevented the precipitation of Chx in solution. As it was demonstrated for the pure API that the precipitation was due to a transformation into a hydrate form, less soluble, it could be assumed that the precipitation occurring in both solution containing a polymer also led to a hydrate form of Chx. However, it could not be confirmed yet but to continuate this work, the residual solid obtained after precipitation should be analyzed using XRD and TGA and the results should be compared with those obtained in the case of pure Chx. The plateau reached in the case of the solution containing PVP was higher compared to the one reached with Lycoat, it can be assumed that the precipitated solid was more soluble in water in the presence of PVP.

During the powder dissolution, the Lycoat showed a higher propensity regarding the inhibition of recrystallization of the amorphous Chx during the dissolution. Nevertheless, after 48 hours of dissolution, no significant difference could be noticed between the two polymers as all mixtures showed similar results. Overall, in all the dissolution set-ups (powder dissolution, intrinsic dissolution and tablet dissolution), the amorphous form of Chx revealed either a similar of a slower dissolution compared to its crystalline counterpart.

In terms of tablet manufacturing, a higher ejection shear stress was obtained for each formulation containing PVP (between 6.5 and 8.8 MPa) compared to the ones containing Lycoat (≤ 6.6 MPa). Furthermore, only the formulation containing the co-milled mixture of Chx and Lycoat exhibited an ejection shear stress (< 1MPa) allowing an insurance of non-defective tablets during the manufacturing. The comparison of the P_y values revealed a better compressibility for the formulation containing the physical mixture of amorphous Chx and Lycoat (P_y = 89 MPa) compared to the corresponding one with PVP (P_y = 116 MPa). However, the formulation containing the co-milled mixture with PVP (P_y = 135 MPa) showed a better compressibility compared to the corresponding one with Lycoat (P_y = 158 MPa).

For industrial manufacturing, it would be interesting to perform further optimization of the formulations. For instance, with an addition of an external lubricant, or of a glidant to improve the flowability or by investigating the use of other excipients and corresponding proportions.

Riboflavin free base

In this work, it was demonstrated that amorphous riboflavin could be obtained for the first time by solid state amorphization of the crystalline Form I using high energy ball milling. The glass transition temperature (Tg = 144°C) and the Cp jump at Tg (ΔCp= 0.68 J/g/°C) could, hence, accurately and for the first time be determined. Upon heating, amorphous riboflavin was found to show a rich pattern of physical transformations, which enlightens the polymorphism of this vitamin. It shows in particular a recrystallization toward Form III, followed by a polymorphic transformation toward Form II occurring at 230°C (ΔH_2 = 34.1 J/g). These two forms appear to be enantiotropically related and the relative stability of the three polymorphs at room temperature appears to rank as the following: I > II > III.

Regarding the dissolution kinetics, the first set up (super-saturated solution) revealed the following order in the dissolution rates during the first 4 h: amorphous>Forms III ≈ Form II>Form I. After 4 h, a drop in the amount of dissolved riboflavin occurred for the amorphous and metastable crystalline forms due to a recrystallization toward a dihydrate. However, the plateau values were still above the solubility of Form I, revealing definitely the faster dissolution of the metastable forms (II, III and amorphous) over the stable crystalline Form I.

The dissolution kinetics in the sink conditions highlighted the influence of the particle size and shape as it revealed another order in the dissolution rates over the first hour: Form I > Amorphous form > Form III >> Form II. However, after 24 hours of dissolution, all the forms reached 100% of riboflavin dissolved. Meanwhile, both the dissolution in the non-sink conditions and the intrinsic dissolution revealed a faster dissolution of the amorphous form compared the crystalline forms. However, no distinction in the dissolution rate could be made between forms I and II. In addition, it allowed to gain knowledge on the ability of the different forms to hold in the form of a compact during the dissolution experiment. Between all the forms, only form III, the least stable polymorph, disintegrated as soon as it came in contact with the dissolution medium.

It was also demonstrated that is was possible to successfully obtain co-amorphous molecular alloys of Rf/polymer with either PVPK12 and Lycoat RS 720 for different compositions of the mixture using high-energy ball milling. If the addition of PVP induced a plasticizing effect compared to Lycoat which presented the opposite effect, neither of the polymer could prevent the recrystallization of amorphous Rf upon heating.

Besides, the Tg for both the Rf/PVP and the Rf/Lycoat alloys was evaluated and, in both cases, it fitted the Gordon-Taylor equation. In the case of PVPK12, this curve was found to show a rather good similarity with the theoretical curve indicating that there were probably very few chemical interactions between the API and the polymer. The solubility of the Rf in the PVPK12 was also determined and was found to be very poor (approximately 13% at 180°C). Therefore, the co-amorphous mixtures of Rf and PVP are unstable as they are highly super-saturated. However, as previously mentioned, these mixtures exhibit high glass transition temperatures which should lead to a kinetic stability.

In the case of Lycoat, for which the Tg could not be determined using the DSC, a fit combining the experimental data obtained with Chx and with Rf allowed an estimation of the Tg of the polymer which was approximately 301°C.

The dissolution kinetics revealed that for both polymers, the physical mixture containing crystalline Rf showed the slowest dissolution rate and the co-milled mixture presented a slight advantage compared to the physical mixture containing amorphous Rf.

However, the results showed that, considering pure crystalline Rf, the addition of PVPK12 seemed to decrease the amount of API dissolved even though similar dissolution rates were observed. Regarding the comparison with pure amorphous Rf, PVPK12 seemed to slow down the dissolution of the amorphous API in both the physical and the co-milled mixture. In the case of Lycoat, even though it seemed to slow down the dissolution of the amorphous API in the case of the physical mixture, the co-milled mixture presented a slight advantage as it showed an increase in the dissolution rate. In order to have a clear idea of the influence of the polymer on the solubility of the API, the evaluation of the solubility of crystalline Rf physically mixed with each polymer should be performed. Furthermore, for more accuracy, the powder dissolution with the mixtures containing Lycoat should also be performed in order to be compared with the dissolution of the mixtures containing PVP.

In conclusion, Lycoat RS 720 seems to be the most suitable polymer for the production of Rf ASDs using co-milling as it both allowed an increase of the Tg and thus, of the physical stability during storage, and an improvement in the dissolution rate compared to pure amorphous Rf.

References

1. Ziaee, A. *et al.* Spray drying ternary amorphous solid dispersions of ibuprofen – An investigation into critical formulation and processing parameters. *European Journal of Pharmaceutics and Biopharmaceutics* **120**, 43–51 (2017).
2. Van den Mooter, G. The use of amorphous solid dispersions: A formulation strategy to overcome poor solubility and dissolution rate. *Drug Discovery Today: Technologies* **9**, e79–e85 (2012).
3. Kanaujia, P., Poovizhi, P., Ng, W. K. & Tan, R. B. H. Amorphous formulations for dissolution and bioavailability enhancement of poorly soluble APIs. *Powder Technology* **285**, 2–15 (2015).
4. Kalepu, S. & Nekkanti, V. Insoluble drug delivery strategies: review of recent advances and business prospects. *Acta Pharmaceutica Sinica B* **5**, 442–453 (2015).
5. Jermain, S. V., Brough, C. & Williams, R. O. Amorphous solid dispersions and nanocrystal technologies for poorly water-soluble drug delivery – An update. *International Journal of Pharmaceutics* **535**, 379–392 (2018).
6. Paufler, P. S. R. Elliott. Physics of amorphous materials. Longman Group Ltd., London, New York, 1984. Pp X + 386. Price: £ 25.00. ISBN 0–582–44636–8. *Crystal Research and Technology* **20**, 1238–1238 (1985).
7. Suga, H. Prospects of Materials Science. From crystalline to amorphous solids. *Journal of Thermal Analysis and Calorimetry* **60**, 957–974 (2000).
8. Johari, G. P. & Shanker, R. M. On the solubility advantage of a pharmaceutical's glassy state over the crystal state, and of its crystal polymorphs. *Thermochimica Acta* **598**, 16–27 (2014).
9. Murdande, S. B., Pikal, M. J., Shanker, R. M. & Bogner, R. H. Solubility advantage of amorphous pharmaceuticals: I. A thermodynamic analysis. *Journal of Pharmaceutical Sciences* **99**, 1254–1264 (2010).
10. Brittain, H. G. *Polymorphism in pharmaceutical solids*. (M. Dekker, 1999).
11. Davey, R. J. Polymorphism in Molecular Crystals Joel Bernstein. Oxford University Press, New York, 2002. ISBN 0198506058. *Crystal Growth & Design* **2**, 675–676 (2002).
12. Yu, L. Polymorphism in Molecular Solids: An Extraordinary System of Red, Orange, and Yellow Crystals. *Acc. Chem. Res.* **43**, 1257–1266 (2010).
13. Thiry, J. *et al.* Continuous production of itraconazole-based solid dispersions by hot melt extrusion: Preformulation, optimization and design space determination. *International Journal of Pharmaceutics* **515**, 114–124 (2016).
14. Kallakunta, V. R. *et al.* Stable amorphous solid dispersions of fenofibrate using hot melt extrusion technology: Effect of formulation and process parameters for a low glass transition temperature drug. *Journal of Drug Delivery Science and Technology* **58**, 101395 (2020).
15. Bohr, A., Boetker, J. P., Rades, T., Rantanen, J. & Yang, M. Application of spray-drying and electrospraying/electospinning for poorly water-soluble drugs: a particle engineering approach. *Curr Pharm Des* **20**, 325–348 (2014).
16. Ousset, A. *et al.* Development of a small-scale spray-drying approach for amorphous solid dispersions (ASDs) screening in early drug development. *Pharmaceutical Development and Technology* **24**, 1–47 (2018).
17. Alqurshi, A., Chan, K. L. A. & Royall, P. G. In-situ freeze-drying - forming amorphous solids directly within capsules: An investigation of dissolution enhancement for a poorly soluble drug. *Scientific Reports* **7**, (2017).
18. Valkama, E., Haluska, O., Lehto, V.-P., Korhonen, O. & Pajula, K. Production and stability of amorphous solid dispersions produced by a Freeze-drying method from DMSO. *International Journal of Pharmaceutics* **606**, 120902 (2021).
19. Vasconcelos, T., Marques, S., das Neves, J. & Sarmento, B. Amorphous solid dispersions: Rational selection of a manufacturing process. *Advanced Drug Delivery Reviews* **100**, 85–101 (2016).
20. Bhujbal, S. V. *et al.* Pharmaceutical amorphous solid dispersion: A review of manufacturing strategies. *Acta Pharm Sin B* **11**, 2505–2536 (2021).
21. Repka, M. A. *et al.* Melt extrusion with poorly soluble drugs – An integrated review. *International Journal of Pharmaceutics* **535**, 68–85 (2018).
22. Brittain, H. G. Effects of mechanical processing on phase composition. *J Pharm Sci* **91**, 1573–1580 (2002).
23. Tsukushi, I., Yamamuro, O. & Matsuo, T. Solid state amorphization of organic molecular crystals using a vibrating mill. *Solid State Communications* **94**, 1013–1018 (1995).

24. Descamps, M., Willart, J. F., Dudognon, E. & Caron, V. Transformation of pharmaceutical compounds upon milling and comilling: the role of T(g). *J Pharm Sci* **96**, 1398–1407 (2007).
25. Willart, J. F., Caron, V. & Descamps, M. Transformations of crystalline sugars upon milling. *J Therm Anal Calorim* **90**, 125–130 (2007).
26. Ngono, F., Willart, J.-F., Cuello, G., Jimenez-Ruiz, M. & Affouard, F. Lactulose: A Model System to Investigate Solid State Amorphization Induced by Milling. *J Pharm Sci* **108**, 880–887 (2019).
27. Otsuka, M., Matsumoto, T. & Kaneniwa, N. Effect of environmental temperature on polymorphic solid-state transformation of indomethacin during grinding. *Chem Pharm Bull (Tokyo)* **34**, 1784–1793 (1986).
28. Willart, J. F. *et al.* Formation of lactose-mannitol molecular alloys by solid state vitrification. *Solid State Communications* **138**, 194–199 (2006).
29. Linol, J., Morelli, T., Petit, M.-N. & Coquerel, G. Inversion of the Relative Stability between Two Polymorphic Forms of (±) Modafinil under Dry High-Energy Milling: Comparisons with Results Obtained under Wet High-Energy Milling. *Crystal Growth & Design* **7**, 1608–1611 (2007).
30. Oliveira, P. F. M., Willart, J.-F., Siepmann, J., Siepmann, F. & Descamps, M. Using Milling To Explore Physical States: The Amorphous and Polymorphic Forms of Dexamethasone. *Crystal Growth & Design* **18**, 1748–1757 (2018).
31. De Gusseme, A., Neves, C., Willart, J. F., Rameau, A. & Descamps, M. Ordering and disordering of molecular solids upon mechanical milling: The case of fananserine. *Journal of Pharmaceutical Sciences* **97**, 5000–5012 (2008).
32. Huang, Y. & Dai, W.-G. Fundamental aspects of solid dispersion technology for poorly soluble drugs. *Acta Pharmaceutica Sinica B* **4**, 18–25 (2014).
33. Van den Mooter, G. *et al.* Physical stabilisation of amorphous ketoconazole in solid dispersions with polyvinylpyrrolidone K25. *European Journal of Pharmaceutical Sciences* **12**, 261–269 (2001).
34. Lehmkemper, K., Kyeremateng, S. O., Bartels, M., Degenhardt, M. & Sadowski, G. Physical stability of API/polymer-blend amorphous solid dispersions. *European Journal of Pharmaceutics and Biopharmaceutics* **124**, 147–157 (2018).
35. Surikutchi, B., Patil, S., Shete, G., Patel, S. & Bansal, A. Drug-excipient behavior in polymeric amorphous solid dispersions. *Journal of Excipients and Food Chemicals* **4**, 70–94 (2014).
36. Serajuddin, A. T. Solid dispersion of poorly water-soluble drugs: early promises, subsequent problems, and recent breakthroughs. *J Pharm Sci* **88**, 1058–1066 (1999).
37. Tambe, S. *et al.* Recent Advances in Amorphous Solid Dispersions: Preformulation, Formulation Strategies, Technological Advancements and Characterization. *Pharmaceutics* **14**, 2203 (2022).
38. Ayenew, Z., Paudel, A. & Van den Mooter, G. Can compression induce demixing in amorphous solid dispersions? A case study of naproxen–PVP K25. *European Journal of Pharmaceutics and Biopharmaceutics* **81**, 207–213 (2012).
39. Gleeson, M. P., Hersey, A., Montanari, D. & Overington, J. Probing the links between in vitro potency, ADMET and physicochemical parameters. *Nat Rev Drug Discov* **10**, 197–208 (2011).
40. Kawabata, Y., Wada, K., Nakatani, M., Yamada, S. & Onoue, S. Formulation design for poorly water-soluble drugs based on biopharmaceutics classification system: basic approaches and practical applications. *Int J Pharm* **420**, 1–10 (2011).
41. Takagi, T. *et al.* A Provisional Biopharmaceutical Classification of the Top 200 Oral Drug Products in the United States, Great Britain, Spain, and Japan. *Mol. Pharmaceutics* **3**, 631–643 (2006).
42. Amidon, G. L., Lennernäs, H., Shah, V. P. & Crison, J. R. A theoretical basis for a biopharmaceutic drug classification: the correlation of in vitro drug product dissolution and in vivo bioavailability. *Pharm Res* **12**, 413–420 (1995).
43. EMA. ICH M9 on biopharmaceutics classification system based biowaivers - Scientific guideline. *European Medicines Agency* https://www.ema.europa.eu/en/ich-m9-biopharmaceutics-classification-system-based-biowaivers-scientific-guideline (2018).
44. Research, C. for D. E. and. M9 Biopharmaceutics Classification System-Based Biowaivers. https://www.fda.gov/regulatory-information/search-fda-guidance-documents/m9-biopharmaceutics-classification-system-based-biowaivers (2023).

45. Pandi, P., Bulusu, R., Kommineni, N., Khan, W. & Singh, M. Amorphous solid dispersions: An update for preparation, characterization, mechanism on bioavailability, stability, regulatory considerations and marketed products. *Int J Pharm* **586**, 119560 (2020).
46. Yazdanian, M., Briggs, K., Jankovsky, C. & Hawi, A. The 'high solubility' definition of the current FDA Guidance on Biopharmaceutical Classification System may be too strict for acidic drugs. *Pharm Res* **21**, 293–299 (2004).
47. Macheras, P. & Karalis, V. A non-binary biopharmaceutical classification of drugs: the ΑΒΓ system. *Int J Pharm* **464**, 85–90 (2014).
48. Butler, J. M. & Dressman, J. B. The developability classification system: application of biopharmaceutics concepts to formulation development. *J Pharm Sci* **99**, 4940–4954 (2010).
49. Benet, L. Z., Broccatelli, F. & Oprea, T. I. BDDCS applied to over 900 drugs. *AAPS J* **13**, 519–547 (2011).
50. Broccatelli, F., Cruciani, G., Benet, L. Z. & Oprea, T. I. BDDCS Class Prediction for New Molecular Entities. *Mol. Pharmaceutics* **9**, 570–580 (2012).
51. Chemistry (IUPAC), T. I. U. of P. and A. IUPAC - dissolution (D01806). https://goldbook.iupac.org/terms/view/D01806 doi:10.1351/goldbook.D01806.
52. Chemistry (IUPAC), T. I. U. of P. and A. IUPAC - solution (S05746). https://goldbook.iupac.org/terms/view/S05746 doi:10.1351/goldbook.S05746.
53. Clugston, M. & Flemming, R. *Advanced Chemistry*. (OUP Oxford, 2000).
54. Sou, T. & Bergström, C. A. S. Automated assays for thermodynamic (equilibrium) solubility determination. *Drug Discovery Today: Technologies* **27**, 11–19 (2018).
55. Chemistry (IUPAC), T. I. U. of P. and A. IUPAC - solute (S05744). https://goldbook.iupac.org/terms/view/S05744 doi:10.1351/goldbook.S05744.
56. Bellantone, R. A. Fundamentals of Amorphous Systems: Thermodynamic Aspects. in *Amorphous Solid Dispersions: Theory and Practice* (eds. Shah, N., Sandhu, H., Choi, D. S., Chokshi, H. & Malick, A. W.) 3–34 (Springer, 2014). doi:10.1007/978-1-4939-1598-9_1.
57. Seager, R. J., Acevedo, A. J., Spill, F. & Zaman, M. H. Solid dissolution in a fluid solvent is characterized by the interplay of surface area-dependent diffusion and physical fragmentation. *Sci Rep* **8**, 7711 (2018).
58. Chemistry (IUPAC), T. I. U. of P. and A. IUPAC - solubility (S05740). https://goldbook.iupac.org/terms/view/S05740 doi:10.1351/goldbook.S05740.
59. Janssens, S. & Van den Mooter, G. Review: physical chemistry of solid dispersions. *J Pharm Pharmacol* **61**, 1571–1586 (2009).
60. Noyes, A. A. & Whitney, W. R. THE RATE OF SOLUTION OF SOLID SUBSTANCES IN THEIR OWN SOLUTIONS. *J. Am. Chem. Soc.* **19**, 930–934 (1897).
61. Dokoumetzidis, A. & Macheras, P. A century of dissolution research: from Noyes and Whitney to the biopharmaceutics classification system. *Int J Pharm* **321**, 1–11 (2006).
62. Siepmann, J. & Siepmann, F. Mathematical modeling of drug dissolution. *International Journal of Pharmaceutics* **453**, 12–24 (2013).
63. Jacobs, C., Kayser, O. & Müller, R. H. Nanosuspensions as a new approach for the formulation for the poorly soluble drug tarazepide. *Int J Pharm* **196**, 161–164 (2000).
64. Loftsson, T. & Duchêne, D. Cyclodextrins and their pharmaceutical applications. *Int J Pharm* **329**, 1–11 (2007).
65. Berge, S. M., Bighley, L. D. & Monkhouse, D. C. Pharmaceutical salts. *J Pharm Sci* **66**, 1–19 (1977).
66. Rautio, J. *et al.* Prodrugs: design and clinical applications. *Nat Rev Drug Discov* **7**, 255–270 (2008).
67. Lavasanifar, A., Samuel, J. & Kwon, G. S. Poly(ethylene oxide)-block-poly(L-amino acid) micelles for drug delivery. *Adv Drug Deliv Rev* **54**, 169–190 (2002).
68. Potta, S. G. *et al.* Development of solid lipid nanoparticles for enhanced solubility of poorly soluble drugs. *J Biomed Nanotechnol* **6**, 634–640 (2010).
69. Vo, C. L.-N., Park, C. & Lee, B.-J. Current trends and future perspectives of solid dispersions containing poorly water-soluble drugs. *Eur J Pharm Biopharm* **85**, 799–813 (2013).
70. Hicks, J. F. G. Glass formation and crystal structure. *J. Chem. Educ.* **51**, 28 (1974).
71. Hancock, B. C. & Zografi, G. Characteristics and significance of the amorphous state in pharmaceutical systems. *J Pharm Sci* **86**, 1–12 (1997).

72. Garside, J. Nucleation. in *Biological Mineralization and Demineralization* (ed. Nancollas, G. H.) 23–35 (Springer, 1982). doi:10.1007/978-3-642-68574-3_3.

73. Yoreo, J. & Vekilov, P. Principles of Crystal Nucleation and Growth. *Reviews in Mineralogy & Geochemistry - REV MINERAL GEOCHEM* **54**, 57–93 (2003).

74. Karpukhina, N., Hill, R. G. & Law, R. V. Crystallisation in oxide glasses – a tutorial review. *Chem. Soc. Rev.* **43**, 2174–2186 (2014).

75. Descamps, M., Dudognon, E. & Willart, J.-F. *The amorphous state*. (Wiley-VCH, 2019). doi:10/18033.

76. Karthika, S., Radhakrishnan, T. K. & Kalaichelvi, P. A Review of Classical and Nonclassical Nucleation Theories. *Crystal Growth & Design* **16**, 6663–6681 (2016).

77. Kelton, K. F., Greer, A. L. & Thompson, C. V. Transient nucleation in condensed systems. *Journal of Chemical Physics* **79**, 6261–6276 (1983).

78. Oxtoby, D. W. Homogeneous nucleation: theory and experiment. *J. Phys.: Condens. Matter* **4**, 7627 (1992).

79. Turnbull, D. Kinetics of Heterogeneous Nucleation. *The Journal of Chemical Physics* **18**, 198–203 (2004).

80. Kelton, K. F. & Greer, A. L. Test of classical nucleation theory in a condensed system. *Phys Rev B Condens Matter* **38**, 10089–10092 (1988).

81. Kelton, K. F. Crystal Nucleation in Liquids and Glasses. in *Solid State Physics* (eds. Ehrenreich, H. & Turnbull, D.) vol. 45 75–177 (Academic Press, 1991).

82. Turnbull, D. Phase Changes. in *Solid State Physics* (eds. Seitz, F. & Turnbull, D.) vol. 3 225–306 (Academic Press, 1956).

83. Burger, A. & Ramberger, R. On the polymorphism of pharmaceuticals and other molecular crystals. I. *Mikrochim Acta* **72**, 259–271 (1979).

84. Burger, A. & Ramberger, R. On the polymorphism of pharmaceuticals and other molecular crystals. II. *Mikrochim Acta* **72**, 273–316 (1979).

85. Wolde, P. R. ten & Frenkel, D. Homogeneous nucleation and the Ostwald step rule. *Physical Chemistry Chemical Physics* **1**, 2191–2196 (1999).

86. Edueng, K., Mahlin, D. & Bergström, C. A. S. The Need for Restructuring the Disordered Science of Amorphous Drug Formulations. *Pharm Res* **34**, 1754–1772 (2017).

87. Dinunzio, J. C. *et al.* Fusion production of solid dispersions containing a heat-sensitive active ingredient by hot melt extrusion and Kinetisol dispersing. *Eur J Pharm Biopharm* **74**, 340–351 (2010).

88. Schönfeld, B., Westedt, U. & Wagner, K. G. Vacuum drum drying – A novel solvent-evaporation based technology to manufacture amorphous solid dispersions in comparison to spray drying and hot melt extrusion. *International Journal of Pharmaceutics* **596**, 120233 (2021).

89. Qiang, W., Löbmann, K., McCoy, C. P., Andrews, G. P. & Zhao, M. Microwave-Induced In Situ Amorphization: A New Strategy for Tackling the Stability Issue of Amorphous Solid Dispersions. *Pharmaceutics* **12**, 655 (2020).

90. Gupta, M. K., Vanwert, A. & Bogner, R. H. Formation of Physically Stable Amorphous Drugs by Milling with Neusilin. *Journal of Pharmaceutical Sciences* **92**, 536–551 (2003).

91. Willart, J.-F. *et al.* Solid-state amorphization of linaprazan by mechanical milling and evidence of polymorphism. *J Pharm Sci* **102**, 2214–2220 (2013).

92. Elisei, E. *et al.* Crystalline Polymorphism Emerging From a Milling-Induced Amorphous Form: The Case of Chlorhexidine Dihydrochloride. *Journal of Pharmaceutical Sciences* **107**, 121–126 (2018).

93. Graeser, K., Strachan, C., Patterson, J., Gordon, K. & Rades, T. Physicochemical Properties and Stability of Two Differently Prepared Amorphous Forms of Simvastatin. *Crystal Growth & Design* **8**, 128–135 (2008).

94. Huang, S. & Williams, R. O. Effects of the Preparation Process on the Properties of Amorphous Solid Dispersions. *AAPS PharmSciTech* **19**, 1971–1984 (2018).

95. Bisrat, M. & Nyström, C. Physicochemical aspects of drug release. VIII. The relation between particle size and surface specific dissolution rate in agitated suspensions. *International Journal of Pharmaceutics* **47**, 223–231 (1988).

96. Kesisoglou, F., Panmai, S. & Wu, Y. Nanosizing — Oral formulation development and biopharmaceutical evaluation. *Advanced Drug Delivery Reviews* **59**, 631–644 (2007).

97. Fukunaka, T., Sawaguchi, K., Golman, B. & Shinohara, K. Effect of particle shape of active pharmaceutical ingredients prepared by fluidized-bed jet-milling on cohesiveness. *J Pharm Sci* **94**, 1004–1012 (2005).

98. Willart, J.-F., Carpentier, L., Danède, F. & Descamps, M. Solid-state vitrification of crystalline griseofulvin by mechanical milling. *Journal of Pharmaceutical Sciences* **101**, 1570–1577 (2012).

99. Willart, J. *et al.* Direct crystal to glass transformation of trehalose induced by ball milling. *Solid State Communications* **119**, 501–505 (2001).

100. Dujardin, N. *et al.* Solid state vitrification of crystalline α and β-D-glucose by mechanical milling. *Solid State Communications* **148**, 78–82 (2008).

101. Willart, J. F., Dujardin, N., Dudognon, E., Danède, F. & Descamps, M. Amorphization of sugar hydrates upon milling. *Carbohydrate Research* **345**, 1613–1616 (2010).

102. Le Barc'H, N., Grossel, J. M., Looten, P. & Mathlouthi, M. Kinetic study of the mutarotation of D-glucose in concentrated aqueous solution by gas-liquid chromatography. *Food Chemistry* **74**, 119–124 (2001).

103. Papon, P., Leblond, J. & Meijer, P. H. E. *The Physics of Phase Transitions*. (Springer, 2002). doi:10.1007/978-3-662-04989-1.

104. Fecht, H. J. Defect-induced melting and solid-state amorphization. *Nature* **356**, 133–135 (1992).

105. Martin, G. & Barbu, A. PHASE STABILITY UNDER IRRADIATION. in *Decomposition of Alloys: the Early Stages* (eds. Haasen, P., Gerold, V., Wagner, R. & Ashby, M. F.) 70–76 (Pergamon, 1984). doi:10.1016/B978-0-08-031651-2.50014-8.

106. Martin, G. & Bellon, P. Driven Alloys. *Solid State Physics - Advances in Research and Applications* **50**, 189–331 (1996).

107. Hancock, B. C. & Parks, M. What is the true solubility advantage for amorphous pharmaceuticals? *Pharm Res* **17**, 397–404 (2000).

108. Alonzo, D. E., Zhang, G. G. Z., Zhou, D., Gao, Y. & Taylor, L. S. Understanding the behavior of amorphous pharmaceutical systems during dissolution. *Pharm Res* **27**, 608–618 (2010).

109. Wl, C. & S, R. Pharmaceutical applications of solid dispersion systems. *Journal of pharmaceutical sciences* **60**, (1971).

110. Hancock, B. C., Shamblin, S. L. & Zografi, G. Molecular mobility of amorphous pharmaceutical solids below their glass transition temperatures. *Pharm Res* **12**, 799–806 (1995).

111. Taylor, L. S. & Zografi, G. Spectroscopic characterization of interactions between PVP and indomethacin in amorphous molecular dispersions. *Pharm Res* **14**, 1691–1698 (1997).

112. Saluja, H., Mehanna, A., Panicucci, R. & Atef, E. Hydrogen Bonding: Between Strengthening the Crystal Packing and Improving Solubility of Three Haloperidol Derivatives. *Molecules* **21**, 719 (2016).

113. Saraf, I. *et al.* Forced Solid-State Oxidation Studies of Nifedipine-PVP Amorphous Solid Dispersion. *Mol. Pharmaceutics* **19**, 568–583 (2022).

114. Frank, D. S. & Matzger, A. J. Probing the Interplay between Amorphous Solid Dispersion Stability and Polymer Functionality. *Mol Pharm* **15**, 2714–2720 (2018).

115. Baird, J. A. & Taylor, L. S. Evaluation of amorphous solid dispersion properties using thermal analysis techniques. *Adv Drug Deliv Rev* **64**, 396–421 (2012).

116. Lin, X. *et al.* Physical Stability of Amorphous Solid Dispersions: a Physicochemical Perspective with Thermodynamic, Kinetic and Environmental Aspects. *Pharm Res* **35**, 125 (2018).

117. Gordon, J. M., Rouse, G. B., Gibbs, J. H. & Risen, W. M., Jr. The composition dependence of glass transition properties. *The Journal of Chemical Physics* **66**, 4971–4976 (2008).

118. Nair, R., Nyamweya, N., Gönen, S., Martínez-Miranda, L. J. & Hoag, S. W. Influence of various drugs on the glass transition temperature of poly(vinylpyrrolidone): a thermodynamic and spectroscopic investigation. *Int J Pharm* **225**, 83–96 (2001).

119. Meng, F., Gala, U. & Chauhan, H. Classification of solid dispersions: correlation to (i) stability and solubility (ii) preparation and characterization techniques. *Drug Dev Ind Pharm* **41**, 1401–1415 (2015).

120. Mahieu, A., Willart, J., Dudognon, E., Danède, F. & Descamps, M. A New Protocol To Determine the Solubility of Drugs into Polymer Matrixes. *Molecular pharmaceutics* **10**, (2012).

121. Sun, Y., Tao, J., Zhang, G. G. Z. & Yu, L. Solubilities of crystalline drugs in polymers: an improved analytical method and comparison of solubilities of indomethacin and nifedipine in PVP, PVP/VA, and PVAc. *J Pharm Sci* **99**, 4023–4031 (2010).

122. Marsac, P. J., Li, T. & Taylor, L. S. Estimation of Drug–Polymer Miscibility and Solubility in Amorphous Solid Dispersions Using Experimentally Determined Interaction Parameters. *Pharm Res* **26**, 139–151 (2009).

123. Marsac, P. J., Shamblin, S. L. & Taylor, L. S. Theoretical and Practical Approaches for Prediction of Drug–Polymer Miscibility and Solubility. *Pharm Res* **23**, 2417–2426 (2006).

124. Bellantone, R. A. *et al.* A Method to Predict the Equilibrium Solubility of Drugs in Solid Polymers near Room Temperature Using Thermal Analysis. *Journal of Pharmaceutical Sciences* **101**, 4549–4558 (2012).

125. Amharar, Y., Curtin, V., Gallagher, K. H. & Healy, A. M. Solubility of crystalline organic compounds in high and low molecular weight amorphous matrices above and below the glass transition by zero enthalpy extrapolation. *International Journal of Pharmaceutics* **472**, 241–247 (2014).

126. Knopp, M. M. *et al.* A Promising New Method to Estimate Drug-Polymer Solubility at Room Temperature. *Journal of Pharmaceutical Sciences* **105**, 2621–2624 (2016).

127. Latreche, M., Willart, J. F., Guerain, M., Danède, F. & Hédoux, A. Interest of molecular/crystalline dispersions for the determination of solubility curves of drugs into polymers. *International Journal of Pharmaceutics* **570**, 118626 (2019).

128. Van Duong, T. & Van den Mooter, G. The role of the carrier in the formulation of pharmaceutical solid dispersions. Part II: amorphous carriers. *Expert Opin Drug Deliv* **13**, 1681–1694 (2016).

129. Tekade, A. R. & Yadav, J. N. A Review on Solid Dispersion and Carriers Used Therein for Solubility Enhancement of Poorly Water Soluble Drugs. *Adv Pharm Bull* **10**, 359–369 (2020).

130. Démuth, B. *et al.* Downstream processing of polymer-based amorphous solid dispersions to generate tablet formulations. *International Journal of Pharmaceutics* **486**, 268–286 (2015).

131. Sauer, A., Warashina, S., Mishra, S. M., Lesser, I. & Kirchhöfer, K. Downstream processing of spray-dried ASD with hypromellose acetate succinate – Roller compaction and subsequent compression into high ASD load tablets. *Int J Pharm X* **3**, 100099 (2021).

132. Huffine, C. L. & Bonilla, C. F. Particle-size effects in the compression of powders. *AIChE J.* **8**, 490–493 (1962).

133. Hiestand, E. N., Wells, J. E., Peot, C. B. & Ochs, J. F. Physical Processes of Tableting. *Journal of Pharmaceutical Sciences* **66**, 510–519 (1977).

134. Leuenberger, H. & Rohera, B. D. Fundamentals of powder compression. I. The compactibility and compressibility of pharmaceutical powders. *Pharm Res* **3**, 12–22 (1986).

135. Van der Voort Maarschalk, K., Zuurman, K., Vromans, H., Bolhuis, G. K. & Lerk, C. F. Stress relaxation of compacts produced from viscoelastic materials. *International Journal of Pharmaceutics* **151**, 27–34 (1997).

136. Al-Mangour, B. Powder metallurgy of stainless steel: State-of-the art, challenges, and development. in 37–80 (2015).

137. Rada, S. & Kumari, A. Fast dissolving tablets: waterless patient compliance dosage forms. *Journal of Drug Delivery and Therapeutics* **9**, 303–317 (2019).

138. Parupathi, P., Dhoppalapudi, S., Parupathi, P. & Dhoppalapudi, S. Downstream processing of amorphous solid dispersions into tablets. *GSC Biological and Pharmaceutical Sciences* **22**, 170–177 (2023).

139. General Chapters: <1087> INTRINSIC DISSOLUTION. http://www.pharmacopeia.cn/v29240/usp29nf24s0_c1087.html.

140. O'Brien, F. E. M. The Control of Humidity by Saturated Salt Solutions. *J. Sci. Instrum.* **25**, 73 (1948).

141. EMA. ICH Q1A (R2) Stability testing of new drug substances and products - Scientific guideline. *European Medicines Agency* https://www.ema.europa.eu/en/ich-q1a-r2-stability-testing-new-drug-substances-drug-products-scientific-guideline (2018).

142. Medlicott, N. J., Jones, D. S., Tucker, I. G. & Holborow, D. Preliminary release studies of chlorhexidine (base and diacetate) from poly(ϵ-caprolactone) films prepared by solvent evaporation. *International Journal of Pharmaceutics* **84**, 85–89 (1992).

143. Haffajee, A. D., Yaskell, T. & Socransky, S. S. Antimicrobial Effectiveness of an Herbal Mouthrinse Compared With an Essential Oil and a Chlorhexidine Mouthrinse. *The Journal of the American Dental Association* **139**, 606–611 (2008).

144. Zeng, P., Rao, A., Wiedmann, T. S. & Bowles, W. Solubility properties of chlorhexidine salts. *Drug Dev Ind Pharm* **35**, 172–176 (2009).

145. Kondreddy, K., Ambalavanan, N., Ramakrishna, T. & Kumar, R. S. Effectiveness of a controlled release chlorhexidine chip (PerioCol™-CG) as an adjunctive to scaling and root planing when compared to scaling and root planing alone in the treatment of chronic periodontitis: A comparative study. *J Indian Soc Periodontol* **16**, 553–557 (2012).

146. Hosey, C. M., Chan, R. & Benet, L. Z. BDDCS Predictions, Self-Correcting Aspects of BDDCS Assignments, BDDCS Assignment Corrections, and Classification for more than 175 Additional Drugs. *AAPS J* **18**, 251–260 (2015).

147. Directory of Microbicides for the Protection of Materials: A Handbook / edited by Wilfried Paulus - University of Queensland.

148. Farkas, E., Kiss, D. & Zelkó, R. Study on the release of chlorhexidine base and salts from different liquid crystalline structures. *International Journal of Pharmaceutics* **340**, 71–75 (2007).

149. Dubovoy, V. *et al.* Synthesis, Characterization, and Antimicrobial Investigation of a Novel Chlorhexidine Cyclamate Complex. *Crystal Growth & Design* **20**, 4991–4999 (2020).

150. Fullriede, H. *et al.* pH-responsive release of chlorhexidine from modified nanoporous silica nanoparticles for dental applications. *BioNanoMaterials* **17**, 59–72 (2016).

151. Lizambard, M. *et al.* In-situ forming implants for the treatment of periodontal diseases: Simultaneous controlled release of an antiseptic and an anti-inflammatory drug. *International Journal of Pharmaceutics* **572**, 118833 (2019).

152. Sun, R., Zhang, J., Whiley, R. A., Sukhorukov, G. B. & Cattell, M. J. Synthesis, Drug Release, and Antibacterial Properties of Novel Dendritic CHX-SrCl2 and CHX-ZnCl2 Particles. *Pharmaceutics* **13**, 1799 (2021).

153. Alhalaweh, A., Alzghoul, A., Mahlin, D. & Bergström, C. A. S. Physical stability of drugs after storage above and below the glass transition temperature: Relationship to glass-forming ability. *International Journal of Pharmaceutics* **495**, 312–317 (2015).

154. Babij, N. R. *et al.* NMR Chemical Shifts of Trace Impurities: Industrially Preferred Solvents Used in Process and Green Chemistry. *Org. Process Res. Dev.* **20**, 661–667 (2016).

155. Bordet, P. *et al.* Solid State Amorphization of β-Trehalose: A Structural Investigation Using Synchrotron Powder Diffraction and PDF Analysis. *Crystal Growth & Design* **16**, 4547–4558 (2016).

156. Coffman, R. E. & Kildsig, D. O. Effect of Nicotinamide and Urea on the Solubility of Riboflavin in Various Solvents. *Journal of Pharmaceutical Sciences* **85**, 951–954 (1996).

157. Koziol, J. Studies on Flavins in Organic Solvents-I*. Spectral Characteristics of Riboflavin, Riboflavin Tetrabutyrate and Lumichrome. *Photochemistry and Photobiology* **5**, 41–54 (1966).

158. Höhne, G. W. H. Another approach to the Gibbs–Thomson equation and the melting point of polymers and oligomers. *Polymer* **43**, 4689–4698 (2002).

159. Lv, P., Guzik, M. N., Sartori, S. & Huot, J. Effect of ball milling and cryomilling on the microstructure and first hydrogenation properties of TiFe+4wt.% Zr alloy. *Journal of Materials Research and Technology* **8**, 1828–1834 (2019).

160. Krupa, A., Danède, F., Węgrzyn, A., Majda, D. & Willart, J.-F. Thinking of bosentan repurposing – A study on dehydration and amorphization. *International Journal of Pharmaceutics* **622**, 121846 (2022).

161. Han, J. *et al.* Mechanistic insight into gel-induced aggregation of amorphous curcumin during dissolution process. *European Journal of Pharmaceutical Sciences* **170**, 106083 (2022).

162. Jensen, L. G. *et al.* Amorphous is not always better-A dissolution study on solid state forms of carbamazepine. *Int J Pharm* **522**, 74–79 (2017).

163. Zou, Z. *et al.* Dissolution changes in drug-amino acid/biotin co-amorphous systems: Decreased/increased dissolution during storage without recrystallization. *European Journal of Pharmaceutical Sciences* **188**, 106526 (2023).

164. Pitt, K. G. & Heasley, M. G. Determination of the tensile strength of elongated tablets. *Powder Technology* **238**, 169–175 (2013).

165. Joshi, A. B., Patel, S., Kaushal, A. M. & Bansal, A. K. Compaction studies of alternate solid forms of celecoxib. *Advanced Powder Technology* **21**, 452–460 (2010).

166. Hancock, B., Carlson, G., Ladipo, D., Langdon, B. & Mullarney, M. Comparison of the mechanical properties of the crystalline and amorphous forms of a drug substance. *International journal of pharmaceutics* **241**, 73–85 (2002).

167. Heckel, R. W. Density-Pressure Relationships in Powder Compaction. *Transaction of the Metallurgical Society of AIME* 671–675 (1961).
168. Heckel, R. W. An analysis of powder compaction phenomena. *Transaction of the Metallurgical Society of AIME* 1001–1008 (1961).
169. Ilkka, J. & Paronen, P. Prediction of the compression behaviour of powder mixtures by the Heckel equation. *International Journal of Pharmaceutics* **94**, 181–187 (1993).
170. Azad, M. A. *et al.* On-Demand Manufacturing of Direct Compressible Tablets: Can Formulation Be Simplified? *Pharm Res* **36**, 167 (2019).
171. Pitt, K. G., Webber, R. J., Hill, K. A., Dey, D. & Gamlen, M. J. Compression prediction accuracy from small scale compaction studies to production presses. *Powder Technology* **270**, 490–493 (2015).
172. Ghimire, P., Shrestha, A., Sandhya, P., Bidur, C. & Samir, D. Pharmacopoeial comparison of in-process and finished product quality control test for pharmaceutical tablets. *GSC Biological and Pharmaceutical Sciences* **11**, 155–165 (2020).
173. Broman, E., Khoo, C. & Taylor, L. S. A comparison of alternative polymer excipients and processing methods for making solid dispersions of a poorly water soluble drug. *Int J Pharm* **222**, 139–151 (2001).
174. Patterson, J. E. *et al.* Preparation of glass solutions of three poorly water soluble drugs by spray drying, melt extrusion and ball milling. *International Journal of Pharmaceutics* **336**, 22–34 (2007).
175. Nielsen, L. H., Rades, T. & Müllertz, A. Stabilisation of amorphous furosemide increases the oral drug bioavailability in rats. *International Journal of Pharmaceutics* **490**, 334–340 (2015).
176. Kondo, K. & Rades, T. Solventless amorphization and pelletization using a high shear granulator. Part I; feasibility study using indomethacin. *European Journal of Pharmaceutics and Biopharmaceutics* **181**, 147–158 (2022).
177. LYCOAT RS 720 Pregelatinized hydroxypropyl pea starch Medium viscosity. *Roquette.com* https://www.roquette.com/innovation-hub/pharma/product-profile-pages/lycoat-rs-720-hydroxypropyl-pea-starch.
178. Descamps, M., Aumelas, A., Desprez, S. & Willart, J. F. The amorphous state of pharmaceuticals obtained or transformed by milling: Sub-Tg features and rejuvenation. *Journal of Non-Crystalline Solids* **407**, 72–80 (2015).
179. Seo, J.-A. *et al.* The glass transition temperatures of sugar mixtures. *Carbohydrate Research* **341**, 2516–2520 (2006).
180. Salah, A. M. Effets du broyage mécanique sur l'état physique des matériaux pharmaceutiques vitreux. (Lille 1, 2015).
181. *Vitamin and mineral requirements in human nutrition*. (World Health Organization ; FAO, 2004).
182. Bourgonje, A. R. *et al.* The effect of riboflavin supplementation on the systemic redox status in healthy volunteers: A post-hoc analysis of the RIBOGUT trial. *Free Radical Biology and Medicine* **190**, 169–178 (2022).
183. Means, J. A., Grenfell, T. C. & Hedger, F. H. Polymorphism of Riboflavin. *Journal of the American Pharmaceutical Association (Scientific ed.)* **32**, 51–53 (1943).
184. Gloor, A. Process for the purification of riboflavin. (2010).
185. Guerain, M. *et al.* Structure determination of riboflavin by synchrotron high-resolution powder X-ray diffraction. *Acta Crystallographica Section C* **77**, 800–806 (2021).
186. Ferreira, L. T., Alarcon, R. T., Perpétuo, G. L. & Bannach, G. Investigation and characterization by TG/DTG–DTA and DSC of the fusion of Riboflavin, and its interaction with the antibiotic norfloxacin in the screening of cocrystal. *J Therm Anal Calorim* **136**, 581–588 (2019).
187. Latreche, M., Willart, J.-F., Guerain, M., Hédoux, A. & Danède, F. Using Milling to Explore Physical States: The Amorphous and Polymorphic Forms of Sulindac. *Journal of Pharmaceutical Sciences* **108**, 2635–2642 (2019).
188. Joiris, E., Di Martino, P., Berneron, C., Guyot-Hermann, A. M. & Guyot, J. C. Compression behavior of orthorhombic paracetamol. *Pharm Res* **15**, 1122–1130 (1998).
189. Dedroog, S., Pas, T., Vergauwen, B., Huygens, C. & Mooter, G. Solid-state analysis of amorphous solid dispersions: Why DSC and XRPD may not be regarded as stand-alone techniques. *Journal of Pharmaceutical and Biomedical Analysis* **178**, 112937 (2019).

Appendix 1

Co-amorphization of Chx and PVP using spray-drying*

A solvent based approach, i.e. spray-drying was tested for the amorphization of Chx. First of all, the idea was to find a suitable solvent for this technique in which Chx would be soluble in sufficient proportions. However, several organic solvent and mixtures of solvents were tested but the only solvent dissolving Chx (6%) was DMSO. As this particular solvent boils only at 189°C, it is not very appropriate for spray-drying. Furthermore, as the thermal degradation of Chx starts around 150°C, it is not possible An attempt was nonetheless performed, using an inlet temperature around 110°C but in addition, a freeze-drying was performed in order to evaporate as much DMSO as possible. An example of the results obtained can be found below, for a Chx/PVP (50/50, w/w) mixture.
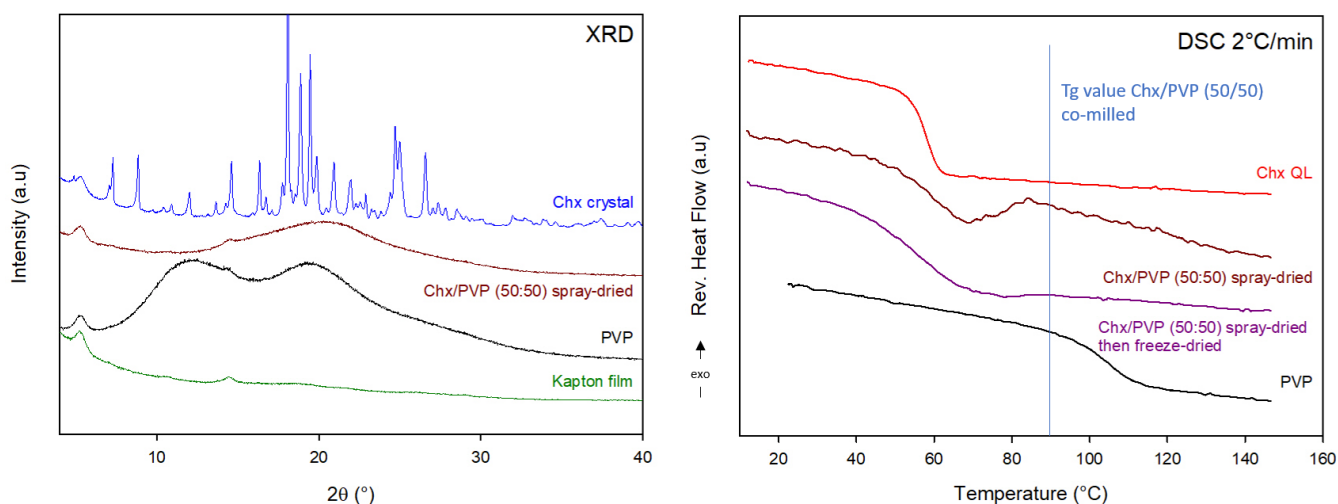

Figure 136 – a) X-ray diffraction patterns of, Chx crystal, Chx/PVP (50/50, w/w) after spray-drying, PVP and Kapton film and b) the DSC scans (2°C/min) with of the Chx quenched liquid, of PVP and of the Chx/PVP (50/50, w/w) mixture both after spray-drying and after spray-drying and subsequent freeze-drying.

The X-ray pattern of the spray-dried mixture only shows a diffusion halo characteristic of an amorphous form. It must be noted that the peaks detected are due to the Kapton film. The DSC thermograms (reversing signal) reveal a depressed Tg for both the spray-dried and the spray-dried then freeze-dried mixture compared to the Tg of the corresponding co-amorphous mixture obtained by co-milling. This can be explained by the significant presence of the DMSO in the sample even though two drying processes were performed. It was thus deduced that a solvent-based process was not a suitable process for Chx.

*These experiments were conducted at the KU Leuven, in the laboratory directed by Prof. Guy Van den Mooter.

Appendix 2

Calculation of the amorphous fraction upon milling

When the heating of the amorphous forms leads to a total recrystallization, the amorphous fraction is usually estimated by calculating the ratio of the of the crystallization and melting enthalpies. However, the melting enthalpy has to corrected in order to consider the temperature difference between the two events.

Therefore, the amorphized fraction of the milled material is thus given by the equation:

$$X_{am}(t) = \frac{\Delta H_c^{Tc}(milled, t)}{\Delta H_m^{Tc}(crystal)}$$

With:

- Tc as average temperature of recrystallization.
- ΔH_m and ΔH_c as the melting and crystallization enthalpies, respectively.
- ΔH_m^{Tc} (crystal) as the enthalpy of melting of the crystal extrapolated at the crystallization temperature T_c

Indeed, as illustrated in the figure below, the melting enthalpy has to be extrapolated at the crystallization temperature of the amorphous material.
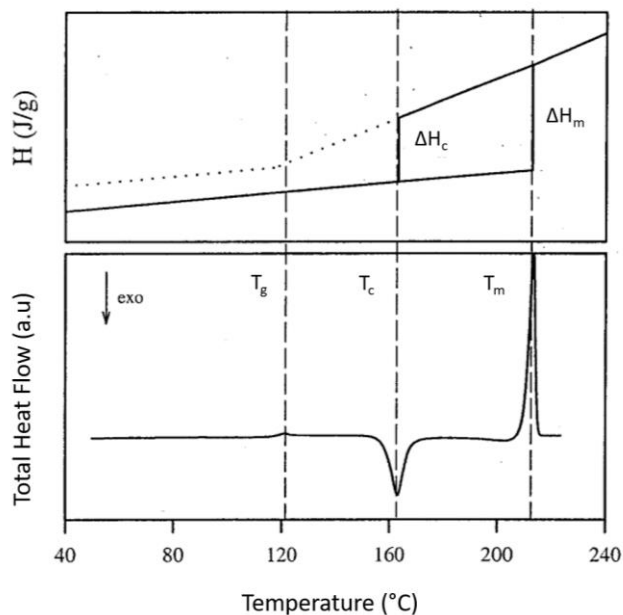
When the recrystallization of the amorphous material and its melting are separated by a wide range of temperatures, the amorphous sample can recrystallize entirely without having its recrystallization enthalpy at the same value as its melting enthalpy. Therefore, the melting enthalpy has to be estimated as if it was occurring at the crystallization temperature, hence, the correction applied.

This correction can be performed as presented below:

$$\Delta H_m^{Tc}(crystal) = \Delta H_c^{Tc}(milled) + (T_m - T_c)\left[\left(\frac{\partial H^{liq}}{\partial T}\right) - \left(\frac{\partial H^c}{\partial T}\right)\right]$$

$$\Delta H_m^{Tc}(crystal) = \Delta H_c^{Tc}(milled) + (T_m - T_c)(Cp^{liq} - Cp^c)$$

Therefore, $\Delta H_m^{Tc}(crystal) = \Delta H_c^{Tc}(milled) + (T_m - T_c) * \Delta Cp$

Furthermore, in our particular case, the amorphous fraction did not recrystallize entirely which is why the ration of the melting enthalpies of the milled material and of the crystal had to be considered as well.

Therefore, $X_{am}(t) = X_{am}(recryst) + X_{am}(not\ recryst)$

And finally: $X_{am}(t) = \frac{\Delta H_c^{Tc}(milled,t)}{\Delta H_m^{Tc}(crystal)} + \frac{\Delta H_m(crystal) - \Delta H_m(milled,t)}{\Delta H_m\ (crystal)}$

Appendix 3

Co-amorphization of Rf and Lycoat using spray-drying*

A solvent based approach, i.e. spray-drying was tested for the amorphization of Rf. First of all, the idea was to find a suitable solvent for this technique in which Rf would be soluble in sufficient proportions. However, several organic solvent and mixtures of solvents were tested but the only solvent dissolving Rf (2%) was DMSO. As this particular solvent boils only at 189°C, it is not very appropriate for spray-drying. An attempt was nonetheless performed, using an inlet temperature around 140°C, but in addition, a freeze-drying was performed in order to evaporate as much DMSO as possible. An example of the results obtained can be found below, for a Rf/Lycoat (50/50, w/w) mixture.
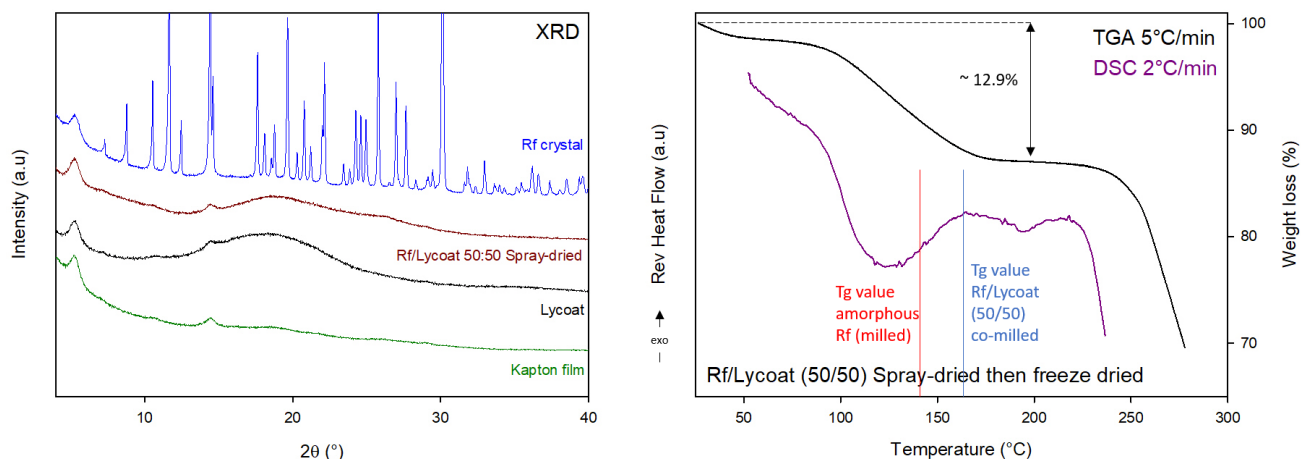

Figure 137 – a) X-ray diffraction patterns of, Rf crystal, Rf/Lycoat (50/50, w/w) after spray-drying, PVP and Kapton film and b) the DSC and TGA scans (2°C/min) of the Rf/PVP (50/50, w/w) mixture after spray-drying and subsequent freeze-drying.

The X-ray pattern of the spray-dried mixture only shows a diffusion halo characteristic of an amorphous form. It must be noted that the peaks detected are due to the Kapton film. The DSC thermogram (reversing signal) reveals a depressed Tg for the spray-dried then freeze-dried mixture compared to both the Tgs of the corresponding co-amorphous mixture obtained by co-milling and of pure amorphous Rf. This can be explained by the significant presence of the DMSO in the sample even though two drying processes were performed. Furthermore, the TGA scan reveals a weight loss of around 12.9% from RT to 200°C which proves the presence of DMSO in the sample. It was thus deduced that a solvent-based process was not a suitable process for Rf.

*These experiments were conducted at the KU Leuven, in the laboratory directed by Prof. Guy Van den Mooter.

Appendix 4

Co-amorphization of Rf and Lycoat using HME*

A heat-based approach, i.e. HME was tested for the amorphization of Rf, using a mini-extruder. Even though Rf is subjected to a strong degradation upon melting, the idea was to try the co-amorphization of the API with a polymer whose Tg would be low enough to prevent this degradation. Furthermore, as this process involves mixing by shear force, the solubilization of Rf in PVP could be forced. Another polymer was also tested, i.e. soluplus as it exhibits a lower Tg (around 75°C) than PVP. An example of the results obtained can be found below, for two Rf/PVP mixtures and for a Rf/soluplus mixture.
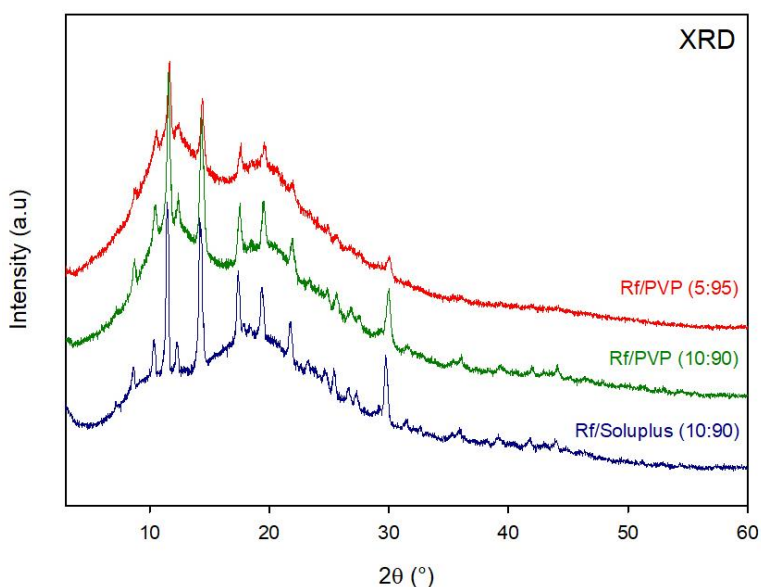

Figure 138 – X-ray diffraction patterns of, Rf/PVP (5/95, w/w), Rf/PVP (10/90, w/w) and of Rf/soluplus (10/90, w/w), after HME process (180°C, 4min mixing, 150rpm).

The X-ray pattern reveal for each mixture tested Bragg peaks corresponding to the characteristic peaks of crystalline Rf. The poor solubility of Rf in those polymers prevented from an amorphization of the API during the process. Therefore, it was deduced that a heat-based approach was not suitable (with our excipients) for the amorphization of Rf.

*These experiments were conducted in Castres (Plateforme Gala), in the laboraorty directed by Dr. Maria-Inês Ré.

Appendix 5

Exploration of the physical states of riboflavin (free base) by mechanical milling

C. Henaff[1,2], J. Siepmann[2], F. Siepmann[2], F. Danède[1], M.-N. Avettand-Fènoël[1], J. Vérin[2], A. Fadel[3], J.-F. Willart[1]

[1] Univ. Lille, CNRS, INRAE, Centrale Lille, UMR 8207

UMET - Unité Matériaux et Transformations F-59000 Lille, France

[2] Univ. Lille, Inserm, CHU Lille, U1008, F-59000 Lille, France

[3]Univ. Lille, CNRS, INRAE, Centrale Lille, Univ. Artois, FR 2638 - IMEC - Institut Michel-Eugène Chevreul, F-59000 Lille, France

Corresponding author: Jean-François Willart

Abstract

Amorphous riboflavin (free base) could be produced for the first time via high energy ball milling of a commercial crystalline form (Form I). Importantly, this solid state amorphization process allowed to circumvent chemical degradation occurring during melting as well as the lack of suitable solvents, which are required for amorphization via spray- or freeze-drying. The amorphous state of riboflavin was thoroughly characterized, revealing a complex recrystallization pattern upon heating, involving two enantiotropic polymorphic forms (II and III) and a dihydrate. The glass transition temperature (T_g) and heat capacity (C_p) jump of the

amorphous form were determined as 144°C and 0.68 J/g/°C. Moreover, the relative physical stability of the different physical states has been elucidated, e.g., at room temperature: I > II > III. The following rank order was observed for the dissolution rates in water at 37 °C during the first 4 h: amorphous > III ≈ II> I. Afterwards, a dihydrate crystallized from the solutions of amorphous and metastable crystalline riboflavin forms, the solubility of which was well above the solubility of the stable Form I.

1. Introduction

Drugs can exist in different physical states, like stable and metastable polymorphic forms [1]–[4], or in an amorphous form [5], [6]. These different forms can potentially have a strong repercussion on their key properties, including in particular their stability during storage [7], [8] and their solubility in aqueous body fluids [9], [10]. Thus, the physical state of a drug might substantially impact the therapeutic efficacy of the treatment. In general, the solubility of a drug increases when the Gibbs free energy of the physical form increases. Thus, often an improvement in solubility comes at the expense of physical stability [11], [12]. Controlling and manipulating the physical state of drugs is, hence, an important practical challenge, in particular for the formulation of poorly soluble drugs [13]–[16]. Furthermore, the physical state of a drug might change during manufacturing and long-term storage [17]. This is why it is essential to explore as thoroughly as possible all the physical states of a drug, their physical (and chemical) (in)stabilities, as well as their solubility and dissolution kinetics [18], [19].

Several processes can be used to render a drug amorphous, including melt quenching [20], hot melt extrusion [21], [22],[23], spray-drying [24], [25], freeze-drying [26], [27], high shear granulation [28] and mechanical milling [29]. The technology "KinetiSol® Dispersing" combines the effects of fusion/heat and frictional/shear energies [30]. Melt quenching and hot melt extrusion have the disadvantage of the need to heat the material up to its melting point, which often induces unacceptable thermal degradation. Spray-drying and freeze-drying require the dissolution of the drug in a solvent, which can also induce chemical changes like mutarotation [31]. Moreover, finding an effective and non-toxic solvent is often a challenge for poorly soluble drugs. Contrary to the previous techniques, the amorphization upon *milling* occurs directly in the solid state, so that it does not require any heating or dissolution stages of the drug. Milling, thus, often allows rendering drugs amorphous without any chemical changes, so that it appears as an interesting alternative to the other amorphization techniques.

Riboflavin ($C_{17}H_{20}N_4O_6$) free base, also known as vitamin B2, is a coenzyme in oxidation and reduction reactions [32]. It is essential for cell growth, and commonly used in parenteral nutrition [33]. Even if it is considered to be a "water soluble" vitamin [34], its solubility in this solvent is very limited, as it only reaches around 0.08 mg/mL at 30°C [35]. Evidence of polymorphism was briefly mentioned in the literature along with different hydrates [36], [37]. However so far, to the best of our knowledge, only the crystalline structure of the commercial form (Form I) could be determined and was found to be orthorhombic (space group $P2_12_12_1$) [38]. Moreover, little is known about its amorphous state, which cannot be obtained by quenching the liquid (because of a pronounced chemical degradation upon melting), nor by spray- or freeze-drying due to the lack of an appropriate solvent [35], [39].

The objective of this paper was to use high energy milling to prepare and thoroughly characterize the amorphous state of riboflavin (free base), which is currently poorly investigated (including for instance the determination of its glass transition temperature and the related heat capacity jump). Special attention was paid to the recrystallization mechanism of the amorphous form upon heating, which revealed to be complex, involving two polymorphic forms. Moreover, the relative stability of the different physical states of riboflavin were to be established and their dissolution kinetics in water at 37 °C to be monitored.

2. Materials and Methods

2.1. Materials

Riboflavin free base (purity 98%), also known as vitamin B2, was purchased from ACROS organics (Geel, Belgium). The material was used as received. Ultra-pure water was obtained from Veolia (Vendin le Vieil, France), acetonitrile (HPLC grade) from Carlo Erba (Val de Reuil, France), formic acid and dimethyl sulfoxide from Sigma Aldrich (Seelze, Germany).

2.2. Ball milling

Ball milling was performed at room temperature (RT) using a high energy planetary mill (Pulverisette 7 Fritsch, Idar Oberstein, Germany). About 1.1g samples were placed into ZrO_2 milling vessels (40mL), containing 7 milling balls (ZrO_2, Ø = 15mm) in order to have a ball/sample ratio of 75:1 w/w. The rotation speed of the solar disk was set to 400 rpm. The reverse mode was selected, so that after each milling cycle, the direction of rotation changed. This rotation speed corresponded to an average acceleration of the milling balls of 5 g (g = 9.81 m/s^2 being the acceleration of gravity). Milling cycles (20 min) were alternated with pause periods (10 min) in order to prevent heating of the samples during the process. Heat-sensitive stickers on the milling vessels indicated that the temperature of the latter reached approximately 35°C under the given conditions [40]. The milling times (t_m) were varied between "zero" (non-milled material) and 32 h, as indicated.

2.3. Thermogravimetric analysis (TGA)

TGA measurements were performed using the Q500 apparatus from TA instruments (Guyancourt, France). A small amount of sample (between 5 and 8 mg) was placed into an open aluminum pan on a weighing scale. Both, the sample and the weighing scale, were kept in a dry atmosphere using a constant

flow rate (50 mL / min) of highly pure nitrogen gas (99.999 %). The temperature reading was calibrated with the measurements of the Curie points of alumel and of nickel (provided by TA instruments). The mass reading was calibrated using certified calibration weights (TA instruments). All scans were performed at 5 °C/min from room temperature to 550 °C.

2.4. Differential Scanning Calorimetry (DSC)

DSC thermograms were recorded with a Q20 apparatus from TA Instruments (Guyancourt, France), connected to a refrigerated cooling system. During all measurements, the calorimeter head was flushed (50 mL/min) with highly pure nitrogen gas (99.999 %). Temperature and enthalpy readings were calibrated using pure indium at the same scan rates as used during the measurements. Small sample sizes (between 2 and 5 mg) were used to provide good thermal conductivity and sharp enthalpic events. The samples were placed in open aluminum pans (container without lid) to allow the release of free water, potentially adsorbed during the milling process. Only when heating to temperatures above the degradation temperature of riboflavin, hermetic high-pressure aluminum pans were used (to avoid any contamination of the DSC cell). For all samples, a preliminary 20 min annealing at 90°C was performed in the DSC in order to remove, as much as possible, the water absorbed during the sample preparation. All scans were performed using an average heating rate of 5 °C/min.

2.5. Hyper Differential Scanning Calorimetry (Hyper DSC)

Hyper DSC scans were recorded at a heating rate of 300 °C/s using the Flash DSC2+ from Mettler Toledo (Viroflay, France), under argon flushing. The high scanning rate allowed by-passing transformations which are kinetically slow, like recrystallizations or polymorphic transformations.

2.6. Powder X-Ray Diffraction (PXRD)

Powder X-ray diffraction measurements were performed with a PanAlytical X'PERT PRO MPD (Almelo, The Netherlands) diffractometer (λCuK_{α} = 1.5418 Å for combined $K_{\alpha}1$ and $K_{\alpha}2$), equipped with an X'celerator detector (Almelo, The Netherlands) allowing acquisition of diffraction patterns from 2θ= 3 to 60 °, with a scan step of 0.0167 °/s. Samples were placed into Lindemann glass capillaries (Ø = 0.7 mm), installed on a rotating sample holder to avoid artifacts due to preferential orientations of crystallites. Thermal treatment of the samples was performed in the calorimeter, followed by sample removal from the DSC pan and immediate PXRD analysis. In some specific cases, to observe the evolution of the sample upon heating, the sample was placed on a metallic plate, in an Anton Paar chamber at atmospheric pressure. The heating rate was set to 5 °C/min.

2.7. ^{1}H Nuclear Magnetic Resonance (NMR)

NMR analyses were conducted on a Brucker AVANCE 300 MHz apparatus (Rheinstetten, Germany) at 20°C. A few milligrams of material were dissolved in 0.5 mL dimethyl sulfoxide in 5 mm diameter NMR tubes. For each sample, 64 scans were recorded (1 scan/s) to improve the signal statistic.

2.8. Scanning electron microscopy (SEM)

SEM pictures were taken to determine the morphology of the particles, using a JEOL Field Emission apparatus (JSM-7800F, Tokyo, Japan). Samples were mounted on a SEM stub, using ribbon carbon double-sided adhesive. To avoid surface charging, samples were chromium coated (100 Å) by electro-sputting under vacuum prior to SEM observations. The observations were performed at 2 kV acceleration voltage, with small probe current and the lowest objective lens aperture to reduce beam damage on the sample surface.

2.9. Riboflavin dissolution kinetics

Excess amounts of riboflavin (about 150 mg) were exposed to 10 mL ultra-pure water in amber flasks. The latter were placed into a horizontal shaker (37 °C, 80 rpm; GFL 3033; Gesellschaft fuer Labortechnik, Burgwedel, Germany). At predetermined time points, 300 µL samples were withdrawn, filtered (PVDF syringe filter 0.22 µm, Agilent technologies, Santa Clara, USA) and analyzed for their riboflavin content by reverse phase HPLC-UV analysis (Waters Alliance 2695 separation module, Waters 2489 UV/vis detector) as follows: 10 µL samples were injected into a polar column (Luna omega 3 µm C18 100 Å, 150 x 4.6 mm; Phenomenex, Le Pecq, France). The flow rate was set to 0.8 mL/min. The mobile phase was a 85:15 (v:v) blend of 0.1% aqueous formic acid solution and acetonitrile. The column was kept at room temperature and the detection wavelength was set to 270 nm. The calibration curve was determined for riboflavin concentrations ranging from 0.1 to 40 mg/L ($R^2 > 0.999$). Each experiment was performed in triplicate. Mean values +/- standard deviations are reported.

3. Results and Discussion

3.1. Solid state amorphization by milling

The blue curve at the top of Figure 1 shows the X-ray diffraction patterns of commercial riboflavin (used as received) recorded at room temperature. It shows many Bragg peaks, which are characteristic of a crystalline state and their positions correspond to that of Form I, recently determined by Guerain et al. [38]. The black curve in Figure 2 shows the TGA scan of a commercial riboflavin (Form I), recorded upon heating (5 °C/min). It shows a significant weight loss (about 70%) starting above 250 °C, revealing a pronounced thermal degradation of the vitamin. Figure 2 also shows the heating DSC scan (5 °C/min) of riboflavin placed in a hermetically closed, high-pressure pan (run 1). It reveals a sharp endothermic peak around 290 °C, which superimposes on a wide exothermic event. The endotherm corresponds to the melting of Form I, while the exotherm is due to the chemical degradation revealed by TGA (Figure 2). It

is worth noting that degradation starts slightly before melting, indicating that the degradation is not due to the melting process itself. This degradation was already reported in literature [41] and prevents from accurately determining the melting temperature of the vitamin and from safely obtaining the amorphous form via a classical quench of the liquid. Figure 3 shows the ^{1}H NMR spectra of both, crystalline (Form I) and melted riboflavin, after dissolution in dimethyl sulfoxide. The two spectra show significant differences, as many new peaks appeared after the melting (e.g. between 2.0 and 2.3 ppm, between 3.8 to 4.2 ppm, between 7.1 to 7.8 ppm and at 11.3 ppm). These peaks confirm the chemical degradation of riboflavin upon melting and the impossibility to obtain the amorphous state by quenching the melt. To overcome this hurdle, we tried to obtain the amorphous state directly in the solid state, by milling [42] the crystalline Form I.

The red curve in Figure 1 shows the X-ray diffraction patterns of riboflavin Form I after 32 h milling. It can be noticed that all Bragg peaks have completely disappeared, leading to the appearance of a large halo of diffusion, characteristic for an amorphous form. The red curve in Figure 2 shows the corresponding heating DSC scans (5 °C/min): recorded using an open pan from 45 to 240 °C (run 2) and a hermetically closed, high pressure pan from 240 to 310 °C (run 3). This latter type of pan was used to avoid the contamination of the DSC cell by the degradation products generated upon melting. The 2 vertical slashes separate the two runs. Run 2 shows a heat capacity (Cp) jump (ΔCp = 0.68 J/g/°C), characteristic of a glass transition. This proves that a direct "crystal to glass transformation" occurred during the milling process. The red curve in Figure 3 shows the ^{1}H NMR spectrum of amorphous riboflavin obtained by milling Form I (32 h). It appears to be identical with the spectrum of the commercial riboflavin, except for one peak at 2.09 ppm, which is attributed to an acetone residue [43], stemming from the cleaning of the NMR tube. Moreover, no signs of chemical degradation were detected compared to the spectrum of the quenched liquid. It, thus, appears that mechanical milling is able to safely produce amorphous riboflavin, making it possible to determine for the first time the glass transition temperature of this compound: Tg = 144°C.

3.2. Polymorphism of riboflavin

In Figure 2 (red curve), further heating of the milling induced amorphous riboflavin (run 2) reveals two exothermic events. The first one occurs at around 185 °C (ΔH_1 = 58.2 J/g) and is characteristic of a recrystallization. The diffractogram of the milled material subsequently heated to 200°C, recorded at room temperature (i.e. just above the first exotherm), is reported in Figure 1 (black curve). It shows well defined Bragg peaks, characteristic of a crystalline state. Moreover, these peaks are clearly different from those characteristic for Form I (see for instance characteristic peaks marked with a ★ or ◆ in Figure 1). This indicates that the recrystallization occurred at 185°C toward another crystalline form of riboflavin, called "Form III" ([37]). The second exotherm in run 2 (red curve in Figure 2) occurs at around 230 °C (ΔH_2 = 34.1 J/g) and is characteristic of a "crystal to crystal" transformation. The diffractogram of the milled material recorded at room temperature after subsequent heating to 240°C (i.e. just above the second exotherm), is also reported in Figure 1 (green curve). It shows well defined Bragg peaks, which are different from those of Forms I and III (see for instance characteristic pics marked with a ★, ◆ or ▲ in Figure 1). This confirms that the second exotherm indicates a polymorphic transformation, and puts into evidence a further polymorphic form of riboflavin, called "Form II" [37]. Above 240 °C, run 3 shows an endothermic peak due to the melting of Form II, being superimposed with the exothermic peak due to the degradation of riboflavin (red curve in Figure 2). It can be noted that the melting of Form II is depressed compared to the melting of Form I.

The green and black curves in Figure 3 show the ^{1}H NMR spectra of both, Form II and Form III. They appear to be identical with the spectrum of Form I, with an additional peak attributed to residual acetone (as for the milled material, please see above). Furthermore, no sign for vitamin degradation was observed, which indicates that the polymorphic forms of riboflavin can be safely produced by the described milling and subsequent heating procedures.

3.3. Influence of the milling time upon recrystallization

Figure 4 shows XRD patterns of riboflavin recorded after various milling times ranging from "zero" (no milling) to 32 h. A progressive flattening and broadening of the Bragg peaks can be noted. The decrease in peak heights indicates the increasing amorphization of the material, while the broadening signals both: size reduction and the deformation of the remaining crystallites induced by the mechanical impacts of the milling balls. After 6 h milling, the Bragg peaks totally disappeared, indicating that the material was fully amorphized. No further evolution of the X-ray diffraction patterns can be detected for longer milling times (up to 32 h).

The corresponding heating DSC scans (5 °C/min) are illustrated in Figure 5. They show the progressive development of a heat capacity (Cp) jump at the glass transition temperature (Tg = 144°C), followed by a crystallization exotherm. The Cp jump becomes stationary from 6 h milling, which confirms that the amorphization upon milling is complete after that time period. The evolution of the exotherm is more complex: It shows in particular a shift from 160 to 180 °C, which reveals an increasing stability of the amorphous fraction for increasing milling times. Moreover, noticeable modifications of the thermograms are still observed for longer milling times. In particular, a second exotherm develops after the recrystallization. It is already detectable after 3 and 6 h milling through a shouldering on the right-hand side of the recrystallization exotherm and then shifts toward higher temperatures up to 230 °C after 32 h milling. This exothermic peak clearly corresponds to the polymorphic transformation "Form III → Form II" identified in *section 3.2*. This indicates that the structural composition of the recrystallized fraction depends on the milling time. To analyze this point in more detail, the structure of the recrystallized material has been investigated by XRD.

Figure 6 shows XRD patterns of riboflavin recorded at room temperature after milling for 50 min, 6, 12 or 32 h and subsequent heating (5 °C/min) to 210, 176, 195 and 200 °C, respectively (i.e. after recrystallization of the milled materials). It shows that for 50 min milling and heating to 210 °C, the X-ray diffraction patterns of the recrystallized material only shows the Bragg peaks of Form I, while Bragg peaks characteristic for Forms II and III cannot be detected. This indicates that for short milling times the portion

of riboflavin, which has been transformed into an amorphous state (Figure 4) recrystallizes entirely towards the initial Form I. This can be explained by the numerous remaining crystallites of Form I after 50 min milling, which act as seeds for the recrystallization of Form I upon heating. Interestingly, complete amorphization upon milling for milling times > 6 h and subsequent heating leads to the crystallization of different polymorphic forms: as it can be seen in Figure 6, the X-ray diffraction patterns of the samples, which had been milled for 6, 12 or 32 h, followed by heating to 176, 195 and 200 °C, do not show the Bragg peaks of Form I. Instead, they show the Bragg peaks of the Forms II and III. Moreover, with increasing milling time the Bragg peaks characteristic of Form III become more pronounced, while those of Form II decrease and finally disappear after 32 hours of milling. This indicates that riboflavin is fully amorphized upon milling for more than 6 h and recrystallizes as a mixture of Forms II and III, with a proportion of Form III, which increases with increasing milling time. Such a behavior could be due to the apparent stabilization of amorphized riboflavin with increasing milling time, shifting the recrystallization range toward higher temperatures, at which the nucleation and growth rates of Form III are higher than those of Form II.

3.4. Phase diagram of riboflavin

To determine the relative stability of Forms I, II and III, it is necessary to rank their melting temperatures. However, the melting temperatures of Forms I and II cannot be accurately determined due to the strong degradation accompanying the melting process (see runs 1 and 3 in Figure 2). Moreover, the melting of Form III cannot be observed as it is preceded by the conversion "Form III → Form II" (see run 2 Figure 2). To overcome these difficulties, the three forms have been analyzed by flash DSC at a heating rate of 300 °C/s. Such a high heating rate makes it possible to by-pass the transformation "Form III → Form II" in order to observe the melting of Form III, and strongly limit the degradation accompanying the melting process. The corresponding scans are reported in Figure 7 and do not show any trace of the transformation "Form III → Form II", nor noticeable degradation. It appears that the melting temperatures of the three forms rank as follows: Tm(I)>Tm(III)>Tm(II). Moreover, the exothermic character of the

transformation "Form III → Form II" seen in run 2 in Figure 2 indicates that the entropy of Form III is higher than that of Form II. As a result, these two forms are enantiotropically related as schematized in the Gibbs free enthalpy diagram reported in Figure 8.

3.5. Dissolution kinetics of the different forms of riboflavin

In order to monitor the dissolution kinetics of the different riboflavin forms, sufficient sample quantities were required (about 150 mg). Form I was used as received. The amorphous form was obtained by milling Form I for 32 h in a high energy planetary mill (Pulverisette 7 Fritsch). Samples of Forms III and II were produced as follows: milling of Form I for 32 h in the planetary mill, followed by heating in a DSC Tzero open pan (5 °C/min) to either 200 or 250 °C, respectively. This procedure was repeated several times in order to produce the required amounts (150 mg). The obtained samples were slightly hand milled and the powders pooled.

Figure 9 shows SEM pictures of the different powders used for dissolution testing. Amorphous riboflavin and Form I powders consisted of tiny particles. The amorphous particles formed aggregates, those of Form I were needle-shaped. In contrast, the particles of Form II and Form III were much larger, because they were prepared by manual milling (versus planetary milling). But at higher magnification, also in these cases, tiny needle-shaped crystals could be observed.

The dissolution kinetics of these powders in ultra-pure water at 37 °C under non-sink conditions (excess of solid riboflavin) are illustrated in Figure 10. Clearly, amorphous riboflavin led to the highest concentration of dissolved riboflavin within the first few hours: up to around 1860 mg/L. But at later time points (after 24 h), this concentration decreased to about 330 mg/L, and then leveled-off. In contrast, Form I was much less soluble (around 90 mg/L) and reached its plateau concentration within the first few hours. Forms II and III reached intermediate concentrations of dissolved riboflavin during the first 4 h: about 450 mg/L. But the latter decreased again, reaching plateau values of approximately 350 and 300 mg/L, respectively, after about 7 d.

The observed vitamin dissolution patterns can be explained as follows: The solubility of the amorphous riboflavin is highest, leading to the highest observed *dissolved* vitamin concentrations. However, at later time points (after at least 4 h), the vitamin recrystallizes into a less soluble form (red curve in Figure 10). Form I exhibits the lowest solubility (which is consistent with the highest melting point observed by flash DSC, Figure 7), leading to the lowest concentrations of dissolved riboflavin. Forms II and III have intermediate solubilities, resulting in intermediate dissolution rates. However, also in these cases a different form precipitates at later time points during the experiment.

To better understand which riboflavin form crystallizes during the dissolution measurements, the solids obtained after 7 d were separated by filtration, dried (under vacuum, room temperature, overnight) and analyzed by XRD and TGA. Figure 11 shows the XRD patterns of the residue obtained at the end of the dissolution study of amorphous riboflavin. Interestingly, it differs from those of Forms I, II and III (see in particular the peak at 4.3 °), but seems to be similar to that of a dihydrate reported in the literature [31]. The TGA scan (5 °C/min) of the residue, which is reported in the insert of Figure 11, shows a mass loss of close to 6.0 % between 20 and 80 °C, while a mass loss of 9.2 % would be expected for the dehydration of a dihydrate. The difference may be attributed to a slight dehydration occurring during the vacuum drying prior to TGA analysis. Moreover, the evolution of the diffractogram of the recrystallized solid upon heating (5 °C/min) to 60 °C – i.e. in the temperature range, in which the water loss was observed – is also reported in Figure 11. It shows the progressive appearance and disappearance of some Bragg peaks, which ultimately leads to a X-ray diffraction patterns characteristic of Form II. All these results, thus, indicate that the amorphous riboflavin dissolved in water, recrystallized toward a dihydrate form, whose dehydration upon heating led to the metastable anhydrous Form II. Please note that identical behaviors were observed for samples, which recrystallized after the dissolution of Forms II and III. The precipitation of the same dihydrate form upon dissolution of amorphous riboflavin and Forms II and III can explain the similar plateau values observed at late time points for these different forms.

4. Conclusion

Amorphous riboflavin (free base) could be obtained for the first time: via high energy milling of a commercial crystalline form (Form I). This solid state amorphization technique was used to avoid the pronounced degradation of the riboflavin, which occurs during melting (and, thus, prevents obtaining the amorphous form via quench cooling of the melt). The glass transition temperature (Tg = 144°C) and the Cp jump at Tg (ΔCp= 0.68 J/g/°C) could, hence, accurately be determined.

Upon heating, amorphous riboflavin was found to show a rich pattern of physical transformations which enlightens the polymorphism of this vitamin. It shows in particular a recrystallization toward Form III occurring at 185 °C (ΔH_1 = 58.2 J/g), followed by a polymorphic transformation toward Form II occurring at 230°C (ΔH_2 = 34.1 J/g). These two forms appear to be enantiotropically related and the relative stability of the three polymorphs at room temperature appears to rank as follow: I > II > III.

Finally, the dissolution kinetics of the different forms in water were evaluated and revealed the following order in the dissolution rates during the first 4 h: amorphous>Forms III ≈ Form II>Form I. After 4 h, a drop in the amount of dissolved riboflavin occurred for the amorphous and metastable crystalline forms due to a recrystallization toward a dihydrate. However, the plateau values were above the solubility of Form I, revealing definitely the faster dissolution of the metastable forms (II, III and amorphous) over the stable crystalline Form I.

Acknowledgements

Declaration of Competing Interest

The Editor-in-Chief of the journal is one of the co-authors of this article. The manuscript has been subject to all of the journal's usual procedures, including peer review, which has been handled independently of the Editor-in-Chief.

CAPTIONS:

Figure 1: X-Ray diffraction patterns of riboflavin Form I recorded at room temperature before and after different mechanical and thermal treatments. From top to bottom: before milling (Form I); after 32 h milling (amorphous form); after 32 h milling and subsequent heating to 200°C (Form III); after 32 h milling and subsequent heating to 240°C (Form II).

Figure 2: TGA scan (5 °C/min) of commercial riboflavin (Form I) and DSC heating scans (5 °C/min) of non-milled (run 1) riboflavin as well as of milled riboflavin (Form I) (runs 2 and 3). The symbol (//) separates run 2 (using a standard open aluminum pan) from run 3 (using a hermetically sealed pan).

Figure 3: ^{1}H NMR spectra of riboflavin Form I non-milled (as received), quenched from the melt, milled for 32 h, as well as of riboflavin Form II and Form III. To better see the small peaks and avoid anarchic superimposition of the different spectra, the highest peaks have been clipped.

Figure 4: XRD patterns of riboflavin Form I recorded after different milling times (t_m) ranging from zero (no milling) to 32 h. The milling times are reported on the right-hand side of each diffraction pattern.

Figure 5: DSC scans (5 °C/min) of riboflavin Form I recorded after different milling times (t_m) ranging from zero (no milling) to 32 h. The milling times are reported on the left-hand side of each thermogram.

Figure 6: XRD patterns recorded at room temperature of riboflavin, which had been milled for 50 min, 6, 12 or 32 h, and subsequently heated (5 °C/min) to 210, 176, 195 or 200°C, respectively.

Figure 7: Flash DSC scans (300 °C/s) of Forms I, II and III of riboflavin.

Figure 8: Phase diagram of riboflavin. The arrows indicate the trajectory of riboflavin during the milling and subsequent heating of Form I.

Figure 9: SEM pictures of the different riboflavin powders used for dissolution measurements.

Figure 10: Dissolution kinetics of the different forms of riboflavin in ultra-pure water at 37°C under agitation (80 rpm) and non-sink conditions: A large excess of non-dissolved vitamin was provided throughout the experiments.

Figure 11: XRD patterns of the solid which reprecipitated during the dissolution study of amorphous riboflavin in water. The samples were heated at 5 °C/min followed by an isothermal of about 13 min (scan duration) at different temperatures (as indicated). Insert: TGA scan (5 °C/min) of the reprecipitated solid (without heating).
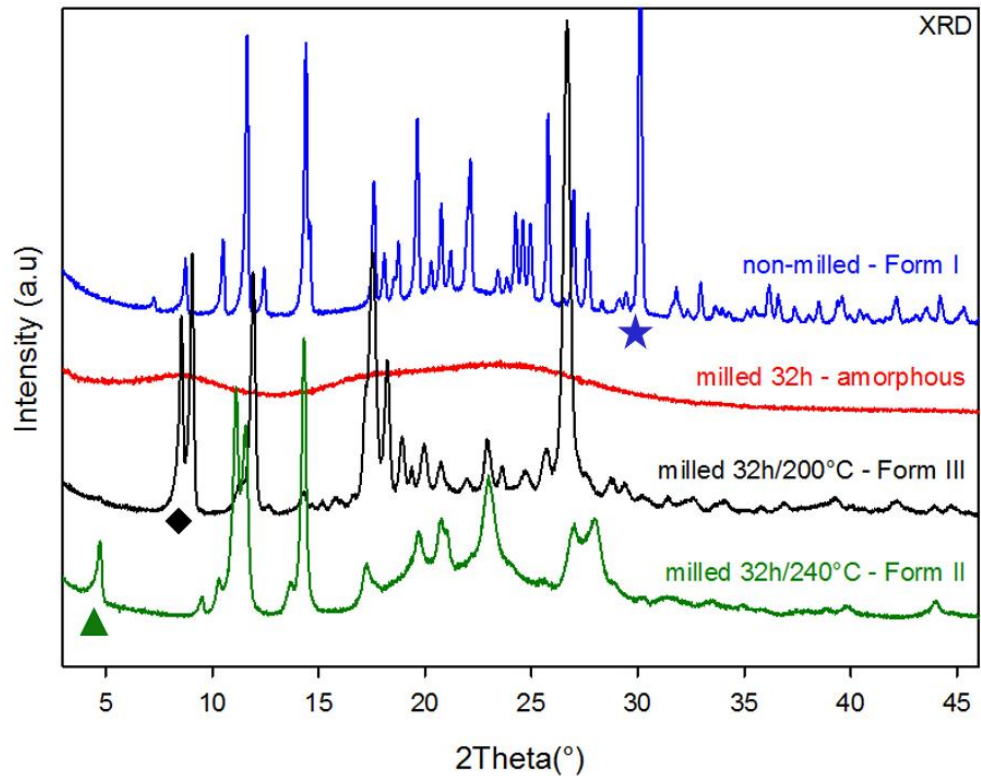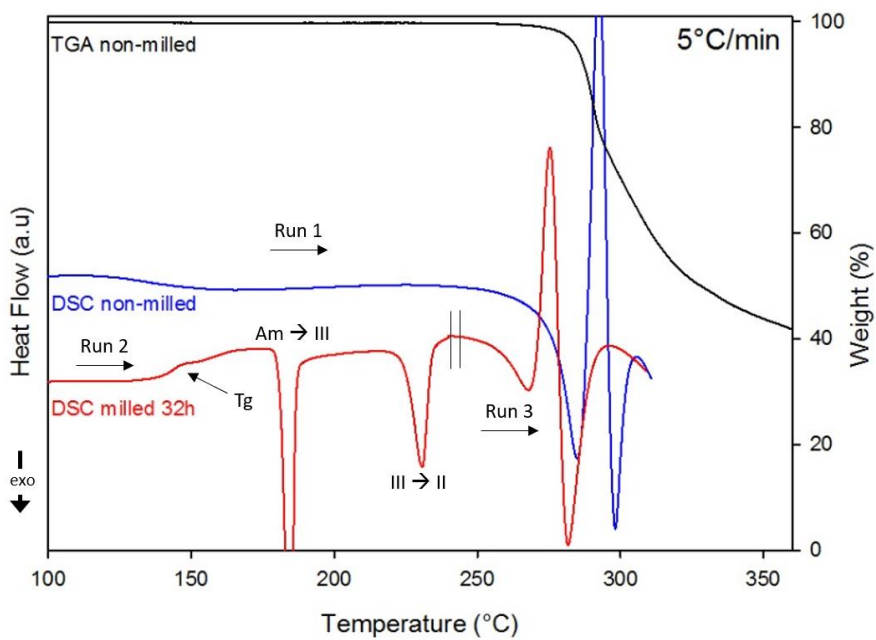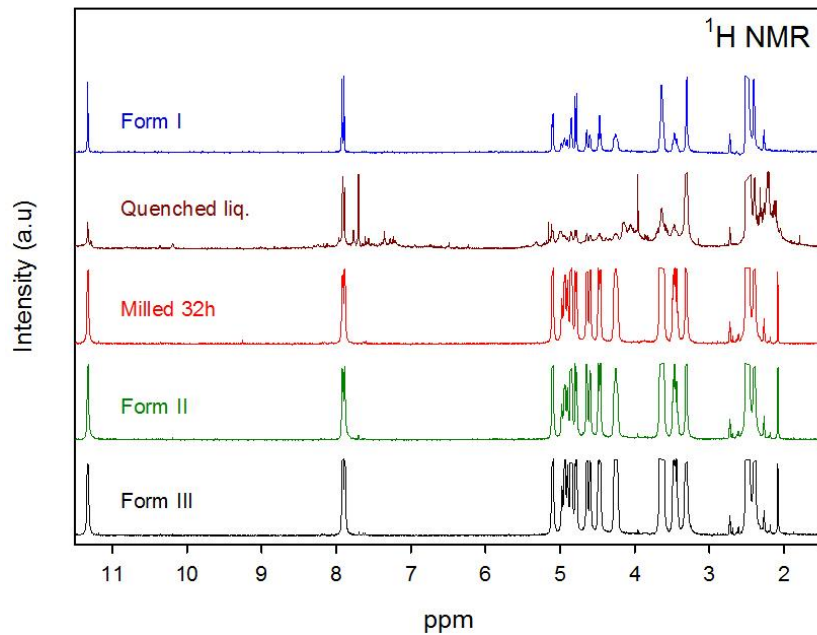
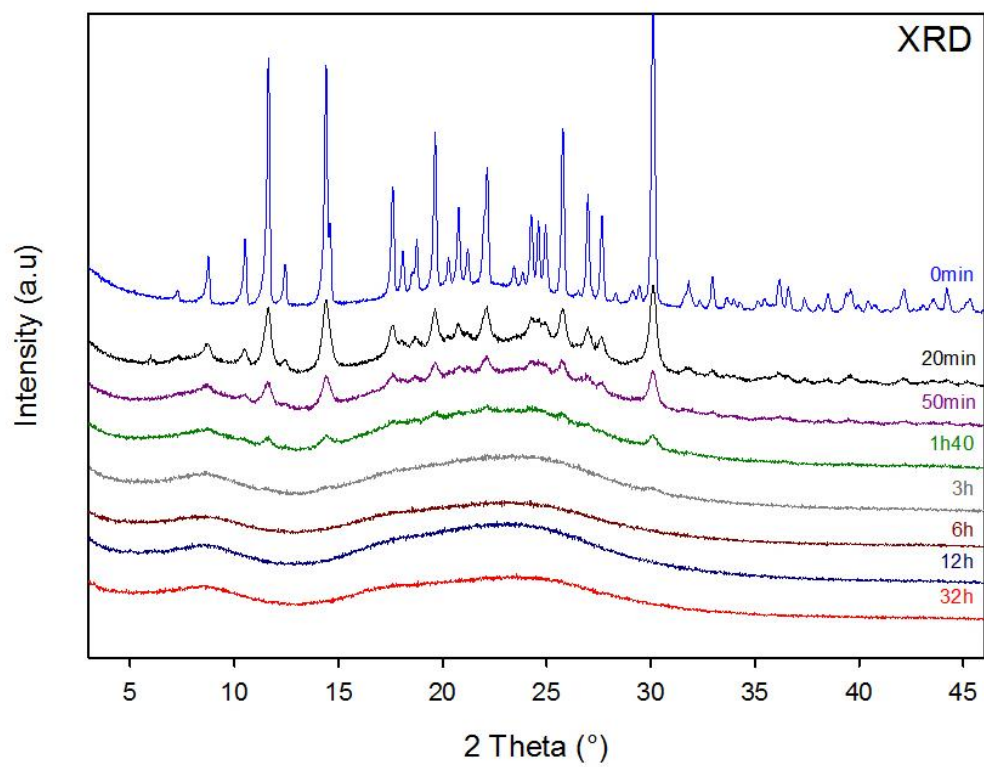# Figure 1

Figure 2

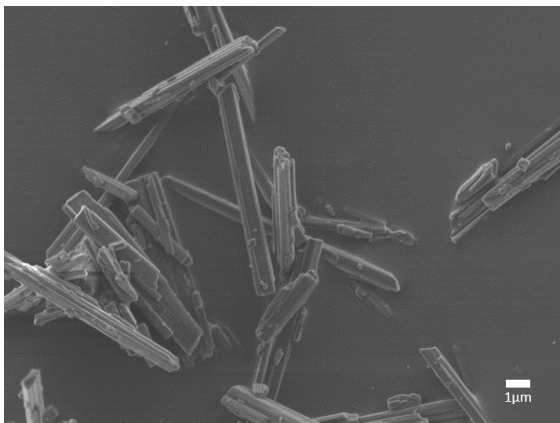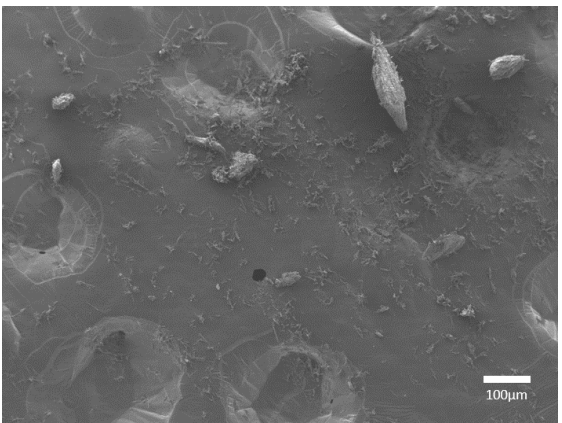# Figure 3

Figure 4

Figure 5
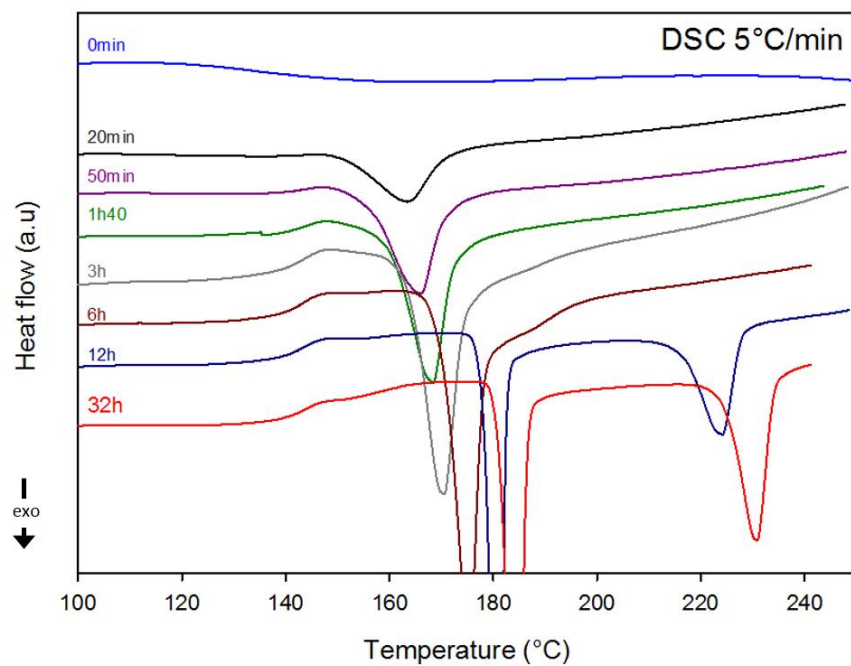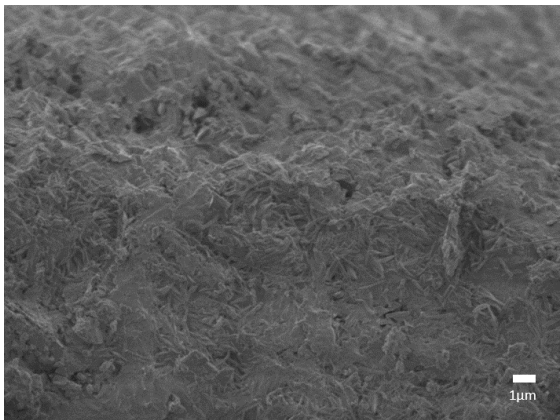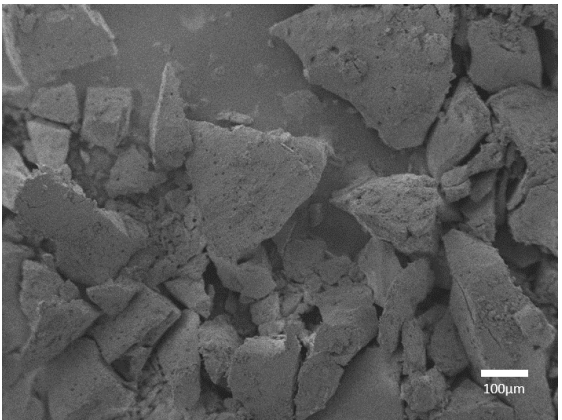

Figure 6
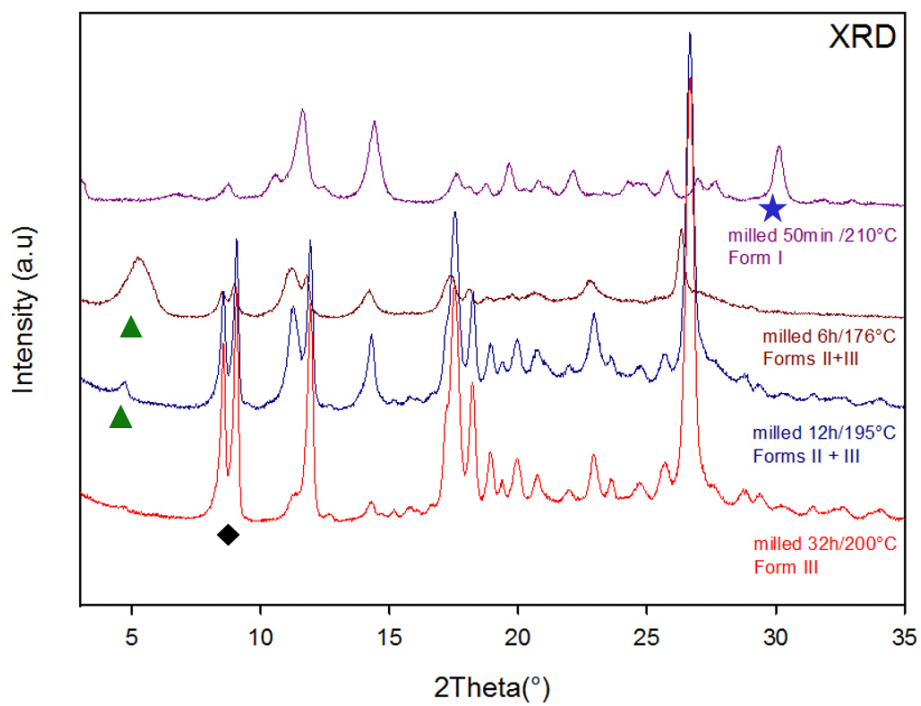
Figure 7
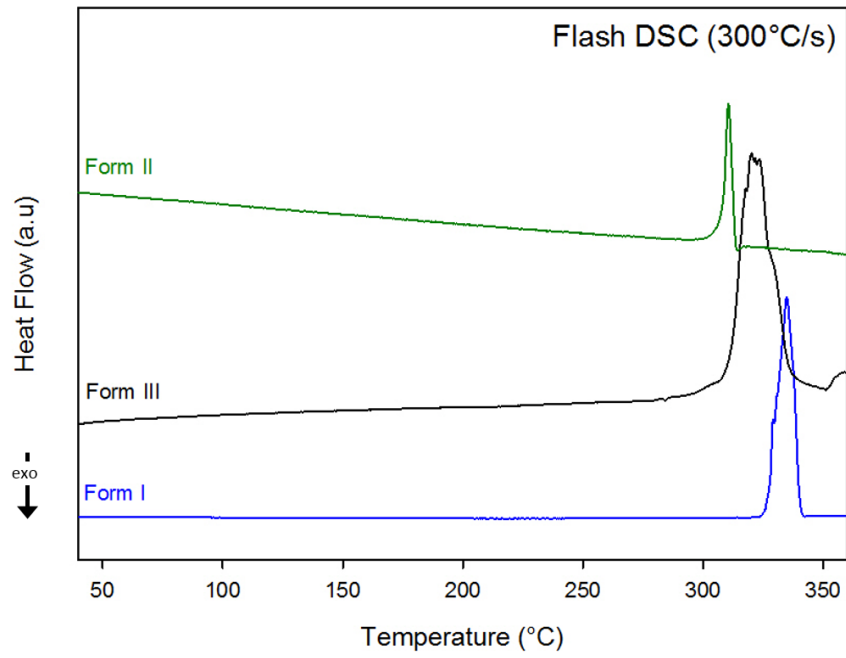
Figure 8
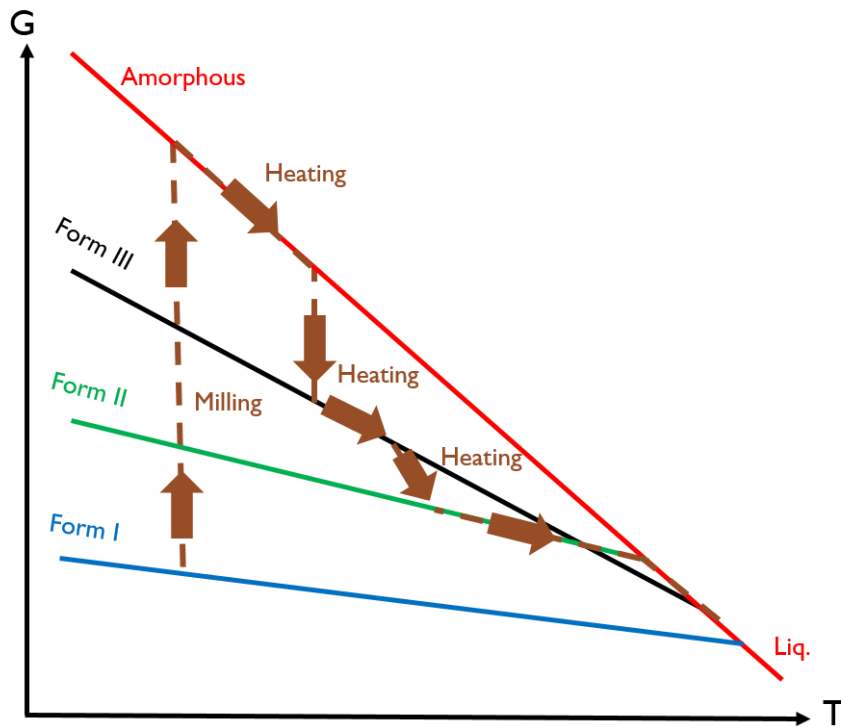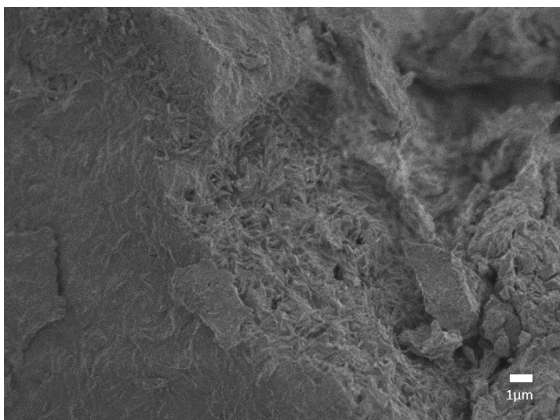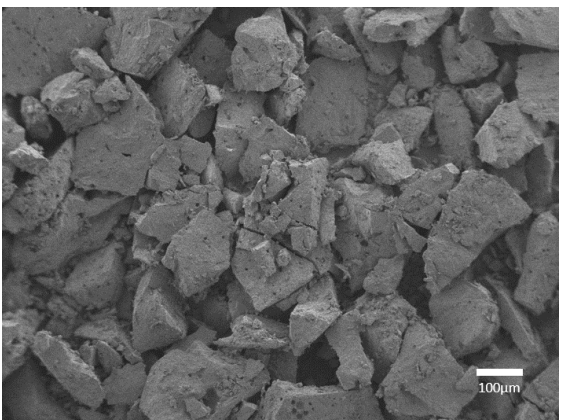
Figure 9

Amorphous
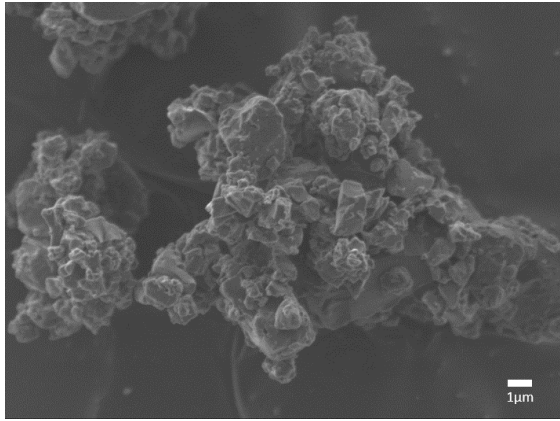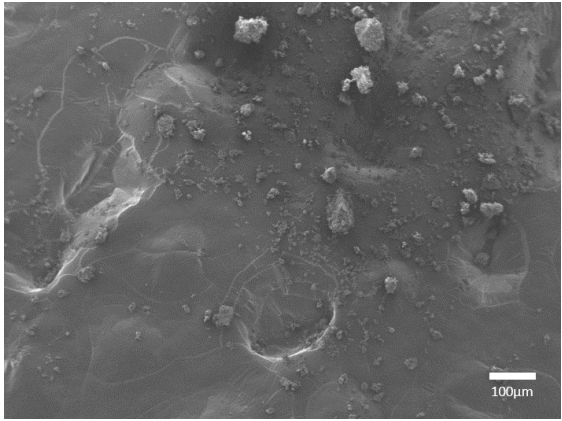
Form I

Form II

Form III

Figure 10

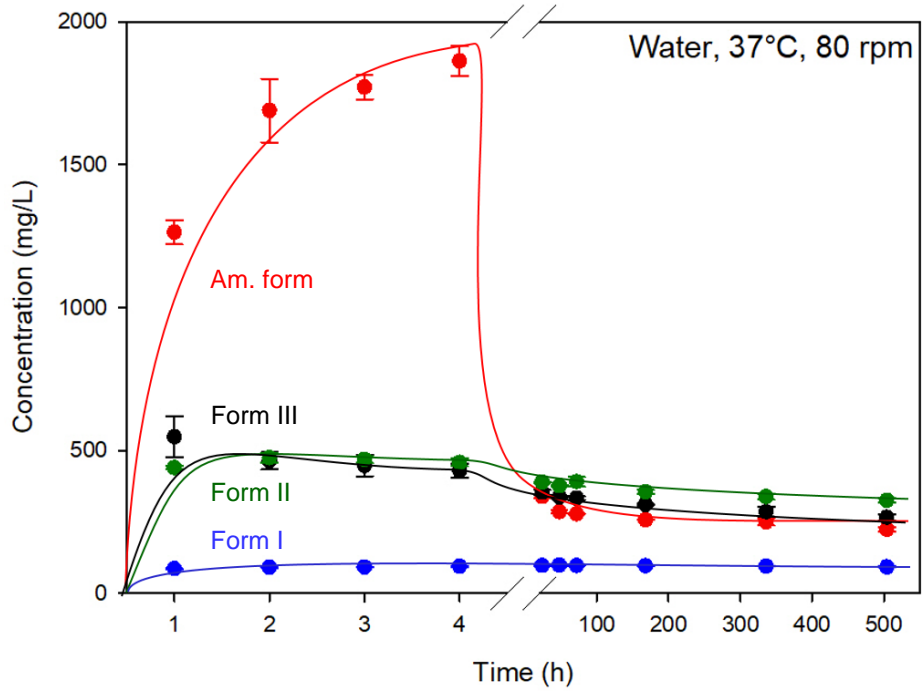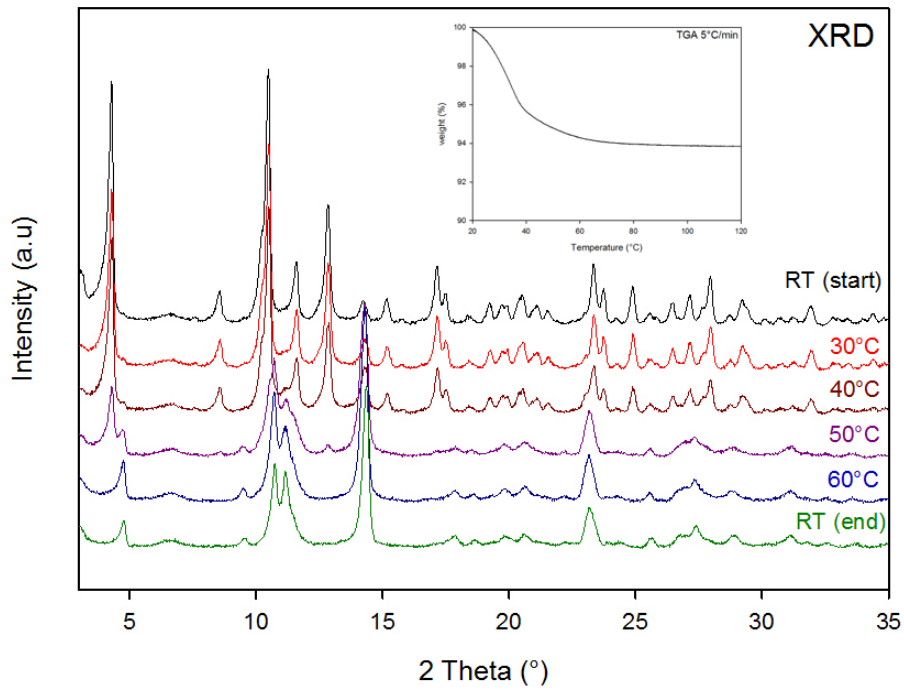# Figure 11

REFERENCES

[1] H. G. Brittain, *Polymorphism in pharmaceutical solids*. in Drugs and the pharmaceutical sciences. New York: M. Dekker, 1999. Accessed: Mar. 10, 2023. [Online]. Available: https://search.ebscohost.com/login.aspx?direct=true&scope=site&db=nlebk&db=nlabk&AN=12783

[2] R. Hilfiker, F. Blatter, and M. von Raumer, "Relevance of Solid-state Properties for Pharmaceutical Products," in *Polymorphism*, John Wiley & Sons, Ltd, 2006, pp. 1–19. doi: 10.1002/3527607889.ch1.

[3] R. J. Davey, "Polymorphism in Molecular Crystals Joel Bernstein. Oxford University Press, New York, 2002. ISBN 0198506058.," *Cryst. Growth Des.*, vol. 2, no. 6, pp. 675–676, Nov. 2002, doi: 10.1021/cg020039a.

[4] L. Yu, "Polymorphism in Molecular Solids: An Extraordinary System of Red, Orange, and Yellow Crystals," *Acc. Chem. Res.*, vol. 43, no. 9, pp. 1257–1266, Sep. 2010, doi: 10.1021/ar100040r.

[5] B. C. Hancock and G. Zografi, "Characteristics and significance of the amorphous state in pharmaceutical systems," *J. Pharm. Sci.*, vol. 86, no. 1, pp. 1–12, Jan. 1997, doi: 10.1021/js9601896.

[6] M. Descamps, E. Dudognon, and J.-F. Willart, *The amorphous state*. Wiley-VCH, 2019. doi: 10/18033.

[7] Y. Sun, L. Zhu, T. Wu, T. Cai, E. Gunn, and L. Yu, "Stability of Amorphous Pharmaceutical Solids: Crystal Growth Mechanisms and Effect of Polymer Additives," *AAPS J.*, vol. 14, pp. 380–8, Mar. 2012, doi: 10.1208/s12248-012-9345-6.

[8] K. A. Graeser, J. E. Patterson, and T. Rades, "Physical stability of amorphous drugs: Evaluation of thermodynamic and kinetic parameters," in *Journal of Pharmacy and Pharmacology*, PHARMACEUTICAL PRESS-ROYAL PHARMACEUTICAL SOC GREAT BRITIAN 1 LAMBETH HIGH …, 2008, pp. A46–A46.

[9] B. C. Hancock and M. Parks, "What is the true solubility advantage for amorphous pharmaceuticals?," *Pharm. Res.*, vol. 17, no. 4, pp. 397–404, Apr. 2000, doi: 10.1023/a:1007516718048.

[10] S. B. Murdande, M. J. Pikal, R. M. Shanker, and R. H. Bogner, "Solubility advantage of amorphous pharmaceuticals: I. A thermodynamic analysis," *J. Pharm. Sci.*, vol. 99, no. 3, pp. 1254–1264, Mar. 2010, doi: 10.1002/jps.21903.

[11] D. Q. Craig, P. G. Royall, V. L. Kett, and M. L. Hopton, "The relevance of the amorphous state to pharmaceutical dosage forms: glassy drugs and freeze dried systems," *Int. J. Pharm.*, vol. 179, no. 2, pp. 179–207, Mar. 1999, doi: 10.1016/s0378-5173(98)00338-x.

[12] A. Mahieu, J. Willart, E. Dudognon, F. Danède, and M. Descamps, "A New Protocol To Determine the Solubility of Drugs into Polymer Matrixes," *Mol. Pharm.*, vol. 10, Dec. 2012, doi: 10.1021/mp3002254.

[13] M. Davis and G. Walker, "Recent strategies in spray drying for the enhanced bioavailability of poorly water-soluble drugs," *J. Control. Release Off. J. Control. Release Soc.*, vol. 269, pp. 110–127, Jan. 2018, doi: 10.1016/j.jconrel.2017.11.005.

[14] J. E. Patterson, M. B. James, A. H. Forster, R. W. Lancaster, J. M. Butler, and T. Rades, "Preparation of glass solutions of three poorly water soluble drugs by spray drying, melt extrusion and ball milling," *Int. J. Pharm.*, vol. 336, no. 1, pp. 22–34, May 2007, doi: 10.1016/j.ijpharm.2006.11.030.

[15] A. T. Serajuddin, "Solid dispersion of poorly water-soluble drugs: early promises, subsequent problems, and recent breakthroughs," *J. Pharm. Sci.*, vol. 88, no. 10, pp. 1058–1066, Oct. 1999, doi: 10.1021/js980403l.

[16] C. Tizaoui, H. Galai, S. Clevers, N. Couvrat, G. Coquerel, and I. B. Rietveld, "The persistence and crystallization behavior of atorvastatin calcium amorphous dispersions in polyvinylpyrrolidone," *J. Drug Deliv. Sci. Technol.*, vol. 72, p. 103375, Jun. 2022, doi: 10.1016/j.jddst.2022.103375.

[17] M. Bauer *et al.*, "On the dimorphism of prednisolone: The topological pressure-temperature phase diagram involving forms I and II," *Int. J. Pharm.*, vol. 624, p. 122047, Aug. 2022, doi: 10.1016/j.ijpharm.2022.122047.

[18] M. A. Neumann, J. van de Streek, F. P. A. Fabbiani, P. Hidber, and O. Grassmann, "Combined crystal structure prediction and high-pressure crystallization in rational pharmaceutical polymorph screening," *Nat. Commun.*, vol. 6, no. 1, Art. no. 1, Jul. 2015, doi: 10.1038/ncomms8793.

[19] R. Censi and P. Di Martino, "Polymorph Impact on the Bioavailability and Stability of Poorly Soluble Drugs," *Mol. Basel Switz.*, vol. 20, no. 10, pp. 18759–18776, Oct. 2015, doi: 10.3390/molecules201018759.

[20] A. Kapourani, T. Tzakri, V. Valkanioti, K. N. Kontogiannopoulos, and P. Barmpalexis, "Drug crystal growth in ternary amorphous solid dispersions: Effect of surfactants and polymeric matrix-carriers," *Int. J. Pharm. X*, vol. 3, p. 100086, Dec. 2021, doi: 10.1016/j.ijpx.2021.100086.

[21] J. Thiry *et al.*, "Continuous production of itraconazole-based solid dispersions by hot melt extrusion: Preformulation, optimization and design space determination," *Int. J. Pharm.*, vol. 515, no. 1, pp. 114–124, Dec. 2016, doi: 10.1016/j.ijpharm.2016.10.003.

[22] V. R. Kallakunta *et al.*, "Stable amorphous solid dispersions of fenofibrate using hot melt extrusion technology: Effect of formulation and process parameters for a low glass transition temperature drug," *J. Drug Deliv. Sci. Technol.*, vol. 58, p. 101395, Aug. 2020, doi: 10.1016/j.jddst.2019.101395.

[23] F. Pöstges, K. Kayser, E. Stoyanov, and K. G. Wagner, "Boost of solubility and supersaturation of celecoxib via synergistic interactions of methacrylic acid-ethyl acrylate copolymer (1:1) and hydroxypropyl cellulose in ternary amorphous solid dispersions," *Int. J. Pharm. X*, vol. 4, p. 100115, Dec. 2022, doi: 10.1016/j.ijpx.2022.100115.

[24] A. Ziaee, A. B. Albadarin, L. Padrela, A. Faucher, E. O'Reilly, and G. Walker, "Spray drying ternary amorphous solid dispersions of ibuprofen – An investigation into critical formulation

and processing parameters," *Eur. J. Pharm. Biopharm.*, vol. 120, pp. 43–51, Nov. 2017, doi: 10.1016/j.ejpb.2017.08.005.

[25]   A. Ousset *et al.*, "Development of a small-scale spray-drying approach for amorphous solid dispersions (ASDs) screening in early drug development," *Pharm. Dev. Technol.*, vol. 24, pp. 1–47, Oct. 2018, doi: 10.1080/10837450.2018.1534861.

[26]   A. Alqurshi, K. L. A. Chan, and P. G. Royall, "In-situ freeze-drying - forming amorphous solids directly within capsules: An investigation of dissolution enhancement for a poorly soluble drug," *Sci. Rep.*, vol. 7, 2017, doi: 10.1038/s41598-017-02676-2.

[27]   E. Valkama, O. Haluska, V.-P. Lehto, O. Korhonen, and K. Pajula, "Production and stability of amorphous solid dispersions produced by a Freeze-drying method from DMSO," *Int. J. Pharm.*, vol. 606, p. 120902, Sep. 2021, doi: 10.1016/j.ijpharm.2021.120902.

[28]   K. Kondo and T. Rades, "Solventless amorphization and pelletization using a high shear granulator. Part I; feasibility study using indomethacin," *Eur. J. Pharm. Biopharm.*, vol. 181, pp. 147–158, Dec. 2022, doi: 10.1016/j.ejpb.2022.11.010.

[29]   J.-F. Willart, M. Durand, L.-E. Briggner, A. Marx, F. Danède, and M. Descamps, "Solid-state amorphization of linaprazan by mechanical milling and evidence of polymorphism," *J. Pharm. Sci.*, vol. 102, no. 7, pp. 2214–2220, Jul. 2013, doi: 10.1002/jps.23573.

[30]   J. C. Dinunzio, C. Brough, J. R. Hughey, D. A. Miller, R. O. Williams, and J. W. McGinity, "Fusion production of solid dispersions containing a heat-sensitive active ingredient by hot melt extrusion and Kinetisol dispersing," *Eur. J. Pharm. Biopharm. Off. J. Arbeitsgemeinschaft Pharm. Verfahrenstechnik EV*, vol. 74, no. 2, pp. 340–351, Feb. 2010, doi: 10.1016/j.ejpb.2009.09.007.

[31]   N. Le Barc'H, J. M. Grossel, P. Looten, and M. Mathlouthi, "Kinetic study of the mutarotation of D-glucose in concentrated aqueous solution by gas-liquid chromatography," *Food Chem.*, vol. 74, no. 1, pp. 119–124, Jul. 2001, doi: 10.1016/S0308-8146(01)00139-X.

[32]   World Health Organization and Food and Agriculture Organization of the United Nations, Eds., *Vitamin and mineral requirements in human nutrition*, 2nd ed. Geneva : Rome: World Health Organization ; FAO, 2004.

[33]   S. S. de Farias *et al.*, "Microencapsulation of riboflavin with galactomannan biopolymer and F127: Physico-chemical characterization, antifungal activity and controlled release," *Ind. Crops Prod.*, vol. 118, pp. 271–281, Aug. 2018, doi: 10.1016/j.indcrop.2018.03.039.

[34]   A. R. Bourgonje *et al.*, "The effect of riboflavin supplementation on the systemic redox status in healthy volunteers: A post-hoc analysis of the RIBOGUT trial," *Free Radic. Biol. Med.*, vol. 190, pp. 169–178, Sep. 2022, doi: 10.1016/j.freeradbiomed.2022.08.008.

[35]   R. E. Coffman and D. O. Kildsig, "Effect of Nicotinamide and Urea on the Solubility of Riboflavin in Various Solvents," *J. Pharm. Sci.*, vol. 85, no. 9, pp. 951–954, Sep. 1996, doi: 10.1021/js960012b.

[36]   J. A. Means, T. C. Grenfell, and F. H. Hedger, "Polymorphism of Riboflavin," *J. Am. Pharm. Assoc. Sci. Ed*, vol. 32, no. 2, pp. 51–53, Feb. 1943, doi: 10.1002/jps.3030320205.

[37]   A. Gloor, "Process for the purification of riboflavin," US7670800B2, Mar. 02, 2010 Accessed: May 22, 2023. [Online]. Available: https://patents.google.com/patent/US7670800B2/en

[38]   M. Guerain *et al.*, "Structure determination of riboflavin by synchrotron high-resolution powder X-ray diffraction," *Acta Crystallogr. Sect. C*, vol. 77, no. 12, pp. 800–806, 2021, doi: 10.1107/S2053229621012171.

[39]   J. Koziol, "Studies on Flavins in Organic Solvents-I*. Spectral Characteristics of Riboflavin, Riboflavin Tetrabutyrate and Lumichrome," *Photochem. Photobiol.*, vol. 5, no. 1, pp. 41–54, 1966, doi: 10.1111/j.1751-1097.1966.tb05759.x.

[40]   A. Dupont, M. Guerain, F. Danède, and J. F. Willart, "Evidence of transient amorphization during the polymorphic transformation of sorbitol induced by milling," *Int. J. Pharm.*, vol. 623, p. 121929, Jul. 2022, doi: 10.1016/j.ijpharm.2022.121929.

[41]   L. T. Ferreira, R. T. Alarcon, G. L. Perpétuo, and G. Bannach, "Investigation and characterization by TG/DTG–DTA and DSC of the fusion of Riboflavin, and its interaction with the antibiotic norfloxacin in the screening of cocrystal," *J. Therm. Anal. Calorim.*, vol. 136, no. 2, pp. 581–588, Apr. 2019, doi: 10.1007/s10973-018-7696-7.

[42]   E. Elisei, J.-F. Willart, F. Danède, J. Siepmann, F. Siepmann, and M. Descamps, "Crystalline Polymorphism Emerging From a Milling-Induced Amorphous Form: The Case of Chlorhexidine Dihydrochloride," *J. Pharm. Sci.*, vol. 107, no. 1, pp. 121–126, Jan. 2018, doi: 10.1016/j.xphs.2017.07.003.

[43]   N. R. Babij *et al.*, "NMR Chemical Shifts of Trace Impurities: Industrially Preferred Solvents Used in Process and Green Chemistry," *Org. Process Res. Dev.*, vol. 20, no. 3, pp. 661–667, Mar. 2016, doi: 10.1021/acs.oprd.5b00417.

Abstract

Poor aqueous drug solubility is a major hurdle for the development of innovative medical treatments. This thesis project is dedicated to optimizing the therapeutic efficacy of two model drugs whose crystalline forms exhibit a very low solubility: chlorhexidine (free base) and riboflavin (free base). The aim is to improve the solubility of these drugs by formulating them in an amorphous state as molecular dispersions in a polymer matrix. To that extend, detailed characterization of the physical properties of the stable crystalline drugs, their metastable polymorphic forms, and their amorphous forms obtained directly in the solid state by mechanical milling were required. Moreover, an evaluation of their respective dissolution kinetics was performed. In addition, the possibility of producing molecular dispersions of each drug in polymeric matrices (PVPK12 and Lycoat RS720) in the solid state by mechanical milling was demonstrated, and their release kinetics determined. These dissolution kinetics were compared with those of a physical mixture in which the drug is crystalline and of a physical mixture in which the drug is amorphous, in order to determine both the influence of the drug's physical state and to assess the advantage of having the amorphous drug molecularly dispersed in the polymer. The physical characterizations are performed using TGA, XRD, DSC and SEM and the dissolution performances are evaluated using different experimental set-ups including: powder dissolution, intrinsic dissolution and tablet dissolution.

Résumé

La faible solubilité de certains médicaments en milieu aqueux est un obstacle majeur pour le développement de traitements médicamenteux innovants. Ce projet de thèse est dédié à l'optimisation de l'efficacité thérapeutique de deux principes actifs modèles dont les formes cristallines sont très peu solubles : la chlorhexidine (base libre) et la riboflavine (base libre). L'objectif est d'améliorer la solubilité de ces principes actifs en les formulant à l'état amorphe sous formes de dispersions moléculaires dans une matrice de polymère. Cela a nécessité une caractérisation préalable fine des propriétés physiques des principes actifs cristallins stables, de leurs formes polymorphiques métastables, et de leurs formes amorphes obtenues directement à l'état solide par broyage mécanique. De plus, leurs cinétiques de dissolution respectives ont été déterminées. Par ailleurs, la possibilité de réaliser des dispersions moléculaires avec chaque principe actif dans des matrices polymères (PVPK12 et Lycoat RS720) à l'état solide par broyage mécanique a été démontrée et leurs cinétiques de libération respectives ont été déterminées. Ces cinétiques ont été comparées à celles d'un mélange physique dans le lequel le principe actif est cristallin et à celles d'un mélange physique dans lequel le principe actif est amorphe. De cette manière il a été possible à la fois de déterminer l'influence de l'état physique du principe actif et d'évaluer l'avantage de former une dispersion moléculaire amorphe du principe actif dans la matrice de polymère. Les caractérisations physiques sont effectuées en utilisant les techniques suivantes : ATG, RX, DSC et les performances de dissolution sont évaluées en utilisant différentes techniques expérimentales telles que : la dissolution des poudres, la dissolution intrinsèque et la dissolution de comprimés.